

The loading path dependence of sand constitutive behaviour and its relationship with pressure dip in sand piles

By

Qiong Xiao

B.Eng, M.Sc

Thesis submitted to the University of Nottingham

for the degree of Doctor of Philosophy

June 2017

Declaration

This thesis entitled "The loading path dependence of sand constitutive behaviour and its relationship with pressure dip in sand piles" is submitted to the Department of Civil Engineering, The University of Nottingham, for the degree of Doctor of Philosophy.

The work in this thesis was completed solely by Qiong Xiao, under the supervision of Dr. Xia Li and Prof. Hai-Sui Yu. Where other sources were used, full references are given.

Qiong Xiao

June 2017

Acknowledgements

I would like to express my sincerest thanks to my supervisors, Dr. Xia Li and Prof. Hai-Sui Yu, for their patient guidance, valuable advice, understanding and encouragement during my PhD study. Their great supervision and working attitude not only have enlightened my research but also will encourage me in the future when pursuing a career in geotechnical engineering.

I am deeply grateful to the University of Nottingham for the financial support from the Dean of Engineering Research Scholarship for International Excellence to carry out this project. My deepest gratitude also extends to my internal examiner, Dr. Paul Langston. His valuable suggestions on the technical contents have been helpful.

I am also sincere grateful to the University of Nottingham High Performance Computing Facility, which improved the simulation efficiency greatly.

Moreover, to the colleagues in the Nottingham Centre for Geotechnical (NCG) for the fun and memorable time shared with you. Appreciation also goes to Dr. Peng Yue and Mrs Jingyi Shen for their continued support and friendship over these years.

Last but not least, I would like to thank my parents for their endless love, unconditional support and encouragement through this long and challenging period in my life.

Abstract

The subject of granular materials attracts substantial interests from both the academic and engineering communities. Their ubiquitous existences in nature and industries certify their engineering importance. Although relatively straightforward at the particle scale, the collective response of granular materials could be very complicated. The pressure dip under a sand pile is one among many intriguing phenomena that granular materials exhibit. It refers to a small dip in pressure appearing underneath the sand pile with the peak pressure observed away from the centre of the sand pile. Since first reported by Hummel and Finnan (1920), this counter-intuitive phenomenon has attracted extensive research endeavours in the past few decades. It is now generally believed that the construction history is crucial to the pressure dip formation, but a quantitative explanation is not yet available.

An in-depth explanation in pressure dip formation would range three different scales: the particle-scale, the continuum-scale when the material could be treated as a representative volume element (RVE) and the system scale, in this case, the scale of the sand pile. Discrete element method (DEM) is a great tool in the study of granular materials by modelling it directly from the particle scale. This research sets out to investigate the pressure dip formation of granular materials using the discrete element method.

It is however noted that the dimension of the system that DEM can practically simulate is limited. Therefore, the research project is achieved by conducting DEM simulation of sand pile and DEM simulation of elementary behaviour in parallel. Numerical experiments have been carried out using discrete element method to simulate the formation of sand pile in the three-dimension (particle diameter of $[1.2 \pm 0.4] mm$) with the base plane diameter of $260 mm$, following three different procedures: a) boundary removal method; b) rain

deposition and c) point deposition. Pressure dip phenomenon is observed following the point deposition but not the boundary removal method and rain deposition method. The stress distribution of invariants p,q,b are studied within the sand pile at the final stage. The boundary removal method and rain deposition method result in a larger confining pressure and deviatoric stress in the centre than the point deposition method, with b value approximately 0.2 for the three methods. This differences in pressure profiles suggest that the history dependence and the loading path dependence of granular materials play a central role in explaining the pressure dip formation.

Discrete element simulations have also been conducted to investigate the RVE stress-strain responses of the granular materials. The numerical algorithm previously proposed by Li et al. (2013; 2016) has been implemented in LIGGGHTS. Numerical experiments have been conducted to study the effect of void ratio and the intermediate principal stress ratio b on the material response to proportional loading, as well as to non-proportional loading using the radius expansion method. It shows the peak and critical stress ratio are both decreased with the increase of b value. With regards to the non-proportional loading path, significant plastic deformation is observed especially with a larger stress ratio.

The packing following all the three construction methods are in a loose state. And their initial structures are different from that following the radius expansion method. A sample is extracted from the deposited specimen under the boundary removal method to study the impact of the initial state. A smaller shear stress with a larger void ratio is observed for the deposited sample than the radius expansion prepared sample for the triaxial shear. Furthermore, under the rotation shear, the size of strain trajectory is increased larger for the deposited sample when increases the stress ratio.

The "stress-force-fabric" (SFF) relationship is employed to interpret the effect of internal structure on material constitutive behaviour. Due to the higher value of average particle size and larger probability of strong contact force for the deposited sample, it produces a larger average coordination number and directional averaged contact force, accompanied with a smaller degree of fabric anisotropy and contact force anisotropy. This may be the reason of the lower shear resistance during shearing.

Post-processing of the particle-level stress data from the sand pile simulations suggests that granular materials form different internal structure and experience different stress history following different construction methods. For the point deposition, a larger magnitude of σ_{rz} and a higher degree of fabric anisotropy are observed in the central region at the progressive stages. It implies that the constitutive phenomenon has a relationship with the path of the construction history. In addition, the point deposition test also generates a larger rotation of the major principal stress direction than the boundary removal and rain deposition tests. According to RVE simulations, it suggests the granular materials are under a triaxial compression loading path and a rotational loading path underneath the apex for the rain deposition and point deposition respectively. This increases the probability of forming arches and granular materials may experience a higher plastic deformation underneath the central apex during the point deposition.

The particle-scale mechanism has been carried out to study the material behaviour with the loading path dependence of sand pile. Different stress field is observed with various construction histories. It demonstrates the pressure dip phenomenon may relate to the memory of the fabric anisotropy and the potential effect of plastic deformation. Moreover, a better understanding in this problem is believed to improve the problems of silos,

retaining wall and embankments. It may be useful for the development of constitutive modelling of the stress field.

Table of contents

Declaration ..... **I**

Acknowledgements ..... **III**

Abstract ..... **V**

Table of contents ..... **IX**

List of figures ..... **XV**

List of tables ..... **XXIII**

Nomenclature ..... **XXV**

Chapter 1 Introduction **1**

1.1 Background and motivation 1

1.2 Scope of the research 2

1.3 Aims and objectives 3

1.4 Thesis structure 4

Chapter 2 Literature review **7**

2.1 Introduction 7

2.2 The pressure dip phenomenon in sand pile 8

2.2.1 Experimental observations 8

2.2.2 Analytical explanations 16

2.2.3 Numerical investigations 23

2.3 Constitutive behaviour of granular materials 31

2.3.1 Anisotropy of granular materials 32

2.3.2 Loading-path dependence of granular materials 35

2.4 Micro-scale observations and "SFF" relationship 41

2.4.1 Experimental study on fabric 42
2.4.2 Fabric of granular material 43
2.4.3 Directional distribution of vectors 46
2.4.4 Particle-scale observations on material responses 47
2.4.5 Stress-force-fabric relationship 53
2.5 Summary 56
Chapter 3 Methodology 59
3.1 Principles of DEM 60
3.1.1 Calculation cycle 60
3.1.2 Calculation of Motion 61
3.1.3 Contact constitutive model 62
3.1.4 Damping 70
3.1.5 Mechanical time-step determination 70
3.1.6 The development and availability DEM software 72
3.2 LIGGGHTS 73
3.2.1 Contact models in LIGGGHTS 73
3.2.2 Damping model in LIGGGHTS 77
3.2.3 Time-step in LIGGGHTS 79
3.2.4 Procedures to run a LIGGGHTS simulation 80
3.3 Numerical algorithm to simulate elementary behaviour 81
3.3.1 The polyhedral boundary 83
3.3.2 Evaluation of strain and stress behaviour 88
3.3.3 Applying a loading increment 92
3.4 Summary 95
Chapter 4 Sand pile simulation 97
4.1 Introduction 97
4.2 Material properties 98
4.3 Boundary removal test 102
4.3.1 Implementation of the numerical model 102
4.3.2 Observation of sand pile formation 105

4.3.3 Final base pressure profile 108
4.3.4 Progressive development of base pressure profile 112
4.4 Rain deposition test 115
4.4.1 Implementation of the numerical model 115
4.4.2 Observation of sand pile formation 117
4.4.3 Final base pressure profile 118
4.4.4 Progressive development of base pressure profile 120
4.5 Point deposition test 121
4.5.1 Implementation of the numerical model 121
4.5.2 Observation of sand pile formation 123
4.5.3 Final base pressure profiles 124
4.5.4 Progressive development of base pressure profile 125
4.6 Discussion of sand pile following different construction histories 127
4.7 Summary 133

Chapter 5 Numerical implementation of elementary test in LIGGGHTS135

5.1 Introduction 135
5.2 Implementation in LIGGGHTS 136
5.2.1 Boundary formation 138
5.2.2 Control of boundary 138
5.2.3 Control of loading 139
5.2.4 Servo-control of different stages 140
5.3 Validation with previous simulation results 142
5.3.1 Material properties 142
5.3.2 Sample generation stage 143
5.3.3 Drained triaxial shear test 144
5.3.4 Drained rotational shear test 148
5.4 Observations on the sample uniformity 152
5.4.1 Material properties 153
5.4.2 Sample generation stage 153
5.4.3 Consolidation stage 154
5.4.4 Drained triaxial shear tests 159

5.4.5 Drained rotation shear tests 163
5.5 Summary 166
Chapter 6 Constitutive behaviour of granular materials **169**
6.1 Introduction 169
6.2 Macro-scale observations 170
6.2.1 Impact of void ratio 171
6.2.2 Impact of the intermediate principal stress ratio 172
6.2.3 Drained rotation shear 174
6.3 Micro-scale observations 178
6.3.1 Stress-force-fabric relationship 178
6.3.2 Impact of void ratio 182
6.3.3 Impact of intermediate principal stress ratio 186
6.3.4 Drained rotational shear test 190
6.4 Impact of initial structure 191
6.4.1 Macro-scale observations 192
6.4.2 Micro-scale observations 198
6.5 Summary 204
Chapter 7 Interpretations of material response and pressure dip phenomenon **207**
7.1 Introduction 207
7.2 Loading history dependence of sand pile 208
7.2.1 Progressive force chains network 208
7.2.2 Observations of stress distribution 210
7.2.3 Spatial distribution of the stress behaviour 211
7.2.4 The stress behaviour at representative element regions 225
7.3 Comparison with the continuum theory 228
7.4 Observations of internal structure 230
7.4.1 Progressive distribution of average coordination number 230
7.4.2 Progressive spatial distribution of fabric anisotropy 234
7.5 Observations of contact force behaviour 249

7.6 Summary 255

Chapter 8 Conclusions and future work **259**

8.1 Observations of sand piles 259

8.2 Three-dimensional developed numerical algorithm 260

8.3 Constitutive material behaviour 260

8.4 Interpretation the pressure dip phenomenon of sand pile 261

8.5 Recommendations for future work 263

Appendix **267**

A. Sand pile **267**

A.1 Impact of friction coefficient 267

A.2 Preliminary tests of boundary removal method 268

B. Developed technique for RVE material behaviour **278**

B.1 Information of the algorithm in LIGGGHTS 278

C. Particle-scale mechanisms of sand piles **279**

C.1 The stress behaviour at different representative element regions 279

References **283**

List of figures

Chapter 2

Figure 2.1 Vertical pressure distribution on the base plate (Smid and Novosad, 1981) 9

Figure 2.2 Sand pile generates with different construction histories (after Vanel et al., 1999) 10

Figure 2.3 Wedge-shape piles form with different construction histories (after Vanel et al., 1999) 11

Figure 2.4 Contact orientations distribution with different pouring methods: 12

Figure 2.5 Pressure profile with the influence of base plane deflection (Ooi et al., 2008) 13

Figure 2.6 The probability of chains orientation inside the sand pile:.....14

Figure 2.7 The mean orientation angle with the distance to the centre: 15

Figure 2.8 Regular packing of sand pile 17

Figure 2.9 The coordinate system for stress-continuity equation (Wittmer et al., 1997) 18

Figure 2.10 The FPA model for pressure dip phenomenon (after Wittmer et al., 1996).....21

Figure 2.11 The stress distribution inside sand pile (Ai et al., 2013) 25

Figure 2.12 The principal axes of stress inside the sand pile: 26

Figure 2.13 Contact orientations for concentrated and distributed deposition (Ai et al., 2011) 28

Figure 2.14 Contact force orientation for concentrated and distributed deposition (Ai et al., 2011) 28

Figure 2.15 The orientation distribution with various aspect ratio (Zhu et al., 2013) 29

Figure 2.16 The probability distribution of contact force (Zhu et al., 2013) 30

Figure 2.17 The stress-strain behaviour with plane strain test (Oda et al., 1978) 36

Figure 2.18 Stress ratio behaviour on the direction of principal stress axes (Miura et al., 1986) 37

Figure 2.19 The strain increment in the stress space (Miura et al., 1986) 39

Figure 2.20 The changes of principal stress directions under the construction of embankment 40

Figure 2.21 The evolution of strain trajectory with various void ratio (Yu et al., 2015).....41

Figure 2.22 Definition of contact normal, contact force and contact vector 45

Figure 2.23 The deviatoric magnitude of fabric and force anisotropy under the 48

Figure 2.24 The deviatoric magnitude of fabric and force anisotropy under the 49

Figure 2.25 The distribution of fabric for the dense sample under drained triaxial test 50

Figure 2.26 The strain trajectory (a) dense sample; (b) loose sample (Yang et al., 2015) 52

Figure 2.27 The trajectory of contact normal for the dense and loose samples (Yang, et al., 2015) 52

Figure 2.28 Distribution of contact normal, average normal and tangential force at peak in .54

Chapter 3

Figure 3.1 One DEM calculation cycle (after Itasca,1999) 61

Figure 3.2 The forces and torques acting on the particle i from contacting particle j 62

Figure 3.3 Normal contact force (Johnson, 1985) 63

Figure 3.4 The tangential contact force (Johnson, 1985).....66

Figure 3.5 The estimation of the contact force in LIGGGHTS 76

Figure 3.6 The relationship of the restitution coefficient and damping constant (Tsuji et al., 1992) 77

Figure 3.7 The velocities of two contacted particles (Vu-Quoc and Zhang, 1999) 78

Figure 3.8 The simulation procedures in LIGGGHTS 82

Figure 3.9 One cycle of a loading step.....83

Figure 3.10 Polyhedral boundary formed with N=12 84

Figure 3.11 The convex polyhedron with labelling IDs of Figure 3.10 86

Figure 3.12 Volume calculation with ID 1 88

Chapter 4

Figure 4.1 The baffle boundary and base plane boundary in the horizontal and vertical directions 101
Figure 4.2 The numerical model of boundary removal test (unit: mm) 104
Figure 4.3 The progressive behaviour during sand pile formation 106
Figure 4.4 The information of sand pile at the final stage 107
Figure 4.5 The stress distribution on the base plane with the average scheme method 108
Figure 4.6 An example of Voronoi tessellation generation 109
Figure 4.7 The pressure profile on the base plane at the final stage 110
Figure 4.8 The evolution of shear stress with the radius distances 111
Figure 4.9 The progressive pressure profiles on the base plane 113
Figure 4.10 The pressure profiles on the base plane for the boundary removal method 114
Figure 4.11 The numerical model of rain deposition test 115
Figure 4.12 The progressive behaviour during sand pile formation 117
Figure 4.13 The shape of the sand pile for the rain deposition method 118
Figure 4.14 The evolution of normal pressure on the base plane at the final stage 119
Figure 4.15 The evolution of shear stress with the radius distances 119
Figure 4.16 The progressive evolution of normal pressure on the base plane 121
Figure 4.17 The numerical model of hopper deposition test 122
Figure 4.18 The progressive stages of the point deposition test 123
Figure 4.19 The shape of the sand pile at the final stage 124
Figure 4.20 The behaviour of pressure distribution at the final stage 125
Figure 4.21 The evolution of shear stress with the radius distances 125
Figure 4.22 The progressive pressure profiles of the point deposition method 126
Figure 4.23 The pressure distribution at the ultimate stage with different methods 128
Figure 4.24 The evolution of shear stress at the final stage with different methods 129
Figure 4.25 Behaviour of p values at different layers at the final stage 130

Figure 4.26 The evolution of q value and b value at the final stage 132

Chapter 5

Figure 5.1 An example of the sample generation procedures.....144

Figure 5.2 The stress path for the drained triaxial shear test 145

Figure 5.3 The stress invariants behaviour with R=0.01m, N=8 146

Figure 5.4 The behaviour of stress ratio 147

Figure 5.5 The evolution of void ratio 147

Figure 5.6 Illustration of principal stress rotation and stress path 149

Figure 5.7 The evolution of stress invariants and principal stress direction.....150

Figure 5.8 Stress behaviour during rotation shear: (a) stress components; (b) stress trajectory 151

Figure 5.9 The behaviour of strain trajectory for the dense and loose samples.....152

Figure 5.10 The force chains for sample with a section of 5mm in y direction under R=0.01m 154

Figure 5.11 The force chains behaviour at the end of consolidation stage 157

Figure 5.12 The behaviour of confining pressure within different radial distances 158

Figure 5.13 The probability distribution of p value with various shapes of boundary.....159

Figure 5.14 The evolution of void ratio and stress ratio with various boundaries at R=0.01m 160

Figure 5.15 The evolution of stress-strain responses with R=0.02m for dense samples 161

Figure 5.16 The force chains behaviour at different stages for the dense samples 162

Figure 5.17 The behaviour of stress invariants during the rotation of principal stress directions 164

Figure 5.18 The force chains behaviour at different rotation angles with various shapes.....165

Chapter 6

Figure 6.1 The characteristics of stress ratio and void ratio with the evolution of shear strain 172

Figure 6.2 The evolution of stress ratio and void ratio with various b values 173
Figure 6.3 The critical stress ratio with various b values 173
Figure 6.4 The behaviour of critical friction angle with various b values 174
Figure 6.5 The evolution of stress behaviour with different stress ratios 176
Figure 6.6 The evolution of strain behaviour with different void ratios 177
Figure 6.7 Diameter of strain trajectory at different stress ratios 178
Figure 6.8 The stress invariants calculated from SFF relationship with radius expansion method 181
Figure 6.9 The evolution of coordination number under various void ratios 183
Figure 6.10 The characteristics of fabric anisotropy with various initial void ratio 184
Figure 6.11 The characteristics of average contact force with various void ratios 185
Figure 6.12 The characteristics of contact force tensor with various void ratios 186
Figure 6.13 The evolution of coordination number with various b values 187
Figure 6.14 The evolution of anisotropy degree and b value for the contact normal 188
Figure 6.15 The critical fabric anisotropy with various b values 188
Figure 6.16 The evolution of average contact force with various b values 189
Figure 6.17 The evolution of anisotropy degree and b value of contact force 190
Figure 6.18 The evolution of fabric anisotropy behaviour with different stress ratios 191
Figure 6.19 Evolution of the stress ratio and void ratio 193
Figure 6.20 The probability distribution of contact force under various preparation methods 194
Figure 6.21 The distribution of void ratio and average contact force inside samples 194
Figure 6.22 The behaviour of stress invariants 195
Figure 6.23 The evolution of strain invariants 196
Figure 6.24 The stress behaviour during rotation of principal stress directions 197
Figure 6.25 The strain behaviour during the rotation of principal stress directions 197
Figure 6.26 The diameter of strain trajectory at various stress ratios 198

Figure 6.27 The stress invariants estimated from SFF for the deposited sample 199

Figure 6.28 The evolution of coordination number 199

Figure 6.29 The characteristics of fabric anisotropy.....200

Figure 6.30 The evolution of averaged contact force 201

Figure 6.31 The evolution of the contact force anisotropy.....201

Figure 6.32 The evolution of contact normal tensor with $\eta = 0.3$.....203

Figure 6.33 The evolution of fabric anisotropy behaviour with $\eta = 0.5$ 203

Chapter 7

Figure 7.1 Force chains network for different construction histories 209

Figure 7.2 The observation of p value on the base plane 211

Figure 7.3 The behaviour of σ_{rr} at the final stage with various preparation methods.....214

Figure 7.4 The behaviour of $\sigma_{\theta\theta}$ at the final stage with various preparation methods 214

Figure 7.5 The behaviour of σ_{zz} at the final stage with various preparation methods 214

Figure 7.6 The behaviour of σ_{rz} at the final stage with various preparation methods 214

Figure 7.7 The progressive behaviour of σ_{rr} for the boundary removal test.....216

Figure 7.8 The progressive behaviour of $\sigma_{\theta\theta}$ for the boundary removal test 216

Figure 7.9 The progressive behaviour of σ_{zz} for the boundary removal test 217

Figure 7.10 The progressive behaviour of σ_{rz} for the boundary removal test.....217

Figure 7.11 The progressive behaviour of σ_{rr} for the rain deposition test 218

Figure 7.12 The progressive behaviour of $\sigma_{\theta\theta}$ for the rain deposition test 219

Figure 7.13 The progressive behaviour of σ_{zz} for the rain deposition test.....219

Figure 7.14 The progressive behaviour of σ_{rz} for the rain deposition test.....220

Figure 7.15 The progressive behaviour of σ_{rr} for the point deposition test 221

Figure 7.16 The progressive behaviour of $\sigma_{\theta\theta}$ for the point deposition test 221

Figure 7.17 The progressive behaviour of σ_{zz} for the point deposition test.....222

Figure 7.18 The progressive behaviour of σ_{rz} for the point deposition test.....222

Figure 7.19 The progressive direction of major principal stress for the layer of [0,2.5]mm .223
Figure 7.20 The directions of major principal stress direction for the layer of [2.5,5]mm ...224
Figure 7.21 Trace of p value at the final stage for the three preparation methods 226
Figure 7.22 The progressive behaviour of traced stress component σ_{rz} 227
Figure 7.23 The displacement of traced region with different construction histories 228
Figure 7.24 The normalised pressure distribution for the point deposition test 229
Figure 7.25 The validation of the closures for the determination of stress distribution 230
Figure 7.26 Average coordination number at the final stage with various preparation methods 231
Figure 7.27 Progressive average coordination number for the boundary removal method ...232
Figure 7.28 Progressive average coordination number of rain deposition test 233
Figure 7.29 Progressive average coordination number for point deposition test 233
Figure 7.30 The progressive contact normal behaviour within the region of r=30mm, z=10mm 235
Figure 7.31 Surface region in the progressive stage with different methods.....236
Figure 7.32 The anisotropy degree of the contact normal in the surface region 237
Figure 7.33 Anisotropy degree within sand pile at the final stage.....238
Figure 7.34 The behaviour of D_{rr} at the final stage with various preparation methods 239
Figure 7.35 The behaviour of $D_{\theta\theta}$ at the final stage with various preparation methods 239
Figure 7.36 The behaviour of D_{zz} at the final stage with various preparation methods 239
Figure 7.37 The behaviour of D_{rz} at the final stage with various preparation methods.....239
Figure 7.38 The degree of fabric anisotropy at progressive stages for boundary removal test 240
Figure 7.39 The progressive degree of fabric anisotropy for the rain deposition test 241
Figure 7.40 The progressive degree of fabric anisotropy for the point deposition test 242
Figure 7.41 The progressive behaviour of D_{rr} for the boundary removal test 243
Figure 7.42 The progressive behaviour of $D_{\theta\theta}$ for the boundary removal test 243

Figure 7.43 The progressive behaviour of D_{zz} for the boundary removal test.....244

Figure 7.44 The progressive behaviour of D_{rz} for the boundary removal test.....244

Figure 7.45 The progressive behaviour of D_{rr} for the rain deposition test 245

Figure 7.46 The progressive behaviour of $D_{\theta\theta}$ for the boundary removal test 245

Figure 7.47 The progressive behaviour of D_{zz} for the rain deposition test.....246

Figure 7.48 The progressive behaviour of D_{rz} for the rain deposition test 246

Figure 7.49 The progressive behaviour of D_{rr} for the point deposition test 247

Figure 7.50 The progressive behaviour of $D_{\theta\theta}$ for the point deposition test.....247

Figure 7.51 The progressive behaviour of D_{zz} for the point deposition test.....248

Figure 7.52 The progressive behaviour of D_{rz} for the point deposition test 248

Figure 7.53 The characteristics of f_0 at the final stage.....250

Figure 7.54 The characteristics of contact force anisotropy at the final stage.....250

Figure 7.55 The progressive behaviour of average contact force for the boundary removal test 251

Figure 7.56 The progressive behaviour of contact force anisotropy for the boundary removal test 252

Figure 7.57 The progressive behaviour of average contact force for the rain deposition test 253

Figure 7.58 The progressive behaviour of contact force anisotropy for the rain deposition test 253

Figure 7.59 The progressive behaviour of average contact force for the point deposition test 254

Figure 7.60 The progressive behaviour of contact force anisotropy for the point deposition test 255

List of tables

Table 4.1 Parameters for the full-scale tests 99

Table 4.2 The information of simulations for the formation of sand piles 102

Table 4.3 The information for inserting particles 103

Table 4.4 The information of the simulations 105

Table 4.5 The information of average contact force at different regions 114

Table 4.6 Surface angles at different layers under different methods at the final stage 127

Table 5.1 Simulation properties 143

Table 5.2 The information of specimens in comparison with Yang (2014) 144

Table 5.3 The material properties for tests of sample uniformity 153

Table 5.4 The information of samples with different boundaries 155

Table 5.5 The information of average contact force at different shear strains 161

Table 5.6 The CPU time for the tests with various sizes and shapes of the polyhedral boundary 166

Nomenclature

Symbols

α	Rotation angle
δ_{ij}	Kronecker delta
Δt	Time-step
$\Delta\varepsilon_v$	Loading increment of volumetric strain
$\Delta\varepsilon_q$	Loading increment of deviatoric strain
$\Delta\eta$	Loading increment of stress ratio
Δb	Loading increment of intermediate principal stress ratio
Δb_ε	Loading increment of intermediate principal strain ratio
Δn_ε	Loading increment of principal strain direction
Δn_σ	Loading increment of principal stress direction
Δp	Loading increment of confining pressure
$\boldsymbol{\varepsilon}, \varepsilon_{ij}$	Strain tensor
ε_v	Volumetric strain
ε_{vtol}	Tolerance of volumetric strain
ε_v^t	Target volumetric strain
ε_q	Deviatoric strain
ε_{qtol}	Tolerance of deviatoric strain
ε_q^t	Target deviatoric strain
η	Stress ratio
η^t	Target stress ratio
η_n	Normal damping coefficient
η_t	Tangential damping coefficient
η_{tol}	Tolerance of stress ratio
λ	Loading factor controlling the loading rate
μ	Friction coefficient
ν	Poisson's ratio
ρ	Density
σ_1	Maximum principal stress
σ_2	Intermediate principal stress
σ_3	Minimum principal stress
σ_{ij}	Stress tensor
σ_{rr}	Radius direction component of stress tensor

σ_{xx}	X-direction component of stress tensor
σ_{yy}	Y-direction component of stress tensor
σ_{zr}	Z-R space component of stress tensor
σ_{zz}	Z-direction component of stress tensor
ω	Coordination number
$\boldsymbol{\omega}^{w}$	Boundary rotational velocity
θ	Lode angle
ϑ	Repose angle
b	Intermediate principal stress ratio
b_{ε}	Intermediate principal strain ratio
$b_{\varepsilon tol}$	Tolerance of intermediate principal strain ratio
b_{ε}^{t}	Target intermediate principal strain ratio
b_{σ}^{t}	Target intermediate principal stress ratio
D_{ij}	Deviatoric part of contact normal tensor
D_q	Anisotropy degree of contact normal
d^{j}	Plane function constants
E	Young's modulus
$E_c(\boldsymbol{n})$	Probability density distribution along normal direction $\boldsymbol{n}$
E^{*}	Effective Young's modulus
E_0	Surface area, 2D 2π, 3D 4π
$\boldsymbol{e}$	Restitution coefficient
e	Void ratio
$\boldsymbol{F}, F_{ij}$	Deformation gradient tensor
$\boldsymbol{F}_d$	Deviatoric deformation gradient tensor
$\boldsymbol{F}_v$	Volumetric deformation gradient tensor
f_{ub}	Unbalance force
f_{ac}	Average contact force
f_{cont0} f_0	Direction average of mean contact force on all directions
f_{cont}	Contact force
G	Shear modulus
G^{*}	Effective shear modulus
G_{ij}	Deviatoric part of contact force tensor
h_i	Idealised height of sand pile
h_0	Actual height of sand pile
K_{ij}^{f}	Contact force tensor
K_{ij}^{v}	Contact vector tensor
k_n	Normal stiffness

k_t Tangential stiffness

N Number of sides for polyhedral boundary

N_c Number of contacts

$\boldsymbol{N}_{ij}$ Contact normal tensor

N_p Number of particles

$\boldsymbol{n}$ Unit contact normal direction

$\boldsymbol{n}_1^s$ Maximum principal stress direction

$\boldsymbol{n}_2^s$ Intermediate principal stress direction

$\boldsymbol{n}_3^s$ Minimum principal stress direction

$\boldsymbol{n}_o^w$ Wall normal direction of polyhedral boundary

p Mean confining pressure

p_{lb} Lower bound of mean confining pressure

p^t Target confining pressure

q Deviatoric stress

R Radius of polyhedral boundary

R_b Radius distance of base plane

R_d Representative radius distance

r Particle radius

r_{lo} Minimum size of particle radius

r_{hi} Maximum size of particle radius

$\boldsymbol{t}^w$ Plane vectors

V_{sam} Sample volume

V_p Particle volume

V_l Volume of a layer

$\overline{V_p}$ Average particle volume

v_{cont}, l Contact vector

v_{cont0} Direction average of mean contact vectors on all directions

$\boldsymbol{v}_o^w$ Boundary translational velocity

X Interacted coordinates of polyhedral boundary

X_o^w Wall central coordinates of polyhedral boundary

Abbreviations

BCC Bouchaud-Cates-Claudin

CFD Computational Fluid Dynamics

DEM Discrete element method

FEM Finite element method

FPA Fixed principal axes

IFE Incipient failure everywhere

OSL Oriented stress-linearity

PSD	Particle size distribution	SFF	Stress-Force-Fabric
RVE	Representative volume element		

Chapter 1 Introduction

1.1Background and motivation

Granular materials are widespread in nature and industry, for instance, sand, gravel, rock, rice and mining. Their ubiquitous existences certify their engineering importance and attract substantial interests from both the academic and the engineering communities, such as the applied mathematical, agriculture, the chemical engineer and civil engineer. The response of a system is very complicated in consequence of the collective response of granular materials. Sand, as a typical example of granular materials, plays a significant role in the construction and the infrastructure safety related to our daily life, for instance, the silos and earth dams.

The pressure dip under a sand pile is one among many intriguing phenomenon of granular materials. It refers to a significant dip underneath the central apex of the sand pile, which might expect the peak pressure. This counter-intuitive phenomenon was first reported by Hummel and Finnan (1920) and has attracted extensive research endeavours in the past few decades. This phenomenon is studied with the experimental, continuum approach and the numerical investigations. Several factors are proposed to have a relationship with this phenomenon, for instances, the shape of particles and the deposition height. It is now generally believed that the construction history is crucial to the pressure dip formation, but a quantitative explanation is not yet available.

This project is motivated to give a new direction to explain the counter-intuitive phenomenon with the progressive particle-scale mechanisms. The impact of construction history is studied in terms of the stress, force and fabric subjected to the subsequent loading following different construction histories. It could also give an insight of the practical

operations such as the silos, the construction of embankments and dams and the slope stability.

1.2 Scope of the research

The pressure dip phenomenon refers to the stress distribution interacted with the base plane. The complexity material response is originated from the dependence and variability of the material internal structure. With regards to the continuum mechanism, the material could be treated as a representative volume element (RVE). To explain the formation of pressure dip phenomenon, the project would range three different scales: the particle-scale, the continuum-scale and the system scale, in this case, the scale of the sand pile.

Discrete element method (DEM) is a great tool in the study of granular materials by modelling it directly from the particle scale. Employing the DEM, it could observe the continuum behaviour for the real properties of particles without any additional assumptions. Hence, the research sets out to investigate the formation of pressure dip using DEM. However, it is noted that the dimension of the system that DEM can practically simulate is limited. Thus, the project is achieved by conducting DEM simulation of sand pile and DEM simulation of representative volume elementary behaviour in parallel. In this project, tests are performed based on the open-sourced discrete element software LIGGGHTS (LAMMPS Improved General Granular and Granular-heat Transfer Simulations, www.cfdem.com), depending on the rich functions and high performance computation.

First, it will undertake the numerical experiments of sand pile formation following three different procedures as: 1) boundary removal method; 2) rain deposition method; 3) point deposition method. The stress distribution on the base plane will be studied with various construction histories.

In geotechnical problems, the stress-strain behaviour of granular materials is an interesting subject with great complexity, which has drawn much attention in the past few decades. The soil responses are also proposed to have memory effect and dependence of loading paths (Miura et al., 1986; Sitharam et al., 2002; Yang, 2013). To understand the material behaviour, the RVE stress-strain response of materials in sand pile will be studied under the specified loading paths. A numerical algorithm proposed by Li et al. (2013; 2016) will be implemented into LIGGGHTS with the independent control of the magnitudes and directions of the principal stresses. The impact of void ratio, intermediate principal stress ratio, the magnitudes of principal stresses, the directions of principal stresses and the initial state will be studied on the behaviour of material response.

Experimental and numerical observations demonstrated that the characteristics of strength and stress-strain responses relevant to the material anisotropy. The anisotropy could be classified as the inherent anisotropy and induced anisotropy with respect to the in-situ loading conditions and the geological process of materials respectively. The "stress-force-fabric" (SFF) relationship will be applied to observe the influence of internal structure on the material continuum behaviour. Combined with the particle-scale observations of stress, force and internal structure from sand pile, it will provide an interpretation of the formation of the pressure dip phenomenon. With the results of simulation tests, it could highlight the effect of fabric on the design of geotechnical problems, such as the bearing capacity of building foundations. In addition, it could also provide information for the development of the constitutive model.

1.3 Aims and objectives

This project considers the geotechnical problems of the sand pile and elementary test for the specific loading paths. The research mainly involves two aims. One is employing the

multi-scale approach to study the continuum material behaviour of the sand pile. The other one is improving the understanding of stress distribution.

In order to achieve the aims, the following objectives require reaching,

1, To reproduce the impact of construction history on the pressure profile, tests are performed with three different preparation methods as the boundary removal, rain deposition and point deposition.

2, To achieve the development of the numerical technique for the RVE material response in LIGGGHTS.

3, To explore the structure and loading history dependence of granular materials with the observations of RVE simulations at the multi-scale approach.

4, To improve understanding of the presure dip phenomenon by the particle-scale observations of stress, fabric anisotropy and contact force anisotropy at the progressive stages following different procedures.

1.4 Thesis structure

The thesis consists of eight chapters. The content of each chapter is briefly summarised as follows:

Chapter 1 gives a brief research background and states the aims and objectives of this project.

Chapter 2 reviews previous study of sand pile test and granular material behaviour under specified loading paths. Section 2.1 gives a brief introduction of this chapter. Section 2.2 reviews the investigations and interpretations of the pressure dip phenomenon. Section 2.3 presents the constitutive behaviour of granular materials. It involves the influence of

the structural dependence and loading path dependence on the granular materials behaviour. Section 2.4 presents the material responses with the macro-micro relations.

Chapter 3 introduces the methodology for this project. Tests are carried out with the discrete element method. The principles of DEM, related contact models and the damping model implemented in DEM are given in Section 3.2. It also introduces the commonly used commercial and open-sourced DEM software. Section 3.3 introduced the characteristics of applied DEM software LIGGGHTS. The methodology for the implementation of the developed numerical algorithm is presented in Section 3.4.

Chapter 4 investigates the impact of construction history for the sand pile tests following three different procedures. Section 4.2 presents the properties of boundary and materials and basic information for the simulations. Section 4.3 gives the numerical implementation and observations of the boundary removal method. The observations of rain deposition and point deposition are presented in Section 4.4 and Section 4.5 respectively. A discussion is presented in Section 4.6 with different construction histories.

Chapter 5 illustrates the developed tool for virtual elementary experimental test using LIGGGHTS. The simulations are performed with the polyhedral boundary. The models are developed based on the works of Yang (2014) and Li et al. (2013; 2016). Section 5.2 elaborates the characteristics of the polyhedral boundary and the implementation of the numerical technique in LIGGGHTS. The developed tool is checked and compared with Yang (2014) in Section 5.3. Section 5.4 presents the choice of the polyhedral boundary with the impact of sample sizes and various polyhedral shapes under the proportional and non-proportional loading paths respectively. It also includes the information of uniformity material behaviour at different stages to select the polyhedral boundary.

Chapter 6 introduces the constitutive behaviour of granular materials with the structure and loading paths dependence. The simulation tests are conducted with the polyhedral boundary selected in Chapter 5. The material properties are set the same as that used to perform the sand pile test. Section 6.2 gives the material responses for samples prepared with the radius expansion method, referring to generate the particles with a smaller size first and then increase to the target value, under the general loading paths. The impact of initial void ratio, intermediate principal stress ratio, magnitudes and directions of principal stresses is studied in this section. It employs the SFF relationship to interpret the material responses with the effect of internal structure. Section 6.3 studies the material behaviour of the deposited sample for observing the impact of initial state.

Chapter 7 provides a discussion of material responses and pressure dip phenomenon. It aims to explain the phenomenon via the progressive particle-scale mechanisms during the process of sand pile formation. The granular material behaviour is observed with the characteristics of stress, fabric and contact force. Section 7.2 presents the impact of loading history following various construction histories. Section 7.3 compares the base plane stress distribution with the classic continuum theory. The progressive behaviour of fabric anisotropy and contact force anisotropy is provided in Section 7.4 and Section 7.5 respectively. A summary is given in Section 7.6.

Chapter 8 summarises the major conclusions from the project and recommendations for future study.

Chapter 2 Literature review

2.1 Introduction

The stress-strain behaviour of granular materials is an interesting while complicated subject that has drawn much attention in the past few decades. The structure of a sand pile, a common example in nature and industries, is still an area of uncertainty where the "pressure dip" phenomenon (referred to as the peak ground pressure occurring at a certain distance away from the centre of the pile) has not yet been fully understood. This Chapter reviews research studies on the stress-strain behaviour of granular materials in the literature that are particularly relevant to the current study; and is organised into the following five sections.

Section 2.1 presents the structure and organisation of this literature review chapter. Section 2.2 summarises the observations and investigation on pressure dip. The review of studies on this counter-intuitive phenomenon is divided into three parts including analytical, experimental and numerical studies respectively. Section 2.3 summarises previous research findings on constitutive behaviour of granular materials, including the effect of structural dependence and loading paths dependence. Structure anisotropy could either be formed during geological processes or be induced by in-situ loading; and hence could be subdivided into two categories: induced anisotropy and initial anisotropy, which will be reviewed separately. Section 2.4 proceeds to address the significance of loading-path dependence by reviewing research studies on structure evolution and material response to both proportional and non-proportional loadings. The effect of material anisotropy on the macroscopic granular material behaviour is also addressed through some particle-scale mechanisms simulated using DEM. Finally, a brief summary is presented in Section 2.5.

2.2 The pressure dip phenomenon in sand pile

"Sand pile" is a common form of existence for granular materials, usually seen in mining industries, construction sites, and pharmaceutical/production processes, as well as in the children's playground on the beach. A counter-intuitive phenomenon has been discovered about the base plane pressure profile of a sand pile. A significant dip in pressure may be observed beneath the apex of the sand pile. This is well known as the "pressure dip" phenomenon. Hard experimental evidence of this phenomenon was provided by Smid and Novosad (1981) and Jotaki and Moriyama (1979). Much research attention and extensive investigations were focused on the stress distributions in order to explain this mysterious phenomenon since the 1990s. This section summarises the key research work on the experimental, analytical and numerical aspects respectively.

2.2.1 Experimental observations

The pressure profile in granular materials has been studied since the 1920's. Most of the investigators were interested in the problem of pressure distribution related to the stability of earth embankments and dams (Hummel and Finnan, 1920; Trollope, 1956; Trollope, 1957). Hummel and Finnan (1920) studied the stress distribution with different shapes of sand. The pressures were measured using pressure cells mounted in a nominally horizontal base made of 25*mm* thick wooden planks. They observed the dip phenomenon in sand piles having conical and prismatic shapes, with the degree of dip being larger for the conical pile than for the prismatic counterpart. However, their results were disputed due to the properties of the pressure cells (Parry, 1954).

In recent decades, most of the research has been inspired by the tests of Smid and Novosad (1981), who found a significant dip of pressure under the central apex of conical sand piles,

measured using pressure cells mounted in a horizontal steel base. The platform consisted of rigid steel plates and had the dimensions of $2\times2m^2$. The degree of the pressure dip is increased with the increase of the height of the sand pile.

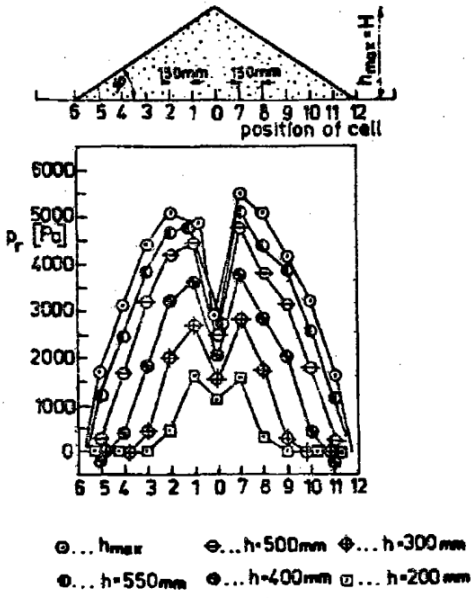
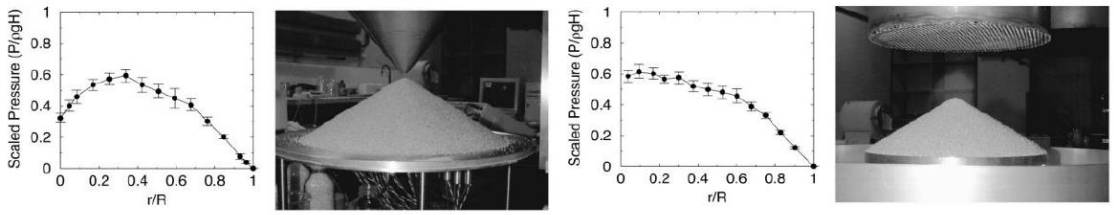


Figure 2.1 Vertical pressure distribution on the base plate (Smid and Novosad, 1981)

Subsequently, with the development of the technology and equipment, experimental tests were performed to observe the pressure dip phenomenon considering various factors, for instance, the construction histories (Vanel et al., 1999; Geng et al., 2001b). Figure 2.2 below shows the large-scale experimental tests and results by Vanel et al. (1999) based on different methods for constructing their sand piles. They created different construction histories by varying the application of hopper and the cylindrical sieve boundary. The tests were conducted using a particle diameter size distribution of $[1.2\pm0.4]mm$. The sand pile was formed on the base plane with the diameter of $260mm$. The dimension of the hopper outlet diameter was about $11.7mm$ (around 10-particle size). The diameter of the cylindrical sieve boundary was $260mm$, the same as the base plane according to Figure 2.2(2). From their test results based on a hopper boundary, the maximum pressure occurred at about $0.3R$

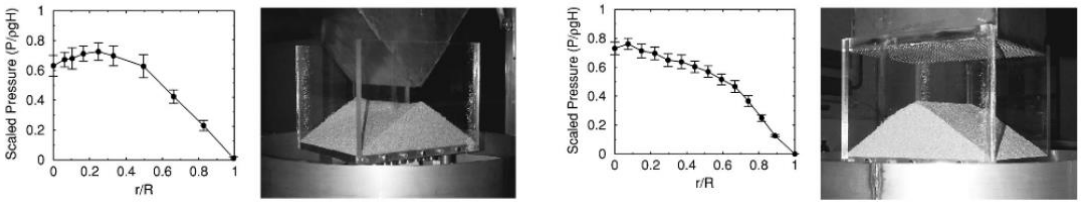
distant away from the centre of the pile (*R* refers to the sand pile radius). While with the cylindrical boundary, the peak pressure occurred in the centre of the sand pile without exhibiting the pressure dip phenomenon.



(1) "localize-sourced" deposition (2) "raining" deposition

Figure 2.2 Sand pile generates with different construction histories (after Vanel et al., 1999)

The shape of sand piles was also taken into account in some research studies to determine the stress distribution under the apex. Vanel et al. (1999) further carried out experimental tests on wedge-shaped piles. The wedge-shaped boundary was employed with an outlet that was $11.7mm$ by $200mm$ as seen from Figure 2.3(1) for the "localize-soured" deposition test. The dimensions of the base plane were $200mm \times 260mm$. A rectangular box was applied in the "raining" deposition test with the same dimensions as the base plane. A sieve boundary with $4mm$ diameter holes was generated at the outlet of the rectangular boundary. Figure 2.3(2) displays the image of the experimental tests and the corresponding results of normal pressure on the base plane. No pressure dip phenomenon is observed when using the "raining" deposition method. For the "localize-sourced" deposition test where the pressure dip phenomenon was observable, the degree of the pressure dip was lower under the wedge-shaped pile, compared with the conical pile as Figure 2.2(1) above. They supposed that the dip phenomenon related to the flow of particles during the pile formation.



(1) "localize-sourced" deposition (2) "raining" deposition

Figure 2.3 Wedge-shape piles form with different construction histories (after Vanel et al., 1999)

With the development of some non-destructive evaluation techniques, such as the photoelasticity, X-ray CT and image analysis, experimental investigations on the micromechanics behaviour of granular materials were possible. Geng et al. (2001b) provided insights of contact orientation distributions subjected to different construction histories using photoelastic materials. The tests were performed on materials having a larger particle size than sand. They used disks having two diameters of $9mm$ and $7mm$ respectively. The heap had a base length of $1300mm$ and a height of $300mm$. Three different sample preparation methods were adopted, as the fixed height point source (FHPS) method, the slowly moving point source (SMPS) method and the extended sources (ES) method. For the FHPS method, the height of the filling insert was fixed at the distance of $570mm$ above the base. In SMPS, the insert was slowly lifted up to create a steady flow of the materials. The ES method is similar to the "raining" deposition method and strips of either cardboard or Plexiglas were placed in the central portion to control the flow rate.

Geng et al. (2001b) aimed to explain the counter-intuitive phenomenon with an investigation of the internal structure. The results of contact orientation and contact force orientation are provided in Figure 2.4 with the above-mentioned three sand pile generation methods. The experimental results show that different contact angles and texture resulted from different heap formation methods. Stronger anisotropies were observed for the localise-sourced deposition method in contrast with the extended source procedure. The

orientation of contacts had a tendency to be in an isotropic condition for the ES method. The effect of particle segregation was also taken into account to understand the pressure dip phenomenon. However, their results showed no prominent particle segregation when compared to experimental tests of Liffman et al. (1992; 1994). Liffman et al. (1992; 1994) found that the pressure dip phenomenon appeared when small particles laid on the base of the pile. Geng et al. (2001b) argued that the sand pile might be under a relatively dense condition, which limited the particles to segregate.

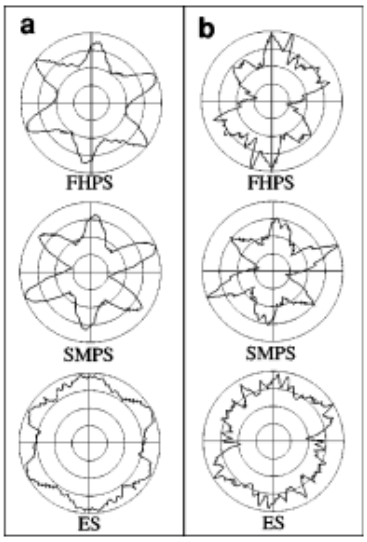


Figure 2.4 Contact orientations distribution with different pouring methods: (a) comparison of all particles; (b) comparison of particles on the force chains (Geng et al., 2001b)

Ooi et al. (2008) showed progressive stress profiles with various base plane conditions to study the impact of base deflection. A stiff base with a radius of 554*mm* was used in the rigid base test. In the flexible base test, a 1220*mm* square thin plate was employed with four corners supported to allow the boundary to be deflected into a dome shape. Figure 2.5 shows the results at the final stage of the sand pile formation. It displays that the magnitude and width of the pressure dip were enhanced with the flexible boundary in comparison with

the rigid base.

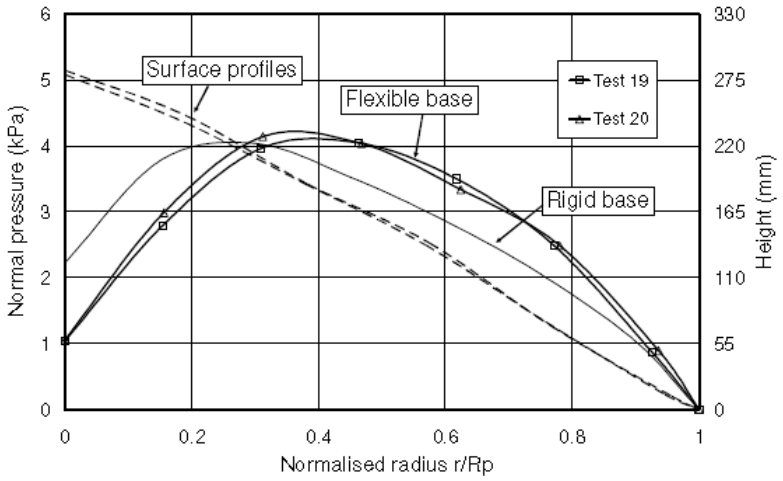


Figure 2.5 Pressure profile with the influence of base plane deflection (Ooi et al., 2008)

It has also been reported that the pressure dip phenomenon was affected by particle properties such as the size, particle size distribution (PSD), shape and roughness of particles (Zuriguel et al., 2007; Zuriguel and Mullin, 2008). Zuriguel and Mullin (2007) performed two-dimensional experimental tests using the particles made from the photoelastic materials with the shape of circular, elliptic and pear-shaped cylinders. They found that smaller particle sizes and non-spherical particles such as ellipsoid and pear shape could generate a larger repose angle. In addition, the results revealed that the pressure dip phenomenon was more obvious for the elliptical particles and pear-shaped cylinders than for the spherical particles.

Zuriguel and Mullin (2007; 2008) proposed to explain this phenomenon using the preferred orientations and magnitudes of the primary and secondary forcechain behaviour. The characteristics of the primary force chains were described by Edwards and Oakeshott (1989) and Cates et al. (1999). The primary force chains referred to the strong contacts (can roughly be regarded as linear chains) transferring stresses from one particle to another in contact. The other particles alongside the chains played a minor role and could be seen as

the secondary force chains in the contact network. Zuriguel and Mullin (2007) presented the behaviour of chains orientation with various shapes as presented in Figure 2.6. The orientation of disks displayed a second peak in the bimodal distribution in the left and right side of the sand pile. However, for the elliptic cylinders, the orientations of the secondary chains were smaller in contrast with the disks as the curves were flatter at the regions where the primary chain orientations exhibited peaks. Hence, they argued that the secondary force chains would reduce the pressure dip phenomenon inside the pile.

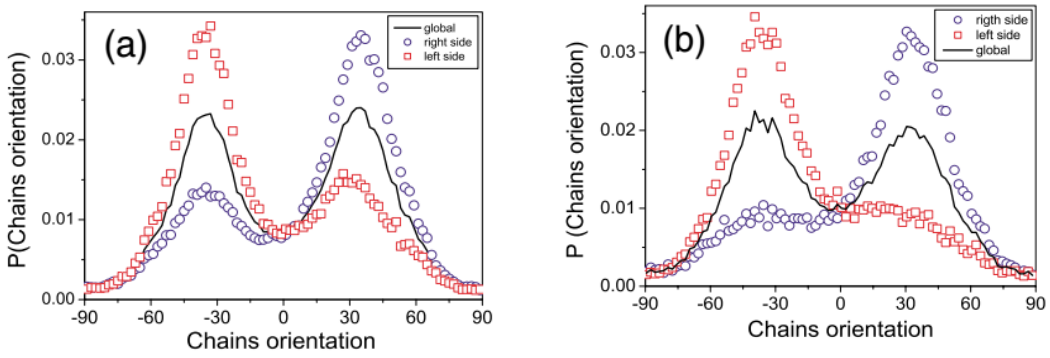


Figure 2.6 The probability of chains orientation inside the sand pile:

(a) mixture of disks; (b) the elliptic cylinders (Zuriguel and Mullin, 2007)

Zuriguel and Mullin (2008) further investigated the average angle of chain orientations inside the sand pile. Figure 2.7 presents the variation of mean orientation with different particle shapes. It could be observed that the main difference is in the core region of the sand pile. The pear-shaped cylinders had the largest angle ϕ in this region, which also has a higher dip degree. Hence, they concluded that a correlation between the mean orientation and the pressure dip phenomenon existed.

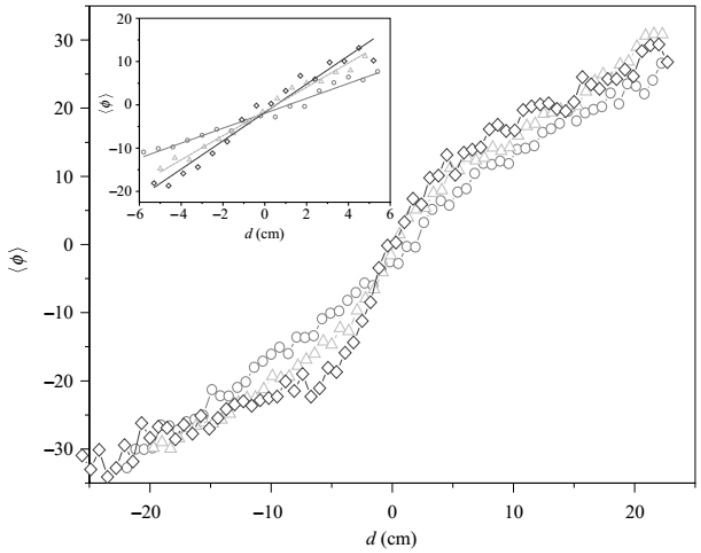


Figure 2.7 The mean orientation angle with the distance to the centre:

(1) circles: disks; (2) triangles: elliptic cylinders; (3) diamonds: pear-shape cylinders

(Zuriguel and Mullin, 2008)

Furthermore, Zuriguel and Mullin (2008) compared results of two-dimensional and the three-dimensional analyses they performed. Results show that the dip degree was higher in 3D conical pile. They argued that a greater degree of arches was produced in the 3D test. In addition, for the three-dimensional test, the pressure dip phenomenon appeared at relatively early stages during the process of pile formation.

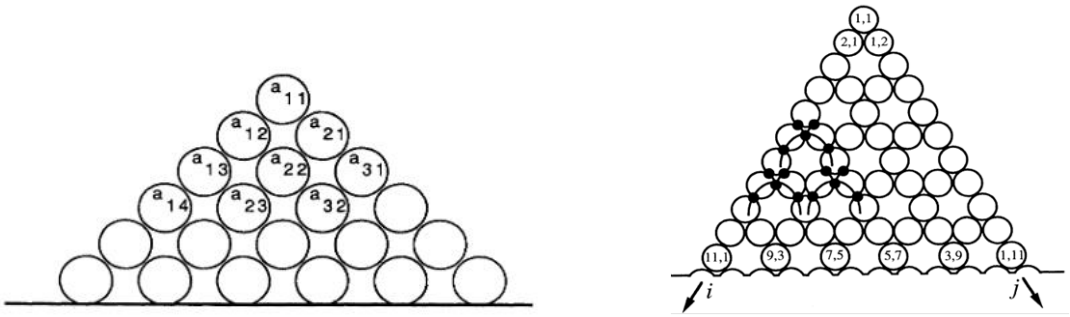
Ai (2010) also investigated the pressure dip phenomenon due to the deposition properties such as the deposition rate, deposition height and deposition jet dimension. To a certain extent, the rate of particles flowing through a funnel is a critical issue. He found that increasing the deposition rate resulted in a higher pressure dip degree while reducing the width for the peak pressure. However, in his research, increasing the pouring height had a negligible effect on the pressure dip phenomenon.

2.2.2 Analytical explanations

Over the last couple of decades, physicists and mathematicians focused on the stress "propagation" based on the static equilibrium condition combined with certain constitutive assumptions. Edwards and Oakeshott (1989) analysed this phenomenon by studying the stress transmission under a 2D pyramid. They explained that arches formed at an angle steeper than the repose angle of their constituent materials, which transmitted the stress sideways from one arch to another.

2.2.2.1 Packing of particles

Force propagation has been studied to explain the pressure distribution with discrete particles inside the pile. Hong (1993) performed an interesting analysis on the stress distribution inside a hexagonally packed pyramid-shaped granular pile and concluded that the normal force acting on each grain was identical for the bottom layer with the regularly packed shape. Hence, he proposed that the irregular arrangement of particles, the existing voids inside them, and the supported boundary may lead to a reduced load for the sand pile. Huntley (1993) further considered the vacancy effects inside the granular pile, and showed that identical normal force was obtained for each particle on the boundary, same as in the vacancy-free system. Thus, he suggested that the pressure dip phenomenon observed in experiments related to the friction, the random packing and/or some other three-dimensional effects.



(a) vacancy-free system (Hong, 1993) (b) vacancies system (Huntley, 1993)

Figure 2.8 Regular packing of sand pile

2.2.2.2 Radial stress distribution

In parallel, an approach based on continuum mechanics is applied to explain the counter-intuitive phenomenon. Some good reviews could be found in the area of constitutive models to understand the stress propagation in the sand pile with various geometries (Savage, 1997; Savage, 1998; Wittmer et al., 1996).

The continuum-mechanical description was based on the equations of stress continuity in a cohesionless granular media. In a static equilibrium, the forces acting on a small element must balance. Eqs.(2.1) to (2.3) give the expression of the stress continuity for a conical sand pile in the three dimensions (Wittmer et al., 1996).

$$\partial_r \sigma_{rr} + \partial_z \sigma_{zr} = \beta\left(\sigma_{\chi\chi} - \sigma_{rr}\right)/r \tag{2.1}$$

$$\partial_r \sigma_{rz} + \partial_z \sigma_{zz} = g - \beta\sigma_{rz}/r \tag{2.2}$$

$$\partial_\chi \sigma_{ij} = 0 \tag{2.3}$$

in which $\beta = 1$ and r, χ and z are coordinates under the cylindrical polar coordinate system as shown in Figure 2.9. The positive z-direction is treated as downward vertical to

the base plane. g refers to the gravity acceleration. The granular medium is assumed with constant density which is normalised to be equal to 1 (dimensionless). The approach considers the sand pile is symmetry at the axis of $r = 0$, so that the stresses $\sigma_{rx} = \sigma_{zx} = 0$. σ_{ij} is the symmetric stress tensor in i, j. For the two dimensions, the parameter β is set to zero in Eqs.(2.1) and (2.2), with $r = |x|$; x refers to the horizontal direction in the Cartesian coordinate system.

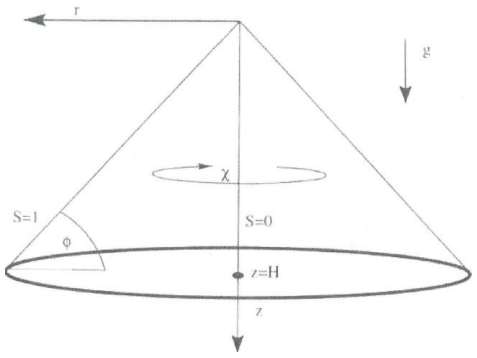


Figure 2.9 The coordinate system for stress-continuity equation (Wittmer et al., 1997)

An additional postulate is required to close the above theoretical static equilibrium equations. Four different continuum approaches have been used for determining the stress distributions. The approaches are named as the incipient failure everywhere (IFE), Bouchaud-Cates-Claudin (BCC), fixed principal axes (FPA) and the oriented stress-linearity (OSL) models, respectively, as detailed in the follows (Wittmer et al., 1997, Savage, 1998).

2.2.2.3 The IFE model

The IFE model is based on the Mohr-Coulomb rigid-plastic model, which assumes that granular materials are marginally unstable at everywhere. Thus, the shear force is measured

as the product of $\tan\varphi$ and the normal force at every point. The constitutive relationship is shown as follows

$$\sigma_{rr} = \sigma_{zz} \frac{1}{\cos^2 \phi} \left[\sin^2 \phi + 1 \pm 2 \sin \phi \sqrt{1 - \left(\cot \phi \sigma_{zr} / \sigma_{zz} \right)^2} \right] \tag{2.4}$$

in which ϕ is the angle of friction for the materials. In the simplest geometries, the expression take – or + in Eq.(2.4) for the "active" and "passive" regions respectively according to the Mohr-Coulomb model. The negative root, conventionally referred to an "active" solution, shows a hump instead of a dip in the vertical normal stress beneath the apex. With the "passive" solution, the pressure dip phenomenon exists (Savage, 1997). This approach is disputed as the incipient failure condition can reliably be assumed at the surface of the pile (Wittmer et al., 1996).

2.2.2.4 The BCC model

For the BCC model, proposed by Bouchaud et al. (1995), the components of vertical and horizontal normal stress are treated as proportional. The assumption is a simplified constitutive relationship based on the work of Janssen (1895) to investigate silos. They proposed phenomenological equations for illustrating the stress in the two-dimensional geometries. They argued that the stress propagated along "light cones" as a wave equation, where the coordinates of vertical and horizontal play the roles of time and space respectively. The wave-like behaviour is under the linear part relation and Eq.(2.5) below gives the constitutive relationship,

$$\sigma_{xx} = k_2 \sigma_{zz} \tag{2.5}$$

in which k_2 is a phenomenological parameter describing the geometry of contacts. In their

work, a uniform normal pressure was observed instead of a "dip" revealed in the experimental tests. They suggested that the nonlinearities, such as the arch effect and construction history of the pile, should be taken into account to determine its final state of the static stress. In addition, they found that the amplitude of the density fluctuations and the size of grains reflected the normal stress distributions on the bottom plane.

2.2.2.5 The FPA model

The FPA model, postulated a fixed angle of inclination to the downward vertical for the major principal stress axis, provides a solution for understanding the spatial stress distribution. In this model, the principal stress directions remained unchanged in subsequent loadings. The primary constitutive relation in the case of sand pile geometry in Cartesians is expressed as follows

$$\sigma_{xx} = \eta\sigma_{zz} + \mu sgn(x)\sigma_{xz} \tag{2.6}$$

where η, μ are constants.

Wittmer et al. (1996) investigated this phenomenon with the FPA model. Figure 2.10(1) displays that the FPA model and arches were formed in the centre of the sand pile so that the pressure on the boundary was reduced. They argued that the experimental data obeyed the form of radial stress field (RSF) and the stress at the base could be written as the following expression

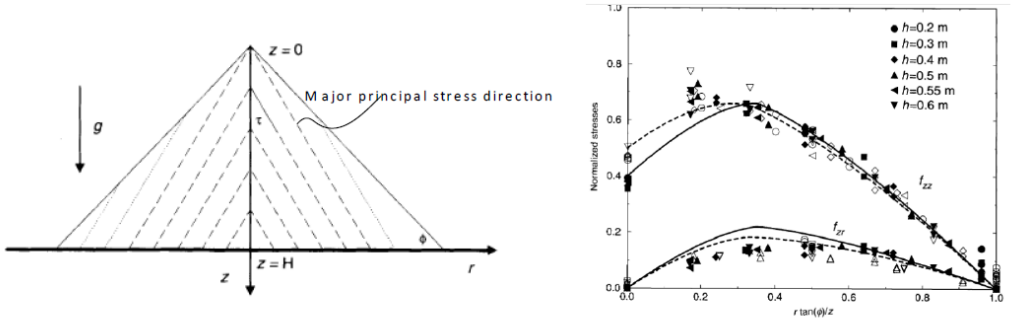
$$\sigma_{ij} = ghf_{ij}\left(r\tan\phi/h\right) \tag{2.7}$$

in which f_{ij} is the reduced stress and h refers to the height of pile. ϕ is the repose angle of the sand pile. The FPA model hypothesises that local constitutive relationship with the consideration of construction history for an element in three-dimensional should be

expressed as

$$\sigma_{rr} = \sigma_{zz} - 2\tan\phi\left|\sigma_{zr}\right| \tag{2.8}$$

The major principal axis everywhere bisects the angle of vertical and the free surface as $\tau = (\pi - 2\phi)/4$. With the FPA model, they assumed that the pressure dip phenomenon depended on the pile construction history from a point source. They suggested that the arches were formed in the central region, which caused the pressure dip phenomenon. Furthermore, their predictions presented a good agreement with the results of Smid and Novosad (1981), displayed in Figure 2.10(2). The experiment results are discrete data represented by markers. In addition, the solid and dash lines are the theoretical results. The difference of two sets of results is due to the second constitutive relationship as the definition of the hoop direction stress. The solid curve refers to a linear relation of $\sigma_{xx} = \sigma_{rr}$ and the dashed curve is based on the Haar-von Karman closure which reads that $\sigma_{xx} = (\sigma_{rr} + \sigma_{zz})/2 - \left[(\sigma_{zz} - \sigma_{rr})^2/4 - \sigma_{zr}^2\right]^{1/2}$.



(1) FPA model (2) Base plane stress distribution

Figure 2.10 The FPA model for pressure dip phenomenon (after Wittmer et al., 1996)

2.2.2.6 The OSL model

The oriented stress linearity model is based on simple hyperbolic equations for the stress

field. This approach could explain the stress screening with silos (Wittmer et al., 1996; Cates et al., 1998). The model assumes a constant arch and effective friction angles inside the sand pile. The following gives the stress filed using the cylindrical polar coordinates with the vertical z-axis oriented downwards

$$\sigma_{rr} = \eta\sigma_{zz} + \mu\sigma_{rz} \tag{2.9}$$

in which $\eta = -\tan\tau\tan\left(\tau - \phi - \pi/2\right)$ and $\mu = -\tan\tau + \tan\left(\tau - \phi - \pi/2\right)$. According to the equation, the BCC model and FPA model are the two special forms of the OSL model. Taking $\mu = 0$ in Eq.(2.9), OSL model reduces to the BCC model while in the case of $\eta = 1$ and $\mu = -2\tan\phi$, the FPA model is obtained. The closures of BCC, FPA and OSL models are under the solution of the elastoplastic model which assumes that the material in the inner core region is in an elastic state, whereas the outer region exhibits a plastic behaviour when it is close to or at yielding.

Cates et al. (1998; 1999) proposed a new class of elastoplastic model models with the stress transmission in granular materials described by hyperbolic equations. They observed a "fragile" behaviour that the medium was unable to support certain types of "incompatible" loads without a plastic arrangement. This behaviour may be appropriate due to the integrity of the medium arisen adaptively via the internal jamming process in response to a load. They hypothesised that the force chains developed until it could just support the applied load and remained in contact if no incompatible load was applied. With the "fragile" model, they predicted that the characteristics of force chains and particles arrangement had a large difference beneath the sand pile with different construction histories.

The above analytical approaches provide an illustration of the radial stress field on the base plane at the final stage. The progressive stress state is not considered in these approaches.

In such a case, the numerical simulation is performed to observe the progressive behaviour with different construction histories, as reviewed in the following Section 2.2.3.

2.2.3 Numerical investigations

2.2.3.1 Investigations with the finite element method

In recent decades, the numerical simulation method becomes more popular due to the fast development of techniques. The numerical method is employed to solve various kinds of constitutive relations for investigating the granular materials. Two numerical simulation methods, finite element method (FEM) and discrete element method (DEM), are the widely used techniques for studying the granular materials. Many factors, such as the properties of particle and deposition, can also be investigated and compared with the experimental results.

Recently, adopting the FEM software with complex plastic material models, several researchers have successfully predicted the pressure dip phenomenon under the conical sand pile apex (Anand and Gu, 2000; Al Hattamleh et al., 2005b). They conducted elastic-plastic calculations on the basis of a "double-shearing" constitutive model. Anand and Gu (2000) applied the Mohr-Coulomb model to simulate yielding at which state the angle from the maximum principal stress direction to the slip direction was expressed as $\xi = \pm\pi/4 \pm \phi/2$, where ϕ refers to the internal friction angle of the material. Smaller plastic strain and mobilised friction coefficient appeared in the core and surface region of the pile, while they were larger in between. Thus, they thought that the cause of pressure dip was owing to the inhomogeneous plastic strain and non-uniformity distributed internal friction coefficient during the formation of the piles.

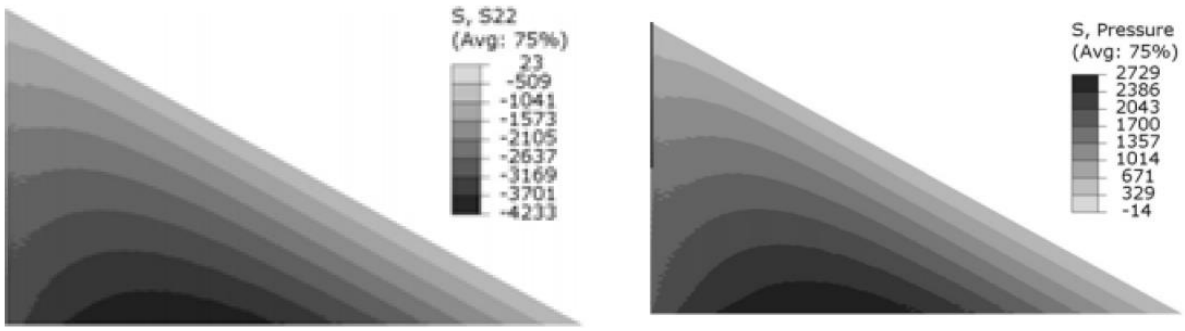
Al Hattamleh et al. (2005b) used a multi-slip formation of the "double-shearing" constitutive model to investigate this phenomenon. They took the initial slip direction as a

material parameter for the simulation, instead of using a fixed direction for the constitutive model by Anand and Gu (2000). For the tests, they found that the vertical plastic strain localised around the apex with the rest of the pile in an elastic state. Thus, they proposed that the strain localisation was the main cause of this phenomenon.

Zhu et al. (2006) continued the numerical research at a continuum scale with an extended dilatant double shearing mechanism. They studied the material behaviour with the consideration of the anisotropic model on the basis of the three-dimensional model proposed by Anand and Gu (2000). A non-zero maximum anisotropy degree was observed inside the sand pile. They found that the internal structure had a relationship with the pressure on the base boundary. In addition, the peak pressure was much higher in their results in comparison with the results of Anand and Gu (2000) without the consideration of any fabric effect.

Furthermore, Ai et al. (2013) investigated the pressure dip phenomenon with different constitutive laws using a progressive mesh activation scheme. Employing the FEM, the "pressure dip" phenomenon was observed at the continuum scale. Figure 2.11(a) below gives the distribution of the vertical stress inside the sand pile. It shows that the "pressure dip" phenomenon propagated up to the apex of the pile. In addition, the degree of "pressure dip" decreased in the locations that were vertically away from the base. The distribution of the equivalent pressure p is also presented as Figure 2.11(b) below, due to the instantaneous elastic modulus related to the value of p. The elastic stiffness increased with the increase of the p value. According to the figure, the largest elastic stiffness also appears in the radial distance away from the centre at each layer. Thus, it gives rise to an elastically softer region in the core region surrounded by a relatively stiffer region without the consideration of the plastic behaviour.

With the advantage of the FEM, they also investigated the effects of the plastic parameters on the behaviour of the "pressure dip" phenomenon. The Poisson's ratio and dilation angle had some influences on the degree of this counter-intuitive phenomenon. In addition, they found that stress-hardening elasticity was vital for enhancing the dip. Depending on the evolution of plastic zones, they suggested that particles were firstly in a plastic state when they were first generated on the pile and then became elastic owing to the increase of the confining stress when subsequent layers were generated.



(a) vertical stress distribution (b) stress p distribution

Figure 2.11 The stress distribution inside sand pile (Ai et al., 2013)

Researchers in recent years have devoted their attention to the impact of the repose angle on the pressure dip phenomenon. Zheng and Yu (2014) investigated the patterns of principal axes of stress (PAS) inside the sand pile with different outlet lengths (W_0). They performed the tests based on two elastoplastic models, i.e. Mohr-Coulomb elastoplastic (MCEP) model and the Drucker-Prager elastoplastic (DPEP) model. The result, as shown in Figure 2.12, presents a larger PAS (α) for the pressure dip case. However, for the test without the phenomenon, the PAS is essentially upright. It could represent the paths of contact force, similar to the "force chains" network. For the local deposition test, the granular materials tended to move laterally within the base plane and resulted in horizontal shear forces which reduced the normal pressure, in particular due to the impact of falling particles.

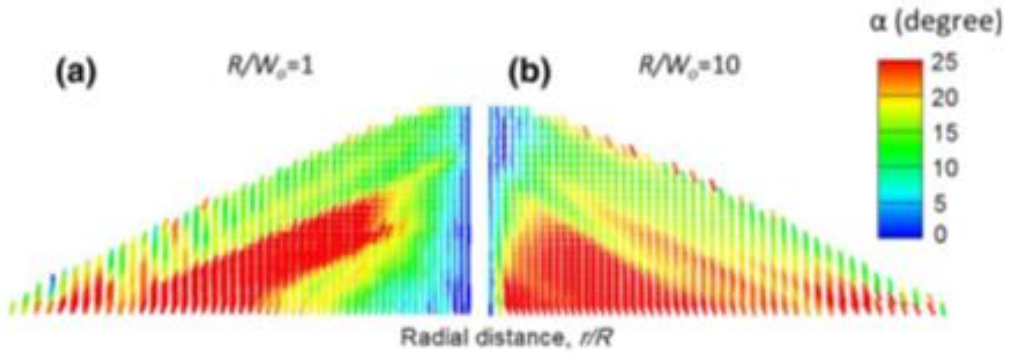


Figure 2.12 The principal axes of stress inside the sand pile:

(a) raining deposition; (b) local deposition (Zheng and Yu, 2014)

2.2.3.2 Investigations with the discrete element method

Cundall and Strack (1979) proposed a distinct element method to simulate a particle system based on the interaction of individual particles. Then, this method is widely used to model the behaviour of granular materials having various geometrical shapes. It could obtain the micro-scale information by mimicking the granular materials at the particle-scale level. Numerous simulations are implemented to study various influencing factors, illustrated in the experimental studies above, to explain this M-shaped distribution on the base plane.

The inter-particle forces and the corresponding torques would be generated due to the interaction of particles at the contact point. The torque would cause the rotation of interacted particles. This parameter plays a vital role to form a stable pile, in particular with the spherical particles. Due to elastic hysteresis or viscous dissipation, a rolling resistance would be produced. Zhou et al. (1999) suggested that the rolling friction was an important factor in the formation of stable piles corresponding to this rotation. They developed the model of Cundall and Strack (1979) with the consideration of this friction coefficient in the dynamic simulation.

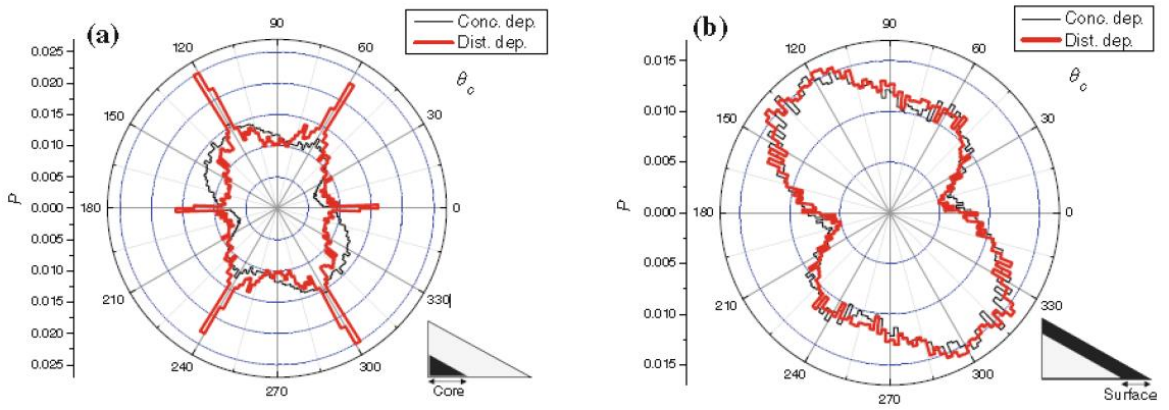
Zhou and Ooi (2009) investigated the pressure distribution based on the DEM developed

by Zhou et al. (1999), considering different particle shapes. The non-spherical particles were generated using constituent spheres. They found that the pressure dip phenomenon was less robust for the spherical particles in comparison with the non-spherical particles. The results were similar to the experimental results of Zuriguel and Mullin (2007; 2008).

Then, with the development of constitutive modelling, the mechanic anisotropy is considered a vital factor in the pressure dip phenomenon. Based on the micro-scale information obtained from DEM, it could give a further insight of force and internal structure inside the sand pile. Numerous studies could be found on directional dependent fabric anisotropy, such as the probability distribution of contact forces and contact vectors inside sand piles (Zhou and Ooi, 2009; Ai et al., 2011; Zhu et al., 2013). Zhou and Ooi (2009) intended to explain this counter-intuitive phenomenon with the characteristics of contact force and granular fabric in terms of the contact orientation and particle orientation. For the concentrated deposition method, the contact orientation was predominantly in the orientations of 60° and 120° within spherical particles. However, considering the non-spherical particles, the contact orientations can be approximated by a second-order Fourier expansion into periodic distribution behaviour. The spherical particles formed a more symmetrical condition and reduced the degree of pressure dip in comparison with the non-spherical tests.

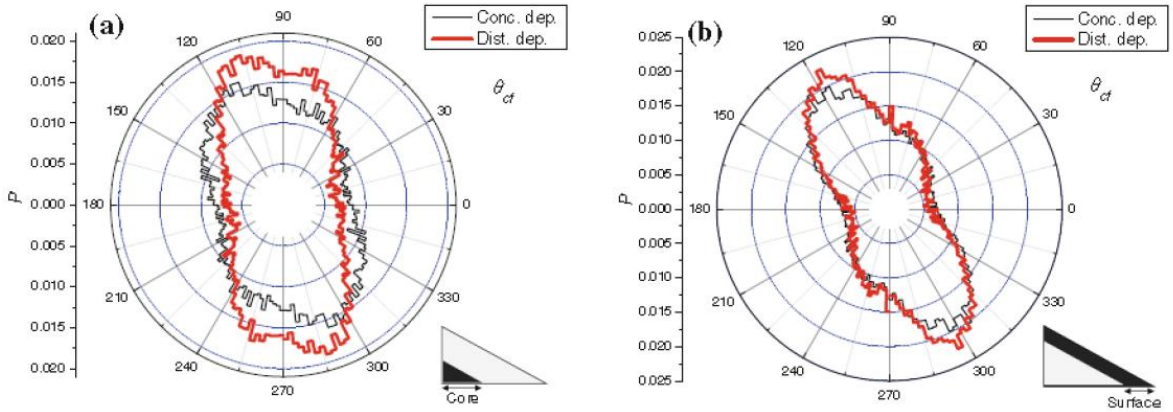
Non-spherical particles can be generated using a clump of spherical particles in DEM. Ai et al. (2011) carried out a two-dimensional simulation test with the concentrated and distributed deposition tests based on the clumped particles. They investigated the fabric within core region and surface region inside the sand pile. Figure 2.13 and Figure 2.14 give the distribution of contact orientation and contact force orientation in the core and surface regions with the two preparation methods respectively. The main difference of the contact orientation and the contact force orientation due to the deposition methods appears in the

core region. The symmetrical orientation was observed for the distributed deposition, while for the concentrated deposition, it produced an inclined contact orientation causing the pressure dip phenomenon.



(a) Core region (b) Surface region

Figure 2.13 Contact orientations for concentrated and distributed deposition (Ai et al., 2011)

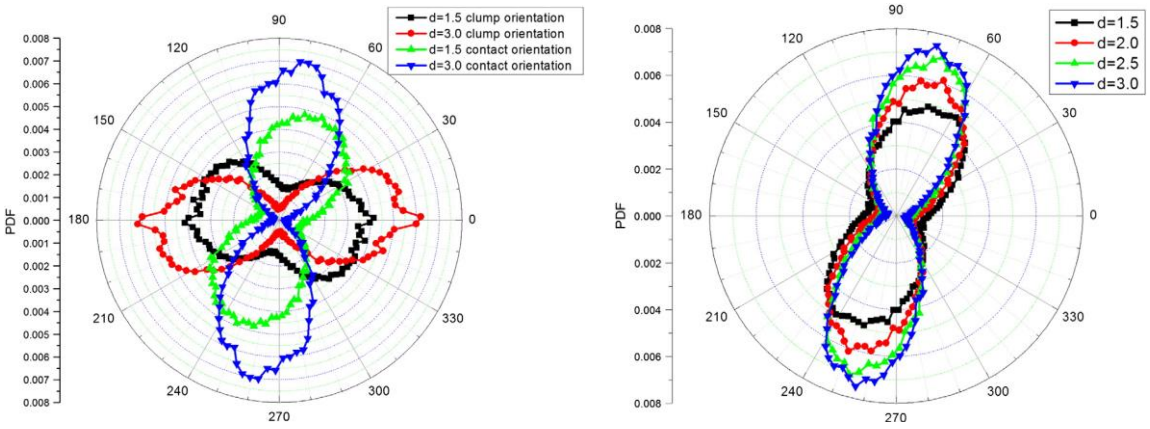


(a) Core region (b) Surface region

Figure 2.14 Contact force orientation for concentrated and distributed deposition (Ai et al., 2011)

The clumps were formed with the assemblies of the same radii whose centres lie on a straight line. The distance between the clumped particles equals the radius of the particle (Zhu et al., 2013). Hence, the parameter of the particle aspect ratio is an important factor that defines the shapes of the simulated particles. It is defined as the ratio of the length to the width of the clump particles. Zhu et al. (2013) considered the impact of the particle

aspect ratio on the behaviour of pressure dip phenomenon. They produced the piles with the particle aspect ratios of 1.5, 2.0, 2.5 ,and 3.0, corresponding to a clump of two, three, four, and five spheres respectively. Results showed that the degree of pressure dip phenomenon increased with the increase of particle aspect ratio. The fabric was studied to understand the pressure dip phenomenon with various values of the particle aspect ratio. Figure 2.15 illustrates the characteristics of the contact orientation, particle orientation and the force direction respectively. Particles were optimally stable in the horizontal direction, especially those with higher aspect void ratios.

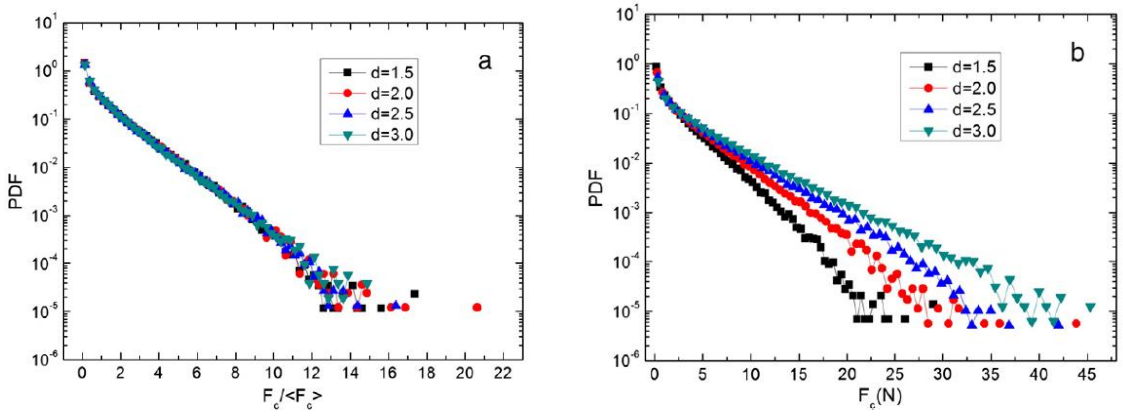


(1) particle and contact orientation (2) resultant force orientation

Figure 2.15 The orientation distribution with various aspect ratio (Zhu et al., 2013)

Zhu et al. (2013) also investigated the probability distribution of the resultant contact force as Figure 2.16 below. Their results were in agreement with the results of Zhou and Ooi (2009). The strong force chains occurred with the increase of the particle aspect ratio due to the slow decay of the force distribution. Combined with the analysis of the distribution of the orientation of contact force, they concluded that the main reason for the appearance of the dip was the more and stronger force chains that were preferentially orientated with steeper direction. Stronger force chains orientated with an inward inclination, which formed arches to reduce the stress transmission, underneath the centre apex for the concentrated

deposition test. With the increase of the particle aspect ratio, the extent of the dip was increased depending on the increase of the orientation angle.



(1) normalised contact force (2) resultant contact force

Figure 2.16 The probability distribution of contact force (Zhu et al., 2013)

Furthermore, the impact of water has also been probed on this phenomenon. Zhao and Tong (2013) proposed that the pressure dip decreased with the impact of water using CFD-DEM software. The macro- and micro-mechanics observations, such as void ratio, coordination number and contact force behaviour, have also been carried out to explain this counter-intuitive phenomenon. They found that the pressure dip phenomenon related to the inhomogeneous internal structures.

The literature review presented above has investigated the "pressure dip" phenomenon in the factors of deposition height, rate, jet-radius as well as the particle shape and the particle aspect ratio. The mobilisation of base friction is suggested as a key factor to produce the contact force orientation and form the internal arches (Anand and Gu, 2000; Ai et al., 2013). It indicates that the rough boundary has a relationship with the counter-intuitive phenomenon. However, in this project, the impact of boundary has not been taken into account. For the DEM numerical simulations, with the consideration of rolling friction coefficient, the sand pile would be easier to reach a stable condition. It could also form a

larger repose angle (Zhou et al., 1999; Zhou et al., 2002; Ai, 2010; Nakashima et al., 2011; Zhao and Tong, 2013). Nevertheless, it would change the initial material properties. As a consequence, the rolling friction coefficient is not taken into account for this project.

The internal structure is proposed to have a relationship with the counter-intuitive phenomenon. The investigations are mainly based on the two-dimensional sand pile in the numerical simulation. In addition, it only considers the materials at the global scale at the final stage. No research has presented the progressive anisotropy behaviour with different construction histories and it is one of the aims of this project. To better understand the materials behaviour inside the sand pile, DEM simulation tests were performed in this project to obtain the particle-scale mechanisms. It could reveal the behaviour of each particle and thus could obtain the anisotropy behaviour of one particle or a representative volume element. This project aims to explain the phenomenon with the progressive evolution of stress, fabric and contact force inside the sand-pile structure under different construction histories, in the three-dimensional condition.

2.3 Constitutive behaviour of granular materials

The pressure distribution of sand piles demonstrated that the stress state within the pile is related to the structure of granular materials. A sand pile, with the pressure dip phenomenon, contains more voids in the centre to form arches for transferring the stress to the outer edges. With respect to the elementary behaviour of granular materials, the stress state is also related to the structural state variables, for instance, the relative density of the structure. The dilatancy is defined as the volume change subjected to the shearing of the granular materials. It is well known that the dilatancy is observed in shearing the dense sand. However, for the loose sand, the structure is contracted even when subjected to the same stress state as in the dense sand.

The experimental and numerical tests are performed in this area to study the effects of different parameters on the dilatancy of granular materials. Bolton (1986) found that sand samples contracted in both dense and loose conditions when subjected to a high confining pressure during shearing. In addition, the principal stress direction affects the material response. The granular materials behaved more dilative when the major principal stress direction perpendicular to the bedding plane under the triaxial compression test, in comparison with the major principal stress direction within the bedding plane (Oda, 1972a; Li and Yu, 2009; Yimsiri and Soga, 2011).

Furthermore, under the rotation shear test, significant contraction behaviour was observed under the constant value of stress invariants (Yang, 2013). It suggests that the dilatancy has a relationship with the internal state even under the same stress ratio and stress state. Li and Dafalias (2000) proposed an expression for dilatancy as a function with the parameter of stress ratio, void ratio, and internal state. The dilatancy rate is expressed as

$$d = d\left(\eta, e, Q, C\right) \tag{2.10}$$

where Q refer to the internal state variable and C is an intrinsic constant.

The following sections review the anisotropy of granular materials and the impact of fabric on the material responses.

2.3.1 Anisotropy of granular materials

Anisotropy is a vital factor affecting the behaviour of granular materials and numerous researches have been studying this issue in the past few decades. Much effort has been made to observe the anisotropic response and investigate the fundamental mechanism. Casagrande and Carillo (1944) were the first to divide the anisotropy fabric into two categories: initial and induced fabric. The initial anisotropy refers to the initial structures

of granular materials according to their constitution, especially in the naturally deposited process. The induced anisotropy is generated due to the structure deformation under the condition of the external loading. The anisotropy of granular materials is profoundly due to its internal structure (fabric) anisotropy. Brewer (1964) first defined fabric as the spatial arrangement of solid particles and associated voids. Hence, the fabric should contain at least three aspects: (1) orientation distribution of elongated particles, (2) contact normal distribution of interacting particles and (3) Void distribution (Oda and Iwashita, 1999).

2.3.1.1 Initial anisotropy

The initial anisotropy mainly depends on the sedimentation process in nature, and, therefore, can be realised by adopting different sample preparation methods in the lab. This anisotropy is specified as the anisotropy before application of external loading. Oda (1972a) and Mulities et al. (1977) demonstrated that different sample preparation methods could form different fabric of granular materials. There are three mainly employed methods for the sample preparation: the deposition method, tapping method and vibration method, in the laboratory tests.

Vaid et al. (1999) investigated the uniformity and ensued fabric of the specimens due to different sample preparation methods. Various contractive and dilative responses resulted from different preparation methods, even when the void ratio and effective stress states were identical in all tests. They found that the moist-tapping method formed a more inhomogeneous sample in contrast with other preparation methods.

Papadimitriou et al. (2005) explored the response of specimens prepared with dry deposition, wet tamping, air pluviation and dry rodding methods, under undrained monotonic triaxial compression and extension tests. In all these tests, the void ratio and confining pressure remained unchanged. Four different responses (e.g. different dilatancy

and hardening responses) were observed corresponding to different initial fabric anisotropy behaviour formed using the various methods. Different initial anisotropy could also be formed using stratified structure due to the segregation of particle size and graded bedding in sand deposits. Employing this approach, Yoshimine and Koike (2005) investigated the stress-strain behaviour by means of a monotonic triaxial loading test and a cyclic triaxial loading test, respectively. Results showed that specimens prepared on the basis of segregated and stratified structure were much more dilative and stiffer in comparison with the homogeneous and uniform samples.

The literature review presented above shows that the initial fabric anisotropy relates to specimen responses (such as the diltancy), in particular the stress resistance and stress-strain behaviour regardless of loading conditions.

2.3.1.2 Induced anisotropy

After specimen formation, the external forces would be exerted on the sample, leading to a continuous anisotropy due to shearing induced plastic deformation. This type of anisotropy could be induced either by stress-controlled or by strain-controlled. It is directly related to the particle orientation as a result of the directional redistribution during the shearing stage. Arthur et al. (1977) investigated the effect of stress-induced anisotropy on dense samples with the application of monotonic shearing at various principal stress directions. The results indicated that the induced anisotropy had a significant impact on the strain for achieving the given target stress ratio.

Oda et al. (1985) discussed the stress-induced anisotropy by studying two-dimensional assemblies of oval cross-sectional rods in biaxial compression tests. During the shearing deformation, the principal axes of fabric tensor rotated toward the principal axes of the stress tensor. It was also concluded that the distribution of contact normal played a major

role in the stress-induced anisotropy.

The induced anisotropy occurs as a consequence of the applied loading. It could be realised by subjecting the test specimen to prescribed stress paths such as the monotonic loading. Thus, different granular material behaviour could be observed with various loading paths due to the formation of distinctive material anisotropy. It could help understand the granular materials responses under continuous shearing.

2.3.2 Loading-path dependence of granular materials

The evolution of stress state of granular materials, in the geotechnical engineering practice, could be evaluated using specified loading paths. In general, loading paths could be classified into being proportional or non-proportional. Parameters such as shape, initial anisotropic condition, void ratio, gradation, sample sizes, drained and undrained conditions also have a great influence on the material behaviour. This section reviews the material behaviour affected by using various loading paths.

In the early decade of the 1970s, the major methods for observing the granular material response were the conventional triaxial compression and extension tests, usually adopting a proportional loading path. Factors such as the intermediate principal stress ratio b values, void ratio and the principal stress directions were usually used to assess the material behaviour. Numerous researchers have been attracted to investigate the soil stress-strain behaviour under the triaxial shear stress path in the past few decades.

Oda et al. (1978) studied the stress-strain relationship using different loading directions under the plane strain test. The different loading directions were realised via various tilting angle δ of an initial horizontal plane as Figure 2.17(b). During the shear test, the cell pressure, referred to as σ_3, was kept constant in the same manner to a conventional triaxial

test. The deviator shear stress was applied by increasing σ_1 and σ_2 in a way that maintained the plane strain condition. Under a series of tests, the maximum peak pressure occurred when the angle was in the vertical direction as shown in Figure 2.17(a). In addition, the pressure was reduced when δ rotated from the vertical to the horizontal direction.

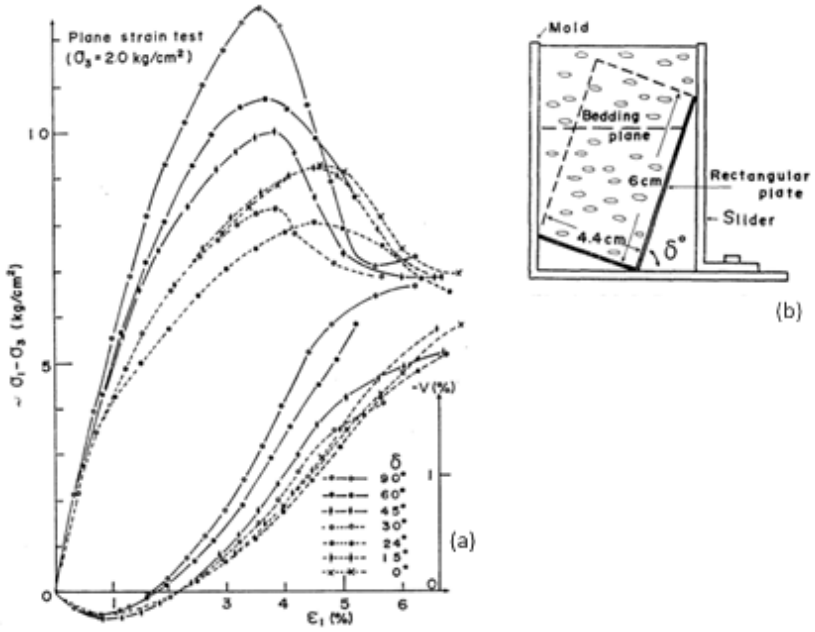


Figure 2.17 The stress-strain behaviour with plane strain test (Oda et al., 1978)

Miura et al. (1986) conducted triaxial tests with different principal stress directions and found that the failure strength was mainly dependent on the principal stress direction. The confining pressure and the intermediate principal stress ratio remained constant during shearing for all the tests. Similar results were obtained by Oda et al. (1978) according to Figure 2.18(a) with different principal stress directions. The fixed principal stress axes are presented in Figure 2.18(b). Results displayed that the peak stress ratio decreased as the loading principal stress axes rotated away from the vertical direction. Note that the deformation behaviour is unaffected by the loading directions if the specimen is isotropic in its mechanical properties. The results, therefore, revealed the importance of the initial fabric anisotropy of samples. They explained that the anisotropic deformation behaviour

strongly related to the shear plane that was fairly parallel to the bedding plane.

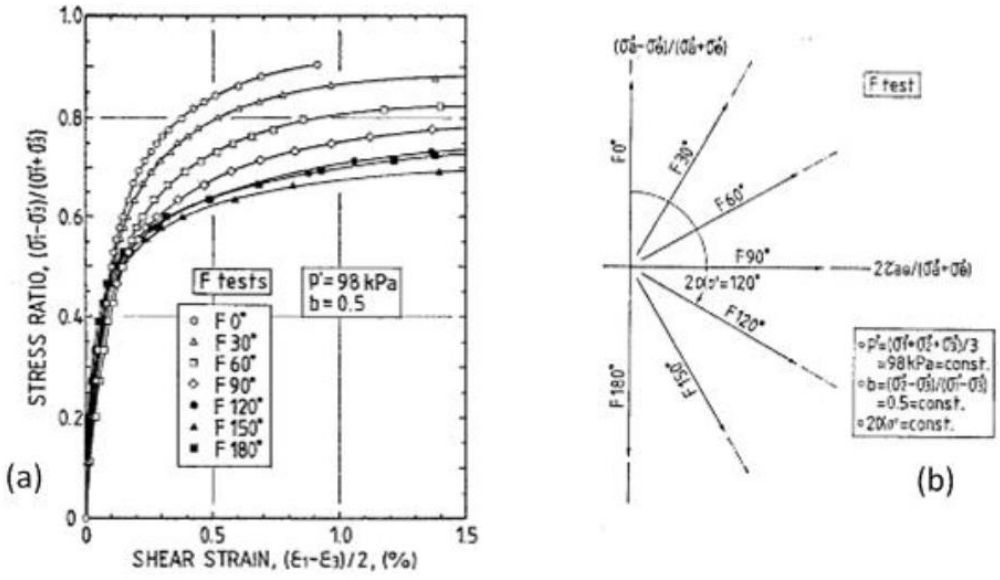


Figure 2.18 Stress ratio behaviour on the direction of principal stress axes (Miura et al., 1986)

Yoshimine et al. (1998) performed undrained monotonic triaxial compression and extension tests on Toyoura sand using the hollow cylinder torsional shear apparatus. They conducted a series of tests with various principal stress directions and intermediate principal stress ratios. Results indicated that the specimen tended to soften when the magnitude of the intermediate principal stress ratio became larger. Similar observations have been made in the triaxial extension test, while the shear behaviour was more contractive and softer in contrast with the triaxial compression test.

With the development of apparatus, non-proportional loading path becomes possible and achievable in the laboratory. With this loading path, significant plastic deformation could be observed. This high level of plastic deformation is encountered in almost all practical geotechnical problems, for instance, the liquefaction of soils during earthquake related to the earthquake-resistance design. Peacocck and Seed (1968) developed a simple shear test apparatus with cyclic shear in the horizontal direction and found that the resistance to

liquefaction was about one third compared with the value obtained using a triaxial test apparatus under the identical condition. Ishihara and Li (1972) developed a triaxial torsion device with the cyclic loading based on the strain-controlled cyclic torsion to understand the liquefaction of saturated sand. They found that the liquefaction behaviour was related to the initial value of K_0 and the lateral stress.

Arthur et al. (1980) employed a specially designed flexible boundary test, named as the Directional shear cell test, to investigate the effects of cyclic rotation of the principal stress directions. Deviations occurred between axes of the stress rate and strain rate at the beginning of the rotation. However, they were faded quickly during the continuous rotation.

Ishithara and Towhata (1983) investigated the stress-strain behaviour with three series of tests, i.e. the cyclic triaxial shear test, the cyclic torsion shear test and the cyclic test with the rotation of principal stress directions, employing a torsional shear apparatus. They found that, with the rotation of the principal axes, the liquefaction resistance of sand was reduced due to a greater amount of excess pore water pressure when compared to the test without rotation.

The hollow cylinder torsional shear apparatus was widely used in the recent decades for investigating soil behaviour under the generalised stress paths involving the rotation of principal stress axes (Miura et al., 1986; Vaid et al., 1990). Miura et al. (1986) investigated the fundamental deformation-strength behaviour of the anisotropic dense sand under the condition of principal stress axes rotation using a hollow cylinder torsional shear apparatus. Under the principal stress axes rotation, the tests were performed with constant principal stresses. Tests with and without the rotation of principal axes were performed respectively. Comparing the results using different loading paths, they found that the samples expanded when increasing shear stress under the fixed principal stress axis loading path, even though

the stress invariants remained constant. However, under the same condition, the samples compacted due to the rotation of the principal axes. Furthermore, the principal strain increment directions were located between the principal stress directions and the principal stress increment directions during rotation. Figure 2.19 presents the strain increment vectors in the stress space. According to this figure, the direction of the strain increments approaches the principal stress axes with an increase of the shear strain.

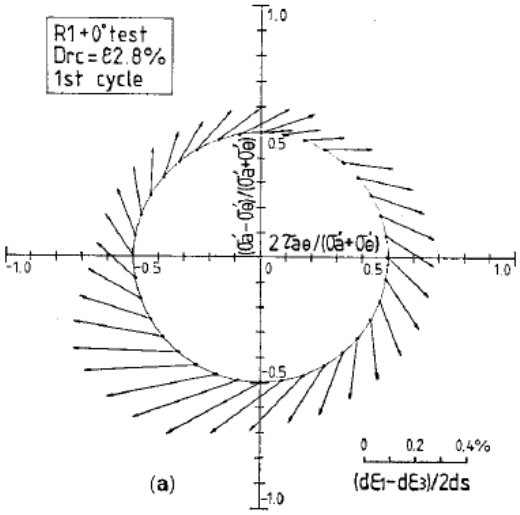


Figure 2.19 The strain increment in the stress space (Miura et al., 1986)

The rotation of principal stress directions is commonly seen under the construction of embankment at different zones. Figure 2.20 gives the contours of principal stress directions with the impact of an embankment. The rotation of the principal stress directions is decreased with the increase of the height under the embankment.

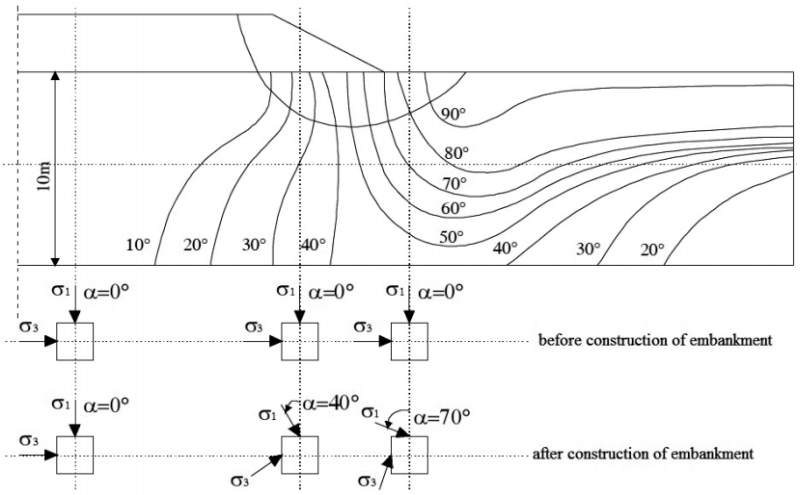
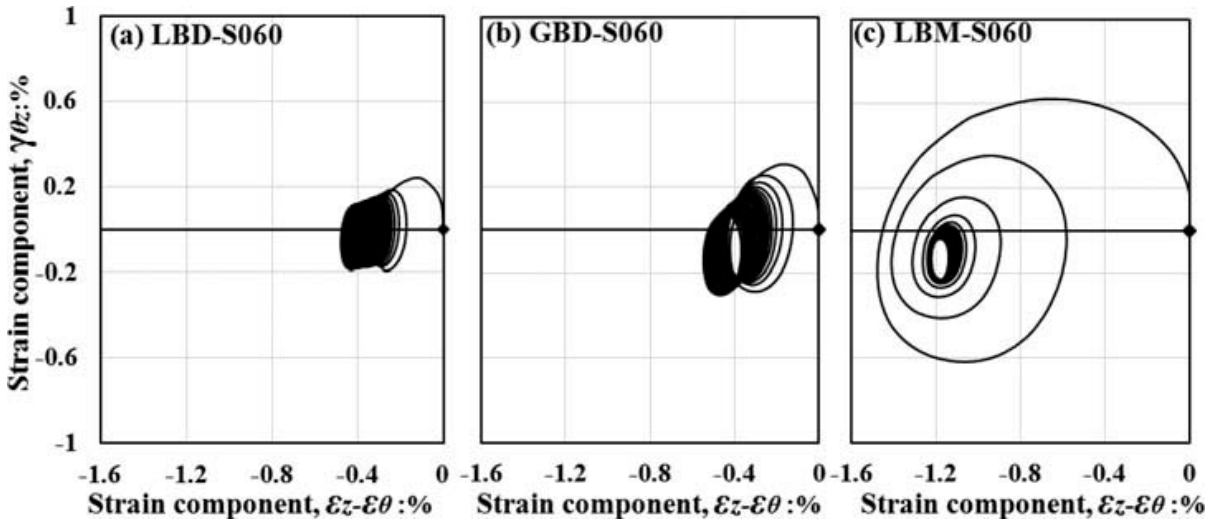


Figure 2.20 The changes of principal stress directions under the construction of embankment (Jardine and Menkiti, 1999)

More recently, a newly developed hollow cylinder apparatus (HCA) becomes the most common equipment for the rotational shear test (Naughton and O'Kelly, 2004; Yang et al., 2007; Tong et al., 2010; Yu et al., 2015). Naughton and O'Kelly (2004) investigated the induced anisotropy behaviour of Leighton Buzzard with the hollow cylinder apparatus (HCA). The samples were first consolidated under an isotropic condition and then loaded under different principal stresses. After that, tests were conducted with the rotation of major principal stress. The results suggested that the response had a complex relationship with the principal stress rotation angle α_ϑ and the intermediate principal stress ratio b value. However, the deviatoric strain and the volumetric strain were independent of the magnitude of α_ϑ.

Yu et al. (2015) observed the drained anisotropic behaviour of saturated granular materials under the rotational shear stress path with experimental test carried out by HCA. The deformation characteristics were affected by the stress level, initial material density and b value. Results also showed that the specimens were mainly contractive and approached an ultimate state of constant void ratio during the shearing stage. Furthermore, samples were

more contractive when increasing the stress ratio and b value. The strain trajectory was more significant under the higher b value as it induced larger strain trajectories in the first few cycles. Figure 2.21 below presents the strain trajectory with different void ratios under the same condition of stress ratio. The strain trajectories were in an ellipse shape in these tests. A larger strain trajectory was observed in the first few cycles when the void ratio was high.



(a) $e = 0.585$ (b) $e = 0.537$ (c) $e = 0.671$

Figure 2.21 The evolution of strain trajectory with various void ratio (Yu et al., 2015)

Literature review shows that the material response and internal structure are loading path dependent. Different material behaviour results from various loading paths, even under the same initial condition. Employing the representative volume element, the stress-strain behaviour could be studied with the specified loading paths.

2.4 Micro-scale observations and "SFF" relationship

Granular materials in nature have various sizes, shapes and usually consist of two phases: solid particles and voids between the particles, leading to different internal structures. The

fabric, denoted as the spatial arrangement of particles and the associated voids, could give insights into granular materials anisotropy behaviour. Numerous researchers, using both experimental and numerical methods, propose that the anisotropy of internal structure is one of the most vital aspects for the better understanding of the mechanics of granular soils. On the premise of quantification for fabric tensor, the fabric anisotropy of granular materials could be investigated. The investigations of fabric based on the experimental and numerical techniques are reviewed in the subsections that follow.

2.4.1 Experimental study on fabric

The experimental investigation on the micromechanics of granular materials is limited before due to their immature techniques. Recently, with the advantage of advanced image analysis techniques, the geometrical information of microstructure could be obtained directly to quantify soil fabric in the laboratory. The methods involve magnetic resonance imaging (MRI), X-ray computed tomography (CT), acoustic emission (AE) and laser aided tomography (LAT) (Tanimoto et al., 1981; Lizak et al., 1991; Konagai et al., 1992; Lee and Dass, 1993; Desrues et al., 1996).

The X-ray has been commonly used in medical science from 1970 and then applied to the microstructure observations. It has been widely used on concrete, soil and rock. This method becomes popular attributing to its quick image capturing ability. Lee and Dass (1993) developed an experimental technique to observe the actual particle packing pattern using X-ray CT. Recently, the CT method, due to its non-destructive nature, is widely used to investigate the cross-sectional images of specimens (Chang et al., 2003; Oda et al., 2004; Wang et al., 2004; Alshibli and Hasan, 2008). Compared with other methods, it could also be used for 3D structures reconstruction. Furthermore, based on this method, Chang et al.

(2003) developed an algorithm to track the deformation of each particle and the variation of their proposed fabric tensors within the specimens at different triaxial loading stages .

Wang et al. (2004) proposed a method to reconstruct a true 3D platform for individual particles and the whole granular system. In this method, the granular system was described using the characteristics of mass centre coordinates for the particles and their morphology representation. With this information, the properties of soil fabric such as the contact normal distribution and local volume fraction could be identified. Oda et al. (2004) employed the X-ray CT method to observe the shear band in microstructure. The 2D and 3D X-ray images showed the particle distribution around the shear band at a microscopic scale.

Another important issue is the stress distribution inside the material skeleton consisting of granular materials. The photoelastic techniques could be used to observe the contact force network inside a granular system (Drescher and De Josselin de Jong, 1972; Oda, 1972a; Oda, 1978; Oda et al., 1985). Drescher and De Josselin de Jong (1972) used the photoelastic technique to verify the double-sliding free-rotating model with disks constituted a two-dimensional analogue granular system. They determined the average stress tensor and the strain-rate tensor within the granular materials using the microscopic information.

2.4.2 Fabric of granular material

Oda and Nakayama (1989) proposed that at least the following three sources of anisotropy should be taken into account to analyse the anisotropy of soils: (1) the anisotropic distribution of contact normal indicating the mutual relation among particles, (2) the preferred orientation of non-spherical voids, and (3) the preferred orientation of non-spherical particles. They introduced the fabric tensor to express the geometry of discrete particles packed concretely and presented a formulated continuum model so that the fabric

tensor is explicitly used in the framework of soil plasticity. In such a case, the following aspects of soil fabric could be investigated at particle-scale.

2.4.2.1 Average coordination number

The effect of void ratio on the material response has been studied through the experimental and numerical tests. Void ratio is regarded as a close link to the average coordination number at particle-scale. The average coordination number refers to the average density of contacts per particle within a granular assembly. It has been widely used to characterise the homogenisation of specimens. Oda (1972a) proposed that the mean value of the coordination number had a clear correlation with the void ratio of granular materials, which is independent of particle size distribution.

2.4.2.2 Directional distribution of contact normal orientations

Kanatani (1984) illustrated the characteristics of inter-particle contact orientation distribution with the proposed different ranks of fabric tensor. They first applied three kinds of tensor determined in terms of a basis with the space of functions on a unit sphere or a unit circle. Figure 2.22 gives the definition of contact normal, contact force and contact vector with spherical and non-spherical particles. In the figure, n^{AB} and n^{BA} are contact normal, f^{AB} and f^{BA} denote contact forces. The contact vector is represented by l^{AB} and l^{BA} in this figure.

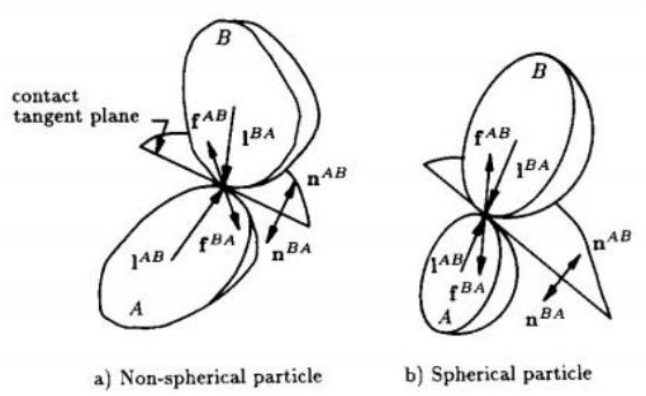


Figure 2.22 Definition of contact normal, contact force and contact vector

(after Bathurst and Rothenburg, 1990)

To characterise the statistics of the directional data with tensor, the contact normal tensor is calculated using the average self-tensor product of the unit normal direction at contact points as follows

$$\boldsymbol{N}_{ij} = \frac{1}{N_c}\sum_{c=1}^{N_c} \boldsymbol{n}_i^c \boldsymbol{n}_j^c \tag{2.11}$$

where N_c refers to the total number of contacts and $\boldsymbol{n}$ is the unit normal direction at the contact point c.

This fabric tensor is made up of an isotropic and a deviatoric parts. Li and Yu (2013) gave a definition of the deviator direction tensor with the $n-th$ rank. In the three-dimensional space with the $2nd$ rank, it is calculated according to the following equation

$$D_{ij} = \frac{15}{2}\left(\boldsymbol{N}_{ij} - \frac{1}{3}\delta_{ij} \right) \tag{2.12}$$

Then, in micromechanics of granular materials, up to the second rank expression, the probability density of contact normal in direction $\boldsymbol{n}_i$ is approximated as

$$E_c(\boldsymbol{n}_i) = \left(1 + D_{ij}\boldsymbol{n}_i\boldsymbol{n}_j\right)/E_0 \tag{2.13}$$

in which E_0 is the surface area of the unit sphere Ω. Hence, in the three-dimensional space, it equals to 4π.

The magnitude of fabric anisotropy could be calculated on the basis of the deviator direction tensor using the following expression in terms of principal stresses

$$D_q = \sqrt{\frac{1}{2}\left(\left(D_1 - D_2\right)^2 + \left(D_2 - D_3\right)^2 + \left(D_3 - D_1\right)^2\right)} = \sqrt{\frac{3}{2}D_{ij}D_{ji}} \tag{2.14}$$

where D_1, D_2, D_3 refer to the major, intermediate and minimum principal fabric values respectively, of the contact normal tensor.

2.4.3 Directional distribution of vectors

For particle-scale analyses, the directional distribution of contact forces and contact vectors should also be characterised. Following Li and Yu (2011; 2013), the second rank contact force tensor is defined as the product of the average contact force and its direction $\left(\boldsymbol{n}_s\right)$ over all the directions. It is evaluated by the tensor product of the average contact force and its unit direction at contact points on the surface area with the following expression

$$K_{ij}^f = \frac{1}{E_0}\frac{1}{N_c}\oint_{\Omega}\left\langle f_{cont}\right\rangle\Big|_{n_i} \otimes \boldsymbol{n}_j d\Omega \tag{2.15}$$

in which N_c is the total number of contacts and $\boldsymbol{n}_j$ is the unit direction. The direction average of mean contact forces on all directions f_{cont0} is calculated as

$$f_{cont0} = \frac{\oint_{\Omega} f_{cont_i} \boldsymbol{n}_i d\Omega}{E_0} = K_{jj}^f \tag{2.16}$$

In the Eq.(2.15) and Eq.(2.16), K_{jj}^f is the trace of the contact force tensor. The contact force tensor could also be divided into isotropic and anisotropic parts, similar to the contact normal tensor illustrated above. The expression of the deviator contact force tensor for the three-dimensional with the second rank is:

$$G_{ij}^f = \frac{3K_{ij}^f}{K_{jj}^f} - \delta_{ij} \tag{2.17}$$

The contact vector tensor can be approximated using the same method adopted for the mean contact vectors on the unit normal direction. It only changes the contact force to the contact vector in the expressions from Eq.(2.15) to Eq.(2.17). The anisotropy magnitudes of contact force and contact vector are calculated according to Eq.(2.14) using the corresponding deviatoric contact force tensor and deviatoric contact vector tensor respectively.

2.4.4 Particle-scale observations on material responses

With the development of numerical technology, the DEM simulation is a useful tool to provide the instant micro-mechanical information of particles and investigate the properties of granular materials at the particle-scale. Employing the fabric tensor and contact force tensor defined above the fundamental insights into the observed macro-scale mechanical behaviour can be obtained. The following reviews the effects of micro-scale responses on the characteristics of the material responses using DEM.

Sitharam et al. (2002) obtained the macro-mechanical and micro-mechanical behaviour of loose and dense specimens made up of the poly-disperse assemblies. DEM tests were

carried out using drained and undrained stress paths respectively in the isotropic compression and triaxial static shear. The micro-scale behaviour, such as the deviatoric magnitude of contact force anisotropy and contact normal anisotropy, are displayed in Figure 2.23. The results show that the dense sample has higher magnitudes of force anisotropy and fabric anisotropy than the loose sample (i.e. the dense sample reached a higher shear strength and stress ratio) at all strain levels prior to steady state under the drained triaxial test.

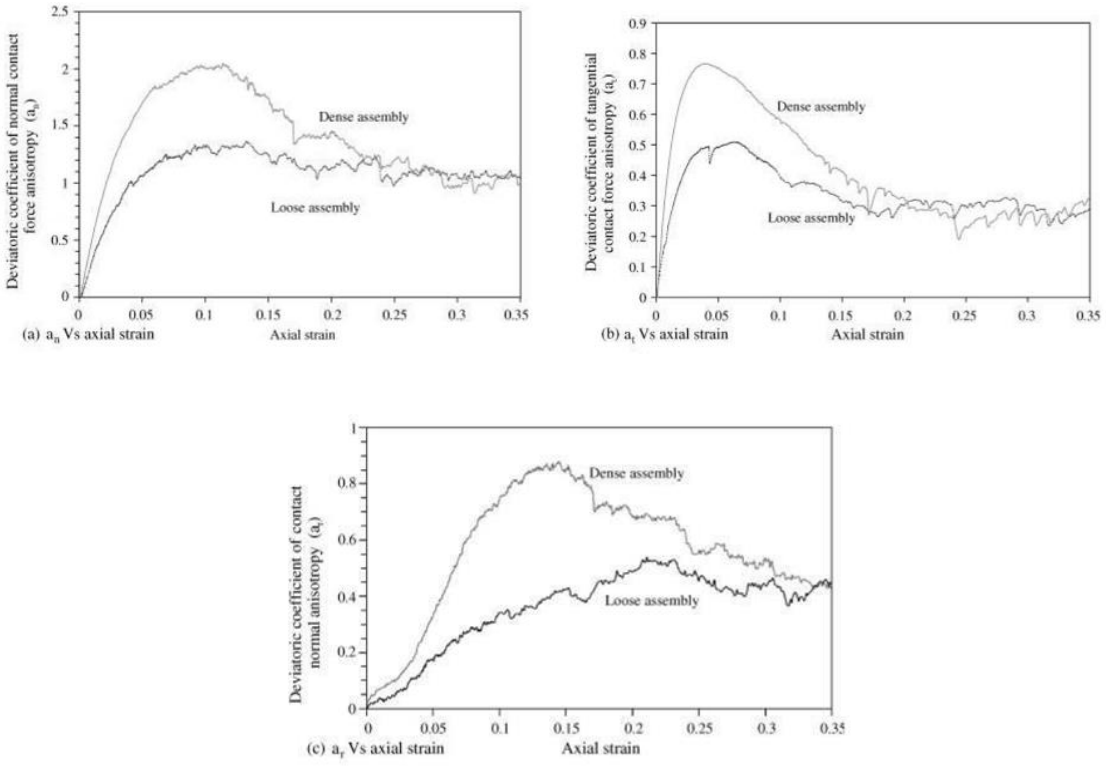


Figure 2.23 The deviatoric magnitude of fabric and force anisotropy under the drained triaxial shear test (Sitharam et al., 2002)

In the undrained triaxial test, the dense sample also has a higher fabric anisotropy magnitude than the loose sample except for in the steady state. Samples exhibited a similar level of fabric at steady state in both the drained and undrained tests. However, in sharp contrast with the similar contact force anisotropy for the drained simulation test at the stead

state, a difference appears for the magnitude of normal contact force anisotropy under the undrained triaxial shear test.

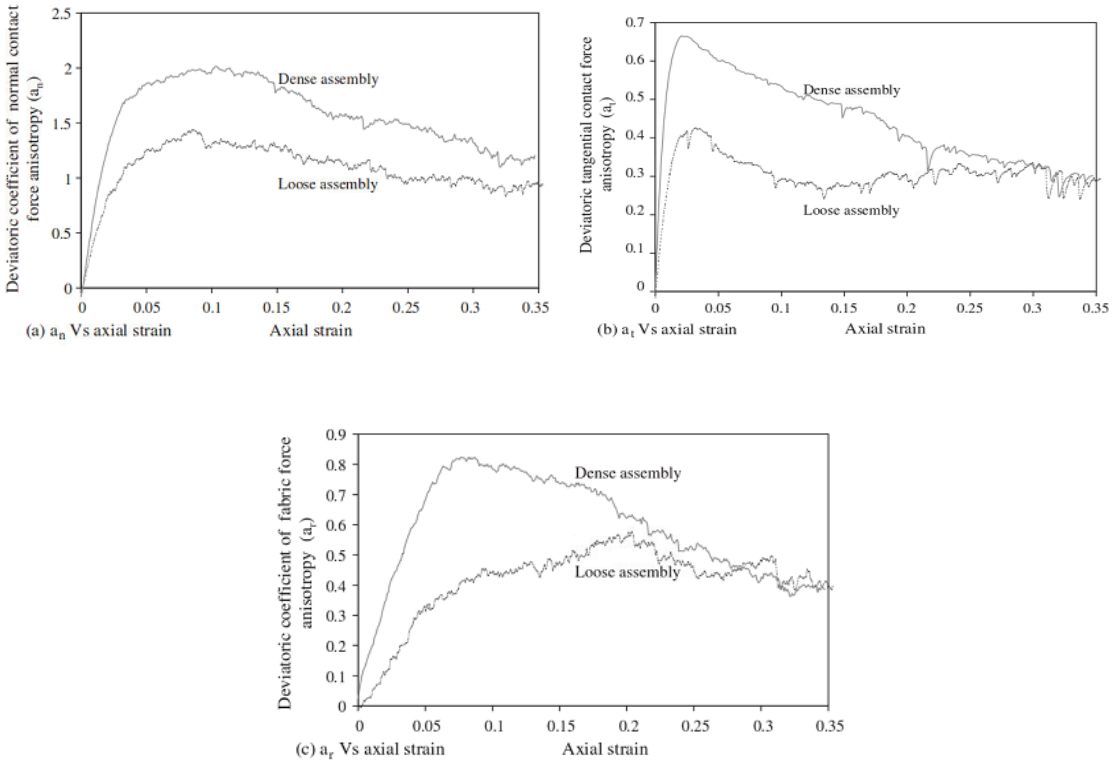
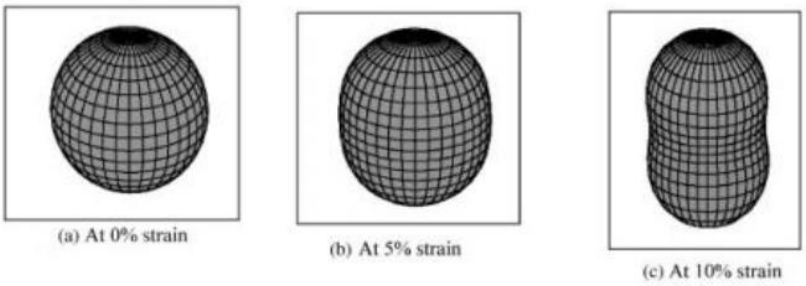


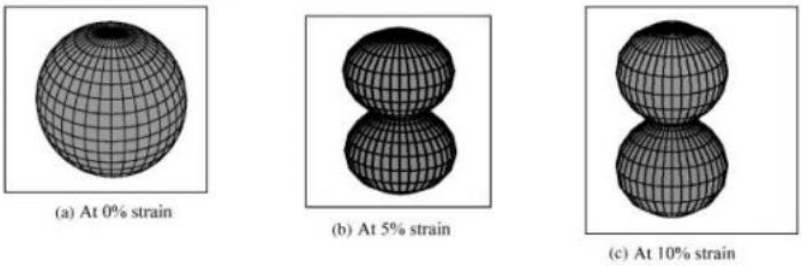
Figure 2.24 The deviatoric magnitude of fabric and force anisotropy under the undrained triaxial shear test (Sitharam et al., 2002)

They also investigated the directional distribution of fabric, such as the normal and tangential contact force distribution and contact normal distribution, at different deviatoric strains. Figure 2.25 illustrates fabric and force distribution within the dense sample in 3D under a drained triaxial shear test. The initial states of the contact normal and normal contact force showed that the sample was under an isotropic condition. The distribution of contact normal and normal contact force transformed into a peanut shape with the increase of deviatoric stress. However, the distribution of tangential contact force exhibited a dumbbell shape during shearing. Loss of contacts was observed in the minor principal stress direction, corresponding to the distribution of contact normal. However, an accumulation of contacts was observed in major principal stress direction. In addition, during the

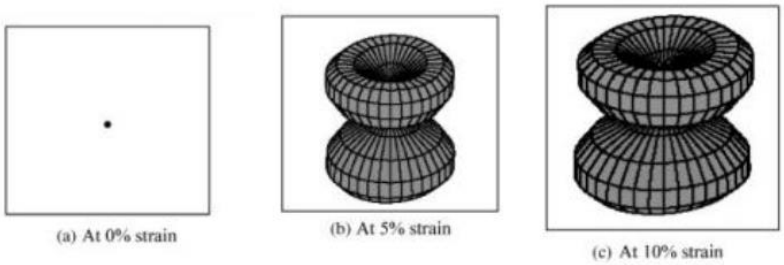
simulation, the degree of anisotropy in the normal contacts varied due to different states of initial anisotropy.



(1) Contact normal distribution



(2) Normal contact force distribution



(3) Tangential contact force distribution

Figure 2.25 The distribution of fabric for the dense sample under drained triaxial test (Sitharam et al., 2002)

Cui and O'Sullivan (2006) studied the micro-mechanics of the direct shear test in 3D. The fabric tensor was employed to quantify the orientations of contacts and the internal structure anisotropy. They found that the specimen macro-scale response was related to the variations in the deviatoric fabric. O'Sullivan and Cui (2009) further studied the particle-

scale material response using fabric anisotropy and coordination number in the strain-controlled cyclic triaxial tests. They found that the variations in the deviatoric stress were less remarkable in comparison with the variations of deviatoric fabric anisotropy under the cyclic loading.

Tests with the non-proportional loading path are also reviewed in with the context of the micro-mechanic behaviour of granular materials. Li and Yu (2010) investigated the granular material behaviour by performing a two-dimensional DEM simulation test. They found a larger stress ratio corresponding to a more anisotropic behaviour in the material fabric and a smaller ultimate void ratio. For specimens at a given stress ratio, the impact of void ratio was only significant in the first few cycles and a unique ultimate void ratio was resulted when increasing the load cycles which means that samples tended to an identical internal structure pattern during continuous shearing.

Further, Yang et al. (2015) developed a 3D rotational shear test using the numerical technique. The strain trajectories are shown in Figure 2.26(a) and (b) for the dense and loose samples respectively. The strain trajectories are similar to those in the experimental test by Yu et al. (2015). Specimens experienced an irrecoverable strain during the stress rotation, in particular in the first few cycles. The size of the strain trajectory for the loose sample was larger than for the dense sample, both in the experimental and numerical tests. According to Figure 2.26, the strain trajectories show a spiral shape for the dense and loose samples. However, the experimental results suggested that the strain trajectory exhibited an elliptical shape.

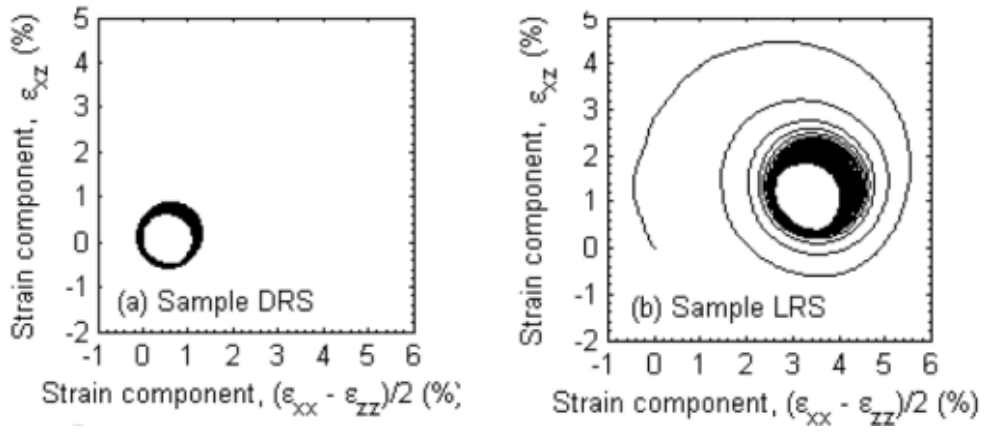


Figure 2.26 The strain trajectory (a) dense sample; (b) loose sample (Yang et al., 2015)

Yang et al. (2015) also observed the evolution of internal structure under rotational shear using DEM. A fabric tensor in terms of contact normal density was employed to examine the characteristics of the internal structure. The fabric anisotropy of the dense and loose specimens was investigated. The evolution of fabric anisotropy exhibited a loading dependence when rotated continuously with a closed cyclic trajectory. Similar results were observed by Li and Yu (2010), the fabric anisotropy and void ratio tended to their ultimate values during continuous rotation shearing. Figure 2.27 below gives the evolution of contact normal. The specimens evolved into a similar internal structure, regardless of the initial void ratio, depending on the similar size of fabric trajectory.

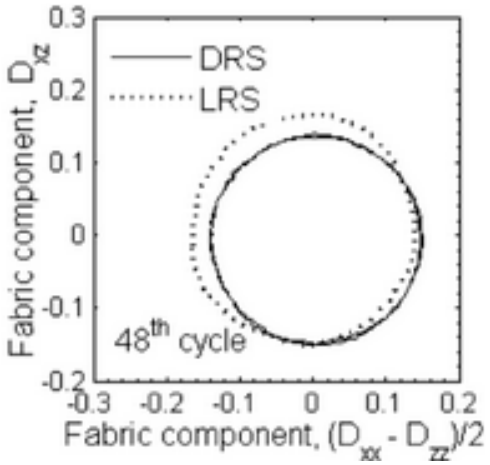


Figure 2.27 The trajectory of contact normal for the dense and loose samples (Yang, et al., 2015)

2.4.5 Stress-force-fabric relationship

The overall response of granular materials is mainly dependent on the micro-scale particle arrangement and contact interactions. Furthermore, understanding of micromechanical response could give a fundamental understanding of the macroscopic behaviour. Hence, recent researchers are paid attention to the particle-scale investigations with the aid of fast growing the numerical simulation. The average volume stress tensor from the macro-structural definition, related to the micro-scale information of contact force and contact vector, is a good starting point to probe the multi-scale investigations. The macro-scale stress tensor expressed by Eq.(2.18) is formulated as the tensor product of contact force f_j^c and contact vector l_i^c at contact point c in the case of the quasi-static condition and which treats the granular assembly interactions as point contacts.

$$\sigma_{ij} = \frac{1}{V}\sum_{c=1}^{M} l_i^c f_j^c \tag{2.18}$$

where σ_{ij} is the average stress tensor within the volume V of the specimen. M denotes the total number of contacts. It is of vital importance to take into consideration of contacts. Each internal-particle contact point is treated as two contacts for the action and reaction forces on the particle obeying the Newton's second law.

Rothenburg and Bathurst (1989) employed Fourier series to estimate the directional distribution of normal and tangential contact forces. The coefficients of direction data were interpreted as the magnitude of corresponding anisotropy degrees. They first proposed the stress-force-fabric (SFF) relationship with this information for the two-dimensional disks and made an effort to probe the fundamentals of macro-micro granular materials responses. The macroscopic strength was related to the microscopic contact force anisotropy and

fabric anisotropy.

Then, Bathurst and Rothenburg (1990) further verified the previously proposed stress-force-fabric behaviour subjected to shear deformations in 2D. Figure 2.28 gives the distribution of contact normal, average normal contact force and average tangential contact force of samples in a biaxial shear test at their peak shear states. Results displayed a progressive loss in the number of contacts oriented in the direction of minimum principal stress. They suggested that the fabric anisotropy was associated with this loss characteristic.

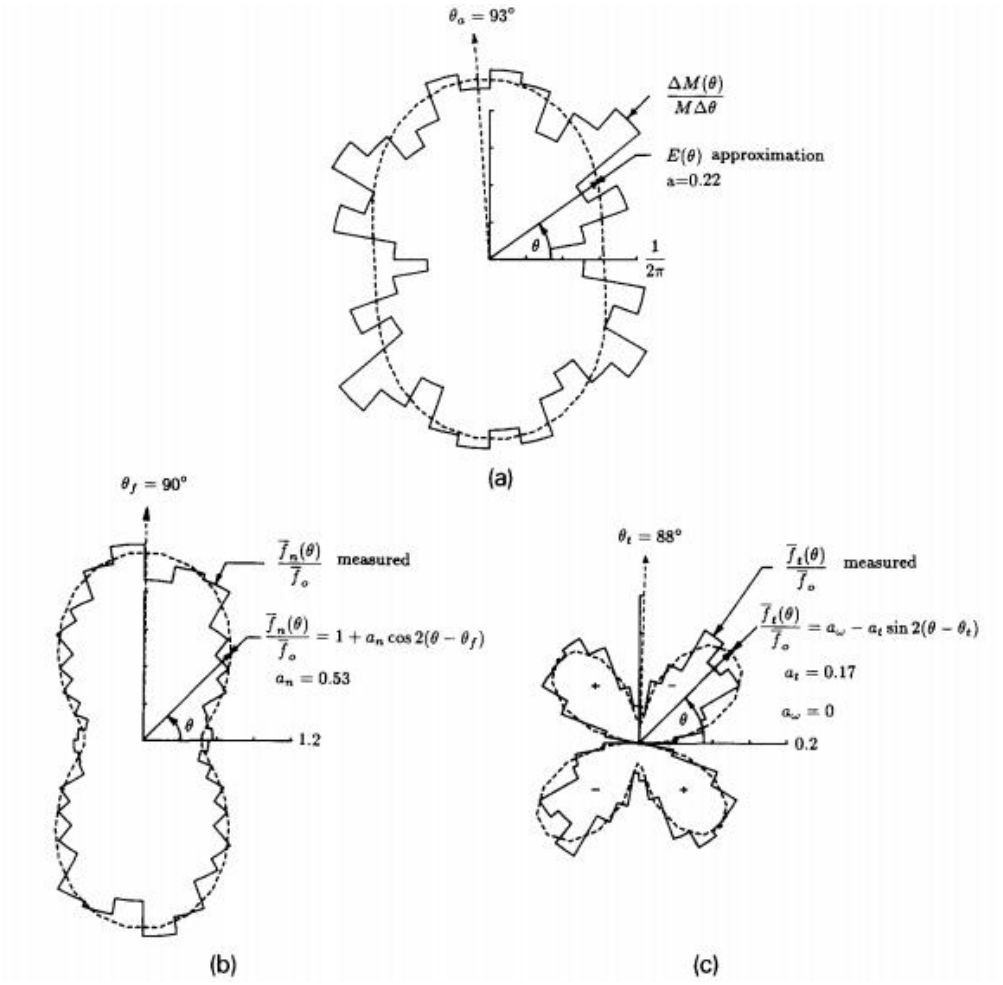


Figure 2.28 Distribution of contact normal, average normal and tangential force at peak in biaxial compression test: (a) contact normal; (b) average normal forces and (c) average tangential force (Bathurst and Rothenburg, 1990)

Later, Rothenburg and Bathurst (1993) extended this relationship to two-dimensional elliptical-shaped particles. Ouadfel and Rothenburg (2001) further developed the SFF expression for three-dimensional ellipsoidal particles. Afterwards, Li and Yu (2011) extended the mathematical formulations to the vector-valued directional data, for the tensors of contact normal, contact force and contact vector, based on the theory proposed by Kanatani (1984).

Following the research of Li and Yu (2013) and Li and Yu (2014), Eq.(2.18) could be converted to Eq.(2.19) with the consideration of contact direction. For the three-dimensional case, a unit sphere Ω is taken into consideration to illustrate all the possible directions. Let e^c denote the probability density of contact normal falling into the stereo angle element $d\Omega$. When $d\Omega \to 0$, the stress tensor is expressed as follows:

$$\sigma_{ij} = \frac{\omega N_p}{V} \iint_{\Omega} e^c(n) \left\langle l_i f_j \right\rangle \Big|_n d\Omega \tag{2.19}$$

where ω is the coordination number. N_p is the total number of particles. In general, via introducing a directional independent scalar ς, the joint product $\left\langle v_i f_j \right\rangle \Big|_n$ could be converted to $\left\langle v_i f_j \right\rangle \Big|_n = \varsigma \left\langle v_i \right\rangle \Big|_n \left\langle f_j \right\rangle \Big|_n$; and Eq.(2.19) could be rewritten as:

$$\sigma_{ij} = \frac{\omega N}{V} \iint_{\Omega} \varsigma e^c(n) \left\langle v_i \right\rangle \Big|_n \left\langle f_j \right\rangle \Big|_n d\Omega \tag{2.20}$$

The directional distribution of fabric and force could give a better understanding of material behaviour, such as the arrangements of particles and particle interaction force based on the particle-scale mechanism. Based on the information of particle interactions, the structural stress-strain relationship would be established in terms of contact normal, contact force and contact vectors.

Li and Yu (2014) gives the definition of a simplified stress-force-fabric relationship in terms of tensor multiplication for both two-dimensional and three-dimensional scenarios:

$$\sigma_{ij} = \frac{\omega N}{V} \varsigma v_{cont0} f_{cont0} \left[\begin{array}{l} \alpha_{2} \left(\delta_{ij} + K_{ij}^{f} + K_{ij}^{v} + K_{jl_1}^{f} K_{il_1}^{v} \right) + \\ \frac{2}{3} \alpha_4 \left(D_{ij} + D_{im_1} K_{jm_1}^{f} + D_{im_1} K_{jm_1}^{v} + D_{l_1 m_1} K_{il_1}^{v} K_{jm_1}^{f} \right) + \\ \frac{2}{5} \alpha_6 \left(D_{k_1 k_2} K_{jik_1 k_2}^{f} + D_{k_1 k_2} K_{il_1}^{v} K_{jl_1 k_1 k_2}^{f} \right) \end{array} \right] \tag{2.21}$$

where $\alpha_{2n} = \begin{cases} \frac{^{2n}C_n}{2^{2n}}, D = 2 \\ \frac{1}{2n+1}, D = 3 \end{cases}$ and $^{n}C_k$ is the number of k-combinations of the n-element set (Li and Yu, 2013). The other symbols refer to the same definition in Eq.(2.11) to Eq.(2.17). Li and Yu (2011; 2013) verified the stress-force-fabric relationship with both proportional and non-proportional loading paths. The predicted stress ratio of this relationship agreed well with the measured values. It demonstrates that the micro-mechanics of the contact force tensor and fabric tensor could explain the macro-mechanics strength characteristics.

2.5 Summary

Granular materials are common in nature exhibiting rich phenomenologies such as sandstorms, avalanches and mudslides. The structure of a sand pile is taken as an example in the geotechnical problems in this project. The sand pile shape is common in nature and industries, for instance, the river gravel sand and mine. The storage and transporting process of granular materials are also in the shape of the pile, in particular with the agricultural grains and mine industries. The "pressure dip" phenomenon is a classical problem observed for the heap and the causes to this phenomenon are still not clear. Studies in this area have been reviewed and it was suggested that the counter-intuitive phenomenon related to the construction history during the formation.

Factors such as the particle shape, flow rate and the particle aspect ratio are also shown to have an impact on this phenomenon. Depending on the development of constitutive modelling, fabric anisotropy (e.g. the contact orientation and particle orientation) is taken into account to explain this phenomenon. It was suggested that this phenomenon was related to the inhomogeneous structure in the core region. However, the results were mainly based on the DEM in 2D with the fabric at the final stage. No studies were found to investigate the progressive fabric anisotropy with respect to the construction history. This project investigates the fabric anisotropy during the process of sand pile formation with different construction histories. It aims to explain this phenomenon with the spatial distribution of stress, force and fabric inside the sand pile.

The sand pile structure shows that the counter-intuitive phenomenon is related to the loading path during the formation. It indicates that the stress state depended on the voids inside the structure and the loading of particles. This is the other aim of this project to study the elementary structural stress-strain behaviour under various loading paths. The behaviour of granular materials is primarily related to the material anisotropy behaviour. The internal structure plays an important role in the granular material anisotropy, which could be categorised into initial anisotropy and induced anisotropy. The initial anisotropy is mainly due to the impact of sample preparation methods. The induced anisotropy results from the loading conditions. Granular material responses have been reviewed considering different initial conditions as well as the proportional and non-proportional loading paths.

The soil fabric studied using experimental and numerical techniques and its effect on the stress state is reviewed. The internal structure determined by the fabric tensor with the directional statistical theory bridges the observation and investigation at the macro-scale and those at the micro-scales, which forms the "stress-force-fabric" relationship. Depending on this relationship, the characteristics of macroscopic strength could be

expressed in terms of microscopic behaviour using deviatoric tensors of contact normal, contact force and contact vector under both the proportional and non-proportional loading paths.

Chapter 3 Methodology

As reviewed in Chapter 2, there are three mainly used approaches to observe the granular material behaviour, as the experimental, analytical and numerical methods. For the analytical approach, it is based on the results of the experimental and numerical tests. The commonly used numerical approaches are the finite element method (FEM) and the discrete element method (DEM). FEM could simulate the large-scale system and require less computation effort. However, it could not present the inside structure and granular materials behaviour. For the experimental method, with the development of the technology, it could present the granular skeleton with a complicated reconstruction method.

DEM is a numerical technique to simulate the dynamic process of a system composed of discrete particles. The program allows finite displacements and rotations of discrete bodies. The movement of particles follows the Newton's second law. The interactions between a pair of particles can be calculated based on the particle overlapping as the pre-defined contact model. It is an approach to simulate the discontinuous granular materials, with the advantageous for the availability of detailed particle scale information, which is crucial to obtain improved understanding in the complex continuum-scale material behaviour from the particle-scale mechanisms. DEM performs simulations based on the information of interacted particles. For FEM, the simulation is undertaken with the assumptions of continuum model for the granular materials. It is therefore chosen as the main research tool in this project. This method has been extensively introduced in the literature review (Cundall and Strack, 1979; Luding 2008).

This chapter only presents the necessary details for completeness. Section 3.1 presents the basic principles of DEM and a brief review on the history and the commonly used DEM software. Section 3.2 introduces the chosen software package LIGGGHTS. And Section

3.3 introduces the numerical algorithm developed to simulate the material responses of the representative elements under general loading paths, followed by a summary in Section 3.4.

3.1 Principles of DEM

DEM is a model based on the individual inter-particle interactions and interacts only at contacts or interfaces between the particles. It contains serval basic assumptions as follows:

1) particles are regarded as rigid assemblies;
2) Based on a soft-contact approach, the rigid particles can be overlapped with a small value, determined by the inter-particle contact force via the force-displacement law.
3) Time-step should be small enough that velocities and accelerations assumed as constants during one time-step without excess computation error.

3.1.1 Calculation cycle

Figure 3.1 below displays a typical DEM calculation cycle as introduced in the manual of PFC3D (Particle Flow Code) (Itasca, 1999). The calculation starts with the evaluation of motions based on Newton's second law, with the information of initial states such as particles geometries, orientations, initial positions and velocities. Based on the contact law and relative inter-particle positions, the resultant forces and moments can be determined and used in the next calculation cycle to update particle and wall positions according to the Newton's second law. With the continuously repeated calculation cycles, the simulation of granular material assembly is achieved.

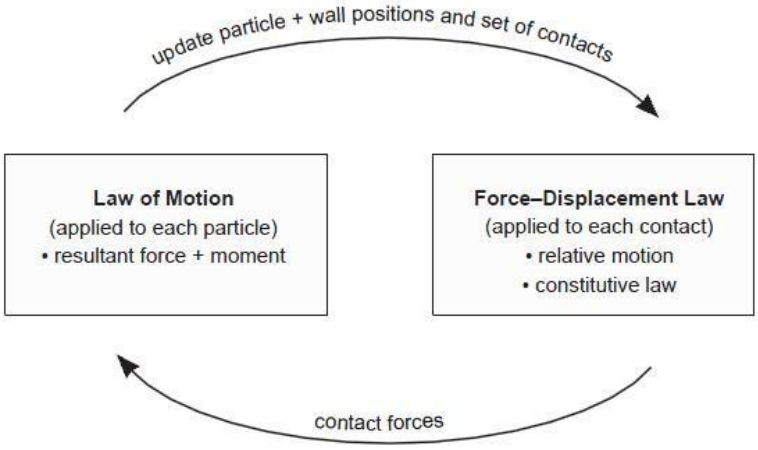


Figure 3.1 One DEM calculation cycle (after Itasca,1999)

3.1.2 Calculation of Motion

As to the particulate phase based on the Lagrangian modelling, the computation of linear and angular velocities for each particle are on the basis of the Newton's second law of motion. The governing equations of translational and rotational motion of a particle with mass and momentum are using Eq.(3.1) and Eq.(3.2) as follows

$$m_i \frac{dv_i}{dt} = \sum_j F_{ij}^c + \sum_k F_{ik}^{nc} + F_i^f + F_i^g \tag{3.1}$$

$$I_i \frac{d\omega_i}{dt} = \sum_j M_{ij} \tag{3.2}$$

where F_{ij}^c and M_{ij} are the contact force and torque for the particle i with the particle j or the boundary, F_{ik}^{nc} represents the non-contact force for the particle i with particle j or other sources. F_i^f and F_i^g refer to the particle-fluid interaction force and the gravitational force acting on particle i respectively. The typical forces and torques involved in the DEM simulation are shown in Figure 3.2.

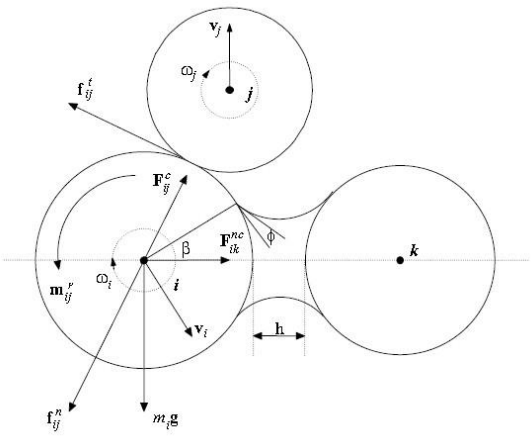


Figure 3.2 The forces and torques acting on the particle i from contacting particle j and non-contacting particle k (Zhu et al., 2007)

3.1.3 Contact constitutive model

The contact law, related the particle interactions to the relative positions between two particles, plays a critical role in the DEM simulation. Generally speaking, a contact model predicts the contact response subjected to both the normal and tangential loading. Hertz (1882) estimated the normal stiffness based on the elastic deformation of two curved surfaces. Then, Johnson (1985) improved the Hertzian theory with a consideration of the adhesion in the contact area, as the well-known elastic contact mechanics theory. Considering the tangential loading, Mindlin (1949) proposed a constant stiffness in tangential with a no-slip model. Then, Mindlin and Deresiewicz (1953) developed the theory with a slip considered at contact edges with continuous shear tractions.

3.1.3.1 The normal force-displacement relationship between two spheres

As pointed out by Hertz (1882), to calculate the normal contact force, the surfaces are assumed to be frictionless so that no shear force and displacement appear. Thus, only z component of displacement is of interest to investigate. Figure 3.3 below displays the

displacement of two equal radii spheres in the $x-z$ space.

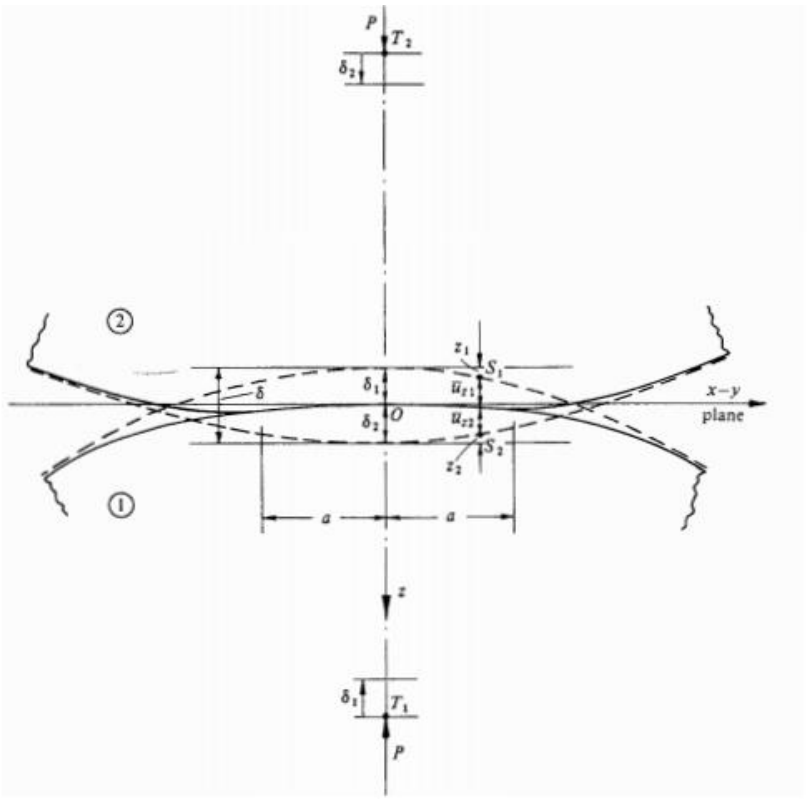


Figure 3.3 Normal contact force (Johnson, 1985)

The problem takes the first contact as an origin of the coordinate system. The $x-y$ plane is considered to the tangent plane for the two surfaces and the z axis lies along the normal directed positively into the lower solid. Each surface regards as under the condition of topographically smooth. The contact area will be circular with the radius denoting as a in the figure above. The separation between the two surfaces can be approximated by an expression of the form

$$h = \frac{r^2}{2R^*} \tag{3.3}$$

where $\frac{1}{R^*} = \frac{1}{R_1} + \frac{1}{R_2}$, $r = \sqrt{x^2 + y^2}$. R_1 and R_2 are the radii of the two bodies respectively.

From Figure 3.3, the two displacements denote as δ_1 and δ_2 respectively for the two bodies. u_{z1} and u_{z2} are the deformations of a pair of points S_1 and S_2 with the same x coordinates on the two entities respectively due to the contact pressure. According to the figure, it could be found that

$$u = u_{z1} + u_{z2} = \delta_1 + \delta_2 - h = \delta_n - \frac{r^2}{2R^*} \tag{3.4}$$

in which δ_n refers to the total deformation of the two entities and u is the total displacement of point S_1 and S_2.

The Hertzian pressure distribution and normal displacement exerted on the circular plane is in the form of

$$P(r) = P_0\left(1 - \frac{r^2}{a^2}\right)^{1/2} \tag{3.5}$$

$$u = \frac{\pi p_0}{4aE^*}\left(2a^2 - r^2\right), r \le a \tag{3.6}$$

where $E^* = \frac{1-\nu_1^2}{E_1} + \frac{1-\nu_2^2}{E_2}$, p_0 refers to the maximum contact pressure, E_1 and E_2 are Young's modulus of the two entities, ν_1 and ν_2 are the corresponding Poisson's ratio. a refers to the radius of the contact area.

Submitting Eq.(3.4) into Eq.(3.6), it could get

$$a = \frac{\pi p_0 R^*}{2E^*} \tag{3.7}$$

$$\delta_n = \frac{\pi p_0 a}{2E^*} \tag{3.8}$$

The total load (P) compressing the solids is determined by

$$P = \int_0^a p(r) 2\pi r dr = \frac{2}{3} p_0 \pi a^2 \tag{3.9}$$

In combination with Eq.(3.9), the circular radius and displacement could be expressed in the form of the total load as

$$a = \left(\frac{3PR^*}{4E^*} \right)^{1/3} \tag{3.10}$$

$$\delta_n = \frac{a^2}{R^*} = \left(\frac{9P^2}{16R^*(E^*)^2} \right)^{1/3} \tag{3.11}$$

3.1.3.2 The tangential force-displacement relationship between two spheres

The tangential stiffness is related to the contact response of tangential loading. Figure 3.4 below gives the tangential contact model with the elastic bodies. Considering the contact of spheres, under a constant normal force P, the distribution of tangential traction produces a uniform tangential displacement of a circular region on the surface. In the figure, T_1 and T_2 are centre of the two contact bodies. A_1 and A_2 denote two points on the interface which were coincident before the application of tangential force. The normal force P gives rise to a contact area and the tangential force Q causes the bodies to deform in shear. The distorted central line indicates the shear displacement. Under the action of Q, the rigid displacements of bodies T_1 and T_2 are denoted as δ_{x1}, δ_{y1} and δ_{x2}, δ_{y2}. $\overline{u_{x1}}$, $\overline{u_{y1}}$ and $\overline{u_{x2}}$, $\overline{u_{y2}}$ are the tangential elastic displacement of points A_1 and A_2. Hence, the absolute displacement of points A_1 and A_2 are $s_{x1} = \overline{u_{x1}} - \delta_{x1}, s_{y1} = \overline{u_{y1}} - \delta_{y1}$ and

$s_{x2} = \overline{u_{x2}} - \delta_{x2}, s_{y2} = \overline{u_{y2}} - \delta_{y2}$.

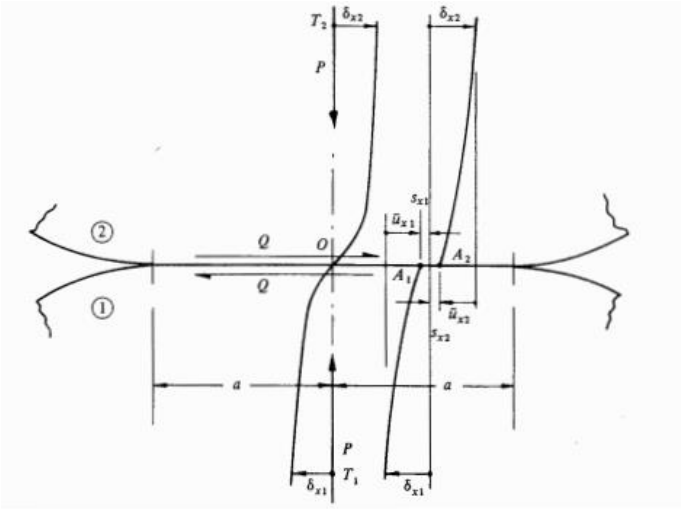


Figure 3.4 The tangential contact force (Johnson, 1985)

A. No-slip contact model

This refers to an extreme case for the response of tangential contact model. The problem is illustrated in Figure 3.4. It refers to the condition that the tangential force is less than the limited friction force. There is no relative motion, referred to as "slip" in the contact area. The region of interfaces is in the "stick" region with the application of tangential force Q. The tangential force causes the elastic deformations without slip at the interface under this condition. If points A_1 and A_2 are in the stick region, the slip s_x and s_y should be zero. Then the tangential displacement is the same for all the points in contact. Taken force Q acting parallel to the x-axis, the corresponding tangential displacement is then also parallel to the x-axis. It would produce a uniform tangential displacement of a circular region on the surface under the distribution of tangential traction. Johnson (1985) gives the relationship between surface displacement and traction in the form of

$$q(r) = q_0(1 - r^2/a^2)^{1/2} \qquad (3.12)$$

in which $q_0 = Q/2\pi a^2$, $r = \sqrt{x^2 + y^2}$. The corresponding displacement is expressed as

$$u = \frac{\pi(2-\nu)}{4G} q_0 a \tag{3.13}$$

Hence, the relative displacement under the force Q between the two bodies T_1 and T_2 is given as

$$\delta_t = u_1 + u_2 = \frac{Q}{8a}\left(\frac{2-\nu_1}{G_1} + \frac{2-\nu_2}{G_2}\right) \tag{3.14}$$

B. Sliding contact model

Sliding refers to the relative displacement over the contact surface at the point of contact. For the sliding model, it is usual to assume that Amontons' law applies at each elementary of the interface. The relationship of normal force Q and tangential force P is as

$$\mu = \frac{|q(x,y)|}{p(x,y)} = \frac{|Q|}{P} \tag{3.15}$$

where μ is the friction coefficient. It is a constant efficient determined by the materials and physical conditions of the interface.

The normal force is given by Hertz theory in elastic constants of two solid spheres as Eq.(3.9). The tangential traction is in expressed as follows with Amontons' law

$$q(r) = \frac{3\mu P}{2\pi a^3}\left(a^2 - r^2\right)^{1/2} \tag{3.16}$$

C. Partial slip contact model

Mindlin (1949) proposed that slip at the contact surface must accompany tangential loading. The method of solution to the problem of partial slip was first published by Mindlin (1949).

Then, Mindlin and Deresiewicz (1953) studied this problem under varying tangential loading with contact of two identical spheres. They suggested that the slip would start at the edge of the contact surface and supposed the slip occurs on an annulus. It assumes that the slip occurs on the annulus from the inner radius c to the boundary radius a. The stick region refers to the inside circular region with a radius of c. The greatest possible value refers to the points of sliding and the distribution of traction is in the form of

$$q'(x,y) = \mu p(x,y) = \mu p_0 \left(1 - r^2 \big/ a^2\right)^{1/2} \tag{3.17}$$

in which p_0 refers to the pressure of fixed normal force P and $r \le a$.

Johnson (1985) proposed that the displacement of traction on the circular region is expressed as

$$\overline{u_x}' = \frac{\pi \mu p_0}{32Ga}\left\{4(2-\nu)a^2 + (4-\nu)x^2 + (4-3\nu)y^2\right\} \tag{3.18}$$

$$\overline{u_y}' = \frac{\pi \mu p_0}{32Ga} 2\nu xy \tag{3.19}$$

The displacement of Eq.(3.17) predicts the slip in any point of the contact region except the origin point. Hence, an additional distribution of traction is considered in the stick region of $r \le c$ as

$$q''(x,y) = -\frac{c}{a} p_0 \left(1 - r^2/c^2\right)^{1/2} \tag{3.20}$$

The tangential displacements within that circle are

$$\overline{u_x}'' = -\frac{c}{a}\frac{\pi \mu p_0}{32Gc}\left\{4(2-\nu)c^2 + (4-\nu)x^2 + (4-3\nu)y^2\right\} \tag{3.21}$$

$$\overline{u_y}^{''} = -\frac{c}{a}\frac{\pi\mu p_0}{32Gc}2\nu xy \tag{3.22}$$

The resultant displacements in the circle $r \le c$ are given by

$$\overline{u_x} = \overline{u_x}^{'} + \overline{u_x}^{''} = \frac{\pi\mu p_0}{8Ga}(2-\nu)(a^2-c^2) \tag{3.23}$$

$$\overline{u_y} = \overline{u_y}^{'} + \overline{u_y}^{''} = 0 \tag{3.24}$$

The relative displacement between two spheres can be written as

$$\delta_x = \overline{u_{x1}} - \overline{u_{x2}} = \frac{3\mu P}{16}\left(\frac{2-\nu_1}{G_1} + \frac{2-\nu_2}{G_2}\right)\frac{a^2-c^2}{a^3} \tag{3.25}$$

The tangential traction acts parallel to the x-axis at all points. In the annulus $c \le r \le a$, the tangential traction is given by $q^{'}$. In the central circle, it is the result of $q^{'}$ and $q^{''}$.

The magnitude of tangential force in the stick region can be found as

$$Q_x = \int_0^a 2\pi q^{'} r dr - \int_0^c 2\pi q^{''} r dr = \mu P\left(1 - c^3/a^3\right) \tag{3.26}$$

Thus $\frac{c}{a} = \left(1 - Q_x/\mu P\right)^{1/3}$ (3.27)

Substituting the Eq.(3.27) into Eq.(3.25), it is given by

$$\delta_x = \frac{3\mu P}{16a}\left(\frac{2-\nu_1}{G_1} + \frac{2-\nu_2}{G_2}\right)\left\{1 - \left(1 - \frac{Q_x}{\mu P}\right)^{2/3}\right\} \tag{3.28}$$

From Eq.(3.27), for very small values of tangential force, it follows linear relationship for no-slip as the slip annulus is very thin. As Q approaches μP, the tangential displacement departs further from no-slip condition until reaches the point of sliding.

3.1.4 Damping

The mechanical system or material would dissipate energy under cyclic stress, which refers to the damping of a vibrating system. Intensive investigations have been studied in the collision between deformed assemblies (Goldsmith, 1960; Walton, 1993). In DEM, the dashpot is applied for the energy dissipation during the simulation through frictional sliding. The widely implemented viscous damping model is developed by Itasca (1999) with a local non-viscous damping for estimating the damping force to achieve the steady-state in a reasonable number of cycles.

Tsuji et al. (1992) introduced a non-linear damping term to DEM simulation. The damping coefficient is modelled by a single degree-of-freedom system with a mass connected to the ground by a spring and dashpot. They stated that the damping term was found heuristically and the damping coefficient was an empirically constant related to the restitution coefficient which is a function of the incoming velocity in elastoplastic collisions (Zhang and Whiten, 1996; Vu-Quoc and Zhang, 1999).

3.1.5 Mechanical time-step determination

To obtain reliable results of motion, the time-step should not exceed a critical time-step in DEM. A number of equations have been proposed for the definition of critical time-step. For a single degree of freedom system, a simplified procedure is implemented to estimate the critical time-step described by a point mass, m, and spring stiffness, k (Cundall and Strack, 1979; O'Sullivan and Bray, 2004). The motion of the point mass is governed by the differential equation: $-kx = m\ddot{x}$. Bathe and Wilson (1976) provided the estimation of a critical time-step corresponding to a second-order finite-difference scheme

$$t_{crit} = \frac{T}{\pi}, \left(T = 2\pi\sqrt{m/k}\right) \tag{3.29}$$

where T is the period of the system.

This above definition refers to the natural frequency with the linear contact stiffness. For non-linear contact stiffness, it is not based on the actual condition estimated in this method. As pointed out by Johnson (1985), during the motions of particles, the distances propagated in waves along the surface of particles. He illustrated two types of wave motion are possible in extended three-dimensional elastic bodies as the dilatational waves and distortion waves. The dilatational waves or pressure waves depend on the material elements fluctuate in volume without shear deformation. The distortional (or shear) waves refer to the elements distort without a change in volume. The speeds of propagation for these waves in isotropic materials are given by

Dilatation: $$c_1 = \left\{\frac{2(1-\nu)G}{(1-2\nu)\rho}\right\}^{1/2} \tag{3.30}$$

Distortion: $$c_2 = \left(G/\rho\right)^{1/2} \tag{3.31}$$

Johnson (1985) found that the difference between the Rayleigh wave speed and distortional wave speed is small. In addition, the energy transferred by dilatation wave is negligible. Hence, in elastic contact problems, the particles treated as behaving in a form of Rayleigh waves propagated along the surface of solid in a granular system with a velocity

$$v = \alpha\left(G/\rho\right)^{1/2} \tag{3.32}$$

where α is the root of the equation

$$\left(2-\alpha^2\right)^4 = 16\left(1-\alpha^2\right)\left(1-\alpha^2 c_2^2/c_1^2\right) \tag{3.33}$$

For simplicity, the critical time-step could be estimated based on the average particle size for simulation.

3.1.6 The development and availability DEM software

Cundall and Strack (1978) first proposed the so-called distinct element method and developed the numerical code named as Ball to mimic the mechanical behaviour of 2D assemblies of granular discs. The TRUBAL program is developed to model the three-dimensional assemblies by Cundall and Strack (1979). They demonstrated that the code could accurately replicate the experiments on steel sphere by Rowe (1962). Then, Cundall (1988) developed it into three-dimensional with any shape of particles. It also involves the features of periodic boundaries, random particle generators, Hertzian contact law, servo-control and 2-D mode.

The origin BALL and TRUBAL codes are led to the current version of PFC2D and PFC3D. The PFC software is first released in 1994 by Itasca as a company studied in the area of geomechanics, hydrogeology and micro-seismicity. It is designed to simulate any mechanical system represented with the assembly of particles and developed over the span around a quarter of a century.

There is other software with the development of computational technology. The EDEM is first developed in 2006 with the University of Edinburgh for the virtual experimental test to simulate the processes the bulk materials such as coal, mined ores and powders in the manufacturing of mining, construction, off-highway and agricultural industries.

Yade is open-sourced software developed by the Grenoble University to implement the computational algorithms for the discrete element method. The code has been developed for shared memory machines using the OpenMPI specification. It is also developed with

the Lattice Geometrical Model for the finite element method.

The LAMMPS is the other open-source software to simulate the discrete assemblies widely used in the field of Molecular Dynamics (lammps.sandia.gov). It also contains a granular package to enable DEM simulation. The LIGGGHTS is based on the LAMMPS software, developed and maintained by Sandia Nation Labs. LIGGGHTS stands for LAMMPS Improved General Granular and Granular-heat transfer simulations. New features are added in such as importing and handling of complex wall geometries from CAD. A feature of moving mesh is also included in the account for moving geometry. The software LIGGGHTS could also be coupled with CFD software to simulate the multiphase environment.

In comparison with the open source software, commercial software has more mature manuals, techniques and services support which is user-friendly to learn and begin. While commonly, the commercial software does not publish the source code that means the software is hard to modify. With regards to the open source software, it is free to download and install. Furthermore, it could access and improve the software via modifying the source code to satisfy own requirements. In addition, it contains the parallel version to save the computation time. Hence, the open-source LIGGGHTS software is selected for this PhD project due to its high-performance computation and rich functions.

3.2 LIGGGHTS

3.2.1 Contact models in LIGGGHTS

The proposed contact model consists of the components of spring, dashpot and slider at contact points. There are two normal contact models commonly implemented in DEM simulations, the linear Hooke contact model and non-linear Hertz contact model, to

simulate the cohesionless granular materials in DEM. This section presents the details of normal stiffness and tangential stiffness with the two contact models respectively in LIGGGHTS.

3.2.1.1 Linear Hooke's contact model

For the Hooke's contact model, the elastic force is in a linear relationship with the inter-particle deformation. The energy dissipation of the model is determined by the damping ratio and the relative velocity. Thus, the total normal contact force is estimated as the following equation

$$F_n = -k_n \delta_n + \gamma_n \Delta v_n \tag{3.34}$$

in which k_n is the normal contact stiffness, δ_n is the normal inter-particle deformation. γ_n refers to the normal damping coefficient and Δv_n is the inter-particle velocity in the normal direction.

The tangential contact force is also determined with the spring-dashpot system. The elastic tangential force is related to the tangential displacement. Considering the damping force, it is related to the tangential relative velocity. The Coulomb friction law should also obey for the tangential contact force when the sliding occurs between inter-particles. Hence, the total tangential contact force is determined as

$$F_t = \int_{t_0}^{t} k_t \Delta v_t dt + \gamma_t \Delta v_t, \ F_t \le \mu F_n \tag{3.35}$$

where k_t and v_t refer to the tangential stiffness and damping coefficient respectively. The integration part represents the relative displacement in the tangential direction from the contact time t_0 to the current simulation time t.

3.2.1.2 Hertz contact model

LIGGGHTS applies the theory to the Hertz-Mindlin contact model designed by a non-linear spring-dashpot mode between particles and/or geometry for the normal and tangential contacts. The normal stiffness is measured based on the Hertz theory of Eq.(3.36) as

$$\mathrm{k_n} = \frac{P}{\delta_n} = \frac{4}{3} E^* \sqrt{\mathrm{R}^* \delta_\mathrm{n}} \tag{3.36}$$

The problem of tangential stiffness is taken as a simplified condition prescribed by the no-slip solution. The tangential stiffness is estimated from Eq.(3.37) as

$$\mathrm{k_t} = \frac{Q}{\delta_t} = 8\mathrm{G}^* \sqrt{\mathrm{R}^* \delta_\mathrm{n}} \tag{3.37}$$

in which G^* is the efficient shear modulus and estimated as $\frac{1}{\mathrm{G}^*} = \frac{2(2-\nu_1)(1+\nu_2)}{E_1} + \frac{2(2-\nu_1)(1+\nu_2)}{E_2}$. E_1, E_2 and ν_1, ν_2 are Young's modulus and Poisson's ratio of the two contact particles respectively. Based on Eq.(3.36) and Eq.(3.37), $k_n / k_t = E^* / 6G^*$.

For the shear interactions, a slider is taken into account for the slip condition. The magnitude of the tangential contact force is limited by the Coulomb frictional force. Figure 3.5 below gives an example of the calculation of the contact force and total force for a particle. It mimics one particle with a plane boundary. A vertical force $(\boldsymbol{N})$ and a horizontal force $(\boldsymbol{T})$ are applied on the particle for generating the overlap with the boundary.

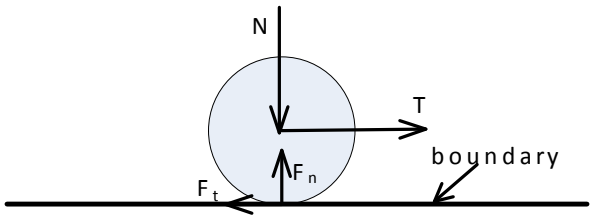


Figure 3.5 The estimation of the contact force in LIGGGHTS

The normal and tangential contact forces, involved with the contact stiffness force and damping force, are expressed in the form

$$F_n = -k_n \delta_n + \gamma_n \Delta u_{p,n} \tag{3.38}$$

$$F_t = \begin{cases} \left| k_t \int_{t_{c,0}}^{t} \Delta u_{p,t} dt + \gamma_t \Delta u_{p,t} \right| \\ \mu_c F_n \left(k_t \int_{t_{c,0}}^{t} \Delta u_{p,t} dt > \mu_c F_n \right) \end{cases} \tag{3.39}$$

in which δ_n and δ_t refer to the normal and tangential overlap of particles, γ_n and γ_t are the normal and tangential damping coefficients. $\Delta u_{p,n}$ and $\Delta u_{p,t}$ are the normal and tangential relative velocities of particles. μ_c is denoted as the friction coefficient. In Eq.(3.39), the integral term represents the relative displacement in the tangential direction from the particles touched time $t_{c,0}$ to the current time t. The velocities and displacements of particles are obtained by the Newton's second law. These values are updated by the time-step integration.

In addition, it conducts a minor improvement for the estimation of inter-particle contact forces in the source code. The original source code makes a mistake on the part of average contact force. It could only calculate the average contact force in the x, y and z

directions respectively, with the command of "compute_reduce", in the input file during the simulation. The source code of inter-particle contact force is improved with a function estimating the total magnitude of each contact force. The value is employed in the input file with this command to calculate and update the average contact force at each step.

3.2.2 Damping model in LIGGGHTS

The restitution coefficient has a relationship with the energy disputation (Tsuji et al., 1992). Later, Zhang and Whiten (1996) analysed the damping coefficient with dimensional analysis for the non-linear Hertz-Mindlin contact model as

$$\gamma = \alpha\sqrt{m^* k} \tag{3.40}$$

where α is a damping constant related to the restitution coefficient $\boldsymbol{e}$ as $\alpha = -\ln(\boldsymbol{e})\sqrt{\frac{5}{\ln^2(\boldsymbol{e})+\pi^2}}\,(\alpha<1)$. LIGGGHTS employs this parameter to define the damping coefficient. Figure 3.6 below gives the relationship between the restitution coefficient and damping constant. The damping coefficient decreases with the increase of restitution coefficient.

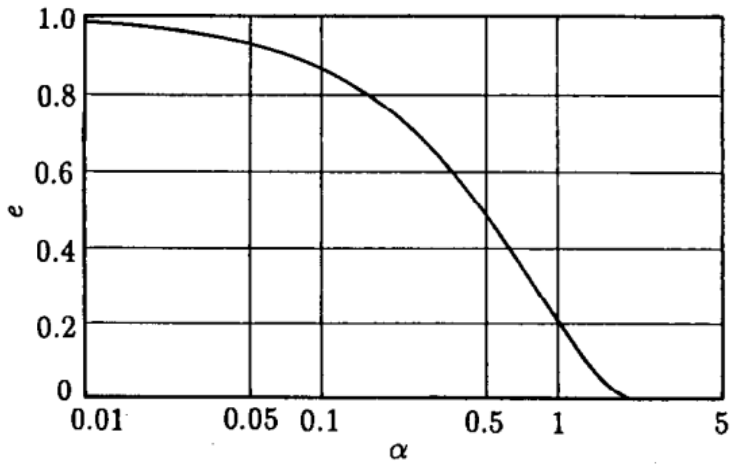


Figure 3.6 The relationship of the restitution coefficient and damping constant (Tsuji et al., 1992)

The velocity is taken as the relative velocity for two colliding particles in the damping model. Figure 3.7 below gives an example of two contact particles i, j. The relative velocity is the velocity vector of the particle i to particle j as $\boldsymbol{v}_r = \boldsymbol{v}_i - \boldsymbol{v}_j$. The relative velocity is divided into the normal and tangential directions corresponding to the normal and tangential damping force. For the normal direction, it only considers the translational velocity in the normal direction. While, for the tangential direction, the rotation shear displacement between the two particles is also taken into account. Eq.(3.41) below gives the estimation of normal velocity $\boldsymbol{v}_n$ and tangential velocity $\boldsymbol{v}_t$ in DEM.

$$\begin{cases} \boldsymbol{v}_n = \left(\boldsymbol{v}_r \cdot \boldsymbol{n}_k\right)\boldsymbol{n}_k \\ \boldsymbol{v}_t = \left[\left(\boldsymbol{v}_r \cdot \boldsymbol{t}_k\right)\boldsymbol{t}_k + \left(\boldsymbol{\omega}_i \times \boldsymbol{R}_i - \boldsymbol{\omega}_j \times \boldsymbol{R}_j\right)\right] \end{cases} \tag{3.41}$$

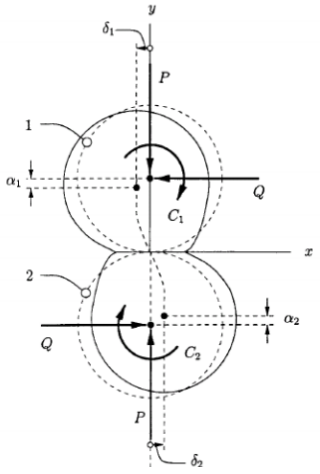


Figure 3.7 The velocities of two contacted particles (Vu-Quoc and Zhang, 1999)

Substituting Eq.(3.36) and Eq.(3.37) into Eq.(3.40), the related normal damping $\left(\gamma_n\right)$ and tangential damping $\left(\gamma_t\right)$ coefficients could be expressed as

$$\begin{cases} \eta_n = -2\sqrt{\frac{5}{6}}\beta\sqrt{S_n m^*} \\ \eta_t = -2\sqrt{\frac{5}{6}}\beta\sqrt{S_t m^*} \end{cases} \tag{3.42}$$

where m^* is the effective mass of two contacted particles as $\frac{1}{m^*} = \frac{1}{m_1} + \frac{1}{m_2}$.

$\beta = \frac{\ln(e)}{\sqrt{\ln^2(e) + \pi^2}}$, $S_n = 2E^*\sqrt{R^*\delta_n}$, $S_t = 8G^*\sqrt{R^*\delta_n}$.

According to Tsuji et al (1992), the damping constant ranges from 0.01 to 0.5 with the restitution coefficient in the span of [0.5, 1.0]. The damping coefficient decreases with the increase of restitution coefficient. Boac et al. (2009) exhibited the properties of a few categories and found the restitution coefficient ranged from 0.5 to 0.7 with the experimental test. For the dynamic process, in order to reduce the simulation time, the restitution coefficient is chosen as 0.5 for the sand pile simulations.

3.2.3 Time-step in LIGGGHTS

On the basis of the principles for DEM above, the main parameters for contact are Young's modulus, radius, restitution coefficient and Poisson's ratio. For DEM simulation, the sufficiently short time step is required to ensure the stability of the system. In LIGGGHTS, it is determined by the time through a particle with the Rayleigh wave proposed by Johnson (1985). The critical time step is measured as Eq.(3.43) (Li et al., 2005). For the simulation test, it considers the time step as 0.2 times of the critical time step.

$$t = \pi r * \sqrt{\frac{\rho}{G}} / (0.1631 * \nu + 0.8766) \tag{3.43}$$

where ρ and r are the density and radius of particles respectively. G is the shear

modulus and ν is the Poisson's ratio.

3.2.4 Procedures to run a LIGGGHTS simulation

An input file is defined with the specific commands determining general characteristics such as the atom type, simulation boundary, material properties and particles generation. The completely defined codes are run with the call of input files. The input file could be generated with four parts as:

1) Set the environment for the simulation test.
2) The basic definitions. Define the geometry of the boundary, properties of the boundary and particles.
3) Select the contact model and related parameters for the simulation test.
4) Run the test with specified requirements.

Data post-processing:

The Paraview software as a post processing software could be used to view the simulation processes. It is an open-source data analysis and visualisation tool. During the test procedures, the files are outputted with the specified particle properties such as velocities, forces and radii. In order to view the results in Paraview, the files are transformed into the *.vtk* format with a python wrapped applications offered in LIGGGHTS website as a post-processing tool.

Numerous researches have been performed using LIGGGHTS in the area of particle packing, liquid bridges and conveyor model (Parteli, 2013; Dou et al., 2014; Derakhshani et al., 2015, Wang et al., 2015). Hence, it is used in this project for the sand pile simulation. To better understand the material behaviour, the representative volume element could be

defined with different regions inside the sand pile. In such a case, a numerical technique is developed for observing the elementary behaviour with different loading paths. It is elaborated in the following Section 3.3.

3.3 Numerical algorithm to simulate elementary behaviour

Researchers present the stress/strain response is loading path and history dependent. The multi-scale methods are used widely in recent decades to probe the materials responses from the particle scale as the information obtained from particle interactions to the continuum scale with the development of the the constitutive relationship. To observe the multi-scale behaviour, it is essential to conduct the DEM simulations with various loading paths. The simulations attempt to mimic the conventional experimental test via reproducing the boundary conditions.

Li et al. (2013) proposed a virtual experimental technique to mimic the real particle geometries with polyhedral boundary, formed with an acute angle for two neighbouring walls, to minimise the arches effect around the corner. They realised and implemented the DEM simulation tests in 2D, with the monotonic and rotational shearing respectively. Yang (2014) continued and developed into 3D with this method. He checked and performed the simulations using the commercial software PFC3D. In this research, the numerical simulation tests are implemented using the same technique based on their work. It aims to realise the general loading paths, involving proportional and non-proportional loading, with the open-source software LIGGGHTS.

In this section, it introduces the details for the polyhedron boundary as well as realising the control of boundary and loading. Hence, it contains three key features as: 1) Boundary

generation in LIGGGHTS; 2) The evaluation of stress and strain behaviour; 3) The realisation of general loading paths. It presents the implementation of the virtual experimental technique on the basis of Li et al. (2013; 2016).

The numerical technique proposed by Li et al. (2013) is implemented into the LIGGGHTS software for mimicking the laboratory test with general loading paths. The typical loading path is achieved via the translational deformation and rotational deformation of the rigid frictional boundary. With the ***.stl*** files, the defined boundary is generated for importing into the software. The general loading path could be achieved via the conditions of the strain-controlled boundary, stress-controlled boundary and mix-controlled boundary. The following flow chart displays the simulation procedures in LIGGGHTS. It starts with boundary generation. Then, it is the compaction stage, following by the consolidation stage to achieve the target confining pressure. Finally, it is the shear stage with the defined loading path.

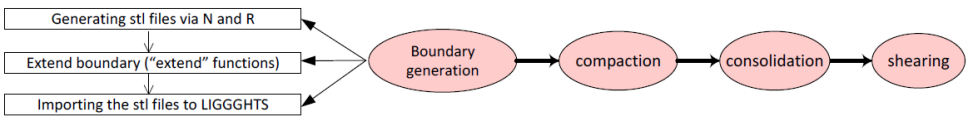


Figure 3.8 The simulation procedures in LIGGGHTS

The loading would be applied in the stages of compaction, consolidation and shear. Figure 3.9 below gives a flow chart of one cycle in the loading stage. Before providing a loading to the boundary, it requires checking the equilibrium condition. The boundary is fixed until satisfying the equilibrium condition. Then, it requires checking the boundary condition to determine the velocities of the boundary and particles. After that, with the updated information of the boundary and particles, it returns to the stage of checking the equilibrium condition and repeats the above procedures until the end of the simulation.

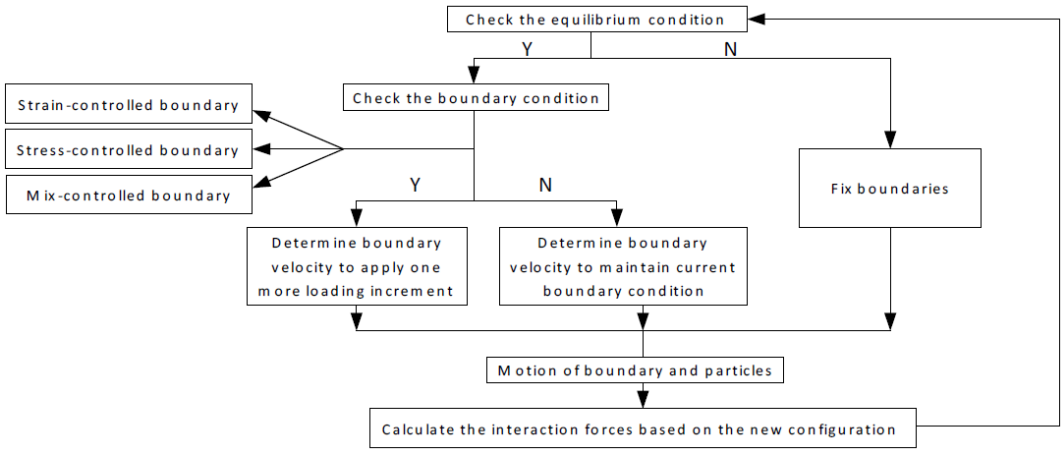
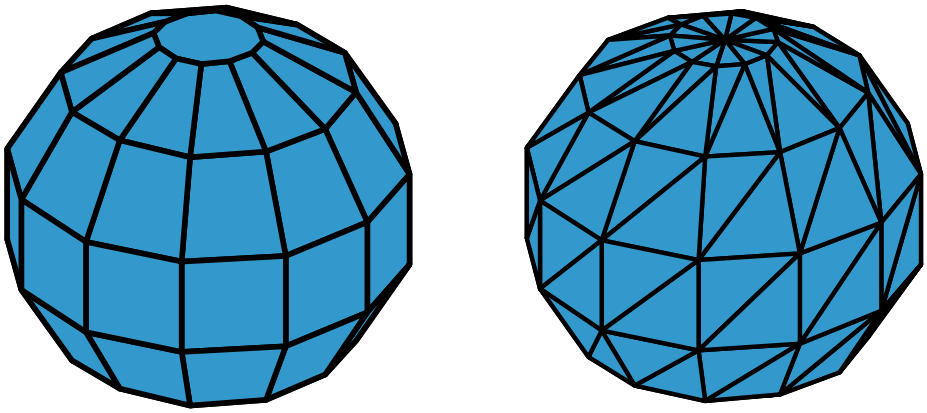


Figure 3.9 One cycle of a loading step

3.3.1 The polyhedral boundary

In order to enhance the sample uniformity, the polyhedral boundary, formed with obtuse angles between any two neighbouring boundaries, is selected to reduce the arching effect. Figure 3.8 above gives the procedures of boundary formation in LIGGGHTS. The boundary, formed by rigid walls, is generated and imported into LIGGGHTS with *.stl* files. The definition and generation of the polyhedron boundary are in accordance with the work of Li et al. (2013; 2016). It is defined by two parameters N and R. N, determined the polyhedral shape, is the number of sides for the wall surface of top and bottom regular polygon. R, controlled the polyhedral size, is the radius of the polyhedron inscribed sphere. Due to the feature of *.stl* files, generated from MATLAB, each surface of the boundary is defined as triangle meshes. An example of the polyhedron boundary formed with $N=12$ is shown in Figure 3.10.



(1) Construction of boundary (2) meshes for the boundary in *.stl* files

Figure 3.10 Polyhedral boundary formed with N=12

After that, the boundary is extended, in order to guarantee no gaps appearing during the simulation test. The initial wall centre coordinates could be acquired with the information in the *.stl* files. Each wall surface is extended without altering the initial wall centre coordinates. The initial wall centre coordinates X_{oJ}^{w} and wall normal directions n_{o}^{w} are given according to the information of *.stl* files. In addition, the information of wall centre coordinates and normal direction would be updated after a deformation. According to the updated boundary information, the vector $\boldsymbol{X}$ of the intersection point would be obtained based on the following Eq.(3.44) and Eq.(3.45)

$$\boldsymbol{X} = \frac{-d_1 \bullet \left(\boldsymbol{n}^2 \times \boldsymbol{n}^3\right) - d_2 \bullet \left(\boldsymbol{n}^3 \times \boldsymbol{n}^1\right) - d_3 \bullet \left(\boldsymbol{n}^1 \times \boldsymbol{n}^2\right)}{\boldsymbol{n}^1 \bullet \left(\boldsymbol{n}^2 \times \boldsymbol{n}^3\right)} \tag{3.44}$$

where $\boldsymbol{n}^1$, $\boldsymbol{n}^2$ and $\boldsymbol{n}^3$ are the wall normal direction of the three unparalleled planes. d_1, d_2 and d_3 are the plane function constants of the three planes expressed in the form of

$$\boldsymbol{n}^1 x + \boldsymbol{n}^2 y + \boldsymbol{n}^3 z + d_i = 0 \tag{3.45}$$

The plane function constants could be determined via substituting the wall centre

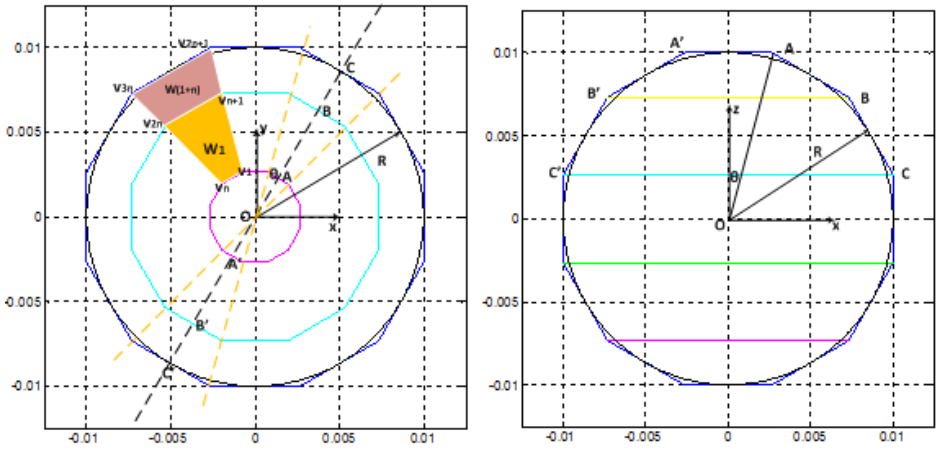
coordinates (x_i, y_i, z_i) and unit wall normal directions of the three planes $(\boldsymbol{n}^1, \boldsymbol{n}^2, \boldsymbol{n}^3)$ into Eq.(3.45) above. Then, take the results back to Eq.(3.44), it could estimate the updated interacted vertex coordinates.

The features of the boundary could be summarised as follows corresponding to Figure 3.10 (Li et al., 2013; Li et al., 2016):

1. Figure 3.10 displays the polyhedron in three-dimensional space. The polyhedron has two parallel surfaces, which are both regular n-sided polygons, perpendicular to the z coordinate axis. These two surfaces, named as the top and bottom surface, have their z vertices coordinates being R and $-R$ respectively with the distance of $2R$. Furthermore, both the transverse and longitudinal sections of polyhedron form regular n-sided polygons. All vertices lie in $n/2$ regular horizontal planes with n vertices of each plane.

2. Figure 3.11(2) presents the convex polyhedron boundary in the vertical direction. θ refers to the angle between the vector to the positive axis direction for the horizontal direction and vertical direction respectively, which equalling to $180°/n$. To determine the cooridnates of the polyhedral boundary, it requires to assign each wall surface with an ID number. According to Figure 3.10, it has n wall surfaces between every two neighbouring horizontal planes. Hence, together with the top and bottom wall surfaces, it has $\left(n/2 - 1\right)n + 2$ walls. W_i, displayed in Figure 3.11(1), refers to the wall id of each surface. v_i in the figure denotes the vertex ID number. It starts with the top wall on the basis of the ID assigned from 1 to n counter-clockwisely and then continued in the layer one level lower. The vertex in the i^{th} layer can be denoted by $v_{[(i-1)n+j]}$, where i ranges from 1 to $n/2$ and j ranges from 1 to n. For convenience, the ID numbers of walls and vertices are labelled top to down and go counter-clockwisely. The ID numbers of side walls, denoted

as the surfaces besides the top and bottom walls, are assigned from 1 to $\left(n/2-1\right)n$. Wall ID 1 is formed by the four vertices $v_1, v_n, v_{n+1}, v_{2n}$ as shown in Figure 3.11(1). Following this convention, the ID of side wall denoted as $\left[(i-1)n+j\right]$ is formed with the set of four vertices with ID of $\left[(i-1)n+j\right],\left[(i-1)n+(j-1)\right],\left[i\cdot n+j\right]$ and $\left[i\cdot n+(j-1)\right](j\neq 1)$, or the set of four vertices with ID $\left[(i-1)n+j\right],\left[(i-1)n+n\right],\left[i\cdot n+j\right]$ and $\left[i\cdot n+n\right]$ when $j=1$. The ID of the top and bottom wall is assigned as $\left(n/2-1\right)n+1$ and $\left(n/2-1\right)n+2$ respectively.



(1) Horizontal planes with label ID (2) the vertical intersection

Figure 3.11 The convex polyhedron with labelling IDs of Figure 3.10

3. All planes perpendicular to the polygons and passing the symmetrical axes, defined by a line passing the mid-point of one edge and centre of the polygon, of the two parallel polygons are symmetrical planes of the polyhedrons. And the intersection planes formed by the symmetrical planes and the polyhedron are also the regular *n*-sided polygons with the inscribed radius of R. Figure 3.11(1) and Figure 3.11(2) display the convex polyhedron in the horizontal projection and vertical intersection. Due to the symmetry, according to Figure 3.11(2), the vertices of vertical polygons lie on the horizontal planes.

From Figure 3.11(2), the vertical coordinates of each layer can $n/2$ be calculated as $z_i = \frac{R}{\cos\theta}\sin\left((2i-1)\theta+90°\right)$ ($i=1,n/2$ refers to the layer level). The side length of the two end walls $AA^{'},BB^{'},CC^{'}$ could also be estimated and then substitute the value to Figure 3.11(1) for measuring the vertex coordinates in the horizontal planes as

$$x_i = \frac{\mathrm{R}\cos\left((2i-1)\theta+90°\right)}{\cos^2\theta}\cos\left((2j-1)\theta\right) \quad , \quad y_i = \frac{\mathrm{R}\cos\left((2i-1)\theta+90°\right)}{\cos^2\theta}\sin\left((2j-1)\theta\right)$$

($j=1,n$ refers to the vertices in the i^{th} horizontal plane). With the information of vertices, the $.stl$ files then could be generated to import the boundary into LIGGGHTS.

The void ratio of the numerical sample in the initial undeformed configuration and deformed configuration, requires the characteristics of sample volume. Furthermore, the information of sample volume is also applied to calculate the stress behaviour. Thus, it is required to estimate the sample volume for a general polyhedron. In the deformed configuration, the top and bottom walls are hexagons while not necessarily regular. The rest boundary walls are quadrangle. For the system, the polyhedron can be subdivided into $(n/2-1)n+2$ numbers of the polygonal pyramid by a straight line connecting each vertex with the origin of the coordinate system. Then, the volume of the polyhedron is the summation of individual volume V_i for the polygonal pyramid, which is given by the pyramid volume formula

$$V_i = \frac{1}{3}A_i h_i \tag{3.46}$$

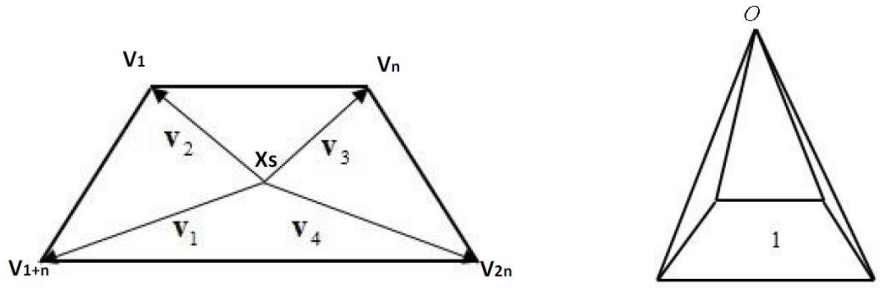
where A_i is the area of the base surface and h_i is the height from the boundary wall surface (base) to the origin (apex). According to Eq.(3.45), as the plane function of each boundary wall, the distance from the origin to the i^{th} wall surface is the absolute value of the constant

d_i, hence, $h_i = d_i$.

To calculate the area of the i^{th} wall surface, the wall surface of the polygonal boundary can be subdivided into a few triangles by straight lines connecting any two neighbouring vertices with the reference point on the surface. The coordinate of the surface reference point is treated as the average of all nodes forming the boundary wall surface. It forms a quadrangle pyramid by connecting its nodes with the origin O using straight lines. Taking wall ID 1 as an example, as Figure 3.12, the wall area is measured as

$$A_i = \frac{1}{2}\left(|\boldsymbol{v}_1 \times \boldsymbol{v}_2| + |\boldsymbol{v}_2 \times \boldsymbol{v}_3| + |\boldsymbol{v}_3 \times \boldsymbol{v}_4| + |\boldsymbol{v}_4 \times \boldsymbol{v}_1|\right) \tag{3.47}$$

With the updated vertex coordinates estimated in Eq.(3.44) and Eq.(3.46), the sample volume would be updated after a deformation configuration.



(1) Wall surace area (2) Quadrangle pyramid

Figure 3.12 Volume calculation with ID 1

3.3.2 Evaluation of strain and stress behaviour

The stress/strain tensor, considering from continuum scale, are defined and linked with the relative forces/displacements of the boundary deformations. The Cauchy stress and Biot strain are adopted to illustrate the stress and strain state of the specimens. To be compliance with the stress/strain state defined in soil mechanics, sign conventions are employed here

with compression regarded as positive. The deformation gradient tensor, expressed as Eq.(3.48), is employed for the accurate description and control of finite strain state.

$$\boldsymbol{F} = \partial \boldsymbol{x} / \partial \boldsymbol{X} \tag{3.48}$$

in which $\boldsymbol{x}$ refers to the deformed configuration and $\boldsymbol{X}$ is defined as the undeformed configuration.

Then, Eq.(3.49) gives the definition of Biot strain without the consideration of rigid body rotation to illustrate the boundary deformation

$$\boldsymbol{\varepsilon} = 1 - \boldsymbol{F} \tag{3.49}$$

In the undeformed configuration, the deformation gradient F_{iJ} can be evaluated as its volumetric average using Gauss's theorem as well as the assumption of uniformity

$$F_{iJ} = \frac{1}{V}\iint_V x_{iJ}\, dV = -\frac{1}{V}\iint_S x_i N_J\, dS \tag{3.50}$$

where V and S are the boundary volume and surface in the undeformed configuration. N_J refers to the unit normal to the boundary surface in the undeformed configuration with the direction pointing inward. The minus sign is required as the application of the divergence theorem. The deformation gradient tensor could be expressed as Eq.(3.51) when the polyhedral boundary is discretized into numbers of polygonal surface elements

$$F_{iJ} = -\frac{1}{V}\sum x_i N_J \Delta S \tag{3.51}$$

in which x_i refers to the area centre coordinates in the deformed configuration at the surface element ΔS. In the three-dimensional, the deformation gradient tensor could be decomposed into a volumetric part and a deviatoric part proposed by Flory (1961) as

$$\boldsymbol{F} = \underbrace{(\boldsymbol{J}^{-1/3}\boldsymbol{F})}_{F_d} \bullet \underbrace{\left(\boldsymbol{J}^{1/3}\mathbf{1}\right)}_{F_v} = \boldsymbol{F}_d \bullet \boldsymbol{F}_v \tag{3.52}$$

where $\boldsymbol{J}$ is the Jacobian determinant as $\boldsymbol{J} = \mathbf{det}(\boldsymbol{F})$. Based on Eq.(3.49), the applied strain increment could be calculated and specified as the translational and rotational velocities of the boundary surfaces. The strain invariants, as the ε_v, ε_q and b_ε, are expressed from the tensor invariants J_1, J_2 and J_3 of a three-dimensional symmetrical second order tensor $\boldsymbol{A} = A_{ij}\boldsymbol{e}_i \otimes \boldsymbol{e}_j$ as

$$\begin{cases} \varepsilon_v = \dfrac{dV - dv}{dV} = 1 - J \\ \varepsilon_q = 2\sqrt{J_2(\boldsymbol{F}_d)/3} = 2\sqrt{J_2(J^{-1/3}\boldsymbol{F})/3} \\ b_\varepsilon = b_F = \dfrac{F_2 - F_3}{F_1 - F_3} = b_{Fd} = \dfrac{F_{d2} - F_{d3}}{F_{d1} - F_{d3}} \end{cases} \quad \begin{pmatrix} J_1(\boldsymbol{A}) = tr(\boldsymbol{A}) = A_{ii} \\ J_2(\boldsymbol{A}) = A_{ij}A_{ji}/2 \\ J_3(\boldsymbol{A}) = A_{ij}A_{jk}A_{ki}/3 \end{pmatrix} \tag{3.53}$$

When the invariants $\varepsilon_v, \varepsilon_q, b_\varepsilon$ of the strain tensor are specified, the deviatoric deformation gradient tensor denoted in Eq.(3.51) could be determined with the evaluation of the Lode angle on the basis of the strain tensor expressed in terms of Eq.(3.54).

$$\tan\theta = \tan\theta_{F_d} = \tan\theta_\varepsilon = \frac{\sqrt{3}b_\varepsilon}{(2 - b_\varepsilon)} \tag{3.54}$$

$J_{2D}(\boldsymbol{F}_d)$, equalling to $J_{2D}(\boldsymbol{F}_\varepsilon)$, can be determined from the deviatoric strain ε_q as $\sqrt{J_{2D}(\boldsymbol{F}_d)} = \sqrt{J_{2D}(\boldsymbol{\varepsilon})} = \sqrt{3}\varepsilon_q/2$. The three principal values are calculated as

$$\begin{cases} F_d^1 = \dfrac{J_1(\boldsymbol{F}_d)}{3} + \dfrac{2\sqrt{J_{2D}(\boldsymbol{F}_d)}\cos\theta}{\sqrt{3}} \\ F_d^2 = \dfrac{J_1(\boldsymbol{F}_d)}{3} + \dfrac{2\sqrt{J_{2D}(\boldsymbol{F}_d)}\cos(2\pi/3 - \theta)}{\sqrt{3}} \\ F_d^3 = \dfrac{J_1(\boldsymbol{F}_d)}{3} + \dfrac{2\sqrt{J_{2D}(\boldsymbol{F}_d)}\cos(2\pi/3 + \theta)}{\sqrt{3}} \end{cases} \tag{3.55}$$

The forces acting on the boundary are used to measure the stress tensor of the polyhedral sample with Cauchy stress tensor as Eq.(3.56)

$$\sigma_{ij} = \frac{1}{V}\iiint_V \sigma_{ij} dV \tag{3.56}$$

where V is the sample volume on the current configuration. Hence, σ_{ij} is the average stress over sample volume V. The expression could be discretised in terms of contact forces $\left(f_j^c\right)$ and contact vectors $\left(l_i^c\right)$ exerted at different contact points in the micro-scale.

$$\sigma_{ij} = \frac{1}{V}\sum_{c\in V} l_i^c f_j^c \tag{3.57}$$

The tensor invariants are also estimated as Eq.(3.53) above. Based on Khan and Huang (1995), the lode angle could also be evaluated from the tensor invariants as

$$\cos 3\theta = -\frac{3\sqrt{3}}{2}\frac{J_{3D}(\boldsymbol{A})}{J_{2D}(\boldsymbol{A})^{3/2}} \tag{3.58}$$

According to Eq.(3.55), the three principal stress values and corresponding principal stress directions could be calculated with the information of the lode angle. Then, the stress invariants, as the mean principal stress (p), deviatoric stress (q), the intermediate principal stress ratio (b) and the stress ratio (η), could be obtained from the principal

stress values of Cauchy stress tensor

$$p = J_1 / 3 = (\sigma_1 + \sigma_2 + \sigma_3) / 3$$
$$q = \sqrt{3J_2} = \sqrt{\left((\sigma_1 - \sigma_2)^2 + (\sigma_2 - \sigma_3)^2 + (\sigma_1 - \sigma_3)^2\right) / 2} \quad (\eta = q / p) \qquad (3.59)$$
$$b = (\sigma_2 - \sigma_3) / (\sigma_1 - \sigma_3)$$

3.3.3 Applying a loading increment

The strain increment $(\Delta\varepsilon_{iJ})$ is achieved via the boundary translational and rotational velocities. The translational velocity of each surface centre is estimated as Eq.(3.60) with the deformation gradient tensor

$$v_{oi}^{w} = \Delta x_{oi}^{w} / \Delta t = \Delta F_{iJ} X_{oJ}^{w} / \Delta t = -\Delta\varepsilon_{iJ} X_{oJ}^{w} / \Delta t \qquad (3.60)$$

The boundary rotational velocity is estimated with the tensor product of the current normal direction $\boldsymbol{n}^{w}$ and target normal direction $\boldsymbol{n}^{wt}$ as

$$\boldsymbol{w}^{w} = \boldsymbol{n}^{w} \times \boldsymbol{n}^{wt} / \Delta t \qquad (3.61)$$

Two in plane vectors $\boldsymbol{t}_1^{w}$ and $\boldsymbol{t}_2^{w}$ are required to determine the wall normal direction after deformation.

$$\boldsymbol{n}_o^{w} = \frac{\boldsymbol{t}_1^{w} \times \boldsymbol{t}_2^{w}}{\left\| \boldsymbol{t}_1^{w} \times \boldsymbol{t}_2^{w} \right\|} \qquad (3.62)$$

where $\left\| \boldsymbol{t}_1^{w} \times \boldsymbol{t}_2^{w} \right\|$ represents the Euclidean normal of vector $\boldsymbol{t}_1^{w} \times \boldsymbol{t}_2^{w}$.

The servo-control mechanism is applied for estimating the imposed boundary condition as the stress-controlled boundary. The following Eq.(3.63) gives the determination of the

strain increment $\left(\Delta\varepsilon_{ij}\right)$ from the stress increment $\left(\Delta\sigma_{ij}\right)$ in terms of the stress invariants $\left(\Delta\sigma\right)^I, \left(I=1,2,3\right)$ and principal stress directions $\left(\alpha_{\Delta\sigma}\right)^I$.

$$\begin{cases} \left(\Delta\varepsilon\right)^I = \dfrac{1+\nu}{E}\left(\Delta\sigma\right)^I - \dfrac{\nu}{E}\Delta\sigma_{kk} \\ \left(\alpha_{\Delta\varepsilon}\right)^I = \left(\alpha_{\Delta\sigma}\right)^I \end{cases} \tag{3.63}$$

in which E is the estimated nominal Young's modulus and ν is the Poisson's ratio. $\left(\alpha_{\Delta\varepsilon}\right)^I$ is the principal strain direction at this strain increment $\left(\varepsilon_{ij}\right)$. In this study, tests are performed with the non-linear Hertz contact model. Hence, E is treated as Young's modulus of the particles defined in the input file.

The sample should under a quasi-static condition during the simulation test. It should check the sample equilibrium condition first before applying a loading on the boundary. The unbalance force ratio, estimated as the ratio of the average unbalance force and average contact force, is taken into account for the equilibrium condition. If the ratio is less than 0.01 as Eq.(3.64), the specimen refers to reach a quasi-static condition. Otherwise, the boundary should be fixed until reaching the equilibrium condition.

$$\frac{f_{ub}}{f_{ac}} \le 0.01 \tag{3.64}$$

where f_{ub} refers to the average unbalance force and f_{ac} denotes the average contact force.

In the numerical simulations, the boundary conditions, monitored by the tolerances, should be satisfied before applying a loading. If the difference between the current boundary conditions and target boundary conditions is smaller than the pre-set tolerance values, it is treated as satisfying the boundary conditions. For the stress-controlled boundary, the

boundary conditions are monitored by the stress invariants and principal directions with the following equations

$$\begin{cases} \left| p - p^t \right| < p_{tol} = \eta_{tol} \cdot \max\left(p, p_{lb} \right) \\ \left| \eta - \eta^t \right| < \eta_{tol} \\ \left| b_\sigma - b_\sigma^t \right| < b_{\sigma tol}, if\, \eta > \eta_{tol} \\ \left| 1 - n_\sigma^i \cdot n_\sigma^{it} \right| < n_{\sigma tol}, if\, \eta > \eta_{tol} \end{cases} \tag{3.65}$$

where p^t, b_σ^t and η^t are the target mean principal stress, intermediate principal stress ratio and stress ratio. The unit vectors n_σ^{it} refer to the target i^{th} principal stress direction. p, η, b_σ and n_σ^i represent the current mean principal stress, stress ratio, intermediate principal stress ratio and i^{th} principal stress directions. The corresponding tolerances are denoted as p_{tol}, b_{tol}, η_{tol} and $n_{\sigma tol}$. p_{lb} refers to the lower bound of the specimen mean principal stress. It is selected as 1kPa for this study. η_{tol} equals 0.001 for these tests. In the simulations, the other tolerances are set as $b_{\sigma tol} = \eta_{tol} \Big/ \max\left(\eta, \eta_{tol}\right), n_{\sigma tol} = \eta_{tol}$.

For the strain-controlled boundary, the boundary conditions are referred to be satisfied if the following conditions are satisfied

$$\begin{cases} \left| \varepsilon_v - \varepsilon_v^t \right| < \varepsilon_{vtol} \\ \left| \varepsilon_q - \varepsilon_q^t \right| < \varepsilon_{qtol} \\ \left| b_\varepsilon - b_\varepsilon^t \right| < b_{\varepsilon tol}, if\, \varepsilon_q > \varepsilon_{qtol} \\ \left| 1 - n_\varepsilon^i \cdot n_\varepsilon^{it} \right| < n_{\varepsilon tol}, if\, \varepsilon_q > \varepsilon_{qtol} \end{cases} \tag{3.66}$$

in which ε_v^t, b_ε^t and ε_q^t are the target values of the volumetric strain, intermediate principal strain ratio and deviatoric strain. The current volumetric strain, deviatoric strain, intermediate principal strain ratio and i^{th} principal strain directions are denoted as ε_v, ε_q,

b_ε and n_ε^i in the above equations. The i^{th} principal strain direction is represented as the unit vectors n_ε^{it}. The corresponding tolerances are ε_{vtol}, ε_{qtol}, $b_{\varepsilon tol}$ and $n_{\varepsilon tol}$ and they are set as $\varepsilon_{vtol} = p_{tol}/K, \varepsilon_{qtol} = p_{tol}/G, b_{\varepsilon tol} = \varepsilon_{qtol} \Big/ \max\left(\varepsilon_q, \varepsilon_{qtol}\right)$ and $n_{\varepsilon tol} = b_{\varepsilon tol}$.

The loading rate should be kept small to minimise the dynamic effects for maintaining the quasi-static conditions. Eq.(3.67)-Eq.(3.68) give the definition of tolerance for the stress boundary conditions

$$\begin{cases} \Delta p = \operatorname{sgn}\left(p^t - p\right)\min\left(\left|p^t - p\right|, \lambda p_{tol}\right) \\ \Delta \eta = \operatorname{sgn}\left(\eta^t - \eta\right)\min\left(\left|\eta^t - \eta\right|, \lambda \eta_{tol}\right) \\ \Delta b_\sigma = \operatorname{sgn}\left(b_\sigma^t - b_\sigma\right)\min\left(\left|b_\sigma^t - b_\sigma\right|, \lambda b_{\sigma tol}\right) \\ \Delta n_\sigma = \operatorname{sgn}\left(n_\sigma^t - n_\sigma\right)\min\left(\left|n_\sigma^t - n_\sigma\right|, \lambda n_\sigma\right) \end{cases} \tag{3.67}$$

The tolerances of strain boundary conditions are defined as

$$\begin{cases} \Delta \varepsilon_v = \operatorname{sgn}\left(\varepsilon_v^t - \varepsilon_v\right)\min\left(\left|\varepsilon_v^t - \varepsilon_v\right|, \lambda \varepsilon_{vtol}\right) \\ \Delta \varepsilon_q = \operatorname{sgn}\left(\varepsilon_q^t - \varepsilon_q\right)\min\left(\left|\varepsilon_q^t - \varepsilon_q\right|, \lambda \varepsilon_{qtol}\right) \\ \Delta b_\varepsilon = \operatorname{sgn}\left(b_\varepsilon^t - b_\varepsilon\right)\min\left(\left|b_\varepsilon^t - b_\varepsilon\right|, \lambda b_{\varepsilon tol}\right) \\ \Delta n_\varepsilon = \operatorname{sgn}\left(n_\varepsilon^t - n_\varepsilon\right)\min\left(\left|n_\varepsilon^t - n_\varepsilon\right|, \lambda n_{\varepsilon tol}\right) \end{cases} \tag{3.68}$$

where λ is the loading factor which controls the loading increment. It equals to 1 for this study.

3.4 Summary

This chapter gives information on the methodology for this PhD project. An introduction of DEM, including the contact stiffness model and damping model, is presented in this chapter. The open-source software LIGGGHTS is employed for investigating the multi-

scale investigations of granular material response. Due to the advantagous of the freely available source code, it could achieve own specify requirements via modifying the source codes. The major characteristics of this software are introduced, for instance, the implementation of the models. It also provides the introduction of the input files written for a simulation test and viewing the results using this software. Afterwards, Section 3.3 elaborates the numerical tool developed for the structural evolution with the representative volume elementary simulation. The details for the developed source codes in LIGGGHTS would be presented in Chapter 5.

Chapter 4 Sand pile simulation

4.1 Introduction

Sand pile is one classic granular mechanics problem widely observed in nature and industry. It attracts numerous researchers working in this area, including explaining the "pressure dip" phenomenon observed under the central apex. This counter-intuitive phenomenon, referring to the peak pressure appearing at a certain distance away from the centre, would disappear when the sand pile formation changes from the concentrated deposition method to the distributed deposition method (Wittmer et al., 1996; Vanel et al., 1999; Geng et al., 2001b). Various kinds of analytical approaches could be found to explain this phenomenon with the arching phenomenon employing the static theorem (Grindlay, 1995; Wittmer et al., 1997; Savage, 1998) following assumptions on the material stress state. Recent numerical studies further display the phenomenon related to the internal structure, for instance, the contact orientation distribution and contact force orientation distribution. It reveals a link between the pressure dip phenomenon and the construction history of the sand pile (Vanel et al., 1999; Ai et al., 2013).

For the interpretation of this phenomenon, the DEM simulations of sand piles are performed in order to observe the material behaviour at the local-scale. Three different sand pile formation methods, referred to as "boundary removal", "rain" deposition and "point" deposition, are undertaken in this study. The "boundary removal" method refers to how the particles form the sand pile under the self-organised condition after removing the boundary. This is similar to the avalanche phenomenon in nature. Regarding the deposition method, it is commonly seen in the industry such as the storage of river gravel, mine, and materials in the silo. The "rain" deposition and "point" deposition tests are the two widely used

methods for sand pile preparation observed in the literature review. The point deposition method refers to a concentrated deposition, while the rain deposition test is treated as the distributed deposition with an extended outlet length (Zhou et al., 2009; Zhu et al., 2013).

In this project, the outlet length is equal to 10 times the average particle size for the point deposition, which is around 0.046 times the dimension of the base plane. For the rain deposition test, the outlet length is selected to be the same dimension as the base plane. A sieve condition, with the mesh of 6mm diameter hole (as five times average particle sizes), is included at the outlet of the cylinder to control the flow rate. Following this chapter, the elementary material behaviour would be elaborated in Chapter 6 using the developed numerical algorithm in Chapter 5 under different loading paths.

The properties of materials and boundary are presented in Section 4.2. Section 4.3 to Section 4.5 shows the implementation of the numerical model and the simulation results for the three different methods respectively. The pressure profiles and shapes of sand piles are compared and discussed in Section 4.6. Finally, a summary is presented in this chapter.

4.2 Material properties

The LIGGGHTS is employed to reproduce the pressure dip phenomena numerically without the consideration of fluid phase. With the available multi-scale data, the local internal structure and force transmission could be observed to investigate the phenomenon in the particle-scale mechanisms. The recently released version of LIGGGHTS could simulate the non-spherical particles with the clump function in 2016. However, the previous version applied in this project could only model spherical particles.

The simulations undertake with a reference to the experimental tests of Vanel et al. (1999). Sand pile is formed on the base plane in the diameter of 260mm modelled as a rigid flat

but frictional surface. Particles are spheres with a uniform size distribution within the diameter of $[1.2 \pm 0.4] mm$.

Tests are performed with the Hertz-Mindlin contact model. The Young's modulus is 70GPa as the value of silicon to mimic the real properties of granular materials. The particle friction coefficient was chosen about the material repose angle based on the spherical particles, for which the relevant simulations have been presented in Appendix A.1. It shows the repose angle increases no further from 20.1° when the friction coefficient becomes larger than 0.8, which is smaller than the experimental angle of repose, 33° (Vanel et al., 1999). In such a case, the friction coefficients of boundary and particles are both selected as the largest value of 1.0 in this study.

Table 4.1 below gives the properties of particles and boundary for the simulations.

Table 4.1 Parameters for the full-scale tests

Particle shape	Spherical
Particle diameter	1.2 ±0.4mm
Young's modulus of particle	70GPa
Poisson's ratio	0.35
Restitution coefficient	0.5
Friction coefficient	1.0

The number of particles should be determined first before starting the simulation. It is calculated by the sample volume dividing one average particle volume. The number of particles is calculated as

$$N_p = \frac{V_{sam}}{\overline{V_p}} \cdot \frac{1}{(1+e)} \tag{4.1}$$

where V_{sam} refers to the sample volume and $\overline{V_p}$ denotes one average particle volume. e is the assumed void ratio for the specimen.

With the uniform in number particle size distribution, the volume averaged radius is estimated as

$$r_v^3 = \frac{\int_{r_{lo}}^{r_{hi}} r^3 f_N(r)\,dr}{\int_{r_{lo}}^{r_{hi}} f_N(r)\,dr} \tag{4.2}$$

where $f_N(r)$ is a density function obeying the Gaussian distribution with the radius ranged from r_{lo} to r_{hi}, with r_0 referring to the arithmetic mean radius. Then, considering the three specified radius, the volume of one particle is estimated as

$$V_p = \frac{4\pi}{3}\frac{\left(r_{lo}^3 + r_{lo}^2 r_{hi} + r_{lo} r_{hi}^2 + r_{hi}^3\right)}{4} \tag{4.3}$$

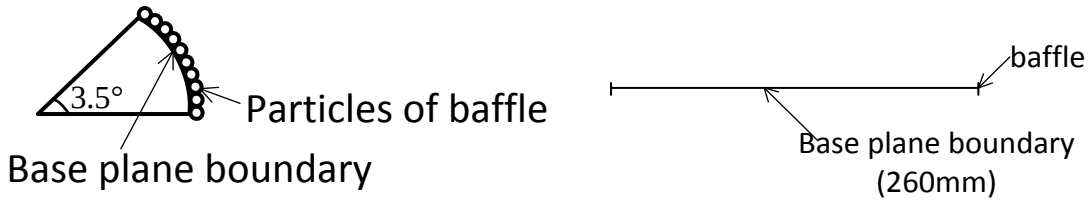
in which r_{lo} and r_{hi} are the minimum and maximum particle radius respectively. For the given uniform particle size distribution between $0.8mm$ and $1.6mm$, the average particle volume is estimated as $1.01mm^3$. Using the angle of repose $30°$ and the assumed void ratio zero, the number of particles can be calculated as 1,314,181.

Due to the spherical grain shape, particles have a rotation velocity with the base plane. In order to avoid excess rotation of particles and speed up the formation of a stable sand pile, a baffle, employing the fixed spherical particles, is formed at the edge of the base plane. The baffle is generated first before inserting particles for both the preliminary and full-scale tests. The properties of particles forming the baffle are the same as the properties of particles generating the sand pile. The particle sizes for baffle are selected as the minimum size of the PSD for the series of tests. The *z*-coordinates are 0, at the same level as the base

plane. The coordinates (x, y) of particles are measured with the radius $(R_b + r_{\min})$ and angle (θ) in the form of

$$\begin{cases} x = (R_b + r_{\mathbf{min}})\sin(n\theta_0) \\ y = (R_b + r_{\mathbf{min}})\cos(n\theta_0) \quad (n = 1, ..., N) \\ z = 0 \end{cases} \tag{4.4}$$

in which R_b is the radius of base plane, $r_{\min}$ refers to the minimum particle size. The number of particles is measured as $N_p = \mathrm{Int}\left(\frac{2\pi(R_b + r_{\min})}{2r_{\min}}\right)$, particles are uniformly distributed at every θ_0, estimated as $\theta_0 = \frac{360°}{N_p}$. Figure 4.1 below presents an example of the locations of the baffle particles in the span of 3.5° for the base plane boundary in the horizontal direction and vertical direction respectively.



(1) horizontal direction (2) vertical direction

Figure 4.1 The baffle boundary and base plane boundary in the horizontal and vertical directions

Particles should reach the equilibrium condition when the simulations are finally terminated to form a stable sand pile. The unbalance force ratio, measured by the unbalance force divided by the average contact force, is taken into account for determining this stage

$$\frac{f_{ub}}{f_{ac}} < 0.001 \tag{4.5}$$

where f_{ub} is the unbalance force and f_{ac} is the average contact force. This is a strict criterion, particularly in cases with relatively loose conditions for sand piles.

Tests are performed with the parallel version of LIGGGHTS software on the Minerva HPC hosted at the University of Nottingham. It has hundreds of computing cores based on the CPU of Intel Sandy Bridge, with the rate ranged from 2.0 GHZ to 2.6 GHZ. 32 cores have been used when carrying out the simulation tests. The following table presents the information of the three simulations respectively after forming the sand pile.

Table 4.2 The information of simulations for the formation of sand piles

	Number of particles	**Cycling steps**	**CPU time**
Boundary removal	616,281	5,815,664	4 weeks
Rain deposition	664,412	78,506,816	9 weeks
Point deposition	602,893	97,870,488	15 weeks

4.3 Boundary removal test

4.3.1 Implementation of the numerical model

The boundary removal test begins with the formation of a sand deposit and particles are in an equilibrium state within a cylindrical container. The sand pile is formed with particles rolling out of the base plane boundary upon the removal of the vertical cylindrical boundary and reaching the self-organised critical condition. This process consists of three stages, 1) Generation stage with particles inserting into the defined region; 2) Deposition stage with particles packing onto the base plane and reaching the equilibrium condition; 3) Sand pile formation stage until the system reaches the equilibrium state again.

The cylindrical boundary is generated with an extension of $20mm$ between the edge of the base plane and the cylindrical boundary, to reduce the boundary effect. The total number of particles used in the simulation depends on the thickness of the packed particle deposit. Before implementing tests with the real-scale particle sizes, preliminary tests are carried out first and shown in Appendix A.2 to design the models, predict the simulation time and determine the progressive critical stages. The preliminary tests indicated that the height of the sand pile was approximately $45mm$. Based on the result, it was decided that the particle deposit was $67.5mm$.

The sample volume is calculated as follows based on the shape of cylinder

$$V_{sam} = \pi R_c^2 h_c \tag{4.6}$$

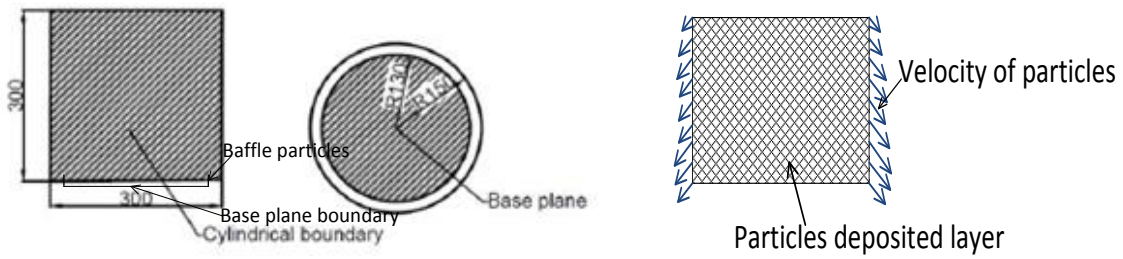
where R_c and h_c are the radius and corresponding height of the cylindrical sample respectively for the boundary removal test.

Table 4.3 below presents the information for estimating the number of particles according to the Eq.(4.1) at the initial stage. The assumed void ratio is selected based on the results of the preliminary tests. The thickness of the region for particles initially generated is selected as approximately two times that of the required height to guarantee enough space.

Table 4.3 The information for inserting particles

volume	$4.77e6mm^3$
Assumed void ratio	0.655
Number of particles	2,853,747
Generate region	$150mm$

The mechanical property of the boundary is applied with the Hertz-Mindlin contact model, with Young's modulus of 700MPa. The other properties are the same as the properties of the particles. Figure 4.2 presents the numerical model in the generation stage and the stage after removing the boundary for the formation of particles. In Figure 4.2(2), the blue vectors present an example of the velocities for particles after removing the cylindrical boundary.



(1) model for particles generation stage (2) model after removing the boundary

Figure 4.2 The numerical model of boundary removal test (unit: mm)

The following gives a detail description of test procedures for this method,

1. Particle generation stage. The particles are randomly inserted into the cylindrical region as presented in Figure 4.2(1).

2. Particle deposition stage. These tests are prepared by particle packing due to the action of self-weight. The gravitational acceleration is $9.81 m/s^2$. The test stops when the sample satisfies the equilibrium condition given in Eq.(4.5).

3. Sand pile formation stage. After particles reach the equilibrium state, the cylindrical container is removed and particles cascade down to form a sand pile. The test continues until the sample achieves the equilibrium condition again.

During the third stage, to reduce the computational effort, particles moving out of the boundary are deleted. In this process, for maintaining the impact of these particles, height

(h_{mb}) is defined as two times of the maximum particle size below the base plane in the *z*-axis direction. Particles are deleted as long as the *z*-coordinates are below the height (h_{mb}).

Table 4.4 The information of the simulations

Height after deposition	$69.5mm$
Critical time-step for full-scale test	$2.04e-6s$
Applied time-step for full-scale test	$4.08e-7s$
Applied time-step for preliminary tests	$2.04e-6s$
CPU time for the preliminary tests	Two days
CPU time for the full-scale test	One month

Table 4.4 above presents the information of the simulations for the full-scale and preliminary tests with the boundary removal tests. The critical time-step is estimated with the application of the minimum particle size using Eq.(3.43). In such a case, the value is 1/5 times that of the time step for the preliminary test based on the five times larger particle size. The time for the deposition stage and formation stage is similar as around two weeks for each stage.

4.3.2 Observation of sand pile formation

Figure 4.3 displays the progressive stages during the sand pile formation. For the post-processing employing ParaView, it is slow to handle the whole sand pile owing to the larger number of particles involved. Hence, the graph is presented with a section cut in the centre of the heap with a thickness of $5mm$ in the *y*-direction.

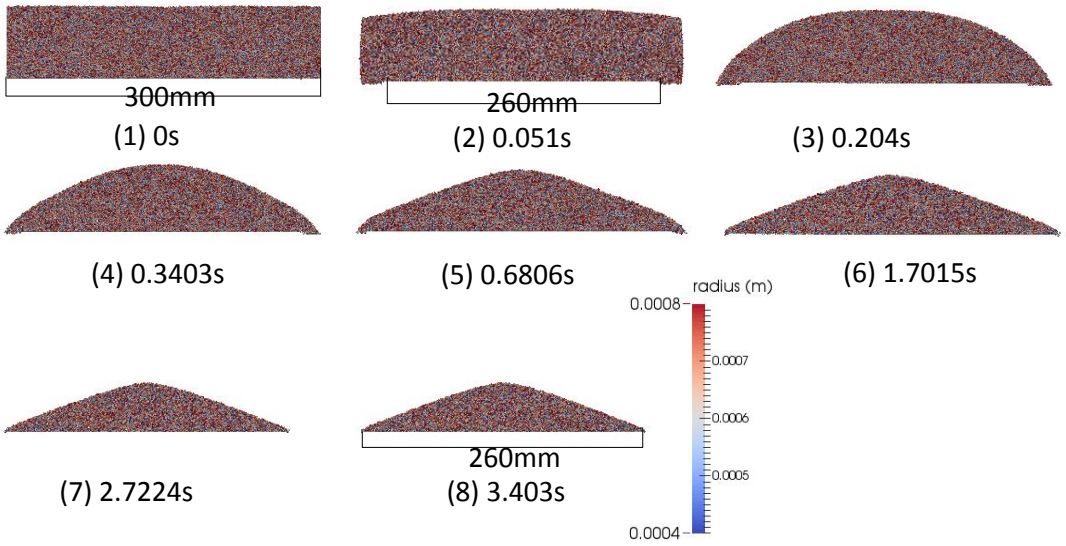


Figure 4.3 The progressive behaviour during sand pile formation

The characteristics of repose angle and void ratio are presented to describe the shape of the heaps. The results are estimated employing the image data analysis method proposed by Kurkuri et al. (2012) with different layers. Particles are identified as belonging to each layer as long as the central coordinates located inside the layer. For each layer, Eq.(4.7) below gives the estimation of volume, void ratio, and surface angle with the shape considering as the frustum of a cone,

$$\begin{cases} V_l = (R_1^2 + R_1 R_2 + R_2^2) h_l / 3 \\ e_i = \dfrac{\left(V_l - \sum_{N_i} 4\pi r_j^3 / 3 \right)}{\sum_{N_i} 4\pi r_j^3 / 3} \qquad \left(i = 1, 2, ..., 5; \mathrm{j} = 1, ..., \mathrm{N}_p \right) \\ \theta_i = \arctan\left(h_l \Big/ \left(R_1 - R_2 \right) \right) \end{cases} \tag{4.7}$$

where V_l is the volume of each layer. R_1 and R_2 are the top and bottom radii of the frustum respectively. h_l refers to the height of the frustum. e_i, θ_i and N_p denote the void ratio, surface angle and the number of particles at the layer N_i respectively. For each layer, the

volume of a particle is calculated as αV_p, where V_p is the volume of particle and α is the ratio of distance located inside the layer divided by the radius distance of the particle.

Figure 4.4 displays the shape of the sand pile with the characteristics of average void ratio and surface angle. The sand pile is divided into five layers. For each layer, the height is $10mm$; approximately eight times the average particle size. The top layer (N_5) is not considered owing to the small number of particles. The peak value of surface angle appears for the base layer, same as in the preliminary tests. In addition, the surface angle decreases with the increase in height.

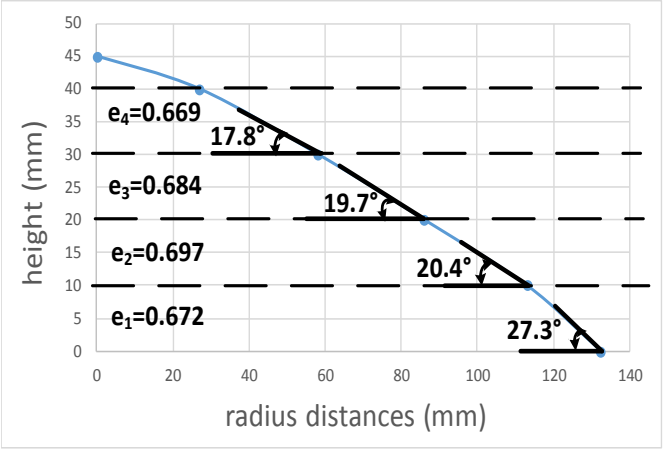


Figure 4.4 The information of sand pile at the final stage

A smoother shape is observed for the full-scale simulation on the basis of the feature of repose angle and a similar average void ratio at each layer, in comparison with the preliminary tests. In addition, a flatter curve is observed near the top surface of the piles for the preliminary tests. However, this phenomenon is reduced for the full-scale test owing to the larger value of the surface angle.

Appendix A.3 discuss the impact of baffle on the results of surface angles with the preliminary tests. For the test with baffle, it shows that the surface angle would increase

approximately 1.6° for the base layer while reducing around 2° for the layer near the top surface. This shows the baffle has a slight influence on the surface angles.

4.3.3 Final base pressure profile

The final stage refers to the particles reaching the equilibrium condition again. The pressure profile is one of the major points of interest regarding the sand pile problem. The DEM provides the results of contact forces for discrete particles. To transform the contact force into stress at representative radius distances, the commonly used method is that of averaging values of the concentric annulus regions respectively. For each region, the pressure is estimated as the total contact force divided by the area of the region. Employing the average scheme, it is possible to determine the global profile as Figure 4.5. However, it cannot reflect the actual condition at the specified radius distance.

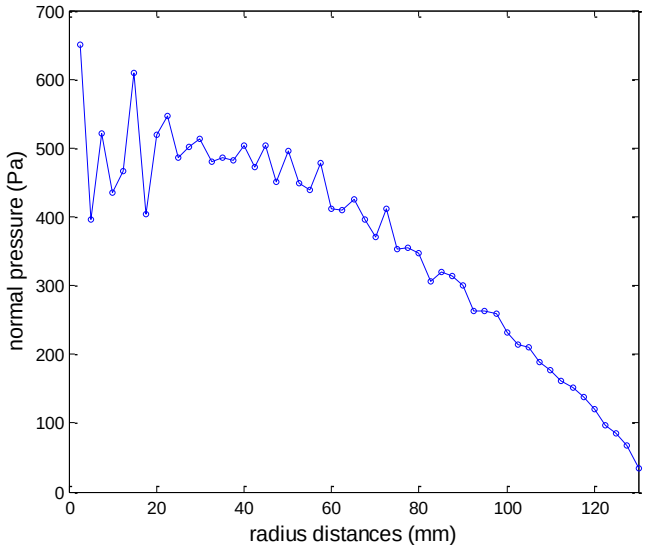


Figure 4.5 The stress distribution on the base plane with the average scheme method

In this project, the Voronoi tessellation method is employed to obtain the stress of each particle. It is constructed based on contact points between particles and the boundary. Based on this feature, the bottom plane is tessellated into multiple small cells. For each cell, it

contains one particle and the cell area can be regarded as the influential area for the particle in contact with the base plane. Hence, the normal pressure/shear stress of the particle is defined as the normal/tangential force divided by the cell area.

The tessellation cells are generated with the Voronoi algorithm of MATLAB software in two-dimensional form. It is achieved by importing the contact points with the base plane. For LIGGGHTS, the contact point is defined as the central coordinates of particles in contact with the boundary. It aims to estimate the pressure distributed on the plane. In such a case, the cells are obtained with coordinates in the (x, y) space to estimate the influential area with the base plane. To acquire the closed boundary, the cells near the edge of the base plane are revised with the dimension of the base plane. An example of Voronoi tessellation plotted in the bottom plane is presented in Figure 4.6, with the black circle depicted the boundary of base plane. It first identifies the cells without the enclosed boundary and then applies the coordinates on the black circle to regenerate the cells on the boundary.

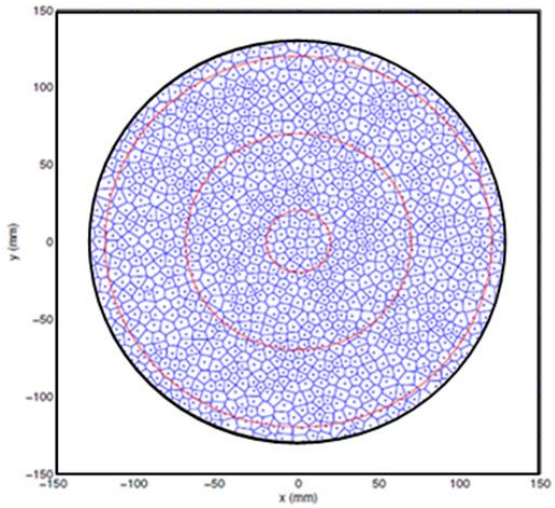


Figure 4.6 An example of Voronoi tessellation generation

For this method, at each representative radius distance (as red circles in Figure 4.6 above), the pressure is calculated with the average value for cells located on the circle. To acquire the trend of the pressure distribution, a sufficient number of points is required. Concerning

the full-scale simulation, the initial and interval representative radius distances are both taken as $2.5mm$, approximately two times the average particle size. Due to the impact of the baffle particles, the Voronoi cells near the edge of the base plane are not taken into account. Figure 4.7 displays the pressure profile at the end of the sand pile formation.

The result is similar in comparison with the preliminary test, as a larger pressure appears underneath the central apex. This may be related to the memory of the preparation method. Owing to the smaller displacement and lower number of particles, it only transfers a less magnitude of contact force in the shear direction and provides a higher value in the central region. Furthermore, due to the lower height of deposit layer for the preliminary test, the peak value is smaller in Figure A.9(b). However, the preliminary test produces a larger magnitude at other regions. Compared with the average scheme method, the voronoi tessellation method reduces the normal pressure slightly, except for the initial radius distance. The tendency is similar for the two methods with the peak pressure appearing underneath the central apex.

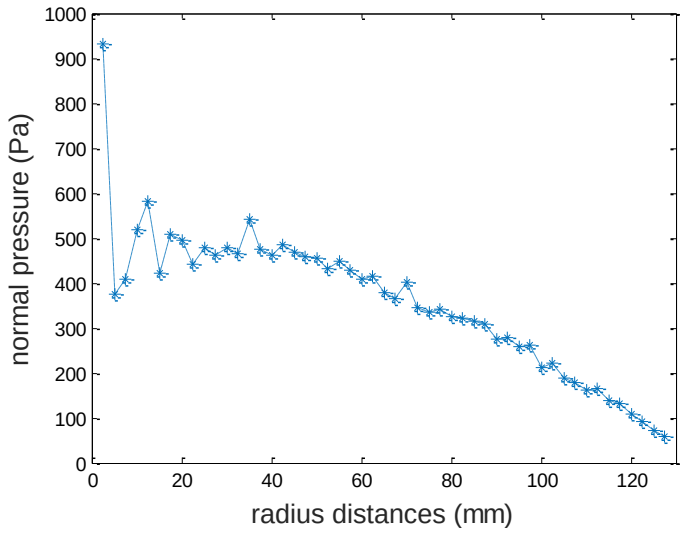


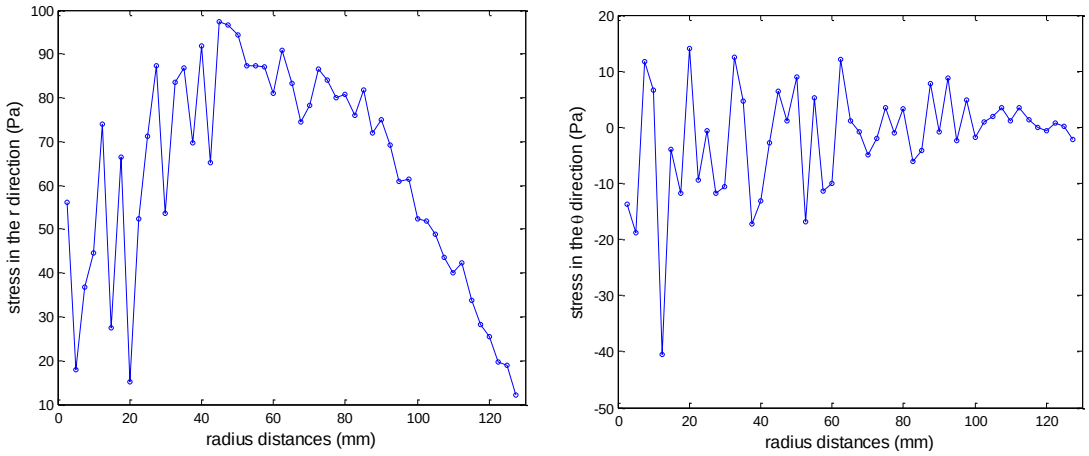
Figure 4.7 The pressure profile on the base plane at the final stage

It also considers the shear stress distributed on the base plane. Due to the symmetrical condition, the cylindrical coordinate system is applied for the data analysis. The coordinates of particles are calculated by the following equation under the cylindrical coordinate system

$$\begin{cases} r = \sqrt{x^2 + y^2} \\ \vartheta = \tan^{-1}\left(y/x\right) \\ z = z \end{cases} \tag{4.8}$$

where (x, y, z) are the coordinates of the particle in the Cartesian coordinate system. In the cylindrical coordinate system, the coordinates are denoted as (r, ϑ, z).

The shear stress is concerned with the radial direction and hoop direction, respectively, for particles in contact with the base plane. With this construction history, the results are slightly fluctuant for both the radial direction and the hoop direction. Compared with the preliminary tests, the radius distance is larger for the peak pressure in the radial direction with a value of $45mm$ and the stress in the hoop direction is close to zero. It demonstrates that the sand pile is more symmetrical with a smaller scale of particles.



(1) radial direction (2) hoop direction

Figure 4.8 The evolution of shear stress with the radius distances

4.3.4 Progressive development of base pressure profile

The progressive development is regarded as the other key aspect on the construction history. It is studied with the evolution of normal pressure portrayed at the progressive critical stages. The initial stage is treated as the stage in which particles are deposited and reach the equilibrium condition. Seven intermediate stages are considered to present the progressive behaviour. The critical stages are considered as $0.005T$, $0.015T$, $0.06T$, $0.1T$, $0.2T$, $0.5T$ and $0.8T$, with the value of $0.017s$, $0.051s$, $0.204s$, $0.3403s$, $0.6806s$, $1.7015s$ and $2.7224s$ ($T = 3.403s$).

The intermediate stages are determined following the preliminary tests; by the height and surface angle of the specimen. For $0.017s$, it refers to the moment after removing the cylindrical boundary. At $0.051s$, the specimen has a displacement of approximately one average particle size in the z direction and the surface angle is near zero. The stage corresponding to $2.7224s$ is one in which formed the shape of sand pile without achieving the equilibrium condition yet. The displacements for the other intermediate stages are $0.15h_d$, $0.33h_d$, $0.7h_d$ and $0.95h_d$ respectively ($h_d = 24.5mm$, refers to the total displacement of the specimen). The pressure profile is plotted with the same initial and interval radius distances as those determined at the final stage.

Based on Figure 4.9, the peak pressure appears under the central apex at each stage. At the initial stage, the normal pressure is almost uniformly distributed on the base plane. After

removing the boundary, the magnitude of normal pressure increases at first. Then, the peak value reduces during the formation of the sand pile. From $1.7015s$ to $3.403s$, the normal pressure is similar owing to the small change in the shape of the sand pile. Compared with the preliminary test, there is a higher increase in pressure for the full-scale simulation after removing the boundary, corresponding to the higher deposit height. In addition, for the real-scale PSD, it also reduces the fluctuations of the results at different stages.

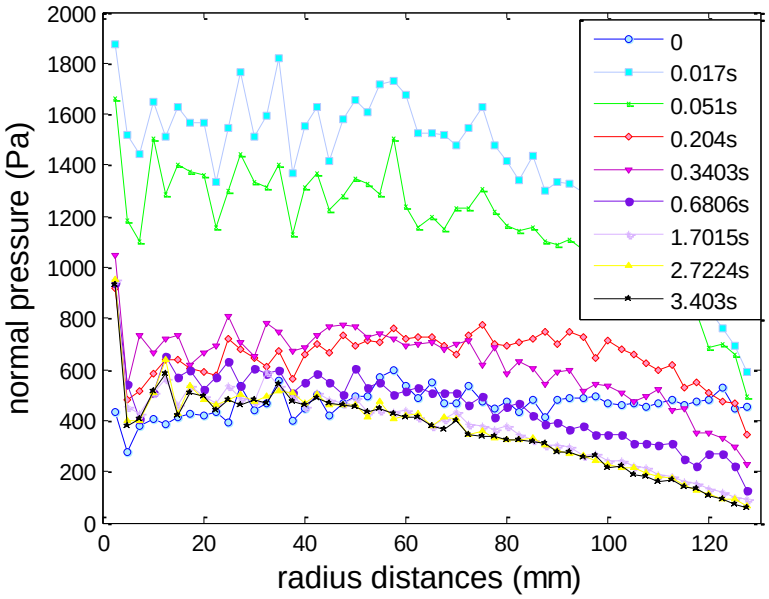
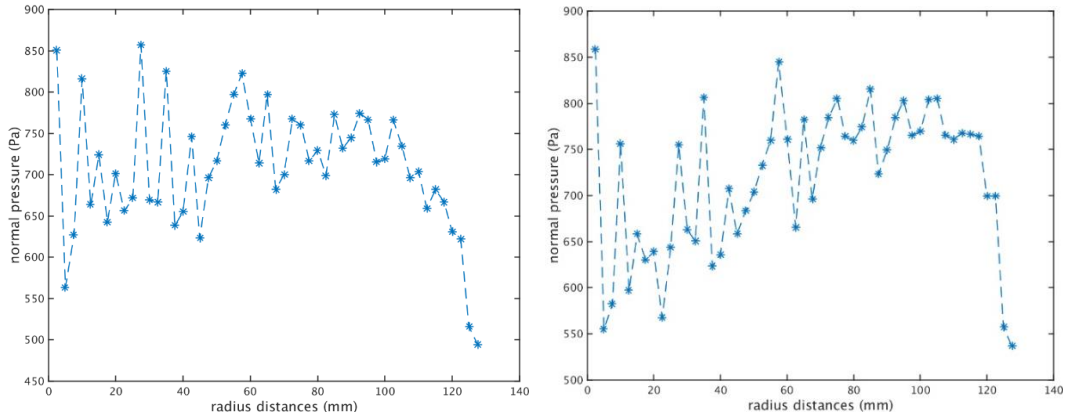


Figure 4.9 The progressive pressure profiles on the base plane

To explain the increase of the pressure after removing boundary, two intermediate stages are considered as $0.0052s$ and $0.0111s$ to study the pressure distribution on the base plane. It shows that, after removing the boundary, the normal pressure increases slightly first due to the impact of the boundary. During the dynamic process, the normal pressure achieves the peak value at $0.017s$.



(1) 0.0052s (2) 0.0111s

Figure 4.10 The pressure profiles on the base plane for the boundary removal method

To further explain the increase of the pressure, the average contact force is studied within the sample at different regions for $0s$ and $0.017s$ presented in Table 4.5. It could be found that the average contact force is reduced after removing the boundary for the radius distance of $[130,150]mm$. However, within the radius distance of $[0,130]mm$, the average contact force is increased with a larger value than the average contact force of the sample. It suggests that some of the average contact force transfers to the intermediate region due to the action of particles during the dynamic process, which increases the average contact force for the region of $[0,130]mm$ and results in the larger normal pressure on the base plane at $0.017s$.

Table 4.5 The information of average contact force at different regions

	Whole sample **Average contact force (e-5N)**			$r_d \in [0,130]mm$ **Average contact force (e-5 N)**			$r_d \in [130,150]mm$ **Average contact force (e-5N)**		
	f_x	f_y	f_z	f_x	f_y	f_z	f_x	f_y	f_z
0s	-8.11	-8.51	-26.1	-8.15	-8.53	-26.7	-8.0	-8.44	-24.3
0.017s	-9.8	-18.9	-71.4	-10.7	-20.6	-79.2	-3.11	-5.72	-13.2

4.4 Rain deposition test

4.4.1 Implementation of the numerical model

For the deposition method, the sample volume is calculated based on the shape of a cone

$$V_{sam} = \frac{\pi}{3} R_s^2 h_s = \frac{\pi}{3} R_s^3 \sin\theta \tag{4.9}$$

in which R_s and h_s refer to the radius and corresponding height of the sand pile. Based on the repose angle of 20.4° from preliminary tests, it requires approximately 8.5e5 number of particles with zero assumed void ratio.

On the basis of the full-scale boundary removal test, it requires approximately two weeks for particles generating and depositing into the container using 32 cores. Considering the simulation time, the particles are continuously inserted and deposited to the base plane to keep the flow of particles. Hence, it only contains the stages of particle generation and sand pile formation.

A hollow cylindrical container is employed and plotted in AutoCAD with a diameter of $260mm$ for designing the model of the distributed deposition, displayed as Figure 4.11. It is imported into the LIGGGHTS with the *.stl* format. According to the preliminary tests, the height of the heap is approximately $45mm$. Hence, the distance between the outlet and base plane is chosen as $60mm$ to avoid the jamming state during the formation stage.

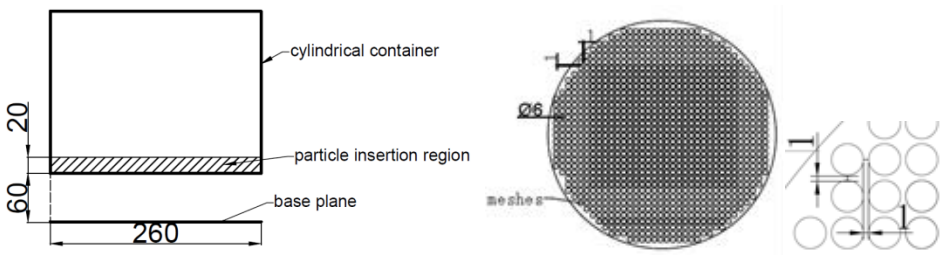


Figure 4.11 The numerical model of rain deposition test

This test is also performed with the Hertz-Mindlin contact model. Due to the complicated sieve boundary for the rain deposition test, it causes a larger rebound height during deposition with Young's modulus of 70GPa . In such a case, the value is reduced to 700MPa for the boundary. The other properties are the same as the properties of the particles.

The procedures are elaborated in the following,

1. Particle generation stage. Particles are randomly inserted as layers, in the shallow region of the cylindrical container portrayed in Figure 4.11. The number of particles is estimated as Eq.(4.1) with h_c considered as approximately equal to twenty average particle sizes and the void ratio assumed as zero. The flow rate is employed to estimate the frequency of the particles insertion. The time (t) is calculated as the particles of the layer moving out of the cylindrical container under the self-weight deposition $\left(t = \sqrt{2r_{hi}/g}\right)$, where r_{hi} refers to the maximum radius size of the particles. The steps (N_s) can be obtained with the defined time step. Then, particles are continuously inserted in the shallow region at each N_s step.

2. Particle deposition and sand pile formation stage. In this stage, the particles are deposited to the base plane under self-weight. The gravitational acceleration is also selected as 9.81m/s^2. Some particles may be moved out of the base plane during this process and they will be deleted to save computational effort.

The two stages are continued until a sufficient number of particles is inserted to form a sand pile.

4.4.2 Observation of sand pile formation

Figure 4.12 presents the process of the rain deposition test, with the sand pile generating layer by layer. Due to the sieve boundary, some particles are not deposited to the base plane but remain on the sieve plane. Owing to the larger number of particles, the graphs are displayed with a section of 5*mm* thickness in the centre of the specimen in the *y*-axis direction.

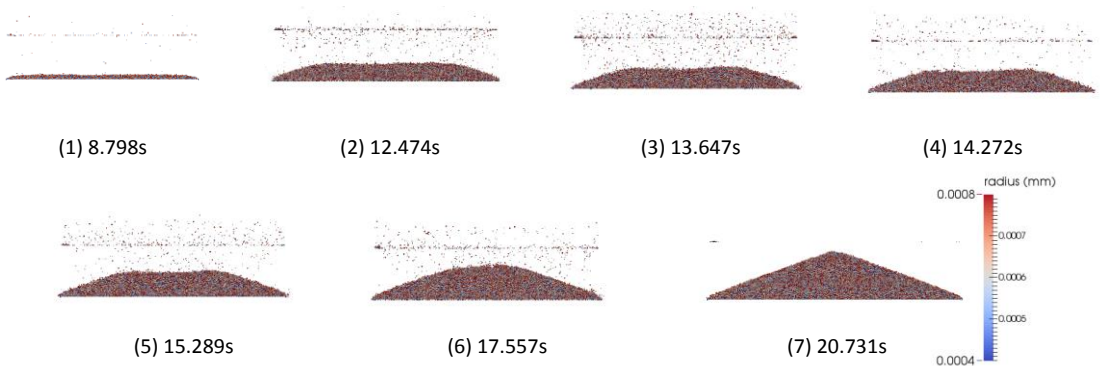
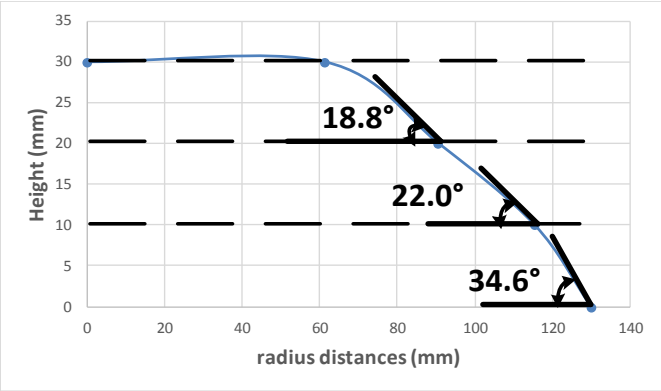
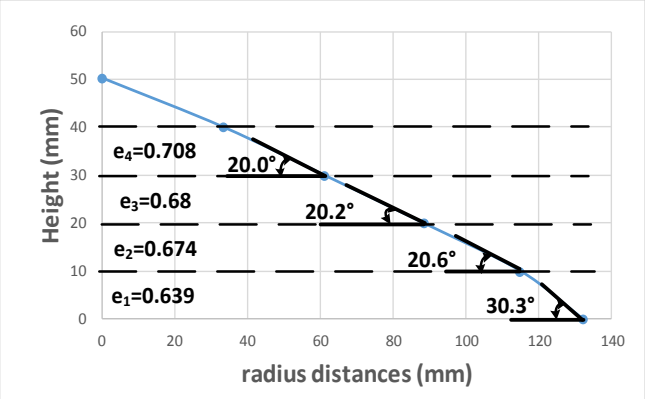


Figure 4.12 The progressive behaviour during sand pile formation

The information of the heap is presented in Figure 4.13 with two different stages as shown in Figure 4.12(5) and Figure 4.12(7), to display the evolution of surface angles during deposition. Depending on the formation layer by layer, a plate is observed with a height of approximately two times the average particle size near the base plane at the final stage. Hence, it increases the surface angle for the base layer. Figure 4.13 shows that the surface angles are both decreased with the increase in height of the pile for the two stages. After achieving the equilibrium state, the surface angle for the base layer is decreased while it is increased for the value of the layer near the top surface. For the three intermediate layers, the surface angles are almost the same, but much smaller than the layer near the base plane. Compared with the boundary removal method, the shape is similar with a larger surface angle at each layer.



(1) 15.289s



(2) 20.731s

Figure 4.13 The shape of the sand pile for the rain deposition method

For the final stage, the feature of the void ratio is also taken into account at each layer with the application of Eq.(4.7). The top layer is not of concern due to the small number of particles. The densest layer appears for the base layer. However, the loosest layer occurs in the layer near the top surface of the heap. In the intermediate layers, the void ratio is similar depending on Figure 4.13.

4.4.3 Final base pressure profile

Figure 4.14 presents the pressure profile with the application of the Voronoi tessellation method at the final stage. The starting radius distance is $2.5mm$; approximately two average particle size. Particles near the edge of the base plane are also not taken into

consideration. The peak pressure appears under the central apex according to the graph without the pressure dip phenomenon.

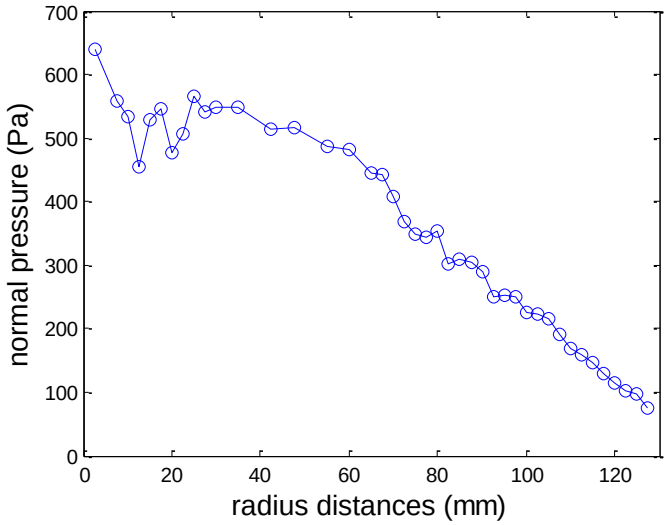
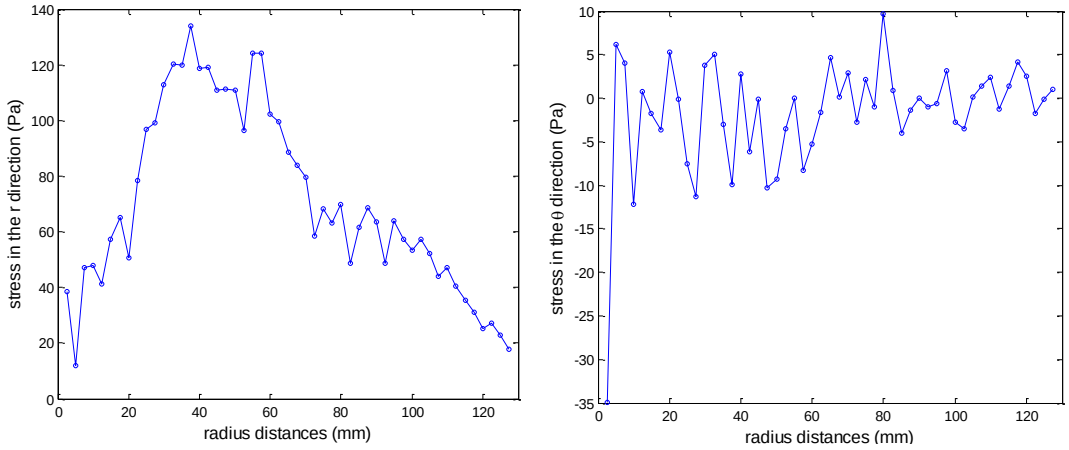


Figure 4.14 The evolution of normal pressure on the base plane at the final stage

The shear stress is also taken into account at the final stage in the cylindrical coordinate system. The results are smoother compared with those of the boundary removal method. In addition, the peak stress in the radial direction appears at the radius distance of $40mm$ under this method. For the stress in the hoop direction, the value is smaller compared with the boundary removal method.



(1) radial direction (2) hoop direction

Figure 4.15 The evolution of shear stress with the radius distances

4.4.4 Progressive development of base pressure profile

The sand pile is generated layer by layer for the rain deposition test. In such a case, the deposition height is regarded as the vital factor to determine the progressive stages. The starting point refers to the beginning of the simulation. Six progressive stages are defined, with heights of $5mm$, $20mm$, $25mm$, $30mm$, $35mm$ and $40mm$, respectively, to observe the evolution of pressure and internal structure. The initial stage refers to the particles generating a layer on the base plane with a height approximately five times the average particle size. In the second stage, the particles form a heap with a height which is approximately half that of the sand pile at the final stage. After that, the interval height is chosen as $5mm$, approximately equal to five average particle sizes, to identify the progressive stages.

The simulation times for the six stages are $8.798s$, $12.474s$, $13.647s$, $14.272s$, $15.289s$, $17.557s$ and $20.731s$ respectively. Figure 4.16 gives the evolution of normal pressure on the base plane at the critical progressive stages. The pressure profile is plotted with the average normal pressure at the representative radius distances using the Voronoi tessellation method. No pressure dip phenomenon appears at each progressive stage. And the peak normal pressure increases with the development of the sand pile.

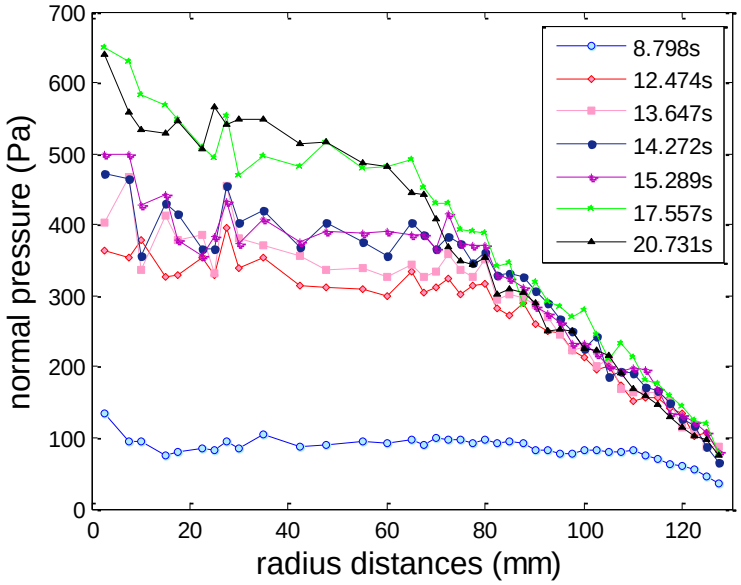


Figure 4.16 The progressive evolution of normal pressure on the base plane

4.5 Point deposition test

4.5.1 Implementation of the numerical model

The procedures of the point deposition test also contain two stages similar to the rain deposition test illustrated in Section 4.4 above. They are also illustrated as: 1) generation stage and 2) sand pile packing and formation stage.

The geometry of the boundary is also plotted in AutoCAD and converted into ASCII STL format for forming the boundary in LIGGGHTS. It is constituted as a hopper, to control the flow rate, located at a distance of $60mm$ above the base plane presented as Figure 4.17. The outlet length is selected as ten times that of the average particle size, the same as that of Vanel et al. (1999).

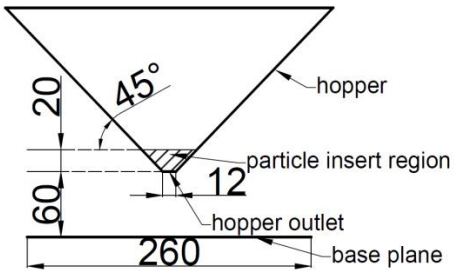


Figure 4.17 The numerical model of hopper deposition test

The test is also carried out with the Hertz-Mindlin contact model, with Young's modulus of 700MPa. The other properties are the same as the properties of the particles.

The following illustrates the procedures for the point deposition test,

1. Particle generation stage. Particles are continuously generated in the shallow region portrayed in Figure 4.17. It also employs Eq.(4.1) to estimate the number of inserting particles with the void ratio assumed as 0 and the total volume calculated as the shape of a frustum cone. A similar approach to that elaborated in Section 4.4.1 is employed to estimate the frequency of particle insertion for maintaining the flow of particles deposited onto the base plane.

2. Particle deposition and sand pile formation stage. This stage is carried out for particles deposited to the base plane, forming the heap. Particles are flown out under the self-gravity condition with an acceleration of $9.81 m/s^2$. The particles moving out of the base plane will also be deleted.

The two stages are continued until the heap is formed with a radius distance of $130mm$.

4.5.2 Observation of sand pile formation

The behaviour of the heap at different stages is presented in ParaView with a section of $5mm$ in the y-axis direction. Under this preparation method, the sand pile transitions from a small size to a large one.

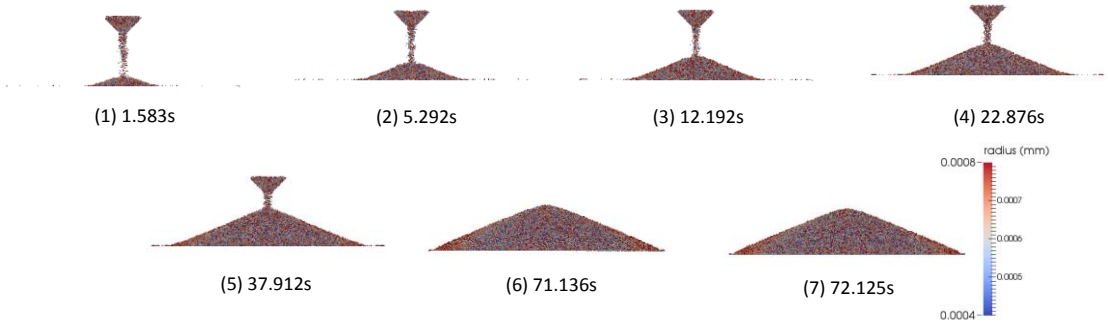
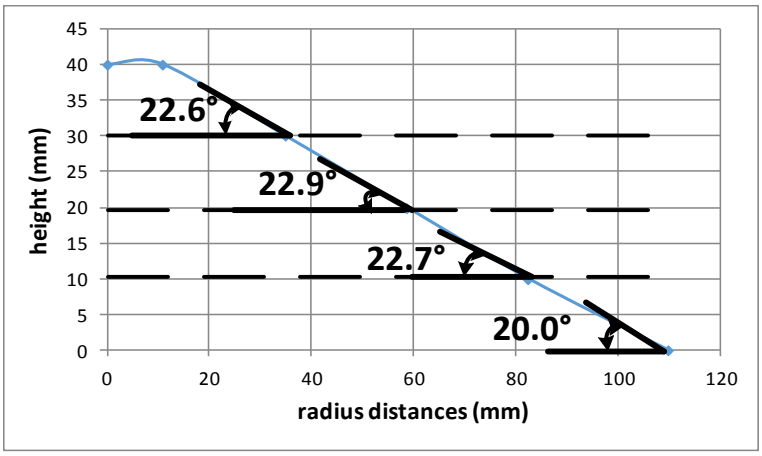


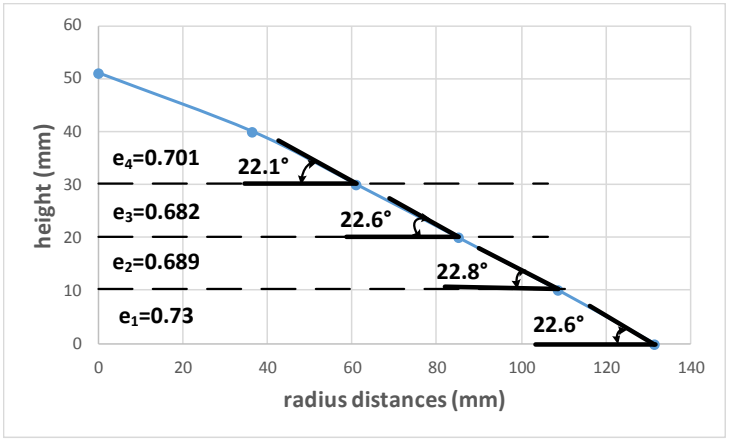
Figure 4.18 The progressive stages of the point deposition test

Figure 4.19 below gives the information of the sand pile with a height of $10mm$ for each layer. To observe the development of the sand pile, two stages of 37.912s and 72.125s are selected to present the surface angles at different layers. The continuous deposition of particles increases the surface angle for the base layer. However, it has a negligible effect for the surface angles of the intermediate layers.

According to Figure 4.19(2), it shows this preparation method produces a relatively flatter base layer accompanying with a steeper top layer and a smoother nearly conical shape of sand pile, compared with the boundary removal and rain deposition tests. At the final stage, it also displays the information of average void ratios of different layers. It illustrates that the loosest layer appears for the base layer, while the densest layer occurs in the intermediate layers.



(1) 37.912s



(2) 72.125s

Figure 4.19 The shape of the sand pile at the final stage

4.5.3 Final base pressure profiles

Figure 4.20 displays the pressure profiles at the final stage without the consideration of pressure near the edge of the boundary. These are also obtained based on the average pressure at the representative radius distances with the application of the Voronoi tessellation method. A pressure dip phenomenon can be observed with the peak pressure appearing at approximately 37.5*mm* from the central apex under this construction method. Owing to the spherical particles and lower value of the repose angle, the degree of pressure dip is smaller in comparison with the results of Vanel et al. (1999).

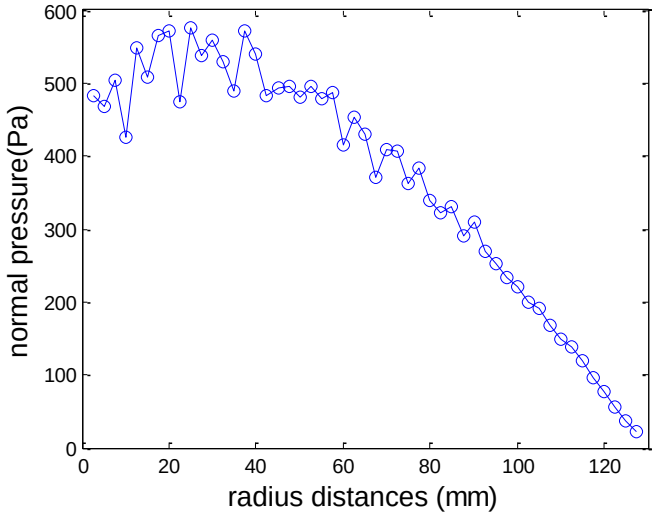
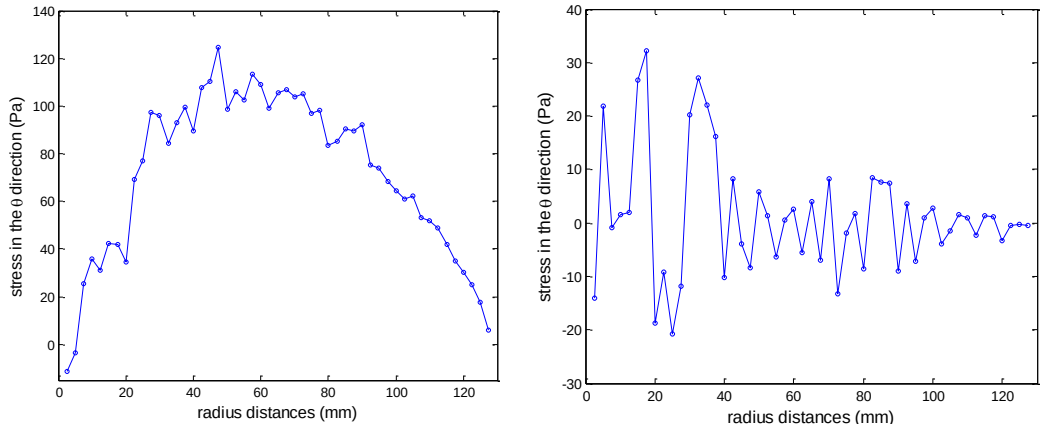


Figure 4.20 The behaviour of pressure distribution at the final stage

The cylindrical coordinate system is also applied to observe the shear stress distribution. For the radial direction, the peak stress is observed at the radius distance of $47.5mm$. Considering the stress in the hoop direction, it contains larger shear stresses within the radius distance of $40mm$ than the boundary removal and rain deposition tests.



(1) radial direction (2) hoop direction

Figure 4.21 The evolution of shear stress with the radius distances

4.5.4 Progressive development of base pressure profile

The evolution of normal pressure is studied for investigating the impact of construction history. Depending on the sand pile forming from a small size into a larger one, the radius

distance of the heap is considered as the critical factor to determine the progressive stages. Six different stages are investigated with the radius distances of $30mm$, $50mm$, $70mm$, $90mm$, $110mm$ and $130mm$ respectively. The initial radius distance is selected as $30mm$ to contain a sufficient number of particles. The interval radius distance is $20mm$, approximately equalling to twenty average particle sizes. The simulation times are $1.583s$, $5.292s$, $12.192s$, $22.876s$, $37.912s$, $71.136s$ and $72.125s$ for the six stages respectively.

Considering the characteristics of the heap, only the particles deposited and formed the sand pile are considered during these intermediate stages, without the consideration of particles located in the hopper and under the flow condition. The pressure profiles are presented in Figure 4.22 and obtained with the Voronoi tessellation method for particles interacting with the base plane. According to the graph, the radius distance for the peak pressure increases during the sand pile formation. From $1.583s$ to $37.912s$, due to the action of particle deposition, the larger pressure appears around the radius distance of $10mm$. Afterwards, as the specimen achieves the equilibrium condition, the pressure is reduced underneath the central apex and the counter-intuitive phenomenon appears.

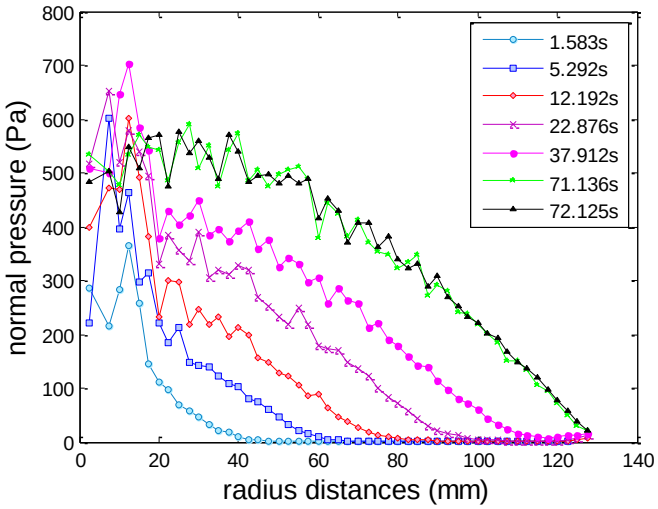


Figure 4.22 The progressive pressure profiles of the point deposition method

4.6 Discussion of sand pile following different construction histories

The above results demonstrate that various shapes and stress distributions are observed following different procedures. Table *4.6* below presents the surface angles and heights of the sand piles at the final stage. The boundary removal process produces a relatively lower height, while a similar height is obtained for the rain deposition and point deposition methods. With regard to the surface angles at different layers, a steeper base layer is obtained by the boundary removal and rain deposition tests, with around 7° larger than the base layer of point deposition test. In contrast, considering the layer near the top surface, the point deposition test produces a relatively larger surface angle. According to the results in Appendix A.3, it shows the impact of the baffle is not that significant for the difference of the surface angles. The results agree with the assumption proposed by Liffman et al. (1992). With a higher angle near the top of the heap, it is easy to obtain a depression underneath the apex for the normal pressure acting on the base plane.

Table 4.6 Surface angles at different layers under different methods at the final stage

	$[0,10]mm$	$[10,20]mm$	$[20,30]mm$	$[30,40]mm$	Height
Boundary removal	27.3°	20.4°	19.7°	17.8°	45*mm*
Rain deposition	30.3°	20.6°	20.2°	20.0°	50.4*mm*
Point deposition	22.6°	22.8°	22.6°	22.1°	51.1*mm*

The pressure profiles are also compared with the three different construction histories at the final stage. For the boundary removal test, it generates a relatively higher pressure for

the smaller displacement and larger initial pressure at $R_d = 2.5mm$. In such a case, the pressure profile is revised with the average value of all the particles located inside the circle region at this radius distance. The counter-intuitive phenomenon is observed for the point deposition test with the peak pressure occurring at the radius distance of $37.5mm$. No pressure dip phenomenon is obtained for the boundary removal and rain deposition tests. Concerning the radius distance near the edge of the boundary, the rain deposition and boundary removal procedures contain more particles in this region depending on the larger surface angles, which results in larger normal pressures than the point deposition test.

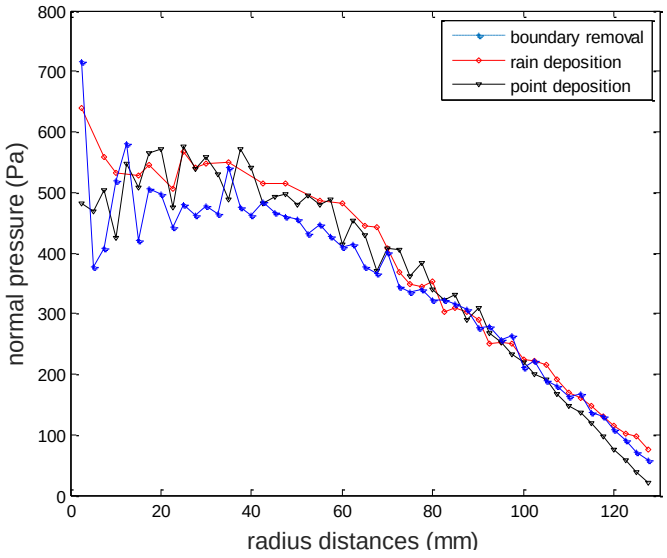
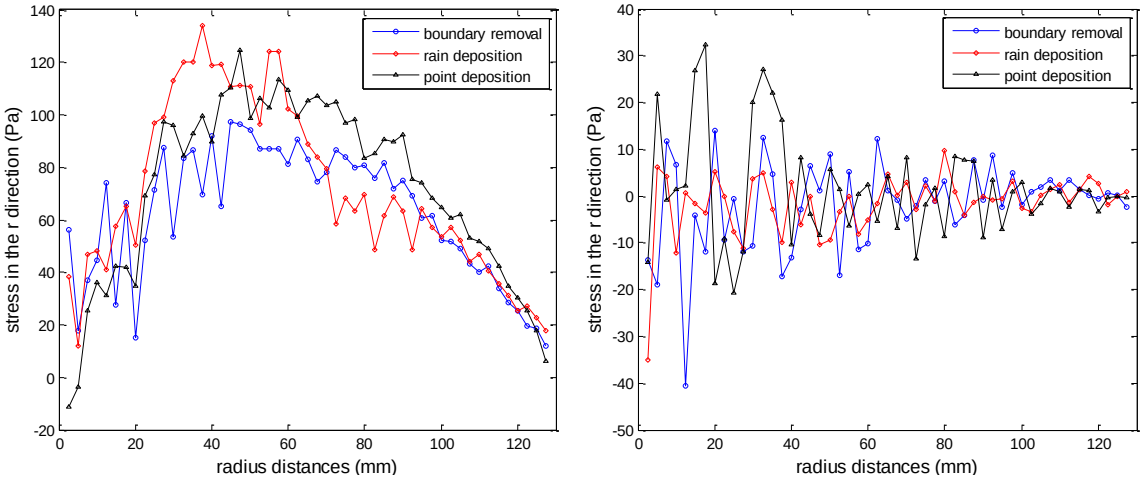


Figure 4.23 The pressure distribution at the ultimate stage with different methods

The literature review proposed a dip in normal stress related to the larger horizontal force in the Cartesian coordinate system (Bagster and Li, 1993; Liffman, 1994; Liffman et al., 1999). This project studies the shear stress distribution in the cylindrical coordinate system with the radial direction and the hoop direction respectively. For the radial direction, the behaviour is similar, with the peak stress appearing at the radius distance of approximately $40mm$. The boundary removal test contains a lower magnitude of stress in the radial direction. However, for the hoop direction, the rain deposition test provides a lower value

at different regions. The point deposition test produces slightly larger magnitudes of stress in the hoop direction within the radius distance of $40mm$. Due to the lower degree of the pressure dip with the spherical particles, the difference is not that much in comparison with the other two different preparation methods.



(1) radial direction (2) hoop direction

Figure 4.24 The evolution of shear stress at the final stage with different methods

To better understand the impact of construction history, the local stress is applied to observe the stress behaviour inside the structure. It is obtained with the stress tensor of each particle in the expression of

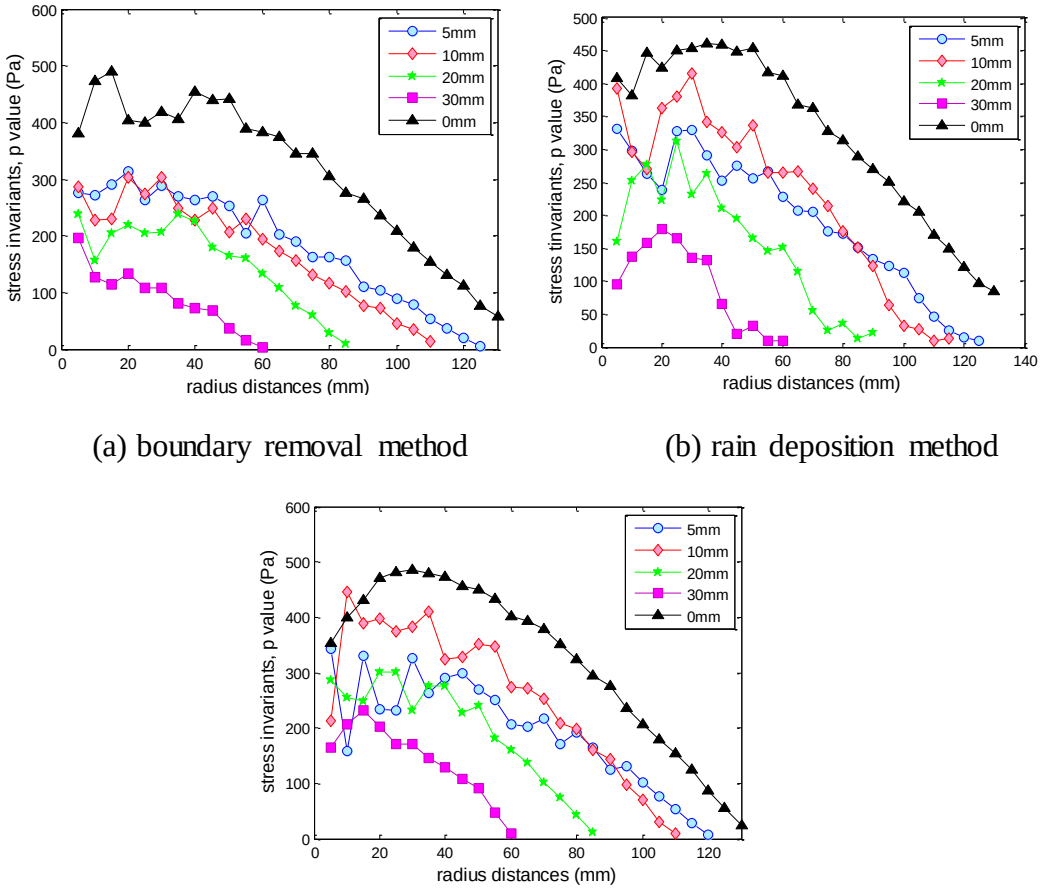
$$\sigma_{ij} = \frac{1}{V_p(1+e)} \sum f_i l_j \tag{4.10}$$

where f and l denote the contact force and branch vector acting on the particle respectively, and V_p refers to the volume of the particle, which is acquired with the assistance of the average void ratio (e) for the specimen.

The stress distribution is considered with the factor of height under various preparation methods at the final stage. Four different heights are selected: $5mm$, $10mm$, $20mm$ and $30mm$, which represent approximately five, ten, twenty and thirty times the average

particle size, respectively. A plane is assumed at the height of each layer to identify the location of particles. Particles are considered to be in the layer as long as the central coordinates located above and interacted with the assumed plane.

To acquire the stress profiles, it is necessary first to estimate the stress invariants and components of each particle. The stress invariants p, q, b are estimated as Eq.(3.58)-Eq.(3.62). Then it calculates the average value of particles located at the specificed radius distance in the span of $\left(R_{d(i-1)}, R_{d(i)}\right)$, where $R_{d(i)}$ refers to the current representative radius distance. Particles are determined as this radius distance as long as the central coordinates located inside the span. The following graphs display the distribution of p values under the three construction histories.



(a) boundary removal method (b) rain deposition method

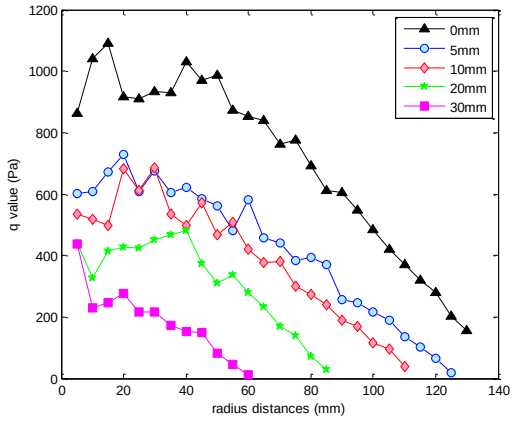
(c) point deposition method

Figure 4.25 Behaviour of p values at different layers at the final stage

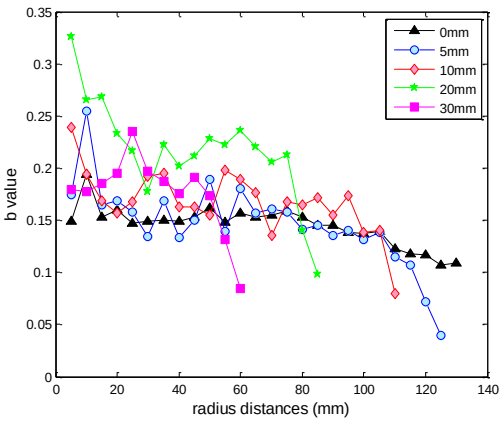
Regarding the boundary removal method, the peak pressure, appearing in the core region at each layer, reduces with the increase in height. For the rain deposition test, the peak pressure appears underneath the apex of the layers with a height of $5mm$. It is interesting to observe that a drop of stress underneath the central apex of the radius distance occurring in the layer of $10mm$, $20mm$ and $30mm$. In addition, the peak pressure is slightly larger for the layer of $10mm$ in comparison with the layer of $5mm$.

In the point deposition test, for the layer of $5mm$, the pressure is lower than the results for the layers of $0mm$ and $10mm$, the same as in the rain deposition method. A decrease of the stress could still be observed underneath the apex at the layer of $10mm$, $20mm$ and $30mm$. The radius distance for the peak pressure is reduced with the increase of height in comparison with the pressure profile on the base plane. The results agree with the investigations of Ai (2013) for the p value obtained with the FEM.

The deviatoric stress and intermediate principal stress ratio are also concerned at different heights with various construction histories, displayed as Figure 4.26. The evolution of the deviatoric stress is similar to the evolution of the confining pressure for each height following different procedures. For the base layer, it contains the largest deviatoric stress for the three methods. Regarding the characteristic of b value, for the higher height, it contains a relatively larger value for all the three tests, with the lowest value provided by the base layer. The results show that the b value is around 0.2 for the three tests.

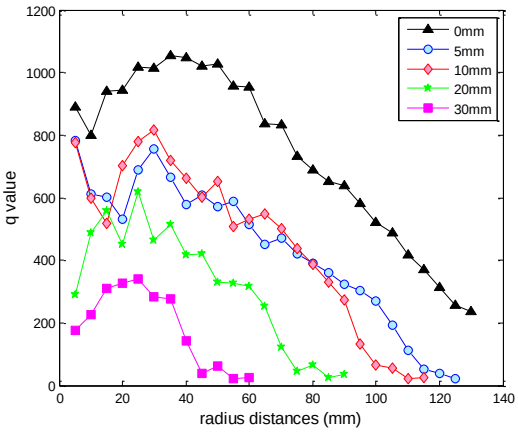


(1) q value

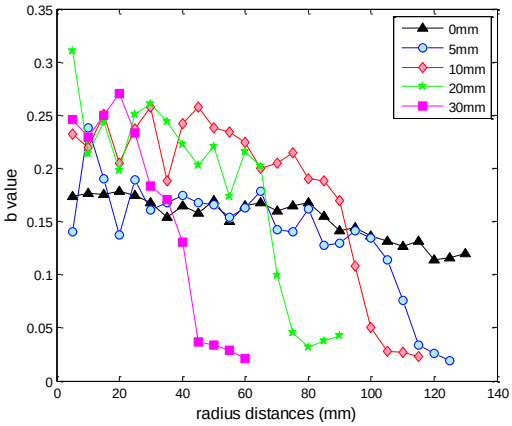


(2) b value

(a) boundary removal method

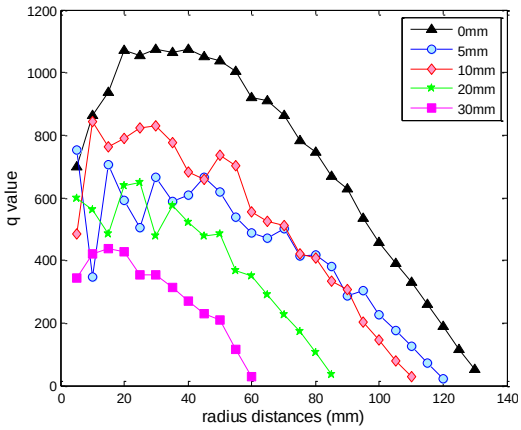


(1) q value

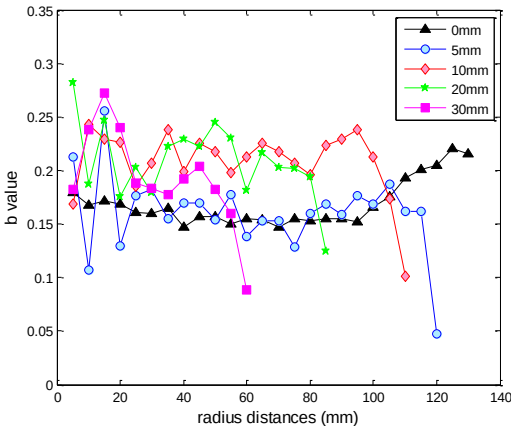


(2) b value

(b) rain deposition method



(1) q value



(2) b value

(c) point deposition method

Figure 4.26 The evolution of q value and b value at the final stage

4.7 Summary

Three different preparation methods: boundary removal, rain deposition, and point deposition, are performed in this chapter. Tests are carried out with reference to Vanel et al. (1999). The surface angles are employed to observe the shape of the sand piles. Under various preparation methods, different shapes are obtained. The point deposition method forms the sand pile with a smaller angle for the base layer. However, it contains a relatively larger surface angle for the layer near the top surface of the heap in contrast to the boundary removal and rain deposition tests. This kind of shape is suggested having a higher probability of reducing the normal pressure in the core region.

The Voronoi tessellation method is applied to obtain the stress of each particle interacting with the base plane. The counter-intuitive phenomenon is observed with the point deposition test. Owing to the smaller repose angle obtained with the spherical shape, the degree of dip is lower in comparison with the results in Figure 2.2 (Vanel et al., 1999). No pressure dip phenomenon appears with the boundary removal and rain deposition approaches. In addition, the shear stress is also concerned with the cylindrical coordinate system in the radial direction and the hoop direction respectively. The point deposition test contains a relatively larger shear stress underneath the central apex in the hoop direction, in comparison with the boundary removal test and rain deposition test. Based on the lower degree of the pressure dip, the difference of the shear stress is not that large.

Furthermore, the stress tensor is applied to obtain the local stress invariants distribution inside the sand pile at different heights following various procedures for the final stage. The evolution of the q value is similar to the characteristics of the p value, with the larger pressure appearing at the base plane. The point deposition test forms a lower value of

confining pressure and deviatoric stress in the core region than the boundary removal method and rain deposition method at the final stage.

Chapter 5 Numerical implementation of elementary test in LIGGGHTS

5.1 Introduction

The study of sand pile concerns the fluid-like and the solid-like states of granular materials depending on particle's kinetic energy. The investigation of the pressure dip formation requires full life-cycle tracing of material packing formation and subsequent restructuring due to overlying loading. It is hence important to understand the elementary material behaviour which involves both proportional and non-proportional loading. This research implemented the algorithm published in Li et al (2013) in LIGGGHTS and used it to investigate the elementary behaviour of granular materials used in Chapter 4. The algorithm was previously implemented in PFC by Li et al (2016). Simulation of this project has been carried out using LIGGGHTS which is run on the high performance computation containing hundreds of computing cores based on the CPU of Intel Sandy Bridge, with the rate ranged from 2.0 GHZ to 2.6 GHZ. Issues arising due to LIGGGHTS implementation are detailed in Section 5.2. Exemplary simulation results are presented in Section 5.3 and compared with previous researcher's results. A discussion is presented in this chapter with the uniformity of the sample in Section 5.4 at the stages of consolidation, triaxial shear and rotation shear, to justify the chosen algorithm.

5.2 Implementation in LIGGGHTS

This section introduces information relating to the developed features in LIGGGHTS for implementing the elementary tests. Tests are performed with the polyhedral boundary to reduce the arching effect generated by the neighbouring walls. The control of loading and boundary corresponds with the work of Li et al. (2013; 2016). The following major factors should be considered to implement the numerical tool:

1) The definition and control of boundary;

For PFC, the rigid massless boundary walls are defined using the centre coordinates and the normal directions. In the case of LIGGGHTS, the boundary is defined by the *.stl* files that are determined with the edge coordinates of walls and the normal directions. Hence, it is necessary to import the *.stl* files to form the boundary.

2) The generation and control of particles;

LIGGGHTS could generate particles with a uniform number particle size distribution. Particles are randomly inserted from the largest size to the smallest ones. One factor that should be emphasised is that LIGGGHTS could only generate particles in a regular region; for instance, this might be the cubic region, rectangular region, cylindrical region and spherical region. In this polyhedral boundary, particles would be inserted in a larger spherical region first and then deleted out of the boundary. This may result in a slightly different distribution of particles.

3) The deformation control of each calculation step;

For particles, the deformation is determined by the contact force with the inter-particle and the boundary. For the boundary control, the deformation is achieved with the translation

displacement and rotational displacement respectively. At each step, after deformation, the *.stl* files would be updated with the coordinates and normal directions.

4) The servo-control of elementary test algorithm;

The servo-control is the main part in performing the simulation with the specified loading conditions. The boundary condition and stress condition should be satisfied before a loading is added.

5) Data output and interpretation;

The information of boundary and particles could be output at defined steps. For the boundary, the information is also saved in the *.stl* format, including the coordinates and the normal directions. The information of particles, the contact information with inter-particles, and the contact information with boundaries could be saved in the separate files as a format of .txt. The format could be transferred to the format *.vtk* and visualised with the ParaView software.

Based on the aforementioned information, the main stages in the process of implementing the algorithm are the generation and control of boundary, and the servo-control stages with different loading paths. The following elaborates the implementation of the tool in LIGGGHTS. The main functions of the elementary tests are developed with the separate packages defined in the source codes. It contains the following five packages: "basiccontrol", "compact", "consolidate", "triaxial_const_b" and "rotation_shear". For each package, a shell script is added to install or remove the files that are compiled with the LIGGGHTS software.

5.2.1 Boundary formation

The shape of the boundary is introduced in Section 3.3. Based on the values N and R, the coordinates of each walls could be determined by employing Eq.(3.44) and Eq.(3.45). Subsequently, the *.stl* files could be written by the MATLAB software based on the triangular meshes of each wall and imported into LIGGGHTS. The sizes of walls are determined by the coordinates of points in the *.stl* files. It would be unclosed space during the deformation. In order to guarantee an enclosure space, the boundary is enhanced for the simulation. The original code of "scale" in the "fix_mesh.cpp" file could increase the size of the boundary in LIGGGHTS including the wall centre coordinates. In such a case, the size of the boundary would be modified without increasing the sufficient space out of the intersection points forming the boundary. Hence, a command named as "extend" is developed on the basis of the "scale" command. The coordinates of walls are determined as $nc-(n-1)c_w$, where n refers to the scale factor, c represents the coordinates of each point, and c_w is the wall centre coordinates. This would maintain the initial wall central coordinates and the size of the boundary with the extension of the walls.

5.2.2 Control of boundary

After the formation of the boundary, the control of the boundary is considered for realising the deformations. The "basiccontrol" package contains the basic functions for the simulations, such as updating boundary information, and the translational and rotational displacements. Files, named as "boundary_control", "stress_strain", "tensor_cal" and "run_initial", are written in this package. A command, named as "run_initial", is defined and modified on the basis of "run" command, in order to call the functions of basic control in the input file and realised with the "run_initial.cpp" file in this package. The initial

conditions for the boundary are defined in the "update.cpp" file, which would be called at the beginning of each stage to set the initial environment.

The information of boundary conditions is written in the "boundary_control.cpp" file, including functions for updating the interacted vertex coordinates, sample volume and displacements of walls. The "stress_strain.cpp" file contains the information of the principal stress/strain values and invariants, with the aid of "tensor_cal.cpp" file, after a deformation during the simulation. These functions would be called at each step.

5.2.3 Control of loading

The stress state is a critical feature to control loading for the elementary boundary test. Appendix B.1 provides the information and flow chart for the estimation of the contact properties in LIGGGHTS. The codes are added in the "fix_wall_gran_hooke_history.cpp" and "pair_gran_hooke_history.cpp" files to estimate the results of total contact force and number of contacts, from the boundary and interacted particles respectively. During simulation, the stress state is controlled with the stress tensor estimated from the "fix_wall_gran_hooke_history.cpp" file. The macro-scale stress tensor from the inter-particle is calculated to form a comparison with the results from the boundary for checking the isotropic condition. In such a case, codes are added in the "dump_local.cpp" file to estimate the results at every N_{st} steps (defined in the input file) for reducing the computation effort.

With respect to the sample condition, the "compute_reduce" file is modified to save the value of unbalance force calculated in the input file. This value would also be invoked to check the loading control at each stage during loading.

5.2.4 Servo-control of different stages

The other four packages, "compaction", "consolidation", "triaxial_const_b", "rotation_shear", are written for performing various categories of loading. For each package, a file named as "update.cpp" is modified for setting the initial conditions. With the consideration of the data analysis at each stage, the "variable.cpp" file is also modified and added with the parameters for outputting and using in the input files. It includes the information of displacements, stress state and strain state for the boundary during loading.

Packages of "compact" and "consolidation" are under the similar loading conditions. They are implemented for compacting the boundary to the target confining pressure with the stress-controlled conditions. The main difference between these two stages is the value of the target confining pressure. For the compact stage, the target confining pressure is defined with 10kPa and the loading rate is limited with the tolerance of volumetric strain. The package contains the file written for the servo-control of the compaction stage. A command named as "run_compact" is defined in this package to call the functions of servo-control, which would be called every step in the input file to realise the loading condition and boundary control during the simulation.

With regard to the consolidation stage, the "servo_consolidate.cpp" file is written for the servo-control of the consolidation stage. In this stage, it involves two kinds of loading conditions. The first refers to the strain-controlled condition as long as the mean principal stress is less than 10kPa. The loading rate is estimated as $\Delta\varepsilon$ denoted in Eq.(3.63) with the minimum stress increment $\left(p_{lb}\right)$ of 1kPa. Otherwise, the specimen is under the stress-controlled condition. It requires checking the boundary stress condition before loading a stress increment. The loading rate is defined as

$\mathrm{sgn}\left(p_{req}-p_{cur}\right)*\min\left(abs\left(p_{req}-p_{cur}\right),\zeta\cdot\max\left(p_{lb},p_{cur}\right)\right)$, where p_{req} and p_{cur} refer to the target and current confining pressure respectively. In this study, ζ is selected for 0.1. These functions are called by the command of "run_consolidate" written in this package in the input file.

Packages of "triaxial_const_b" and "rotation_shear" refer to the shear stage with different loading paths. The loading of "triaixal_const_b" comes under the mix-controlled loading condition. Specimens are loaded with the increase of deviatoric strain while keeping the values of intermediate principal stress ratio (b) and confining pressure (p) constant. The "triax_const_b_ini.cpp" file contains the functions defining the initial condition of the shear stage which would be called by the "update.cpp" file. Employing the similar approach as "run_compact", a command named as "run_shear" is implemented for calling the functions of servo-control determined in the "servo_triax_const_b.cpp" file during shearing. The "variable.cpp" file contains the information of outputting results such as the deviatoric strain, the stress state and the strain state.

The "rotation_shear" package is generated for the rotation of the principal stress directions during the shear stage, while maintaining the stress invariants constant. The initial condition, defined in the "rotation_ini.cpp" file, is also achieved via the "update.cpp" file. The "run_rotate" command is defined in the package to call the functions for the rotation of the principal stress directions in the "servo-rotate.cpp" file. The related variables are also added in the "variable.cpp" file for the consideration of the data analysis, such as the information of rotation angle and the stress state of the specimen.

After generating the packages, it uses the command of "make yes-XXX" or "make no-XXX" to install or remove the functions defined in the specified packages into the original

source codes. ('XXX' refers to the name of the defined package). To run the elementary simulation test, it first undertakes the generation test with the preparation of the specimen. Subsequently, it performs the compaction and consolidation stages for compacting the sample to the target confining pressure. Consequently, the shear stage is conducted with the specified loading path. The details for the procedures of triaxial shear and rotation shear tests are presented in Section 5.3 below.

5.3 Validation with previous simulation results

The proposed model illustrated above should be validated before being used for multi-scale investigation of granular materials under specified stress paths. The control of deformation for the boundary is checked first with the strain-controlled boundary. Tests are performed without the consideration of particles to save the computation effort.

Afterwards, the conditions for the stress-controlled and mix-controlled boundary are validated with the simulations presented below. It displays the results with the proportional and non-proportional loading paths respectively. The specified loading paths involved are fulfilled as the true triaxial shear test and the drained rotation shear test.

5.3.1 Material properties

Tests are performed with the linear Hooke contact model in accordance with the works of Yang (2014) using PFC3D for validating the tool. In such a case, the properties of particles and boundary are selected as the same as his work. Table 5.1 below summarises the properties of boundary and particles. The boundary's properties are identical with the properties of particles. Particles are generated with the same PSD over the range from $0.3mm$ to $0.5mm$. Tests are performed with the polyhedral boundary forming by $N=8$ and $R=0.01m$. According to the LIGGGHTS's features, the critical time-step is calculated

as Eq.(3.43) presented in Section 3.4.

Table 5.1 Simulation properties

density	2700 kg/m^3
radius	[0.3, 0.5] *mm*
Normal and Tangential stiffness	5e5 N/m
Restitution coefficient	0.3
Poisson ratio	0.25

5.3.2 Sample generation stage

The radius expansion method is selected to generate the isotropic sample. Following Yang's work (2014), the number of particles is determined via the target void ratio and the particle size distribution. Particles are randomly generated under the number uniform distribution with the radius reduced by 1.5 times first. The generation region is a bit different compared with his work. Limited to LIGGGHTS software, particles are generated in the circumscribed spherical region, estimated as $R/\cos(\pi/N)$, of the polyhedral boundary. Thus, some of them are out of the system and would be deleted before restoring the size of particles for preparing the sample. The generation stage continues until all the particles achieve the equilibrium condition, which is determined by the unbalance force ratio estimated as Eq.(4.5). Simulations cease when the unbalance force ratio is less than 0.01. Figure 5.1 provides an example of sample generation procedures with the radius expansion method. It presents the behaviour of the sample at a reduced radius size, sample after deleting particles out of the system and restored radius size to generate the specimen. The boundary is displayed as black triangle meshes in the graphs.

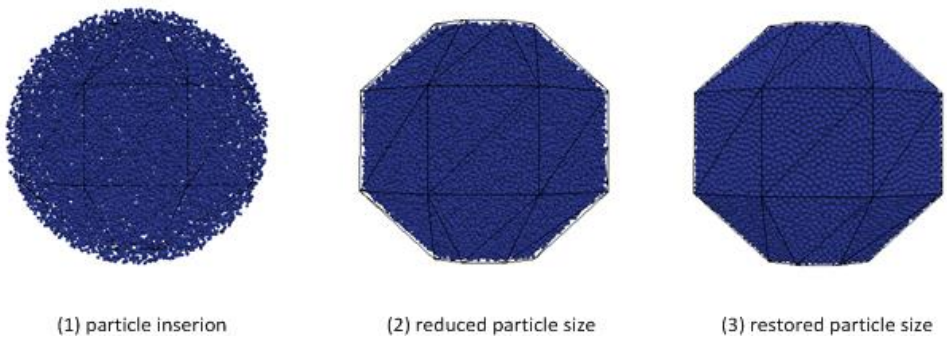


Figure 5.1 An example of the sample generation procedures

Two different void ratios of specimens are prepared with the application of various friction coefficients in the sample preparation stage. Table 5.2 below presents the information of specimens in the stages of sample preparation and consolidation. This may be related to the difference of the model for particle size distribution and the generation procedures between LIGGGHTS and PFC. Then, tests are subsequently performed with different loading paths.

Table 5.2 The information of specimens in comparison with Yang (2014)

	LIGGGHTS		**Yang (2014)**	
	dense	loose	dense	loose
Number of particles	10,835	10,221	11,090	10,151
Confining pressure after sample preparation	402kPa	490kPa	450kPa	478kPa
Void ratio after consolidation ($p = 500$kPa)	0.637	0.795	0.64	0.78

5.3.3 Drained triaxial shear test

5.3.3.1 Procedures of drained triaxial shear test

The drained triaxial shear test has been undertaken with the constant mean principal stress

p and intermediate principal stress ratio b while increasing the deviatoric stress q and deviatoric strain ε_q, displayed as Figure 5.2. Samples are firstly generated and consolidated to the confining pressure of 500kPa. Secondly, at the shear stage of this simulation, there is a mix-controlled boundary test with partially strain-controlled and partially stress-controlled.

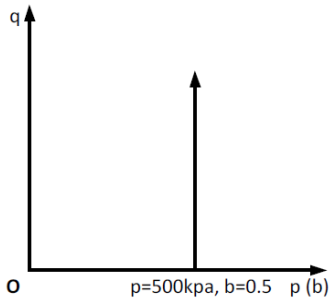


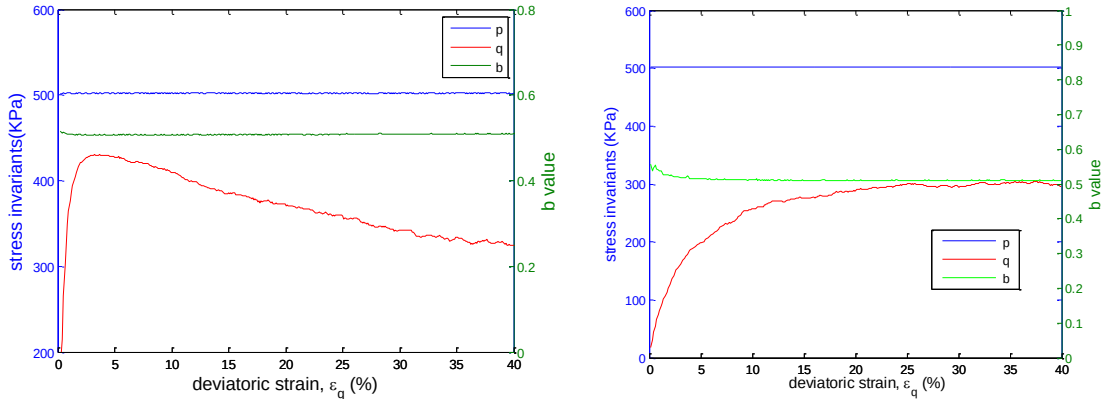
Figure 5.2 The stress path for the drained triaxial shear test

For the stress-controlled boundary, it is realised via controlling the stress invariants to determine the target stress tensor σ_{ij}^t. The stress increment tensor $\Delta\sigma_{ij}$ is achieved as the difference of the current stress tensor σ_{ij}, determined from Eq.(3.57), and σ_{ij}^t. Based on the stress increment, the corresponding strain increment $\Delta\varepsilon_{ij}$ is estimated by the Hook's Law and the strain invariants $\Delta\varepsilon_v$, $\Delta\varepsilon_q$ and Δb_ε could also be determined using Eq.(3.53). The servo-control mechanism is applied for maintaining the target stress boundary condition. If the boundary condition is not satisfied, then only the corresponding strain increment is applied to the boundary for achieving the condition. If it is satisfied, then an additional deviatoric strain increment $\Delta\varepsilon_q^{inc}$ estimated as $\Delta\varepsilon_q^{inc} = \text{sgn}\left(\varepsilon_q^t - \Delta\varepsilon_q\right) * \min\left(\varepsilon_{tol}, abs\left(\varepsilon_q^t - \varepsilon_q\right)\right)$ is applied to the boundary, in which ε_{tol} is around 1.0e^{-4} and $\Delta\varepsilon_q$ is 0.005 in this study. Subsequently, the deviatoric strain increment

is altered to be $\Delta\varepsilon_q + \Delta\varepsilon_q^{inc}$. With the modified information of $\Delta\varepsilon_v$, Δb_ε and principal strain directions, the updated $\Delta\varepsilon_{ij}$ could be obtained according to Eq.(3.49) and Eq.(3.52). Then, the deformation could be applied to the boundary through the translational and rotational velocities calculated as Eq.(3.60) and Eq.(3.61).

5.3.3.2 Results of drained triaxial shear test

The above section illustrates the procedures of the true triaxial shear test. This part elaborates the results of tests in comparison with Yang's work (2014). The stress-strain behaviour is presented in the following figures. According to the graphs, the values of p and b are effectively controlled as around 500kPa and 0.5 respectively during shearing.



(1) dense $(e = 0.637)$ (2) loose $(e = 0.795)$

Figure 5.3 The stress invariants behaviour with R=0.01m, N=8

Figure 5.4 provides the evolution of stress ratio with the increase of deviatoric strain. The behaviour is similar to Yang's work (2014). The peak stress ratio appears at the deviatoric strain of 4% with the value at around 0.84 for the dense sample. No peak value appears for the stress ratio of the loose sample. Concerning the characteristic of loose sample, the growth rate is smaller compared with Yang's (2014) due to the larger initial void ratio. In addition, the value of stress ratio is slightly lower at the ultimate stage than Yang (2014).

This may be related to the different PSD formed after the preparation of the sample depending on the different number of particles.

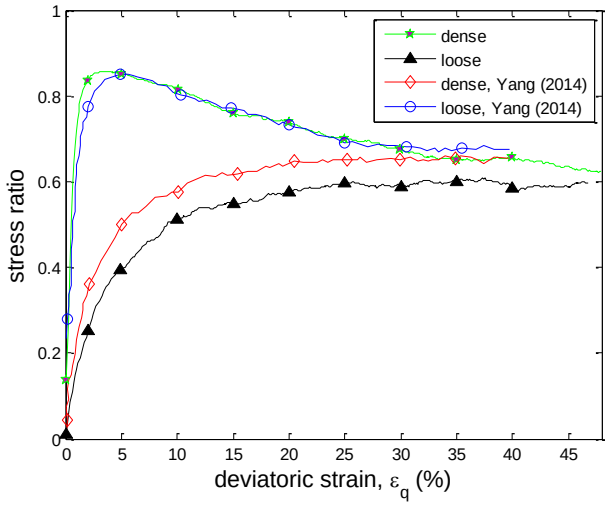


Figure 5.4 The behaviour of stress ratio

The evolution of void ratio is plotted as Figure 5.5 for the two samples. The samples achieve the similar ultimate void ratio at the end of simulation. It decreases with the increase of deviatoric strain for the loose sample; this corresponds with the work of Yang (2014). For the dense sample, the initial void ratio is similar to Yang's findings (2014) and it increases with the increase of shear strain.

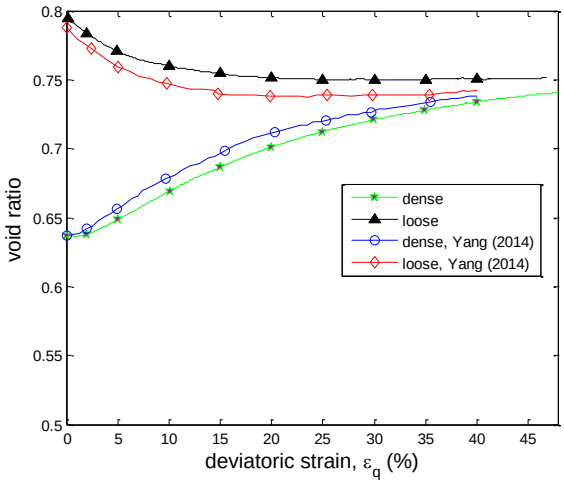


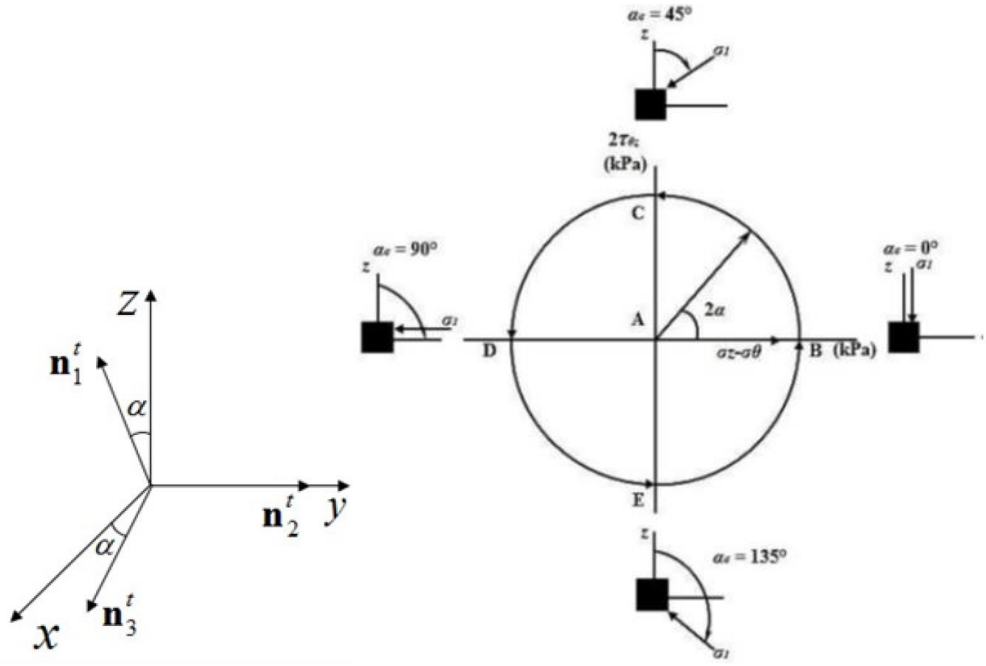
Figure 5.5 The evolution of void ratio

5.3.4 Drained rotational shear test

5.3.4.1 Procedures of drained rotational shear test

The above simulations are conducted with the proportional loading path, defined as the fixing the principal stress direction while the loading ratio of deviatoric stress components is kept constant. In this part, the non-proportional loading path is performed to further validate the developed contact model. It refers to the rotation of principal stress direction while keeping the stress invariants constant. This simulation is implemented with the stress-controlled boundary condition. It aims to mimic the pure principal stress directions rotation test for reproducing the torsional experimental test using hollow cylinder apparatus. The test is undertaken with the major principal direction rotated around the $x-z$ plane while keeping the magnitudes of stress invariants p, b, q constant. The rotated angle α, as shown in Figure 5.6(1), is the direction between the target major principal stress direction and the z-axis direction. With regards to the target intermediate principal stress direction, it keeps fixed along the y-axis during the simulation. Hence, the rotation angle is 2α for the stress path in the deviatoric plane as Figure 5.6(2). Eq.(5.1) below provides the definition of vectors of the target three principal stress directions, with the first row and the last row corresponding to the vectors of the major and minor principal stress directions respectively.

$$n_{ij}^{t} = \begin{bmatrix} \sin\alpha & 0 & \cos\alpha \\ 0 & 1 & 0 \\ \cos\alpha & 0 & -\sin\alpha \end{bmatrix} \tag{5.1}$$



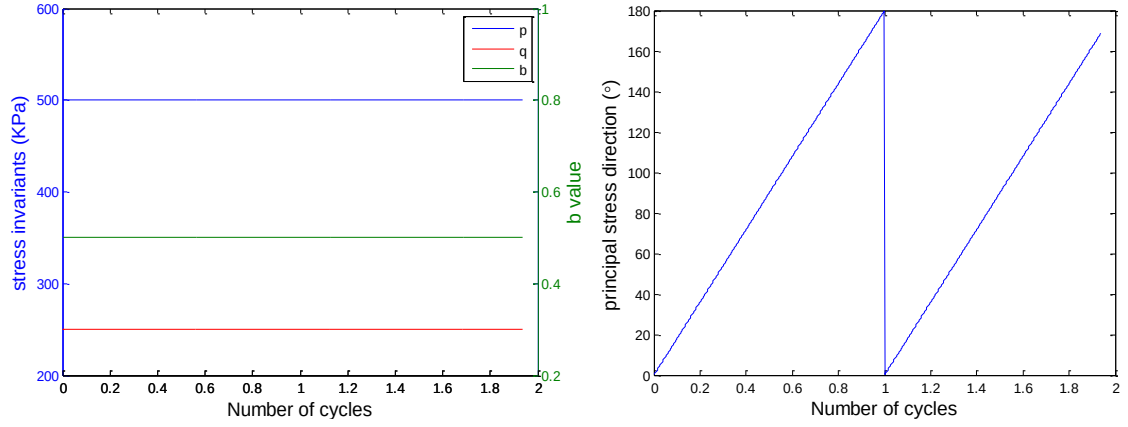
(1) Principal stress rotation (2) Stress path in the deviatoric plane

Figure 5.6 Illustration of principal stress rotation and stress path

The test starts at point D with the principal stress direction $\alpha_\vartheta = 90°$ and rotated the principal stress under the counter-clockwise direction as $D \to E \to B \to C \to D$. In order to satisfy the boundary condition and stress condition, a servo-control mechanism is employed before the rotation of the principal stress direction. The target stress tensor σ_{ij}^t is estimated according to the information of target stress invariants p, b, q. Consequently, a stress increment tensor $\Delta\sigma_{ij}$ is defined as the difference between the target stress tensor and the current stress tensor σ_{ij}. Accordingly, a strain increment tensor $\Delta\varepsilon_{ij}$ can be evaluated and applied to the sample via the specified translational and rotational deformations of the boundary. After satisfying the stress boundary condition, an increment of the principal stress direction ($\Delta\alpha$) is applied for the shear test. The increment is $3.0e-4°$, the same value as Yang (2014), in one calculation cycle. The sample is continuous rotation sheared with the repetition of this process.

5.3.4.2 Results of drained rotational shear test

The samples are monotonically pre-sheared to the target stress conditions p^t, η^t, b^t under the drained true triaxial stress path first. The properties of particles and boundary are also selected as shown in Table 5.1. The prepared isotropic samples are first consolidated to $p = 500\text{kPa}$ and then pre-sheared to $\eta = 0.5$ with $b = 0.5$. After pre-shearing, the void ratios are 0.645 and 0.734 respectively for the dense and loose samples. They differ slightly in comparison with Yang (2014), with the values being 0.64 and 0.75 respectively. The following figures present the results with the dense sample during the rotation shear. The stress invariants are kept constant during the rotation of principal stress directions plotted in Figure 5.7(1). Figure 5.7(2) provides the evolution of the principal stress direction during the rotation shear. For one rotation cycle, the principal stress direction varies from 0° to 180°.

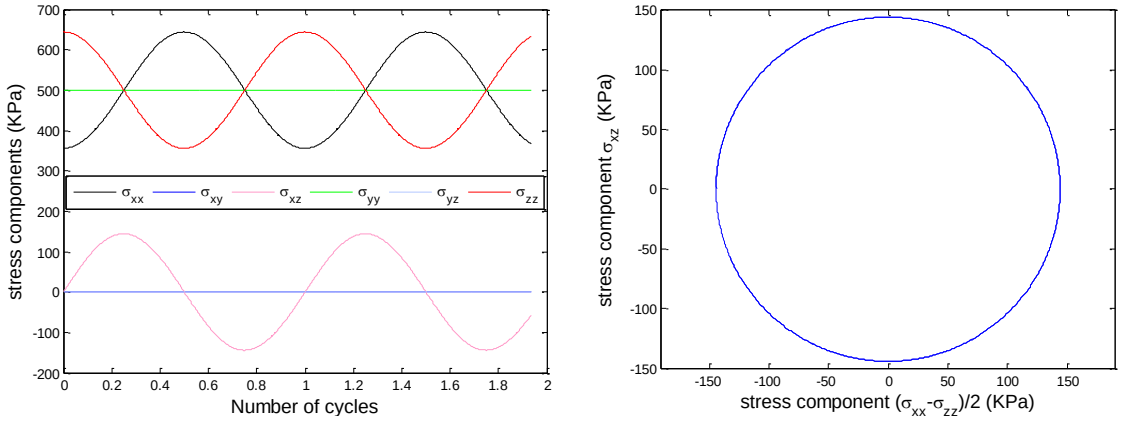


(1) stress invariants (2) principal stress direction

Figure 5.7 The evolution of stress invariants and principal stress direction

The dense sample is taken as an example to present the behaviour of the stress components in Figure 5.8. The components of σ_{xx}, σ_{xz} and σ_{zz} vary periodically during the rotation shear, while the stress components along the direction of y-axis are kept constant as $\sigma_{yy} = 500\text{kPa}$, $\sigma_{xy} = \sigma_{yz} = 0$. Hence, it demonstrates that the intermediate stress direction

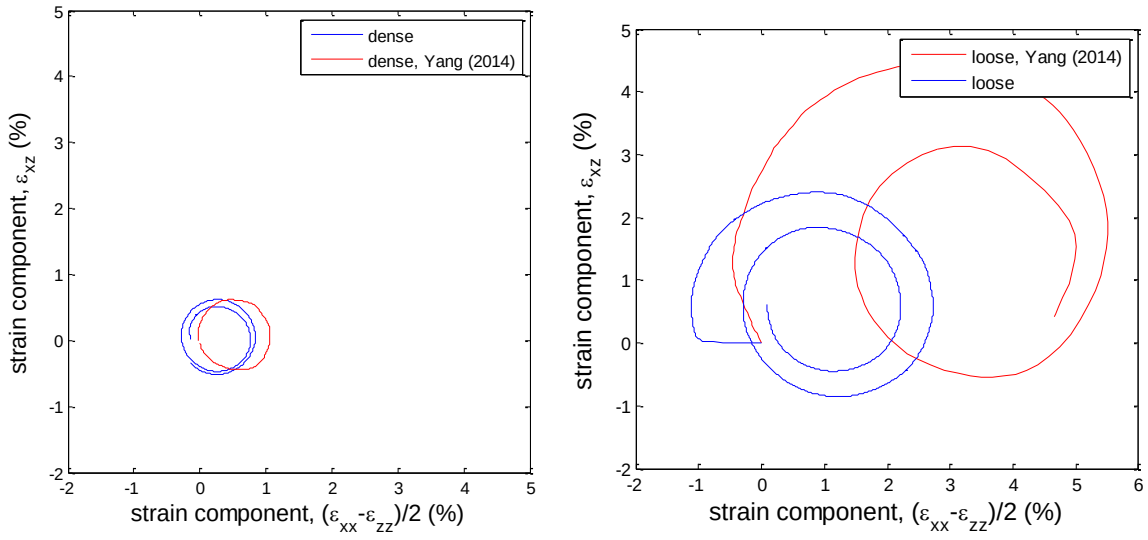
is maintained well in the target direction. The results are similar to Yang's work (2014) on the basis of the circular stress trajectory in the deviatoric plane.



(a) (b)

Figure 5.8 Stress behaviour during rotation shear: (a) stress components; (b) stress trajectory

Specimens are continuously sheared during the two cycles. The strain trajectory is presented in Figure 5.9 below with the dense and loose specimens respectively. The size of strain trajectory is larger for the loose specimen in contrast with the dense sample, which is similar to the work of Yang (2014). The strain path is first in the shape of a spiral and then tends to be the shape of the circle after a few cycles. For the smaller void ratio of the loose sample, the size of strain trajectory is smaller in comparison with Yang (2014). For the dense sample, the size is similar with respect to the similar value of void ratio. A difference is also evident for the centre of the strain trajectory for both the dense and loose sample. It may also depend on the different number of particles.



(1) dense $(e = 0.637)$ (2) loose $(e = 0.734)$

Figure 5.9 The behaviour of strain trajectory for the dense and loose samples

5.4 Observations on the sample uniformity

The polyhedral boundary is formed with the dependence of the two parameters N and R. The number of N is related to the polyhedral boundary shape. Increasing the number of N would result in the boundary nearing a spherical shape. However, the number of walls forming the polyhedral boundary would also increase, which may have an impact on the simulation time. The parameter R would determine the number of particles for the sample.

In this section, tests are undertaken with various values of N and R to observe the uniformity of the specimens for choosing the appropriate values based on the investigation of the material responses. Four different numbers of N are considered as 4, 6, 8 and 10. R is selected as $0.01m$ and $0.02m$, in the ratio R/r of 20 and 40, for the simulations respectively. To obtain different void ratio, the friction coefficients are selected differently in the sample preparation stage.

5.4.1 Material properties

In this part, the specimens are conducted with the non-linear Hertz-Mindlin contact model. The Young's modulus is 7e10Pa as the typical value of the silicon sand. A narrow particle size distribution is selected with the number uniform in the span of $[0.45, 0.55]mm$. Table 5.3 below presents the material properties applied in this section.

Table 5.3 The material properties for tests of sample uniformity

density	2700 kg/m^3
radius	[0.45, 0.55] mm
Young's modulus	7e10 Pa
Restitution coefficient	0.3
Poisson ratio	0.25

5.4.2 Sample generation stage

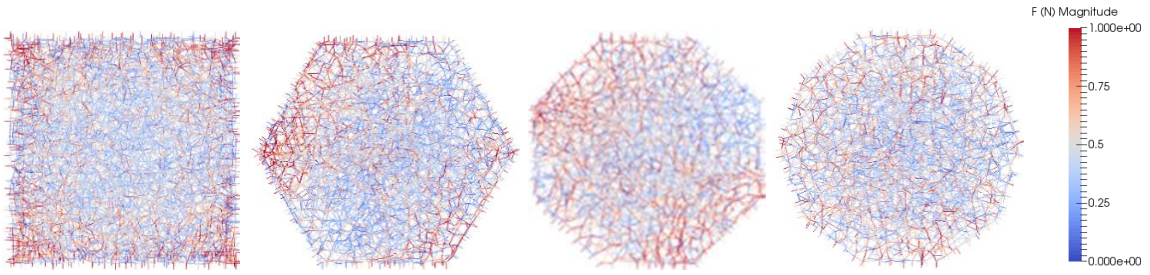
Samples are also prepared with the radius expansion method. Particles are generated with the radius of $r_t/1.5$ first, where r_t denotes the target radius size. The particles are inserted in the circumscribed spherical region first and then deleted that out of the boundary. For this series of tests, the control of sample preparation differs slightly from the test conducted by Yang (2014) in order to observe the uniformity behaviour at the consolidation stage. Hence, the confining pressure should be small after sample preparation. Thus, the radii sizes of particles are gradually restored. To control the growth rate, 1,000 steps are selected for the particles restored stage. For each step, the growth rate of the particle radius is 1.0004, estimated as $1.5^{1/1000}$. Tests are terminated as long as the confining pressure is less than $10kPa$. Tests are performed with the procedures elaborated in Section 5.3 above.

5.4.3 Consolidation stage

After samples are prepared, they are consolidated to the confining pressure of 500kPa. This is performed to observe the arch effect at the end of consolidation stage. The friction coefficient is set as 0.5 for this stage. Owing to the impact of polyhedral boundary, the void ratio varies slightly across the different samples.

5.4.3.1 R=0.01m

For $R=0.01m$, the number of particles is smaller owing to the small size of boundary. Hence, it only concerns the dense condition. The void ratio is 0.646, 0.637, 0.65 and 0.636, with 8369, 5657, 5008 and 5004 number of particles, respectively. Figure 5.10 displays the force chains with $R=0.01m$ at the end of the consolidation stage, with a section in the centre of the sample. The central coordinate of this section is $(0,0,0)$ with the thickness of $5mm$ in the y-axis direction. Limited to the ParaView software, it could only present the force chains with the magnitude of contact force. The average contact force is $0.52N$, $0.506N$, $0.532N$ and $0.48N$ respectively. For the four samples, they all contain the arches near the corner of the neighbour walls, depending on the larger contact force.



(1) N=4 (2) N=6 (3) N=8 (4) N=10

Figure 5.10 The force chains for sample with a section of 5mm in y direction under R=0.01m

5.4.3.2 R=0.02m

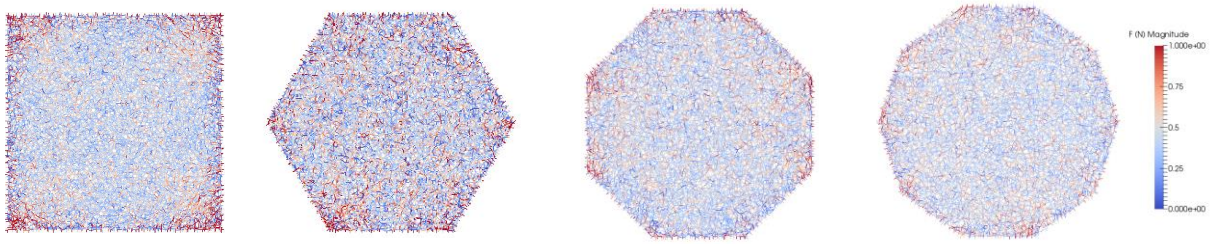
$R = 0.02m$ concerns the impact of various void ratios on the uniformity behaviour at the consolidation stage. The information of samples is provided in Table 5.4 below at the end of this stage. According to Eq.(2.21), to achieve the same confining pressure, the dense sample should contain a larger average coordination number with a smaller directional average contact force, in comparison with the loose sample. For samples with the dense and medium density, the void ratio is similar with various shapes of boundary. Regarding the loose sample, the void ratio increases with the increase of N value.

Table 5.4 The information of samples with different boundaries

Boundary		Number of particles	Void ratio	Average contact force (Unit: N)	Average coordination number
N=4	Dense	74,096	0.61	0.49	5.5733
	Medium	72,395	0.647	0.558	4.8893
	Loose	69,445	0.717	0.688	4.0179
N=6	Dense	51,229	0.618	0.525	4.9446
	Medium	49,997	0.651	0.529	5.0080
	Loose	47,203	0.729	0.69	4.0230
N=8	Dense	45,779	0.61	0.455	5.6918
	Medium	44,712	0.652	0.53	4.9774
	Loose	41,971	0.737	0.698	4.003
	Dense	43,605	0.611	0.45	5.7488

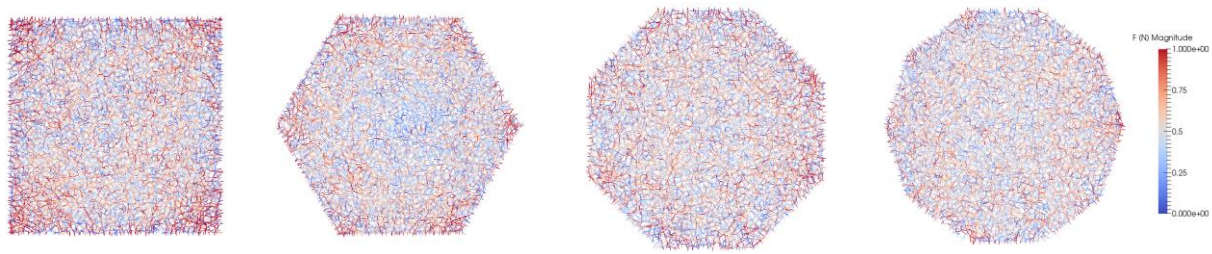
N=10	Medium	42,583	0.654	0.514	5.1516
	Loose	39,954	0.747	0.707	3.9692

The force chains network is also studied to observe the arch effect near the neighbour walls. The graphs are also presented with a thickness of $5mm$ section in the centre of the boundary under the dense, medium and loose conditions respectively. Table 5.4 above provides the information of average contact force for the samples. The contact force is decreased with the increase of N value for the dense and medium samples, except for $N=6$. A peak value appears for $N=6$ under the dense condition. For the loose sample, the average contact force is increased with the increase of N value. The impact of arch effect would be reduced with the increase of void ratio in accordance with the graphs. Additionally, the arch effect is much more obvious for the specimen prepared with $N=4$.



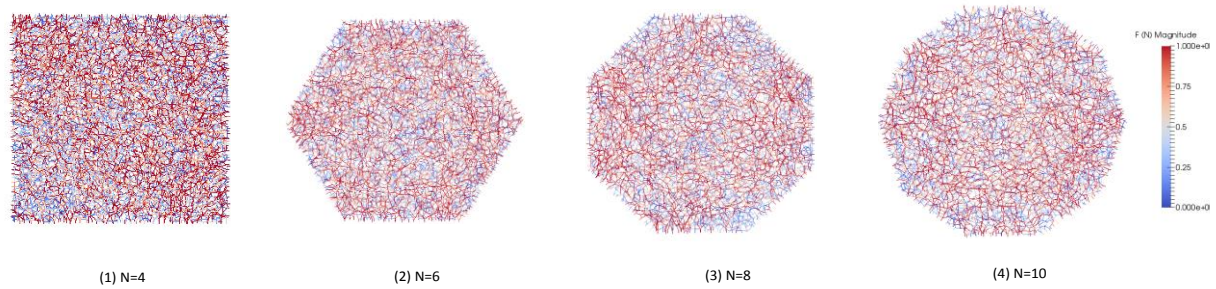
(1) N=4 (2) N=6 (3) N=8 (4) N=10

(a) dense samples



(1) N=4 (2) N=6 (3) N=8 (4) N=10

(b) medium samples



(1) N=4 (2) N=6 (3) N=8 (4) N=10

(c) loose samples

Figure 5.11 The force chains behaviour at the end of consolidation stage

In order to further identify the arch effects, taken the dense sample as an example, the stress state is discussed with the evolution of the radius distance for $R = 0.02m$. The central coordinate of the particle is employed to determine the location for the calculation of the stress tensor. The initial radius distance is selected as $5mm$, around five average particle sizes. The stress state is studied over the range from $5mm$ to $17.5mm$ with the interval radius distance of $2.5mm$. It concerns the confining pressure inside the annulus region between the interval radius distances using in Eq.(4.10). For the intermediate region, the volume is calculated as the difference value of the two spherical regions. With respect to the region near the boundary, the volume refers to the difference value between the sample volume and the inside spherical volume.

In Figure 5.12, R_d denotes the radius distances and r^- refers to the average particle radius size. According to the figure, the confining pressure becomes more similar and nearer to the value of the confining pressure estimated from the boundary with the increase of the N value. Significant difference is observed for the region near the edge of the boundary. For $N = 4$, due to the largest value of confining pressure in this region, it implied that the sample consists of larger arch effects. In addition, the confining pressure is reduced with the increase of N value near the edge of the boundary. It also suggested that the

sample is more uniform for $N=10$, due to the similar confining pressure by contrast with other specimens.

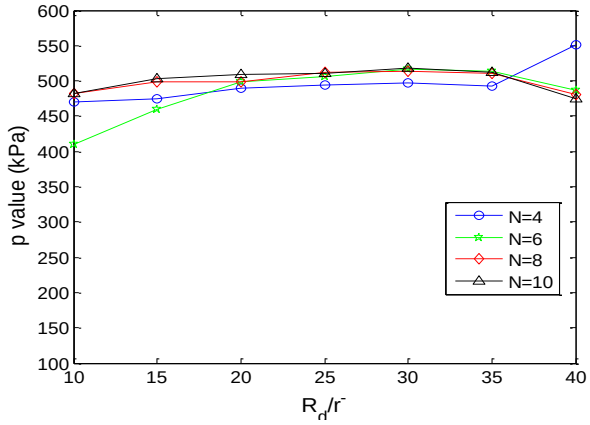


Figure 5.12 The behaviour of confining pressure within different radial distances

The stress tensor, elaborated in Eq.(4.10), is also applied to obtain the local stress state of each particle with the dense samples. The volume of each particle is estimated with the aid of the void ratio of the specimen at the end of the consolidation stage. The probability distribution of confining pressure is studied to further observe the sample uniformity. The start point and the interval point are both taken as 10kPa to estimate the probability in the span. Figure 5.13 below presents the distribution with various shapes of boundary. According to the graph, the peak value appears over the range from 400kPa to 500kPa for each specimen. The behaviour is similar for $N=8$ and $N=10$, with a larger value in the span of $[450,500]$kPa, compared with $N=4$ and $N=6$. Regarding $N=6$, it contains a higher probability for the confining pressure less than 180kPa. It shows that the uniformity condition is better for $N=8$ and $N=10$.

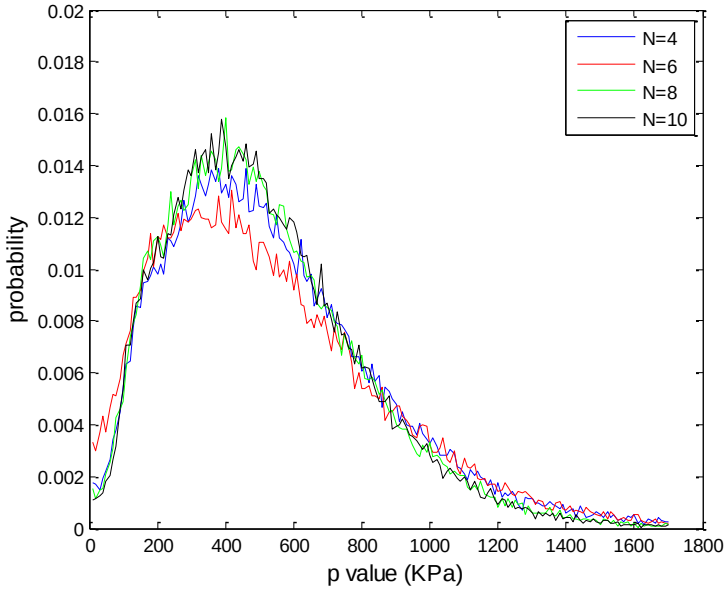


Figure 5.13 The probability distribution of p value with various shapes of boundary

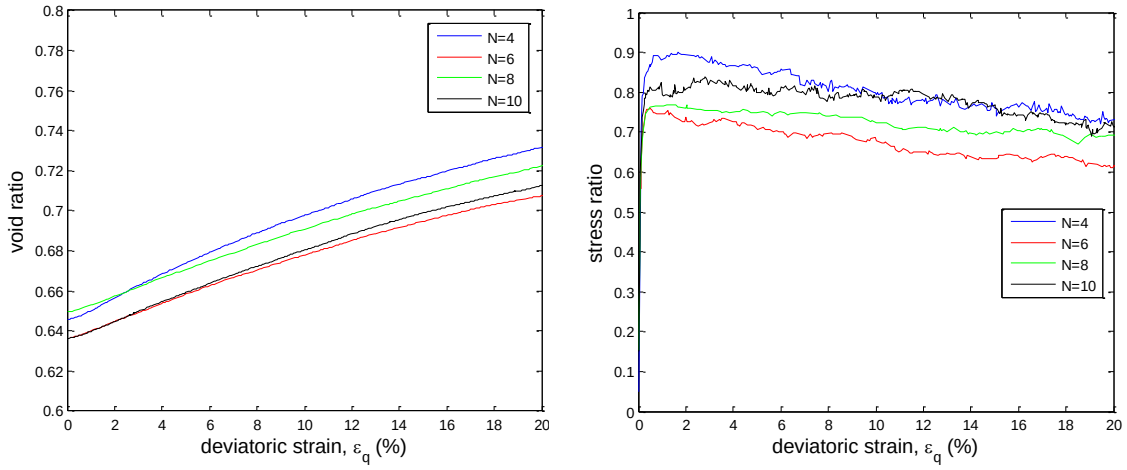
5.4.4 Drained triaxial shear tests

Based on the above results, the arch effects is more obvious with dense samples. This section takes the dense sample as an example to observe the uniformity behaviour with various sizes and shapes. Tests are performed with the confining pressure and intermediate principal stress ratio maintained constant with the value of 500kPa and 0.5 in the shearing stage. The friction coefficient is also set as 0.5 in this stage.

5.4.4.1 R=0.01m

Figure 5.14 shows the stress-strain responses and the behaviour of void ratio for the whole specimen with various boundaries at $R = 0.01m$. The void ratio continuously increases with the increase of the deviatoric strain. Regarding the stress ratio, it reaches the peak value immediately for each sample and reduces with the evolution of shear strain. However, it observes a larger difference for the value of void ratio and stress ratio at the peak stage and the final stage respectively. Compared with the specimens of $N = 6$ and $N = 10$, under the

similar initial void ratio, the peak stress ratio, the void ratio and the stress ratio at the final stage are much larger for the test with $N=10$.

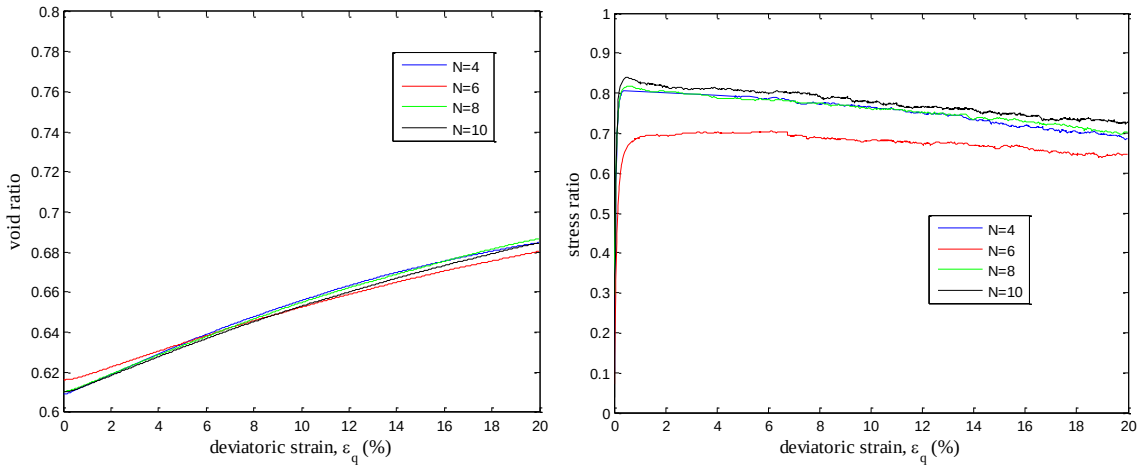


(1) void ratio (2) stress ratio

Figure 5.14 The evolution of void ratio and stress ratio with various boundaries at R=0.01m

5.4.4.2 Results of R=0.02m

For this size of polyhedral boundary, the behaviour of stress ratio and void ratio is presented in Figure 5.15 with different shapes. The evolution of the void ratio is similar in the shearing stage. It is increased slowly with the larger sample size. The stress-strain response is also similar, except for the specimen prepared with $N=6$. This may be related to the higher void ratio in comparison with the other specimens. With the evolution of the shear strain, the stress ratio approaches the similar value at the final stage under various shapes of the polyhedral boundary.



(1) void ratio (2) stress ratio

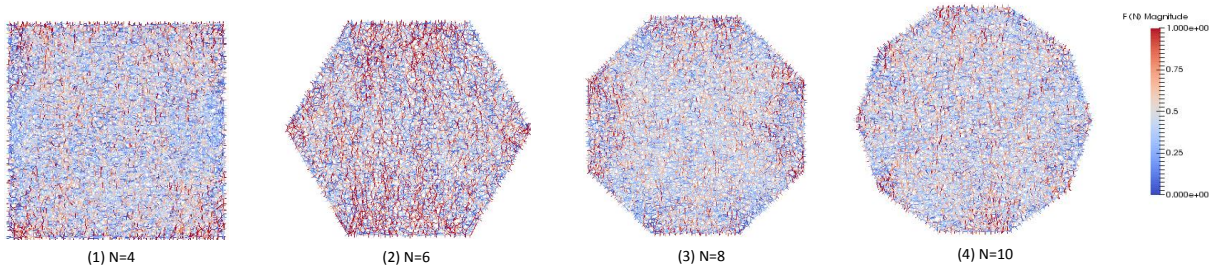
Figure 5.15 The evolution of stress-strain responses with R=0.02m for dense samples

The above drained triaxial shear tests demonstrate that samples with $R = 0.02m$ containing more uniform condition in comparison with the samples prepared by $R = 0.01m$. The force chains are presented for $R = 0.02m$ to further display the sample behaviour inside with a section in the centre of the specimens. The central coordinates of the sections are $(0,0,0)$ with the thickness of $5mm$ in the y direction. It observes the features at the deviatoric strains of 0.01%, 10% and 20% respectively with various shapes of the polyhedral boundary. Table 5.5 below gives the information of average contact force at different shear strains.

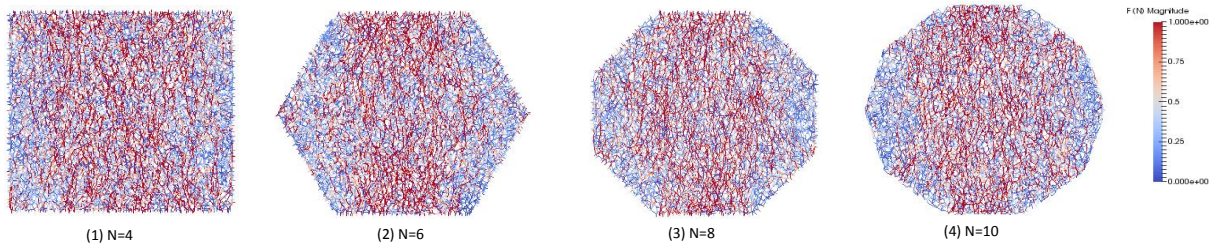
Table 5.5 The information of average contact force at different shear strains

	0.01%	**10%**	**20%**
N=4	0.49N	0.689N	0.702N
N=6	0.488N	0.676N	0.689N
N=8	0.48N	0.676N	0.695N
N=10	0.475N	0.674N	0.696N

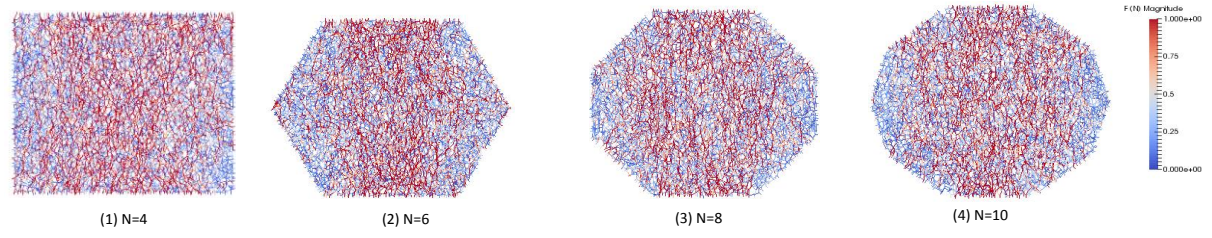
With the increase of shear strain, the average contact force is increased for samples under various N values respectively. At each shear strain, the table shows samples containing a similar average contact force, in particular for $N=8$ and $N=10$. At the initial stage, samples are under the isotropic condition. According to the graphs, the isotropic condition increases with the increase of the N value. During the shearing stage, a larger percentage of strong force chains appear in the centre of the specimens. Additionally, a sample with a larger number of N contains a greater percentage of the strong force chains.



(a) 0.01%



(b) 10%



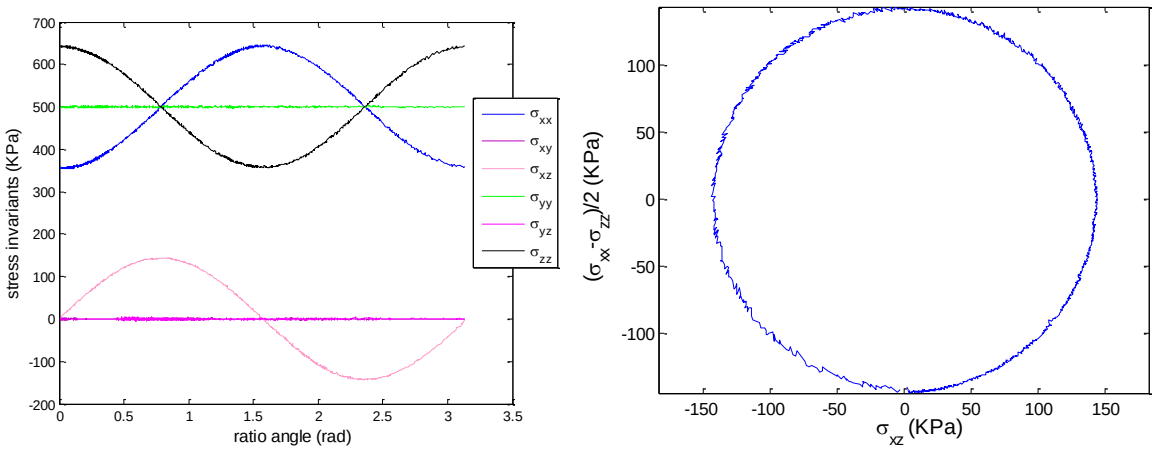
(c) 20%

Figure 5.16 The force chains behaviour at different stages for the dense samples

Concerning the simulation time, it requires around three weeks for the triaxial shear test with $R = 0.02m$. The sample contains a reasonable number of particles and the simulation time is also appropriate under this condition. Hence, the tests are preferred to conduct with $R = 0.02m$. Furthermore, it shows that the results of $N = 6$ are not that well compared with other boundaries. It is better to select the boundary formed with $N = 8$.

5.4.5 Drained rotation shear tests

The results show that samples with $R = 0.02m$ are more uniform based on the evolution of stress ratio under the monotonic loading. To further select the value of N, the drained rotation shear tests are performed with the target stress invariants of $p = 500\text{kPa}$, $\eta = 0.5$ and $b = 0.5$. The dense samples prepared above are employed in this section owing to the more arch effect and first pre-sheared with the triaxial shear test. During the triaxial shear stage, the intermediate principal stress ratio is selected as 0.5. Tests are conducted until reaching the target stress ratio $\eta = 0.5$. The procedures are the same as that elaborated in Section 5.3.4 above. Taking the test with $N = 10$ as an example, the following presents the results of the stress state. The test is performed with the rotation of one cycle. The stress σ_{yy} is kept constant at the value of 500kPa during the rotation. The other stress components as σ_{xz}, σ_{xx} and σ_{zz} are varied periodically, while σ_{xy} and σ_{yz} are maintained around zero with the rotation of principal stress direction. The stress trajectory presents that the stress path behaved as a circle in the deviatoric plane.



(1) stress invariants (2) stress trajectory

Figure 5.17 The behaviour of stress invariants during the rotation of principal stress directions

The force chains network is also presented with the specimen at different rotation angles under the non-proportional loading path. At the initial stage, the specimen is under a relative uniform condition. The strong force chains are uniformly distributed inside the specimens. For $N=4$, it could still observe an obvious arch effect near the corners of the boundary. During the rotation stage, the stronger force chains are increased inside the samples. Additionally, with the rotation of the principal stress directions, the stronger force chains are also rotated inside the specimen. For the test with $N=4$, the arching effect is more obvious, owing to the stronger force chains mainly appearing near the corner of the two neighbouring walls. Considering tests with $N=8$ and $N=10$, the stronger force chains are more uniformly distributed inside the specimen, reducing the arch effect near the neighbour walls during rotation.

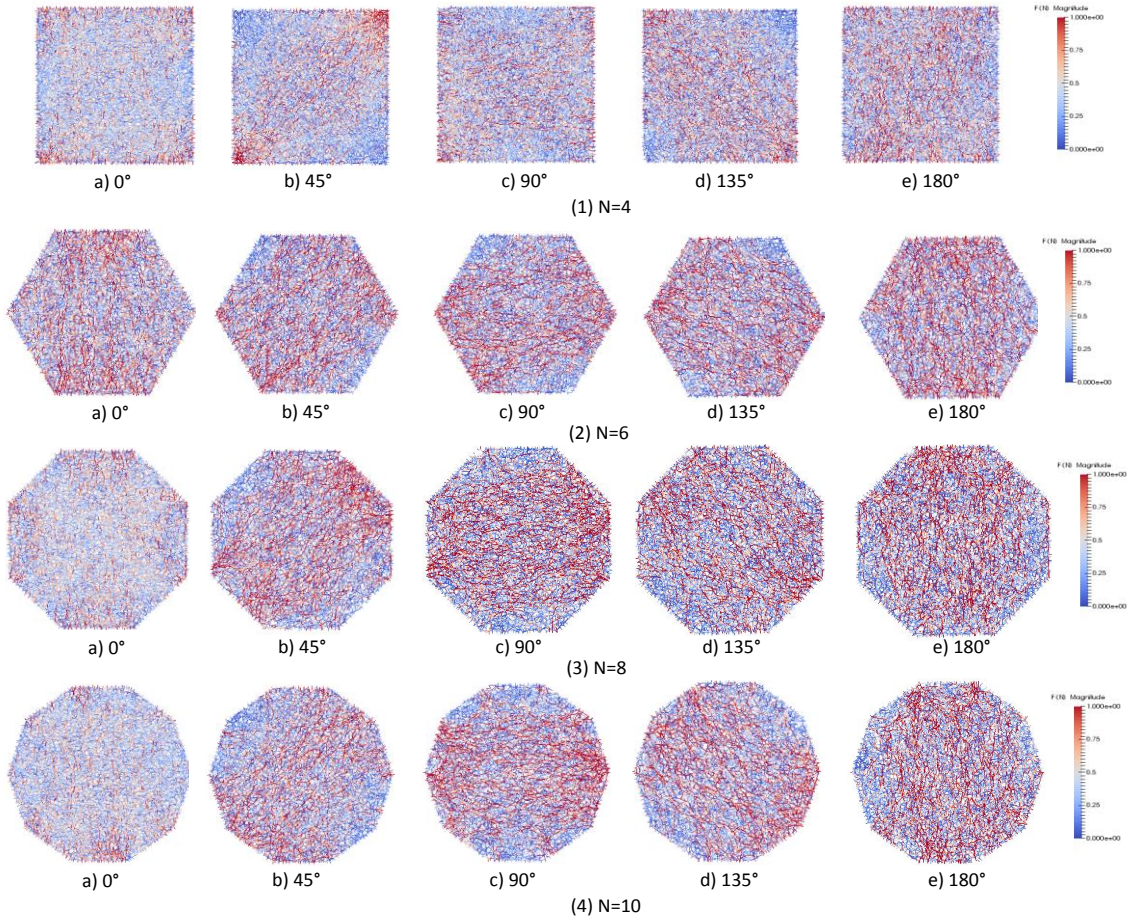


Figure 5.18 The force chains behaviour at different rotation angles with various shapes

The proportional and non-proportional loading paths are discussed above to study the uniformity of the boundary. Concerning the size of the boundary, samples are more uniform with the increase of R. With the consideration of uniformity behaviour, it selects $R = 0.02m$ to perform the elementary test. Tests present that the uniformity of the sample increases with the increase of N value for both the proportional and non-proportional loading paths. The results are similar for the samples with $N = 8$ and $N = 10$. Table 5.6 below presents the CPU time for the simulations under various sizes and shapes of the polyhedral boundary. Concerning the computation effort, for $N = 10$, it requires less simulation time with respect to the more symmetrical stress tensor estimated from the boundary and the relatively smaller number of particles. Hence, the polyhedral boundary is

selected with $R = 0.02m$ and $N = 10$ to perform the elementary test in the following chapter.

Table 5.6 The CPU time for the tests with various sizes and shapes of the polyhedral boundary

	N=4	**N=6**	**N=8**	**N=10**
R=0.01m triaxial shear	3 days	2.5 days	2.1 days	2 days
R=0.02m triaxial shear (20% shear strain)	19.2 days	18.5 days	18.3 days	18 days
R=0.02m rotation shear stage (one cycle)	9 days	8 days	7 days	7 days

5.5 Summary

This chapter illustrates the details for implementing the model of the representative volume elementary test into LIGGGHTS under various loading paths. The numerical model is developed based on the algorithm of Li et al. (2013; 2016) with the polyhedral boundary. The procedures for the drained triaxial shear test and rotation shear test are taken as an example and elaborated in this chapter. To validate the numerical model, tests are performed in accordance with Yang (2014), employing the same contact model and properties for the boundary and particles. The material responses are studied with the true triaxial shear and drained rotation shear tests respectively. Based on the results, a similar phenomenon is observed in comparison with Yang (2014) at different shear strains and rotation angles respectively.

For Yang's tests (2014), the number of particles was relatively small. In order to better present the elementary behaviour, the uniformity behaviour of the specimens and the simulation time are studied to select appropriate values of N and R under the

proportional and non-proportional loading paths. The force chains network is further studied to observe the arch effect with different shapes of the polyhedral boundary. At the end of the consolidation stage, the arch effect is significantly observed for the samples under a smaller size of the polyhedral boundary with various N values. Increasing the size of the polyhedral boundary, it shows the arch effect is reduced. In addition, the arch effect is also decreased with the increase of N value. The local stress behaviour shows that more symmetrical stress tensor is obtained with $N=10$. In addition, the arch effect is also not that obvious with a larger void ratio at the end of the consolidation stage.

For the triaxial shear stage, the stress-strain responses show that samples are more uniform with $R=0.02m$, in comparison with $R=0.01m$. The force chains network shows that the arch effect is more obvious at the initial stage. With the increase of shear strain, it reduces the arch effects for each specimen.

The rotational shear test is undertaken to further determine the value of N. At the beginning of the test, the specimens contain a lower number of strong force chains. During the rotational stage, the number of stronger force chains is increased for all the specimens. Additionally, the stronger force chains are also rotated with the rotation of the principal stress directions. The arch effect is more obvious with $N=4$, due to the stronger force chains occurring near the corner of the neighbour walls at different rotation angles. However, increasing the N value, the stronger force chains are more uniformly distributed inside the specimen during the continuous rotation of principal stress directions.

Combined with the results at different loading stages, samples with $N=8$ and $N=10$ are under a more uniform condition. Concerning the simulation time, it is better to select the boundary with $N=10$ with respect to the relatively small number of particles and more uniform stress tensor obtained from the boundary.

Chapter 6 Constitutive behaviour of granular materials

6.1 Introduction

Chapter 5 describes the development and validation for the implementation of numerical algorithm under general loading paths in LIGGGHTS. In this chapter, the monotonic and rotation shear loading paths are performed to investigate the material behaviour and the micro-scale mechanisms. The results will inform the study of the pressure dip phenomena of sand pile, so the material properties, including the particle size distribution, the contact model and the model parameters, are set the same as those used in the sand pile formation in Chapter 4. In a brief summary, the representative elements are polyhedron described in Chapter 5 with $N = 10$ and $R = 0.02m$. Tests are performed with the Hertz-Mindlin contact model. For mimicking the real properties in natural, Young's modulus is selected as 70GPa, the value for the silicon. The PSD is uniformly distributed with size over the range of $[1.2 \pm 0.4]mm$. The restitution coefficient is set as 0.3. The unbalance force ratio is applied to control the equilibrium condition, defined as the ratio less than 0.01.

As reviewed in Chapter 2, the granular material behaviour depends on the void ratio, the confining pressure and the loading paths (Oda et al., 1978, Sitharam et al., 2002; Yang and Li, 2007). The triaxial shear test is one common method used to investigate the granular material behaviour under the monotonic loading path. It is employed to observe the impact of void ratio and intermediate principal stress ratio on the strength of granular materials. With regards to the process of structure construction, the directions of principal stresses are

non-proportional. Thus, the rotation shear test is investigated with the impact of loading paths. To better understand the granular materials behaviour, the impact of stress ratio is studied with the stress rotation.

Furthermore, the deposition method can produce a different initial structure during packing. The impact of initial state is also investigated in this chapter to observe the material behaviour with the proportional and non-proportional loading paths respectively.

Section 6.2 and Section 6.3 below presents the macro-scale material behaviour and the particle-scale mechanisms respectively under the proportional and non-proportional loading paths for samples prepared with the radius expansion method. The impact of initial structure is displayed in Section 6.4, involving the macro-scale and micro-scale material behaviour. Finally, it gives a summary of this chapter.

6.2 Macro-scale observations

The isotropic samples are prepared with the radius expansion method. Particles are first generated in the circumscribed spherical region with the particle size distribution reduced by $1/1.5$. Then, it deletes the particles out of the polyhedral boundary and restores the sizes of particles to the real-scale values. Afterwards, the tests are cycled until to the confining pressure less than 5kPa.

The friction coefficients are modified to obtain the samples with different void ratios. The dense, medium and loose samples are prepared with the friction coefficients equalling to 0, 0.1 and 0.5 respectively. After samples prepared, they are isotropically consolidated to the confining pressure of 500kPa with $b = 0$. Three different samples are prepared with the number of 31,612, 30,491 and 28,770 particles, corresponded to the void ratio of 0.592,

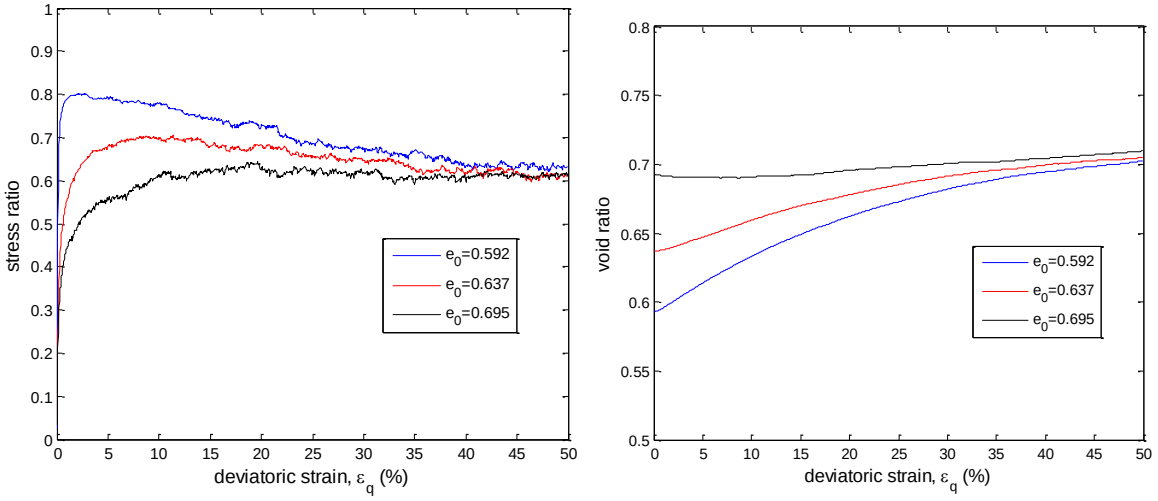
0.637 and 0.695 respectively at the end of consolidation. The friction coefficient is set as 0.5 at the consolidation stage, triaxial shear stage and rotation shear stage.

6.2.1 Impact of void ratio

The impact of void ratio is studied with isotropic samples under the true triaxial shear test. Tests are performed with the $p = 500\text{kPa}$ and $b = 0.5$ while the deviatoric shear strain is increased. The details of the test procedures are the same as that illustrated in Section 5.3.

Figure 6.1 below shows the evolution of stress ratio and void ratio during shearing respectively. For $e_0 = 0.592$, the sample dilates as a result of increasing the shear strain. It achieves the peak stress ratio at the shear strain of 2% first and then decreases with the increase in shear strain. The void ratio continuously increases during simulation. Compared with the dense sample, performed in Chapter 5 with the PSD of $[0.45, 0.55]mm$, the stress ratios at the peak state and critical state are lower with this wider particle size distribution.

A peak stress ratio, with a smaller value in comparison with $e_0 = 0.592$, is observed quickly and followed by a slight decrease for specimen with $e_0 = 0.637$. In addition, the void ratio also increases with the evolution of the shear strain. Regarding the sample with $e_0 = 0.695$, the stress ratio increases with a moderate growth rate to reach the peak value and then remains constant during shearing. The void ratio changes slightly during the simulation for this specimen. The critical stress ratio and critical void ratio are approximately 0.62 and 0.71 respectively according to the critical state definition in soil mechanics. According to the sand pile test, the average void ratio is around 0.675 at the final stage. It is slightly smaller compared with the result of $e_0 = 0.695$ at the ultimate stage.



(1) stress ratio (2) void ratio

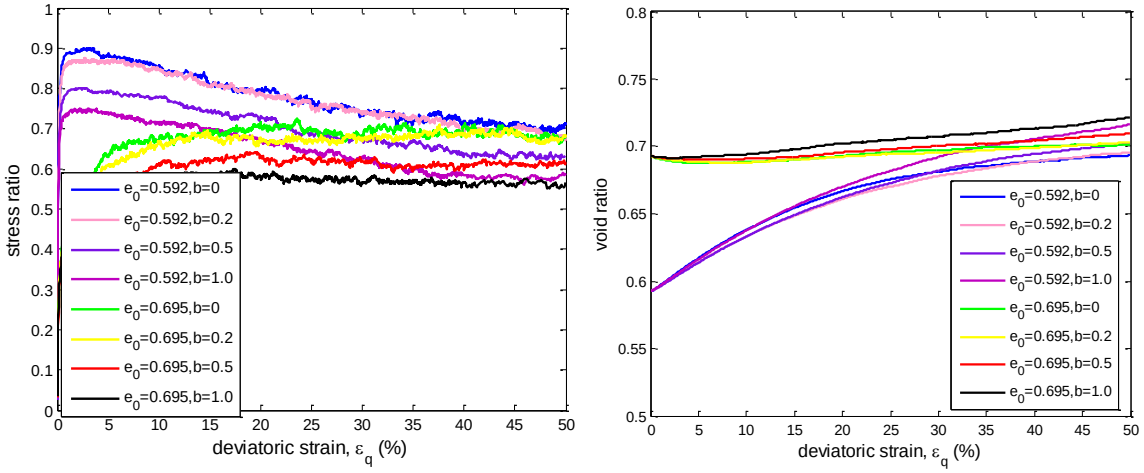
Figure 6.1 The characteristics of stress ratio and void ratio with the evolution of shear strain

6.2.2 Impact of the intermediate principal stress ratio

In Chapter 4, the sand pile shows that the average intermediate principal stress ratio is around 0.2 at the final stage. The material responses are investigated in this section with $b = 0.2$ for samples prepared above with the void ratio of 0.592 and 0.695. The triaxial compression and extension tests are also performed with $b = 0$ and $b = 1$ respectively to study the impact of b value. Samples are sheared with the confining pressure of 500kPa.

The characteristics of stress ratio and void ratio are presented in the following graphs. The sample with $e_0 = 0.592$ achieves the peak stress ratio quickly and continuously reduces during the simulation at each b value. For the series tests of $e_0 = 0.695$, the stress ratio increases with a lower rate to the peak value and then maintains constant. With regards to the behaviour of void ratio, it increases continuously with $e_0 = 0.592$. However, the void ratio changes slightly at each b value for $e_0 = 0.695$. For each sample, a larger critical void ratio is obtained for specimens with a larger b value. However, for the behaviour of stress

ratio, samples produce larger peak values and critical values with the lower b value. Under various initial void ratios, samples achieve the similar critical state at the same b value.



(1) stress ratio (2) void ratio

Figure 6.2 The evolution of stress ratio and void ratio with various b values

To reduce the fluctuation of the results, the critical stress ratio is estimated as the average value in the last 5% results. Figure 6.3 shows that the sample contains a larger critical stress ratio at each b value with $e_0 = 0.592$. The critical stress ratio decreases with the increase of b value.

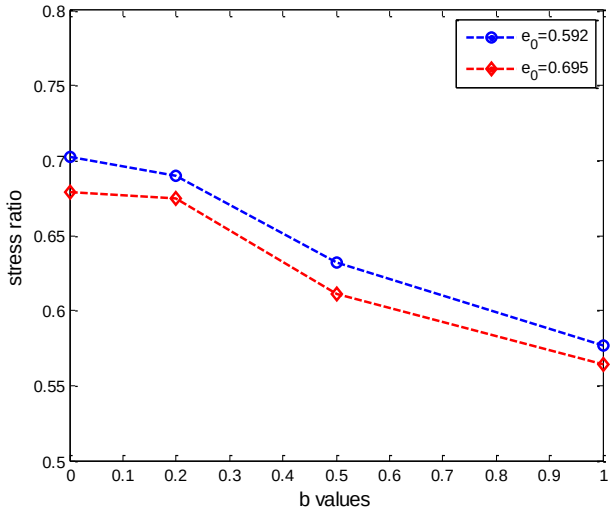


Figure 6.3 The critical stress ratio with various b values

The friction angle, defined as $\phi = \mathbf{arcsin}\left(\left(\sigma_1 - \sigma_3\right) \Big/ \left(\sigma_1 + \sigma_3\right) \right)$, could present the mobilised shear strength (Wood, 1991). The following graph displays the critical friction angle for samples with $e_0 = 0.592$ and $e_0 = 0.695$ under different b values. It is estimated at the shear strain of 50%. The results at $b = 0.5$ are similar to the average repose angle, approximately $21°$ of the three sand pile formation methods. This may be related to the similar void ratio achieved at the critical stage for $b = 0.5$ compared with the results of sand pile tests.

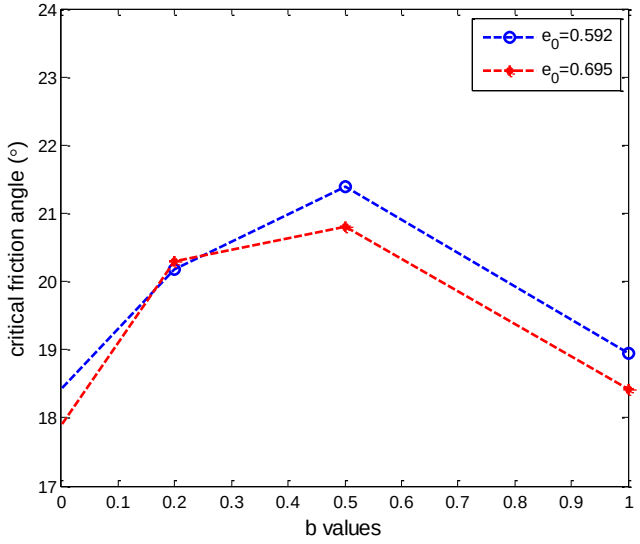


Figure 6.4 The behaviour of critical friction angle with various b values

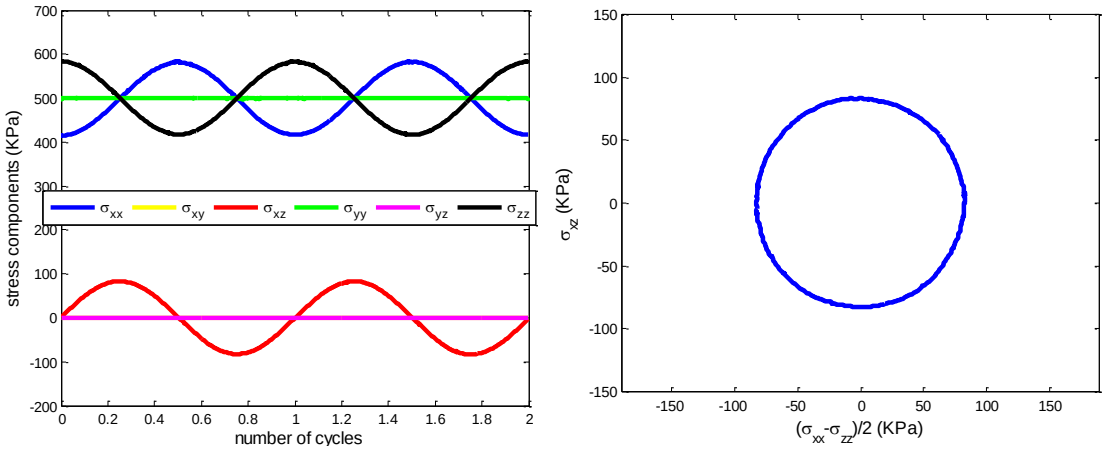
6.2.3 Drained rotation shear

The aforementioned tests discuss the material behaviour with the fixed principal stress directions. This section studies the material responses with the continuous rotation of the principal stress directions in the $x-z$ plane while under the constant magnitudes of the stress invariants p, q and b. The tests are performed to mimic the experimental hollow

cylinder test. Section 5.3 above provides details of the procedures, the tolerance parameters and the rotation rate.

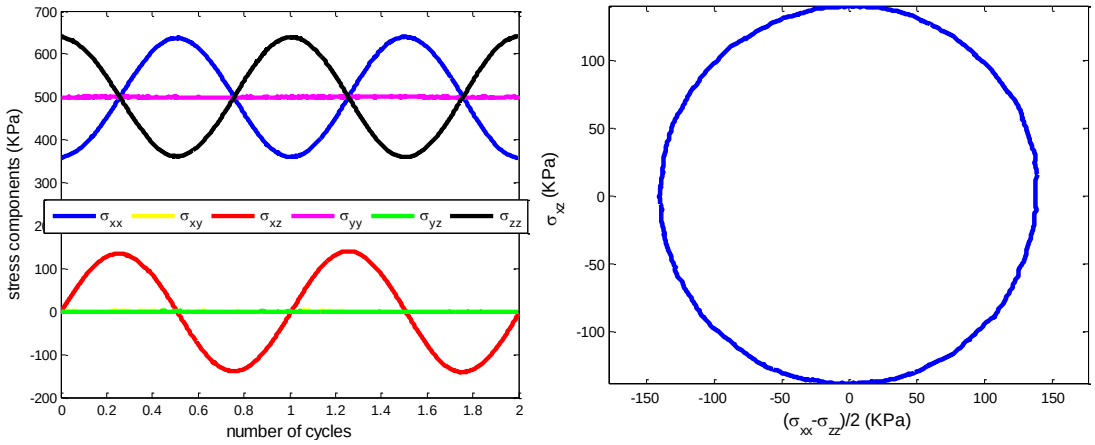
A sample with $e_0 = 0.695$ is considered due to the similar void ratio achieved in comparison with the results of sand piles at the final stage. Two stress ratios, 0.3 and 0.5, are studied on the deformation behaviour of granular materials with this loading path. The sample is first pre-sheared with the triaxial shear test under $b = 0.5$, with respect to the similar critical void ratio and critical friction angle compared with the sand pile tests. The rotation shear test is performed with $p = 500\text{kPa}$ and $b = 0.5$.

Tests are rotated with two cycles under different stress ratios respectively. The evolution of stress components is studied first during rotation presented as Figure 6.5. The stress components, σ_{xx}, σ_{xz} and σ_{zz}, are vibrated periodically with the rotation of the principal stress directions. The stress located in the y direction are maintained constantly at 500kPa during the simulation. The stress trajectory behaves as a circle in the deviatoric plane. Increasing the value of stress ratio, the size of stress trajectory is also increased.



(1) stress components (2) stress trajectory

(a) $\eta = 0.3$

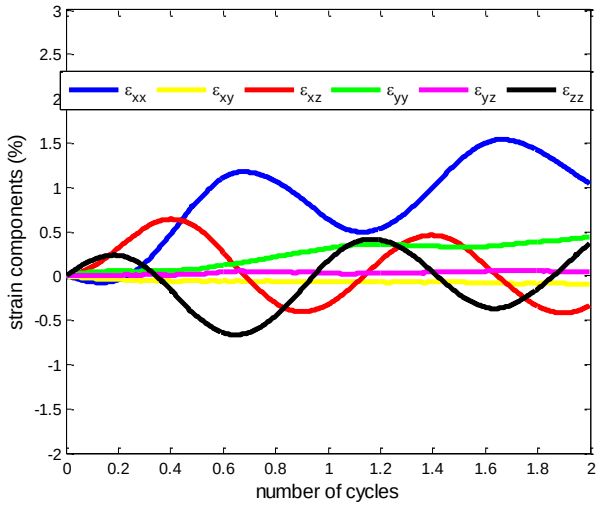


(1) stress components (2) stress trajectory

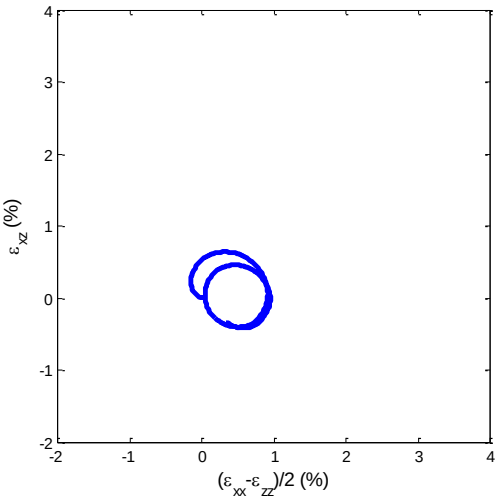
(b) $\eta = 0.5$

Figure 6.5 The evolution of stress behaviour with different stress ratios

The strain responses are also rotated in the $X-Z$ plane with significant plastic deformation. In the figures, the positive values refer to the compaction and the negative value indicates extension in the direction of the specimen. The strain components, ε_{xx}, ε_{xz} and ε_{zz}, are continually varied during the rotation of principal stress directions. ε_{yy} is increased during the simulation while the other two components ε_{xy} and ε_{yz} are maintained at nearly zero. The graphs indicated that when increasing the stress ratio, the deformation of the specimen is also increased. With $e_0 = 0.695$, the sample produces a larger size of the strain trajectory at the first cycle. The size of strain trajectory then becomes similar for each stress ratio during rotation. For $\eta = 0.3$, the strain trajectory is smaller than the result with $\eta = 0.5$.

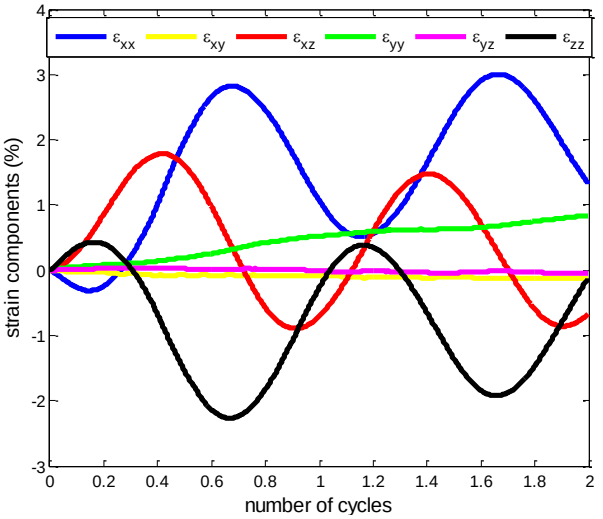


(1) strain components

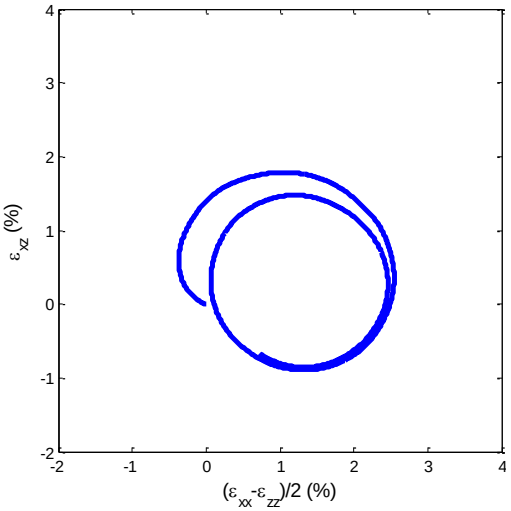


(2) strain trajectory

(a) $\eta = 0.3$



(1) strain components



(2) strain trajectory

(b) $\eta = 0.5$

Figure 6.6 The evolution of strain behaviour with different void ratios

Li et al. (2016) quantified the amount of strain increment per unit amount of stress rotation employing the proposed normalised strain increment defined as $\Delta\varepsilon_{ij}^{R} = \lim_{\Delta\alpha\to 0}\left(\Delta\varepsilon_{ij}/\Delta\alpha\right)$.

In the $X-Z$ plane, the deformation can be presented as $\Delta\varepsilon_{v}^{R} = \Delta\varepsilon_{xx}^{R} + \Delta\varepsilon_{zz}^{R}$,

$\Delta\varepsilon_q^R = \sqrt{\left(\Delta\varepsilon_{xx}^R - \Delta\varepsilon_{zz}^R\right)^2 / 4 + \Delta\varepsilon_{xz}^R \Delta\varepsilon_{zx}^R}$ and $\alpha_{\Delta\varepsilon}^R = \text{atan}\left[2\Delta\varepsilon_{xz}^R / \left(\Delta\varepsilon_{zz}^R - \Delta\varepsilon_{xx}^R\right)\right] / 2$, where $\Delta\varepsilon_q^R$ represents the diameter of the osculating circle for the strain trajectories. Figure 6.7 below presents the strain increment of the 1st cycle and the 2nd cycle with the stress ratio of 0.3 and 0.5. It calculates the normalised strain increment $\Delta\varepsilon_{ij}^R$ with the extracted strain increment $\Delta\varepsilon_{ij}$ occurred during the stress rotation $\Delta\alpha \approx 3°$. Significant plastic strain increment is observed in particular with the 1st cycle. The larger stress ratio results in a higher strain increment.

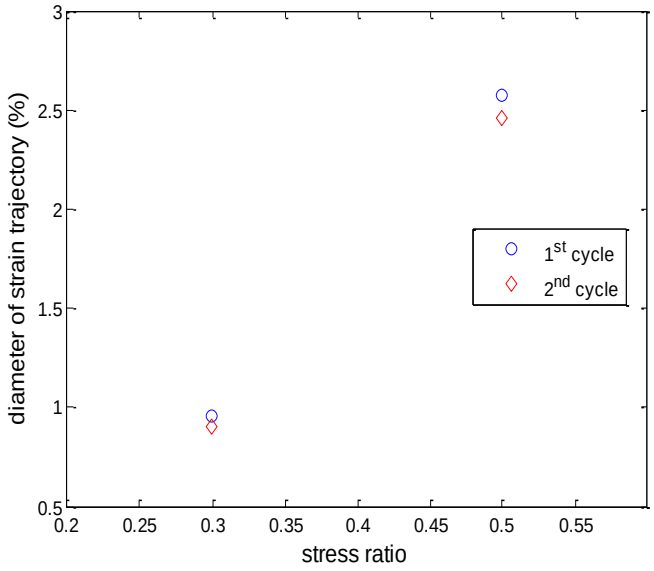


Figure 6.7 Diameter of strain trajectory at different stress ratios

6.3 Micro-scale observations

6.3.1 Stress-force-fabric relationship

Accordingly, with the stress-force-fabric relationship, it demonstrates that the strength state depends on the deviatoric anisotropy of contact force and fabric. The SFF relationship is applied to the interpretation of material behaviour during shearing. It studies this

relationship for tests with $b = 0.5$. The micro-scale stress tensor is estimated based on the tensor of contact normal and contact force following Li et al. (2013; 2014). A simplified expression is employed to obtain this relationship as

$$\sigma_{ij} = \frac{\zeta \omega N v_0 f_0}{V} \Psi\left(D_{ij}, G_{ij}^{cf}, G_{ij}^{cv}\right) \tag{6.1}$$

with $\Psi\left(D_{ij}, G_{ij}^{cf}, G_{ij}^{cv}\right) = \frac{1}{3}\left(\delta_{ij} + G_{ij}^{cf} + G_{ij}^{cv}\right) + \frac{2}{15}\left(D_{ij} + D_{im}G_{mj}^{cf} + D_{im}G_{mj}^{cv}\right)$,

where ω is average coordination number, N refers to the total number of particles, v_0 and f_0 denote the directional average value of contact vector tensor and contact force tensor respectively. V is the sample volume. ζ is a directional independent scalar introduced by Li et al. (2013). It is selected as 1.1 in this project. D_{ij}, G_{ij}^{cf} and G_{ij}^{cv} are the deviatoric tensor of contact normal, contact force and contact vector respectively.

The deviatoric tensor of contact normal $\left(D_{ij}\right)$ could provide an insight into the contact normal distribution. The tensor is estimated as follows: on the basis of the normal direction $\boldsymbol{n}$ at contact point c, the fabric tensor $\left(N_{ij}\right)$ could be obtained. By subtracting the isotropic part in the moment tensor, the fabric deviatoric tensor can be obtained. They are defined to quantify the fabric anisotropy and are expressed as

$$N_{ij} = \frac{1}{N_c}\sum_{c=1}^{N} \boldsymbol{n}_i^c \boldsymbol{n}_j^c \tag{6.2}$$

$$D_{ij} = \frac{15}{2}\left(N_{ij} - \frac{1}{3}\delta_{ij}\right) \tag{6.3}$$

where N_c refers to the total number of contacts, and δ_{ij} is the Kronecker delta.

The approximation of the probability density distribution of contact normal direction is expressed as follows for the second rank

$$E(\boldsymbol{n}) = \frac{1}{E_0}\left(1 + D_{ij}\boldsymbol{n}_i\boldsymbol{n}_j\right) \tag{6.4}$$

in which E_0 is the surface area of the unit sphere Ω. It equals to 4π in the three-dimensional space.

The equation below provides the definition of the contact force tensor $\left(K_{ij}^f\right)$ with the second rank.

$$K_{ij}^f = \frac{1}{E_0}\frac{1}{N_c}\sum \oint_{\Omega} \left\langle f_{cont} \right\rangle \Big|_{\boldsymbol{n}_{ic}} \otimes \boldsymbol{n}_{jc} d\Omega \tag{6.5}$$

in which f_{cont} refers to the contact force at the contact point c. $\boldsymbol{n}_{jc}$ is the corresponding direction of contact normal. The directional average of mean contact forces on all directions refers to f_{cont0} and is calculated as

$$f_{cont0} = \frac{\oint_{\Omega} f_{cont_i}\boldsymbol{n}_i d\Omega}{E_0} = K_{jj}^f \tag{6.6}$$

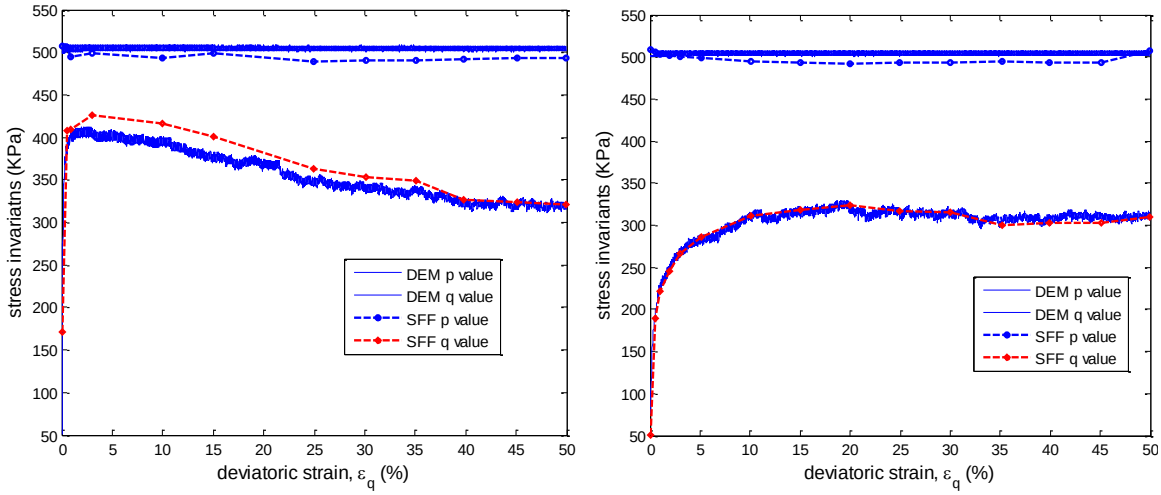
The deviatoric tensor of contact force is in the expression as

$$G_{ij}^{cf} = \frac{3K_{ij}^f}{K_{jj}^f} - \delta_{ij} \tag{6.7}$$

The stress invariants p, q, b are estimated using Eq.(3.55) to Eq.(3.59). Figure 6.8 presents the stress invariants obtained with the SFF relationship of $e_0 = 0.592$ and $e_0 = 0.695$. It could be observed that the confining pressure is around 500kPa at different shear strains respectively. For $e_0 = 0.592$, the deviatoric stress reaches the peak value quickly and then

continuously reduces during shearing. For $e_0 = 0.695$, the increase rate of deviatoric stress is smaller. After achieving the peak value, the deviatoric stress maintains constant.

Based on the results of p and q, it could be found that the results of SFF are close to the simulation results for $e_0 = 0.695$. According to results in Section 5.3, the sample with a lower density would have a more uniformly condition. In addition, the wide particle size distribution may also increase the non-uniform state, which may result in the difference between the simulation results and results of SFF for $e_0 = 0.592$.



(1) $e_0 = 0.592$ (2) $e_0 = 0.695$

Figure 6.8 The stress invariants calculated from SFF relationship with radius expansion method

The above results show that the micro-scale results could represent the macro-scale strength behaviour of granular materials. To better understand the internal structure, the characteristics of the fabric and contact force, for the SFF relationship, are studied in the following sections with the impact of initial void ratio, intermediate principal stress ratio and stress ratio respectively.

6.3.2 Impact of void ratio

The characteristics of average coordination number, contact normal and contact force are studied in this section. Owing to the spherical shape of particles, the anisotropy degree would be small for the contact vector tensor. Hence, it does not take into account for this project.

The average coordination number is related to the characteristic of the void ratio of materials in macro-scale. It is estimated as the total number of contacts dividing the number of particles. With a larger value of coordination number, it refers to the lower value of the void ratio, depending on a particle gaining more contacts from the neighbouring particles.

According to the graph, the average coordination number drops quickly for the sample with the initial void ratio of 0.592. This is related to the increase of the void ratio which decreases the contact numbers of particles. For $e_0 = 0.637$, the average coordinate number decreases with a lower rate. Regarding the test with the initial void ratio of 0.695, the average coordination number changes slightly during shearing. At the large shear strain, the specimens achieve the same coordination number under various void ratios. According to Yang (2014), similar characeristics are observed for the evolution of coordination number with the impact of void ratio. However, the results are slightly smaller at the critical state in comparison with Yang (2014). It may depend on the wide particle size distribution and the larger value of the average particle size.

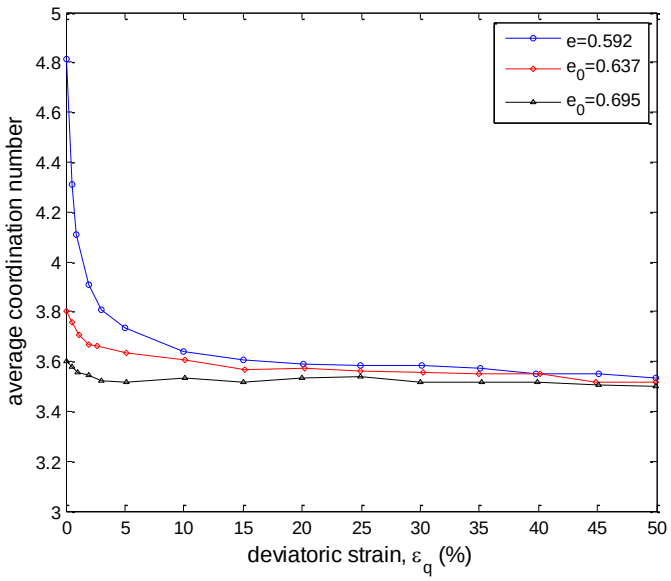


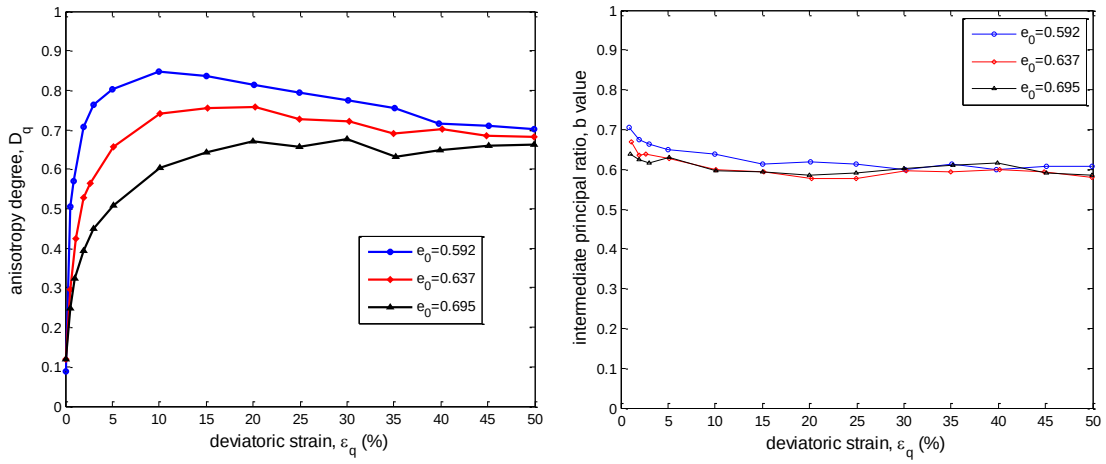
Figure 6.9 The evolution of coordination number under various void ratios

The characteristics of the anisotropy degree of the fabric, contact force and the directional distribution of the fabric tensor and contact force tensor are studied to present the particle-scale behaviour of specimens. The deviatoric fabric tensor D_{ij}, elaborated above, could represent the directional distribution of the contact normal. The deviatoric value $\left(D_q\right)$ of D_{ij}, calculated as $D_q = \sqrt{3D_{ij}D_{ji}/2}$, is studied to present the anisotropy degree of fabric. The intermediate principal ratio is also investigated to show the relationship of the principal fabric values. It is estimated as $b_F = \left(F_2 - F_3\right) \Big/ \left(F_1 - F_3\right)$, where F_1, F_2 and F_3 refer to the major, intermediate and minimum principal fabric value respectively. Figure 6.10 below presents the evolution of D_q and b_F for the tensor D_{ij}.

At the initial stage, samples are under the isotropic condition with the anisotropy degree around zero. When increasing the shear strain, the anisotropic internal structure then develops owing to the external loading. Kruyt (2012) proposed that the changes of the fabric tensor related to the three mechanisms as the contact creation, contact disruption and

contact reorientation. The results suggested that the induced anisotropy is mainly due to the contact disruption. Furthermore, the contact disruption is related to the increased number of disrupted contacts orientated in the minor principal stress direction during the simulation.

The fabric anisotropy degree increases quickly and reaches a peak value for $e_0 = 0.592$ and $e_0 = 0.637$. Afterwards, it continuously decreases during the simulation and reaches a constant value at the end of the simulation. For $e_0 = 0.637$, the peak value of fabric anisotropy degree is slightly lower compared with $e_0 = 0.592$. Regarding the sample of $e_0 = 0.695$, the magnitude of fabric anisotropy increases with a lower rate to achieve the peak value, in comparison with $e_0 = 0.592$ and $e_0 = 0.637$, and then remains constant around 0.62. At the critical stage, the specimens achieve the similar fabric anisotropy degree irrespective of the initial void ratio. For the characteristics of the intermediate principal fabric ratio, it is a bit larger than the intermediate principal stress ratio with the value approximately 0.6 for all the samples during shearing.



(1) anisotropy degree (2) intermediate principal ratio

Figure 6.10 The characteristics of fabric anisotropy with various initial void ratio

The contact force tensor is also studied to characterise the microstructure behaviour of contact force. The details for the estimation of the deviatoric contact force tensor K_{ij} could also be found in Section 2.4. The direction average of mean contact force, anisotropy degree and intermediate principal ratio are studied of the tensor K_{ij}. The average contact force f_0 continuously rises with the increase of shear strain for $e_0 = 0.592$. A lower growth rate is observed for $e_0 = 0.637$ during shearing. However, concerning the sample $e_0 = 0.695$, the average contact force reduces slightly at the initial state and then maintains a steady state. The specimens reach the similar value at the end of the shear stage.

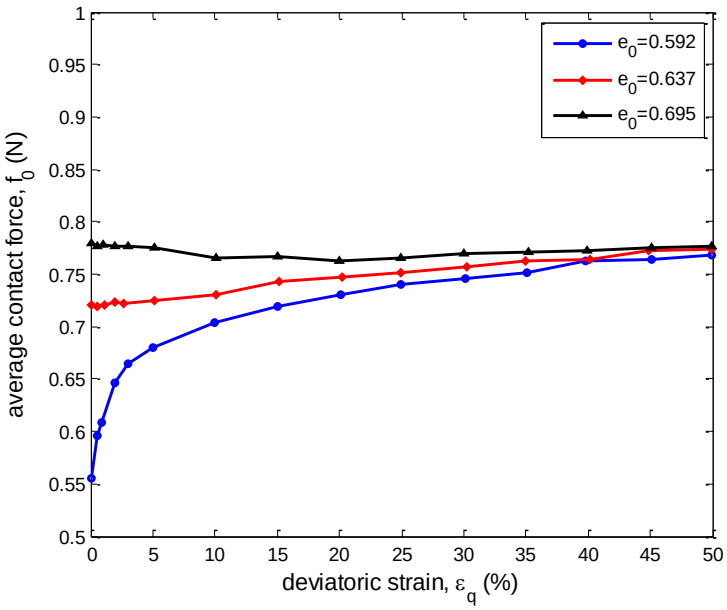
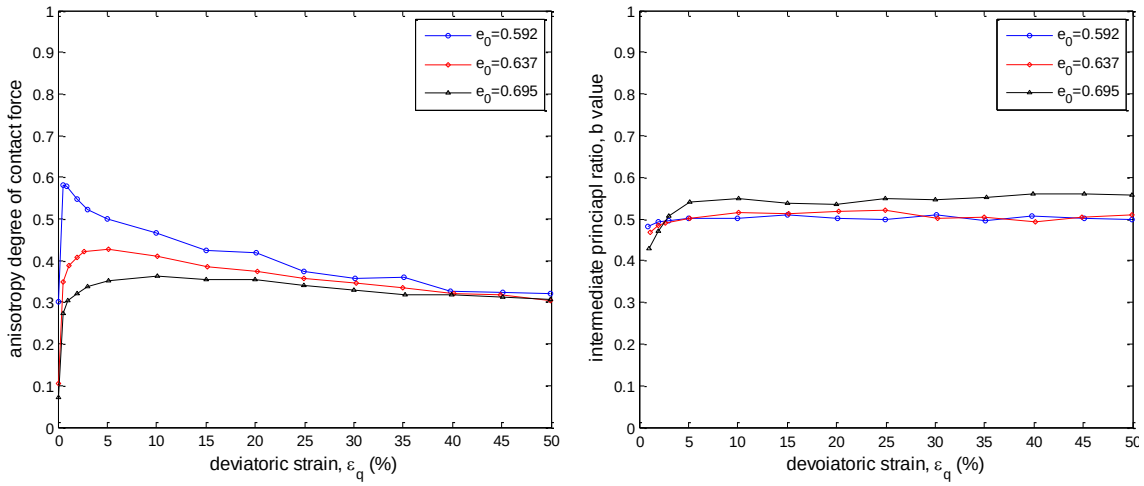


Figure 6.11 The characteristics of average contact force with various void ratios

The characteristic for the anisotropy degree of the contact force is similar to the behaviour of the fabric anisotropy degree. At the peak stage, the largest and smallest degree of fabric anisotropy appear for the sample of $e_0 = 0.592$ and $e_0 = 0.695$ respectively. A peak value is observed quickly for $e_0 = 0.592$ at the shear strain of 1% and then drops and reaches a constant value at the end of the simulation. For $e_0 = 0.695$, the anisotropy degree increases

slowly first and then maintains a constant value during the simulation. Samples achieve the similar value at the critical state. The intermediate principal ratio is also around 0.5 during shearing for all the specimens respectively.



(1) anisotropy degree (2) intermediate principal ratio

Figure 6.12 The characteristics of contact force tensor with various void ratios

6.3.3 Impact of intermediate principal stress ratio

This part studies the impact of intermediate principal stress ratio on the particle-scale mechanism with the evolution of shear strain. Figure 6.13 below presents the feature of coordination number. The impact of b value on the characteristics of average coordination number is negligible. Samples achieve a similar value at the critical stage even at different initial void ratios and b values. Coordination number decreases during the simulation for $e_0 = 0.592$. However, for $e_0 = 0.695$, it is almost constant with the increase of shear strain.

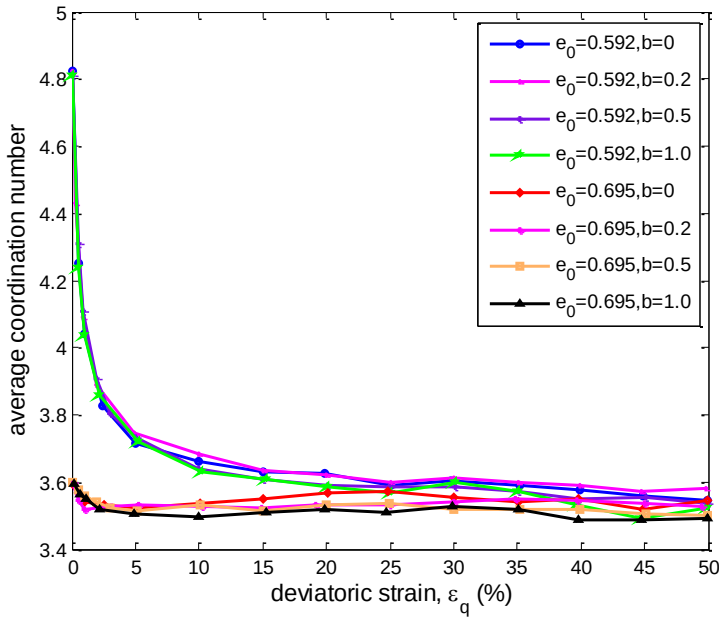
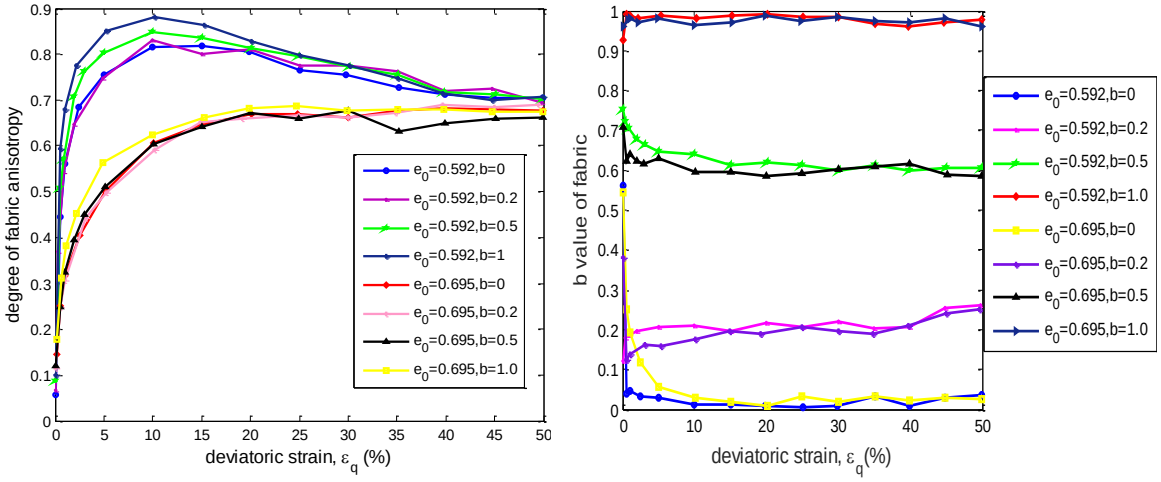


Figure 6.13 The evolution of coordination number with various b values

The evolution of fabric anisotropy is also similar in comparison with the test of $b = 0.5$. A peak value of the anisotropy degree is observed quickly for $e_0 = 0.592$ and then reduces with the evolution of shear strain. For $e_0 = 0.695$, the degree of fabric anisotropy increases slowly and maintains constant during the simulation. According to the graphs, reducing the b value, the peak degree of fabric anisotropy is also decreased. For each test, the intermediate principal fabric ratio is slightly larger than the pre-set intermediate principal stress ratio. This may be related to more significant anisotropy degree formed by the specimens during shearing.



(1) anisotropy degree (2) b value

Figure 6.14 The evolution of anisotropy degree and b value for the contact normal

Figure 6.15 below displays the degree of fabric anisotropy at the critical state with various b values. The critical state refers to the stage at the shear strain of 50%. A similar magnitude of fabric anisotropy is observed at various b values for $e_0 = 0.592$. Sample with $e_0 = 0.592$ contains a more significant anisotropy degree compared with the sample of $e_0 = 0.695$, with the largest difference appearing at $b = 0.5$. This depends on the higher differences of critical stress ratio and critical friction angle observed under this b value.

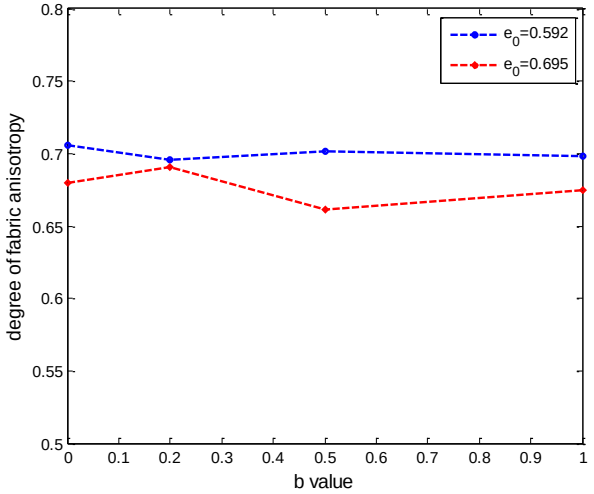


Figure 6.15 The critical fabric anisotropy with various b values

Concerning the characteristics of contact force, the average contact force increases with the evolution of shear strain for $e_0 = 0.592$. However, for $e_0 = 0.695$, the average contact force reduces slightly during the simulation. At each b value, samples achieve the similar critical average contact force. When increasing the b value, the average contact force rises at the critical stage.

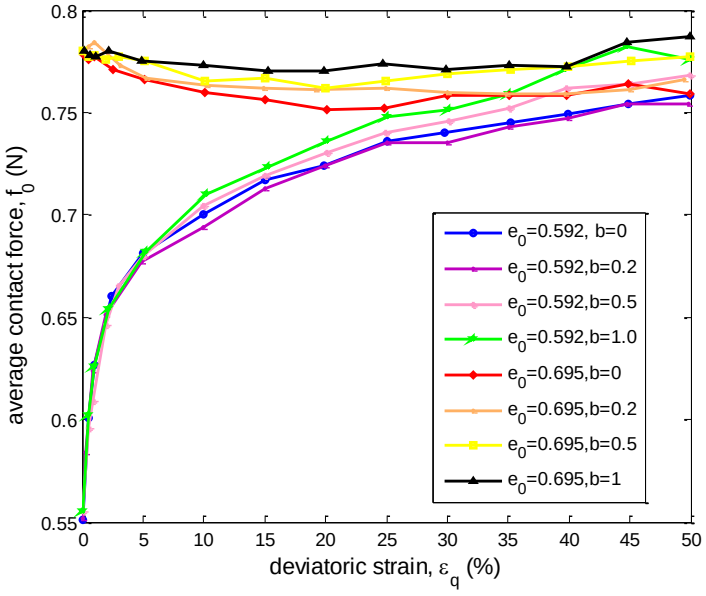
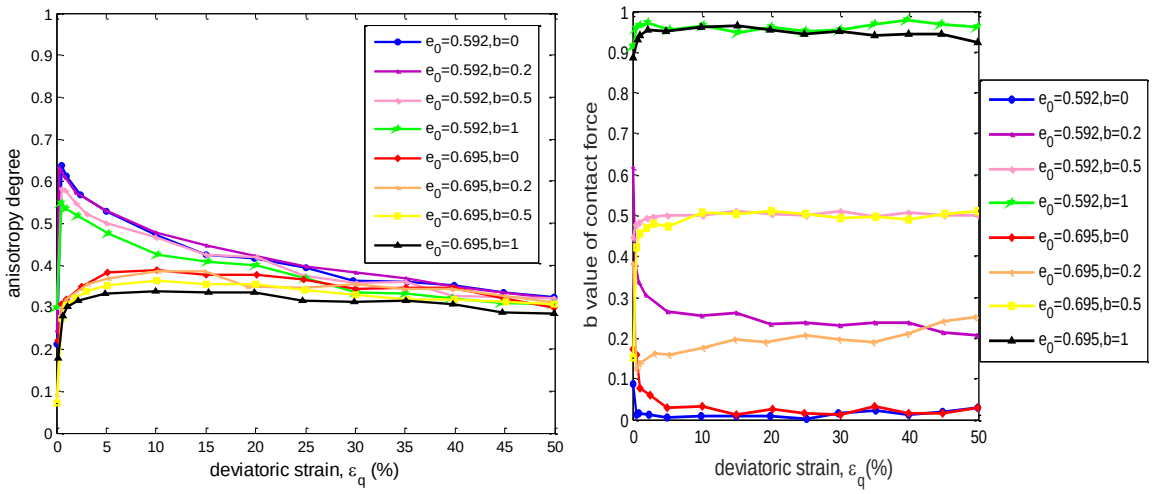


Figure 6.16 The evolution of average contact force with various b values

Figure 6.17 shows a more significant degree of contact force anisotropy is obtained with the lower void ratio for both the peak stage and critical stage. The sample reaches the peak anisotropy degree quickly and then continuously reduces for $e_0 = 0.592$. Regarding $e_0 = 0.695$, the degree of force anisotropy increases slowly and is maintained constant during the simulation. It show that the lower b value results in a larger degree of contact force anisotropy. With regards to the intermediate principal value of contact force, they are all around the pre-set principal stress ratio.

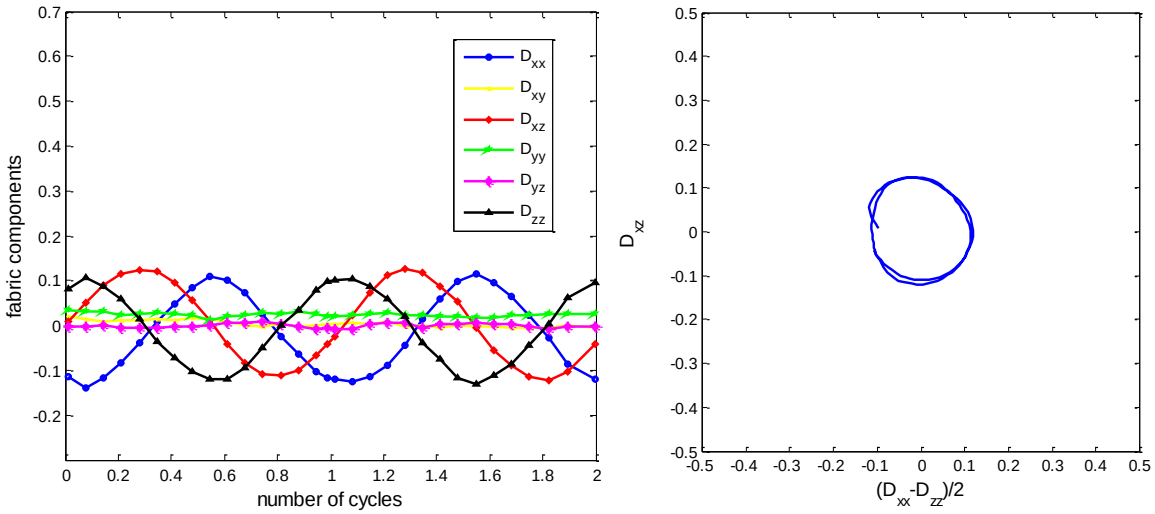


(1) anisotropy degree (2) b value

Figure 6.17 The evolution of anisotropy degree and b value of contact force

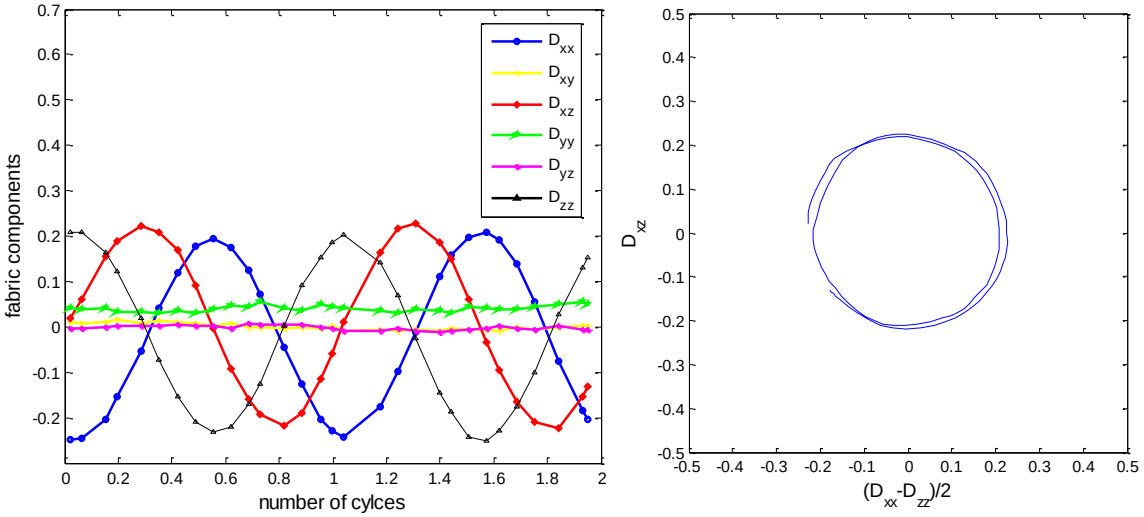
6.3.4 Drained rotational shear test

The fabric anisotropy behaviour in terms of deviatoric contact normal tensor is observed with the evolution of components and fabric trajectory. It studies the micro-scale behaviour in terms of the deviatoric contact normal (D_{ij}) with this loading path. The following graphs are presented with different stress ratios. The fabric components of D_{xx}, D_{xz} and D_{zz} are vibrated periodically during the simulation. Due to a smaller deformation, a lower value of fabric anisotropy is obtained. The fabric trajectory is also rotated in the deviatoric plane with the shape near to a circle. With a lower stress ratio, owing to the smaller strain response, the corresponding fabric components and fabric trajectory are both in a lower condition.



(1) fabric components (2) fabric trajectory

(a) $\eta = 0.3$



(1) fabric components (2) fabric trajectory

(b) $\eta = 0.5$

Figure 6.18 The evolution of fabric anisotropy behaviour with different stress ratios

6.4 Impact of initial structure

The deposition method is employed to investigate the initial anisotropy behaviour of the specimen. In order to further present the material behaviour with the sand pile, the tests are performed with an element inside the sand pile prepared with the boundary removal method.

It selects the stage that particles deposited into the cylindrical boundary and under the equilibrium condition. The sample is prepared with the element located in the central region to avoid the impacts of the boundary and the surface of the sand pile. In the *z*-direction, the dimension ranges from $0.015m$ to $0.055m$. Concerning the *x* and *y* directions, the dimensions both range from $-0.02m$ to $0.02m$. The polyhedral boundary is defined with $R = 0.02m$, $N = 10$ and the central coordinate of $(0, 0, 0.035)m$. Particles, located out of the polyhedral boundary, would be deleted to form the specimen.

After preparing the sample, the gravitation force is removed in the consolidation and shear stages. It would consolidate to the confining pressure of 500kPa for the triaxial shear and rotation shear tests, with the friction coefficient of 0.5. Due to deleting particles interacted with the boundary, it increases the void ratio compared with the results of sand piles. The sample is under a relatively loose condition with $e_0 = 0.832$ using this preparation method. It may be related to a larger friction coefficient, 1.0, applied for the specimen preparation of the sand pile test. The following sections present the results in the macro-scale and micro-scale respectively.

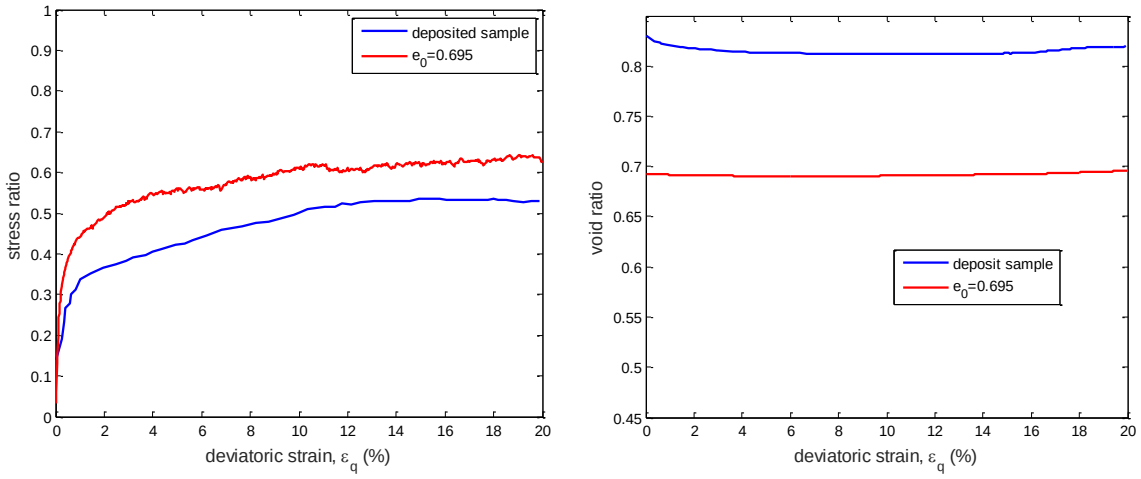
6.4.1 Macro-scale observations

6.4.1.1 Drained triaxial shear test

In the triaxial shear stage, the test is undertaken with the intermediate principal stress ratio of 0.5. It is performed to compare with the results of the radius expansion method and prepare the samples for the rotation shear with different stress ratios.

Figure 6.19 below presents the evolution of stress ratio and void ratio during shearing. The sample behaves as a medium density condition, depending on the less change of the volume

and larger void ratio when compared with sample of $e_0 = 0.695$ at each shear strain. It displays that the sample achieves the critical stage quickly as the stress ratio almost maintaining constant when the deviatoric strain is larger than 15%. In such a case, the simulation is performed with the shear strain of 20%. It shows that the specimen is less shearing resistant, due to a lower stress ratio obtained than the sample of $e_0 = 0.695$.



(1) stress ratio (2) void ratio

Figure 6.19 Evolution of the stress ratio and void ratio

To explain the different material responses observed in Figure 6.19, the initial stage is taken as an example for studying the probability distribution of contact force, average contact force distribution and void ratio distribution, with the results displayed in Figure 6.20 and Figure 6.21 respectively. According to the graphs, the radius expansion method produces a relatively uniform void ratio and average contact force inside the specimen. In addition, it shows that the deposited method produces a larger magnitude of average contact force near the boundary, accompanied with a higher void ratio. This may result in the significant differences in void ratio and shear resistance for the samples.

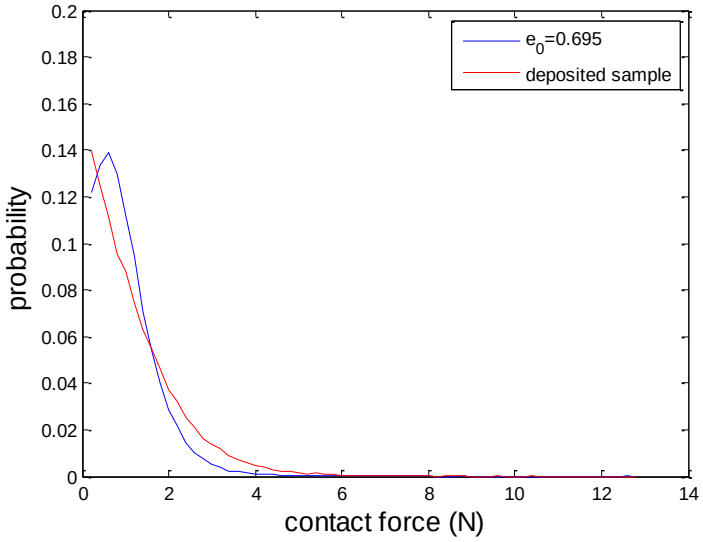


Figure 6.20 The probability distribution of contact force under various preparation methods

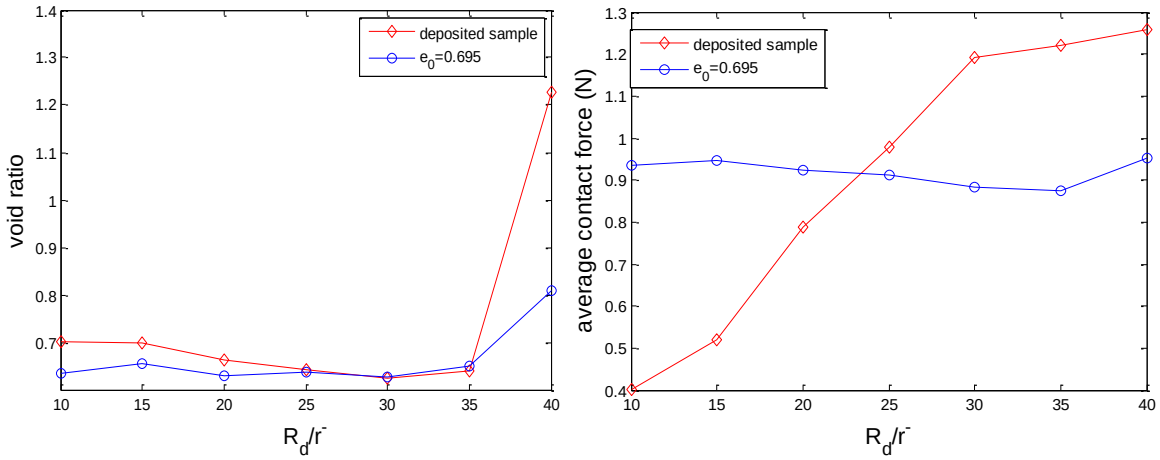
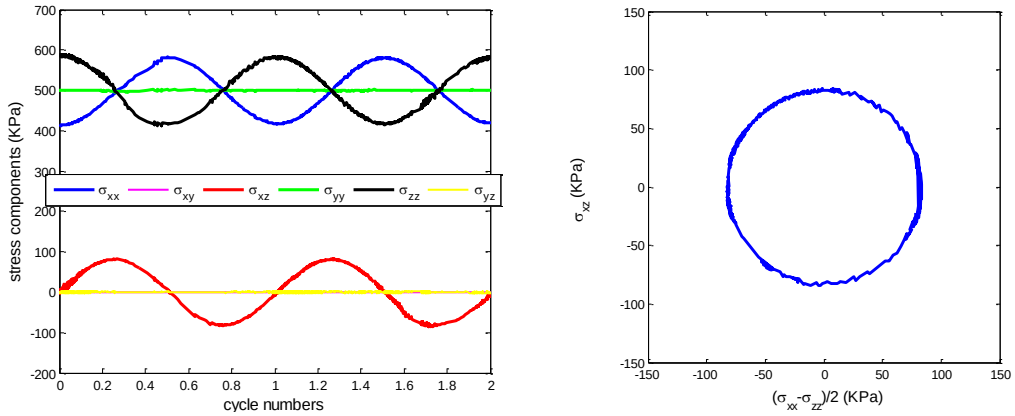


Figure 6.21 The distribution of void ratio and average contact force inside samples

6.4.1.2 Drained rotational shear

The sample prepared with the deposition method is also concerned with the rotation shear test. The target confining pressure is selected as 500kPa. After consolidated to the target confining pressure, the samples are first pre-sheared with the true triaxial loading path. Due to the less shear resistance of the specimen, a lower stress ratio, as 0.3, is taken into account with the material responses for the rotation shear test. Tests are conducted with two cycles under $b = 0.5$.

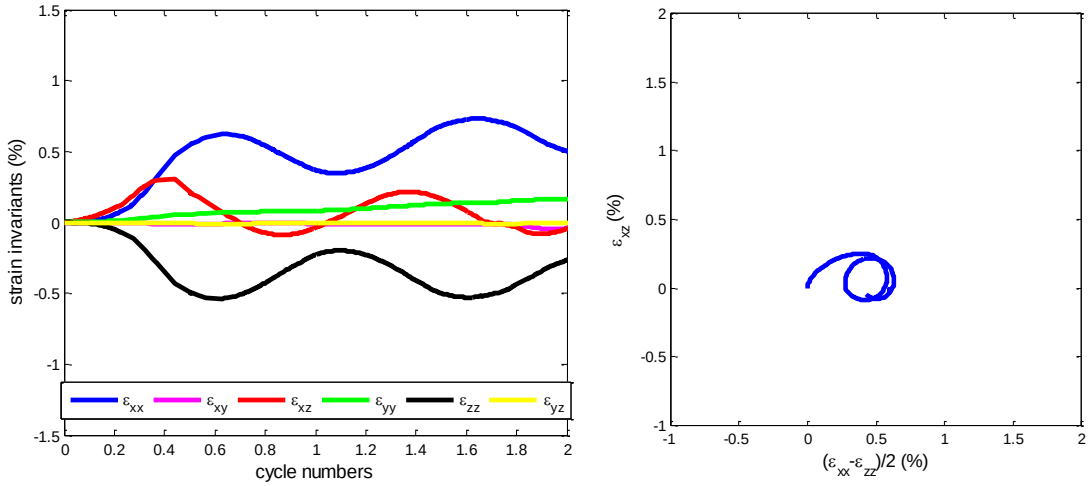
According to Figure 6.22(1), the stresses are maintained constantly and near zero for the stress components σ_{xy} and σ_{yz}. The intermediate principal stress σ_{yy} is at 500kPa during rotation. The other stress components are all vibrated with the rotation of principal stress directions. A circle is observed for the stress trajectory in the deviatoric plane, displayed as Figure 6.22(2).



(1) stress components (2) stress trajectory

Figure 6.22 The behaviour of stress invariants

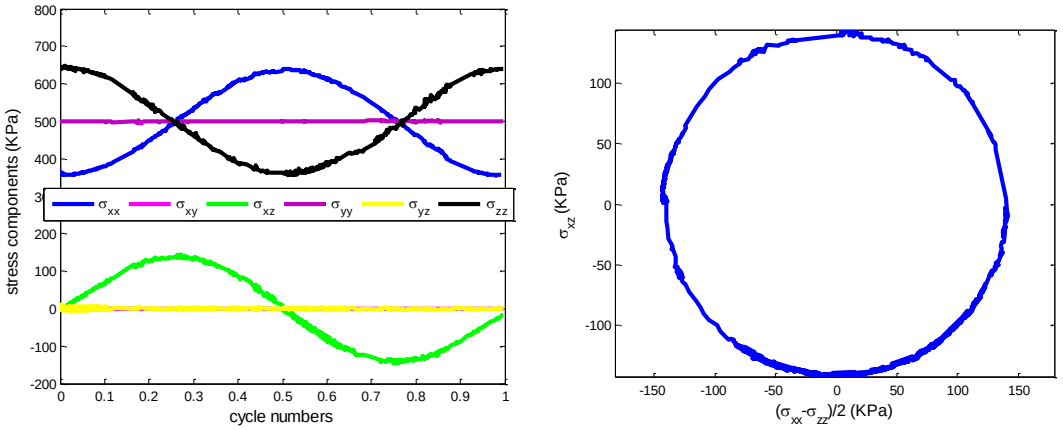
The strain responses are studied to observe the deformation characteristics during the simulation. The strain components, $\varepsilon_{xx}, \varepsilon_{xz}, \varepsilon_{zz}$, are varied with the continuous rotation of the principal stress directions. ε_{yy} is increased during the simulation while ε_{xy} and ε_{yz} are maintained around zero. The strain trajectory is observed as Figure 6.23(2). It behaves as a shape of spiral in the $X-Z$ plane instead of a circle for the stress trajectory.



(1) strain components (2) strain trajectory

Figure 6.23 The evolution of strain invariants

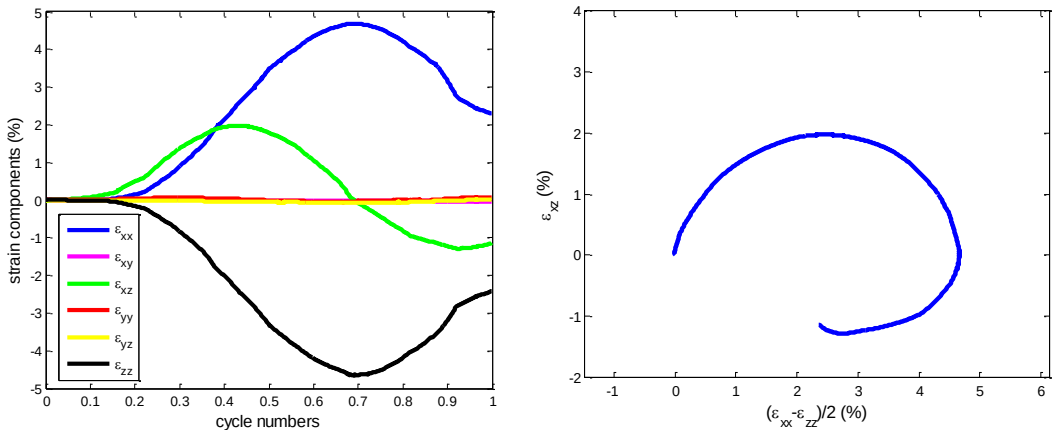
To further observe the material behaviour, a test is performed under the stress ratio of 0.5 for the rotation shear. One cycle is run to observe the major difference for the stress and strain behaviour. The intermediate principal stress ratio is maintained at 0.5 during rotation. Figure 6.24 displays the evolution of stress components and the stress trajectory during rotation. The behaviour is similar to the results with the stress ratio of 0.3. The stress components, σ_{xx} , σ_{xz} , σ_{zz} , are also vibrated during rotation. The other stress components are maintained constantly with the rotation of the principal stress directions. A circle is observed for the stress trajectory with a larger size compared with the stress ratio of 0.3.



(1) stress components (2) stress trajectory

Figure 6.24 The stress behaviour during rotation of principal stress directions

Figure 6.25 below displays the strain responses in terms of strain components and strain trajectory. It can also be observed that ε_{xx}, ε_{xz}, ε_{zz}, are vibrated during rotation, while the strain components ε_{xy}, ε_{yy} and ε_{yz} are almost constantly with this stress ratio. It forms larger sizes of strain responses and corresponded strain trajectory than the test with $\eta = 0.3$.



(1) strain components (2) strain trajectory

Figure 6.25 The strain behaviour during the rotation of principal stress directions

Compared with the results in Section 6.3.3, the results of stress components are more fluctuated for the deposited sample during rotation. The diameter of strain trajectory is also studied for the first cycle under various stress ratios. The deposited sample contains a

smaller value of the strain trajectory for $\eta = 0.3$. However, for a larger stress ratio, the deposited sample produces a larger diameter of strain trajectory than the radius expansion sample.

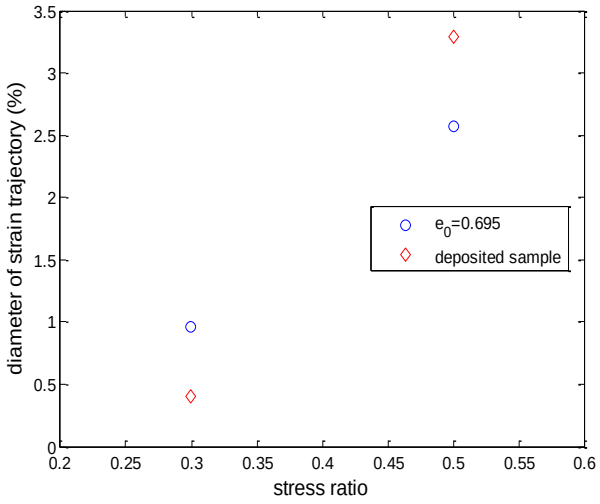


Figure 6.26 The diameter of strain trajectory at various stress ratios

6.4.2 Micro-scale observations

6.4.2.1 Drained triaxial shear test

The micro-scale observations are also taken into account with this sample during shearing. The SFF relationship is first studied with the proportional loading path. The figure below presents the behaviour of stress invariants during the simulation. The stress ratio increases slowly with the deposit method. It could be observed that the results are smaller with the confining pressure approximately 485kPa from SFF, compared with the target confining pressure of 500kPa. This may be owing to the fact that the deposition method increased the initial anisotropy of the sample during the packing stage. The deviatoric stress is increased slowly with a lower value than the sample prepared by the radius expansion method.

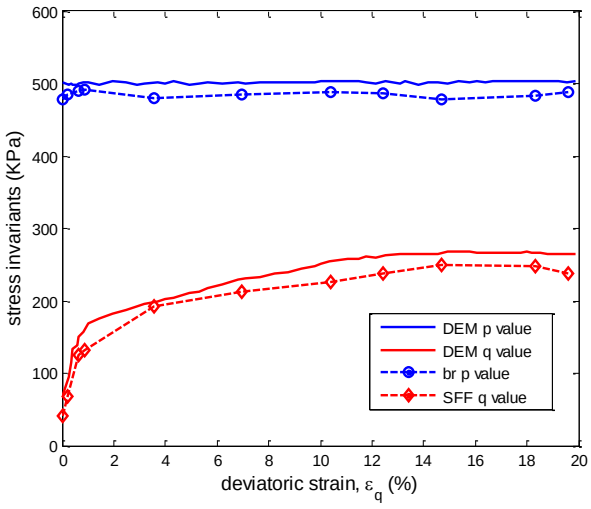


Figure 6.27 The stress invariants estimated from SFF for the deposited sample

To investigate the formation of the lower stress level, the micro-scale factors are studied during shearing and compared with the results of the radius expansion method. The characteristics of average coordination number, contact normal, and contact force tensor are studied. Figure 6.28 presents the evolution of the coordination number. During shearing, the average coordination number slightly increases to a constant value for the deposition method. A lower average coordination number is observed than sample with $e_0 = 0.695$ at the initial stage, and then it becomes larger with the increase of shear strain.

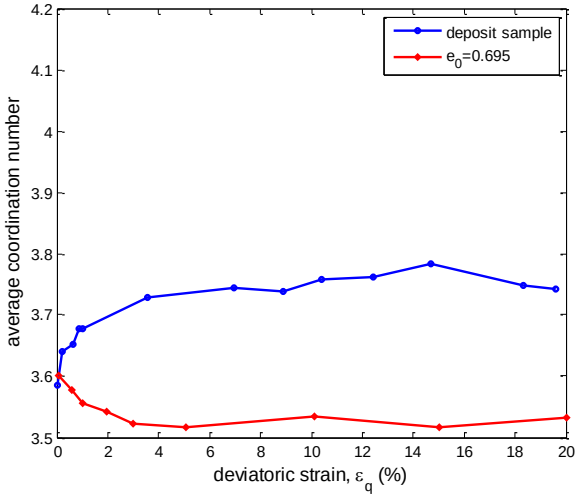
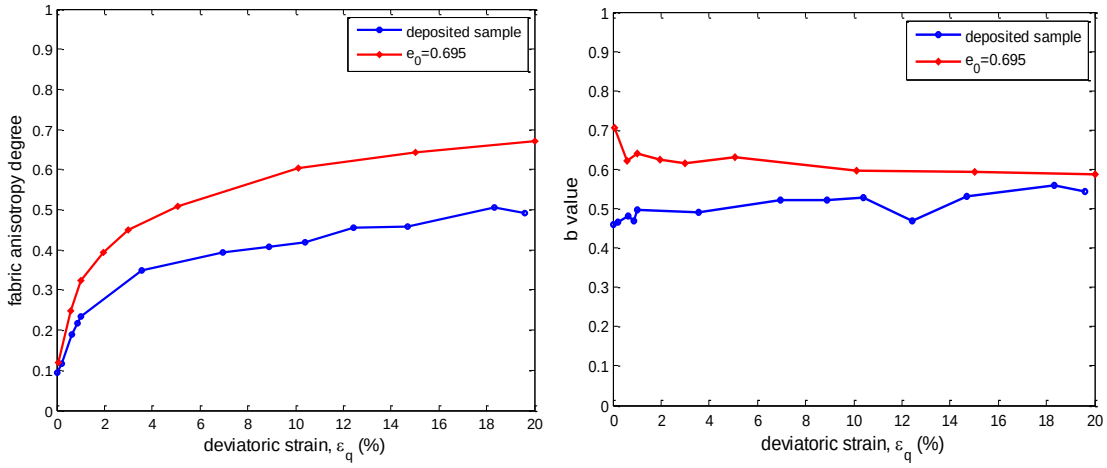


Figure 6.28 The evolution of coordination number

The degree of fabric anisotropy is presented in Figure 6.29. It is calculated based on the deviatoric part of the contact normal tensor (D_{ij}). The degree is increased slowly with the peak value of 0.5. The result is lower in comparison with the sample of $e_0 = 0.695$. With regards to the intermediate principal fabric ratio, it is maintained at around 0.5 during the simulation.



(1) anisotropy degree (2) b value

Figure 6.29 The characteristics of fabric anisotropy

The characteristics of contact force are also taken into account during the simulation. It is presented with the deviatoric contact force tensor, in terms of the average contact force (f_0) and the anisotropy degree. Figure 6.30 presents the evolution of f_0 during the simulation. It reduces slightly to a constant value as the increase of shear strain for both the two samples. The deposited sample contains a larger value of average contact force at each shear strain. During shearing, owing to the higher probability of strong contact force and more voids inside the specimen, this may result in the smaller reduce of the direction average contact force.

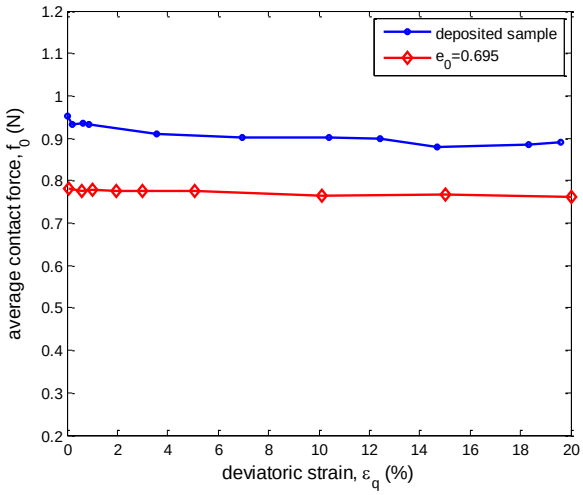
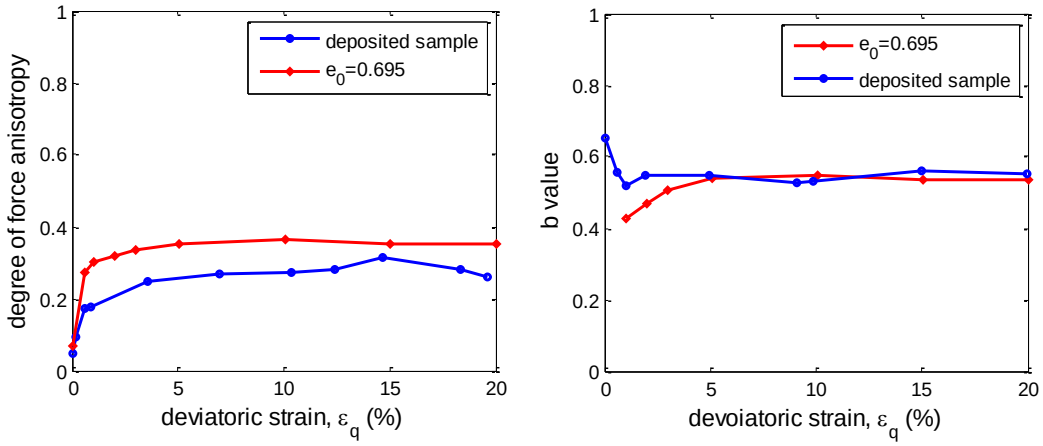


Figure 6.30 The evolution of averaged contact force

The evolution of the contact force anisotropy degree is presented in Figure 6.31. It increases gradually with a smaller peak value compared with the sample of $e_0 = 0.695$. The intermediate principal ratio of contact force is also maintained at approximately 0.5 during the simulation.



(1) anisotropy degree (2) b value

Figure 6.31 The evolution of the contact force anisotropy

For this sample, it contains a smaller number of particles, though with a larger magnitude of average contact force f_0 and the average coordination number. Compared with the test

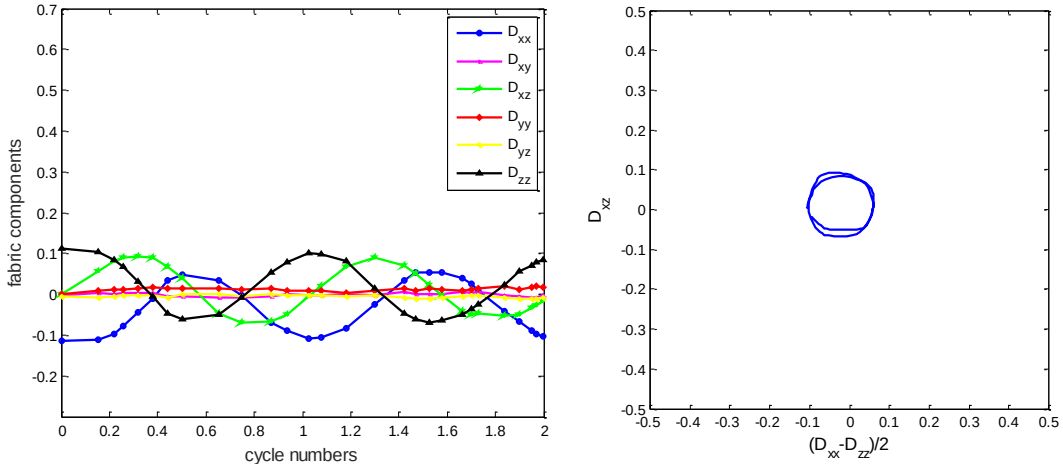
of $e_0 = 0.695$, the magnitude of $(f_0\omega)_{dep} / (f_0\omega)_{rad}$ is smaller than the results of N_{dep} / N_{rad} for the two tests, where $(f_0\omega)_{dep}$ and $(f_0\omega)_{rad}$ refer to the multiply results of directional average contact force and average coordination number for the deposited sample and the radius expansion sample respectively. N_{dep} and N_{rad} denote the corresponding number of particles respectively. According to the SFF relationship, this would result in a lower stress level. In addition, the deposited sample forms a smaller stress ratio with respect to a lower anisotropy degree for the deviatoric tensor of D_{ij} and G_{ij}.

6.4.2.2 Drained rotational shear test

The internal structure is also observed with the non-proportional loading path. Figure 6.32 displays the behaviour of fabric tensor. It can be seen that the fabric components, D_{xx}, D_{xz}, and D_{zz}, are variated period for the rotation shear, similar to the variation of the stress components. The fabric components, D_{xy}, D_{yz}, are around zero during the continuous rotation. Regarding the intermediate fabric component D_{yy}, it increases slowly with the origin value around zero.

The results indicated that the material internal structure is also periodical rotated following the rotation of the major principal stress direction in the $x-z$ plane. The internal structure is dependent on the particles arrangement. The sample produces a lower strain increment and results in smaller amplitudes of fabric components. The fabric trajectory is also studied to show a better view of the fabric evolution. It is also plotted in the deviatoric plane based on the fabric components of D_{xx}, D_{xz}, and D_{zz}, as Figure 6.32(2) below presented in terms of D_{xz} against $(D_{xx}-D_{zz})/2$. The result shows that the fabric trajectory is near to the shape of

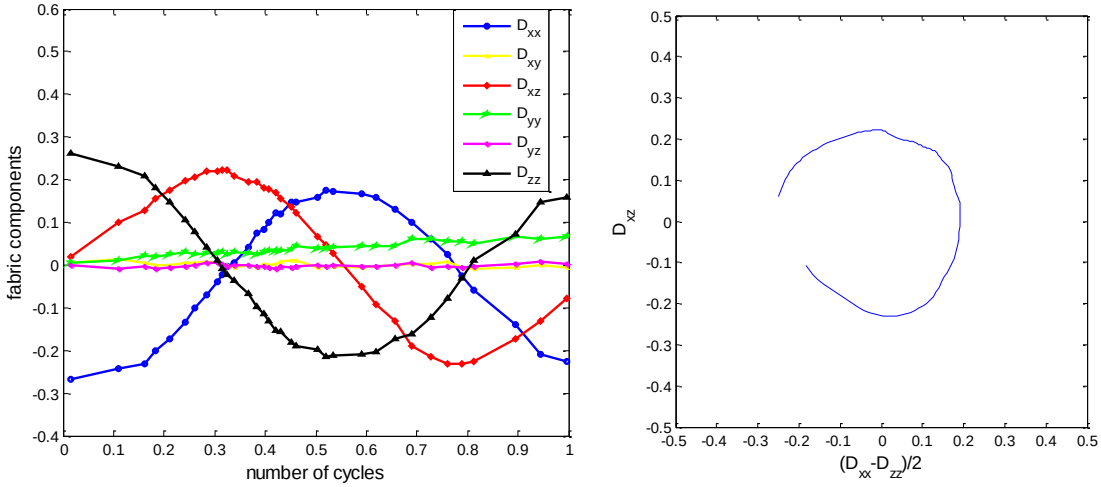
a circle, similar to the results of the stress trajectory. It implies that the magnitude of fabric anisotropy is similar during the rotation of the principal stress directions.



(1) fabric components (2) fabric trajectory

Figure 6.32 The evolution of contact normal tensor with $\eta = 0.3$

The figure below displays the characteristics of fabric with the stress ratio of 0.5. Larger values of fabric components are observed during rotation compared with $\eta = 0.3$. It also produces a larger size of fabric trajectory.



(1) fabric components (2) fabric trajectory

Figure 6.33 The evolution of fabric anisotropy behaviour with $\eta = 0.5$

6.5 Summary

This chapter applies the powerful tool developed in Chapter 5 to have a better understanding of the elementary material behaviour. Based on the material responses of triaxial shear, the sample with a smaller void ratio achieves the peak stress ratio quickly following by a continuous decrease. Under a larger void ratio, the stress ratio is increased with a granular rate to the peak value and then maintains constantly during shearing. Compared with results in Chapter 5, the peak and critical stress ratios are lower with the wide particle size distribution. When increasing the b value, it reduces both the peak stress ratio, critical stress ratio and critical void ratio. For the critical friction angle, at $b = 0.5$, the results are similar to the repose angle of sand pile, depending on the similar void ratio achieved at the critical state to the average void ratio of sand piles.

The "stress-force-fabric" relationship proposed by Li et al. (2013) is applied to the interpretation of the material behaviour under the triaxial shear test. It finds the results of SFF is close to the results of simulations under a larger void ratio, relating to a more uniformly condition according to the uniformity behaviour in Chapter 5. To further understand the material behaviour, the particle-scale mechanism is studied in terms of coordination number, contact normal and contact force. The results of ω and f_0 are increased with a smaller void ratio and decreased with a larger void ratio during shearing. Increasing the b value has a negligible effect on ω for all the samples. Larger values of f_0 and D_q are observed at the critical stage for the sample with a higher b value. Regarding the G_q, it is reduced with the increase of b value.

The material response is dependent on the pre-loading history or the external action like shear. A sample prepared by the deposit method is performed to observe the impact of

initial structure. It forms the specimen in a looser condition and contains a higher probability of larger particle size using this method compared with the radius expansion method. Compared with the radius expansion sample, the deposited sample observes a lower stress ratio with a larger void ratio at each shear strain. In addition, regarding the micro-scale behaviour, the deposited sample produces larger values of ω and f_0 with smaller values of D_q and G_q, which results in the smaller magnitude of shear stress and reduces the shear resistant.

The non-proportional loading path considers the impact of stress ratio for the deformation of specimens prepared with different methods. Increasing the stress ratio, the sizes of the stress trajectory, strain trajectory and fabric trajectory are both increased. Furthermore, the deposited sample produces a larger strain trajectory than the radius expansion sample at $\eta = 0.5$. The fabric trajectory behaves as a shape of circle during rotation, indicating the continuous rotation of internal structure along the stress rotation.

Based on the aforementioned results, different characteristics of stress, internal structure and force are observed with various b values. Hence, it should consider the impact of b value to investigate the strength characteristics in the constitutive modelling. In addition, significant plastic deformation is observed with a higher magnitude of stress ratio during rotation. Without the consideration of the loading paths, it may result in a different consequence of the strain behaviour and corresponding stress behaviour in the constitutive modelling. The factors, forming the SFF relationship, could obtain the strength characteristics of granular materials and explain the RVE material behaviour. They are employed to observe the material behaviour with the spatial distribution of internal structure and stress inside sand pile in the following chapter.

Chapter 7 Interpretations of material response and pressure dip phenomenon

7.1 Introduction

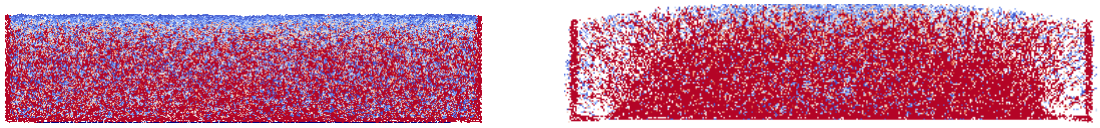
Chapter 4 presents the observations of sand piles with different preparation methods. Then, the granular material behaviour is studied in Chapter 6 under various loading paths with the elementary numerical algorithm developed in Chapter 5, together with observations in terms of micro-scale material behaviour. This chapter aims to further understand this counter-intuitive phenomenon using the particle-scale mechanism, combined with the previous investigations in terms of the initial state and the loading-path dependence. The granular material behaviour is evaluated by studying stress, force and fabric. The literature review showed that the pressure dip phenomenon is related to the construction history (Vanel et al., 1999; Geng et al., 2001b). Section 7.2 presents the force chains network during the formation process. The impact of construction history is studied at the particle-scale employing the local-scale behaviour with the spatial distribution of stress inside sand pile. Section 7.3 compares the stress behaviour with the continuum theory. The characteristics of fabric and contact force are provided in Section 7.4 and Section 7.5 respectively. Finally, a summary of this chapter is presented in Section 7.6.

7.2 Loading history dependence of sand pile

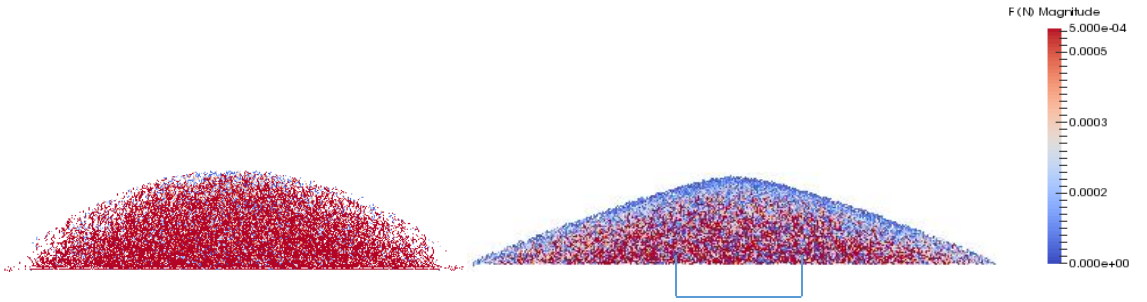
7.2.1 Progressive force chains network

The force chains network displays the orientation of contact forces inside the structure. Figure 7.1 displays the progressive force chains network for different construction histories, and represents the formation of sand pile with various preparation methods. The value of contact force is represented with the coloured bar. To show the behaviour inside, a section with a thickness of $5mm$ was selected in the centre of the sand pile in the y-axis direction.

The strong contact force reduces during the formation of the sand pile in the boundary removal test. For the rain deposition test, the strong force chains are uniformly distributed during the development of the sand pile. In the progressive stages of point deposition test, the sand pile contains strong force chains within the particles deposited region. Within the radius distance of $30mm$, it forms a larger angle with the vertical direction, which increases the contact force in the shear direction and results in the counter-intuitive phenomenon. The rain deposition test produces a higher percentage of strong force chains oriented in the vertical direction under the central apex than the point deposition test.

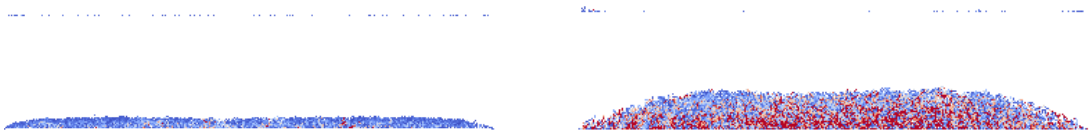


(a) 0s (b) 0.051s

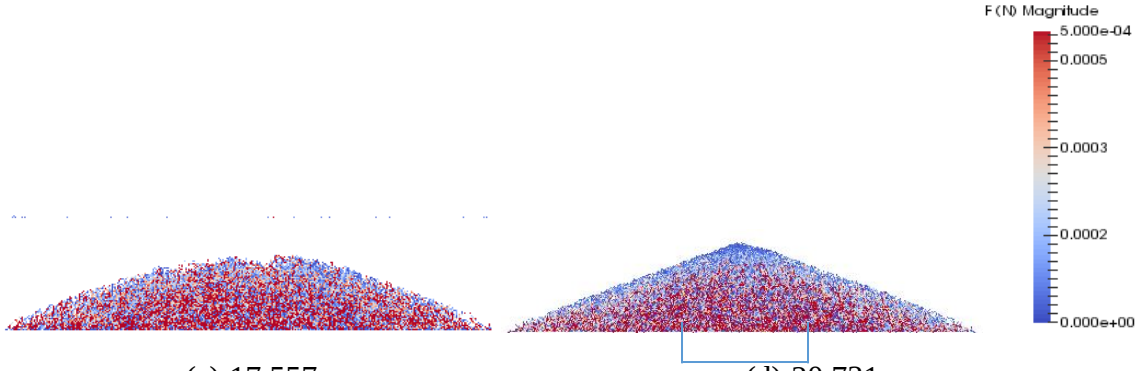


(c) 0.304s (d) 3.403s

(1) boundary removal



(a) 8.798s (b) 12.474s

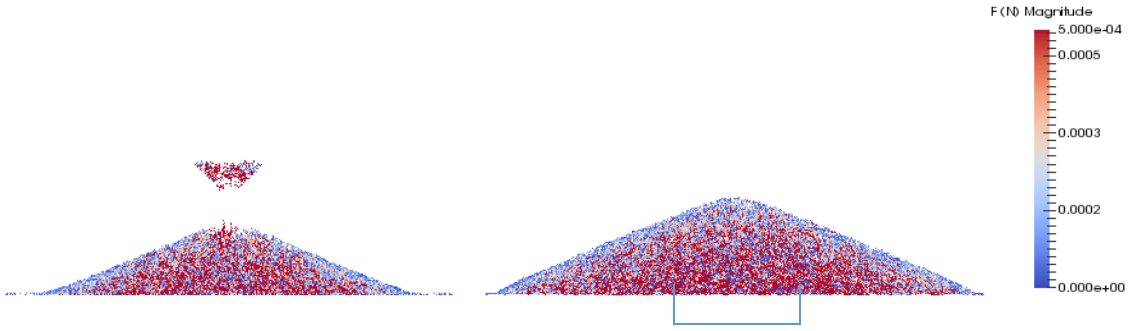


(c) 17.557s (d) 20.731s

(2) rain deposition



(a) 1.583s (b) 5.929s



(c) 37.912s (d) 72.125s

(3) point deposition

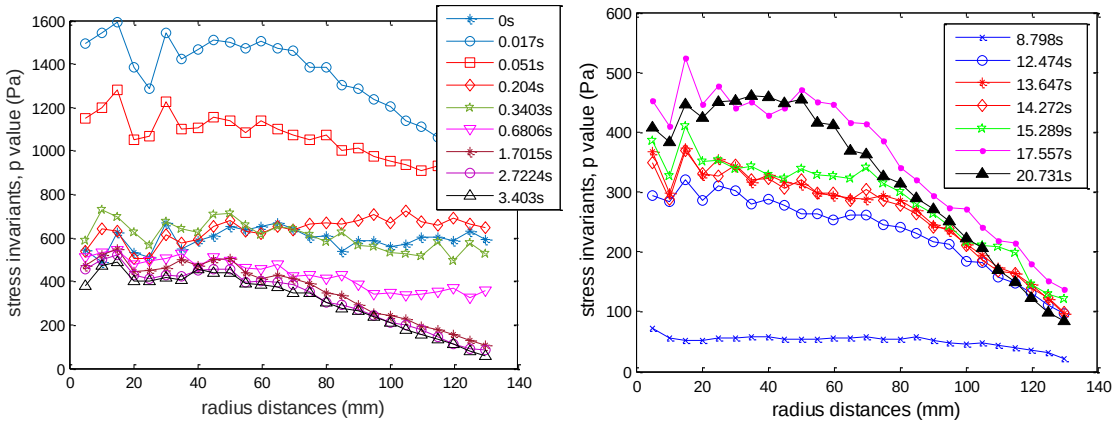
Figure 7.1 Force chains network for different construction histories

7.2.2 Observations of stress distribution

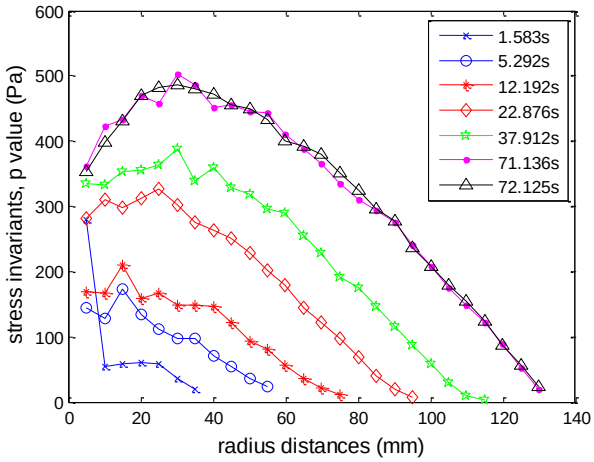
7.2.2.1 Progressive stress behaviour

Section 4.5 studies the stress distribution at the final stage using stress tensor. In this section, it extends the observation to the progressive stress distribution for particles interacted with the base plane using Eq.(4.10). The average void ratio for the specimen is adopted to estimate the stress tensor of each particle. Figure 7.2 below displays the evolution of p value with the radius distances in different preparation methods. The results are slightly smaller compared with those obtained based on the contact force using the Voronoi tessellation method. This may be related to the void ratio considered for each particle. With regards to the boundary removal method, at the initial stage, the p values are uniformly distributed on the base plane. After removing the boundary, the stress increases first, followed by a continuous decrease during the formation of the sand pile. No pressure dip phenomenon is obtained when using this preparation method.

Concerning the deposition methods, the peak stress increases with the development of the sand pile. For the rain deposition test, the peak pressure is observed under the central apex at each stage. After particles achieving the equilibrium condition, the value of the peak pressure decreases slightly. With regards to the point deposition test, the peak pressure appears under the central apex of the sand pile at the initial stage. Then, with the particles deposited, the radius distance for the occurrence of peak pressure increases. In the final stage, the stress distribution is smoother in contrast with that using the Voronoi tessellation method. The pressure dip phenomenon is also observed, with the peak pressure appearing at the radius distance of $37.5mm$. This demonstrates that the stress tensor could capture the stress state inside sand pile at the progressive stages.



(a) boundary removal method (b) rain deposition method



(c) point deposition method

Figure 7.2 The observation of p value on the base plane

7.2.3 Spatial distribution of the stress behaviour

To further investigate the stress behaviour, the evolution of the components of the stress tensor is taken into account with the spatial distribution. Depending on the symmetrical condition of the sand pile, the results are presented using the cylindrical coordinate system. The following gives the transformation of a tensor from the Cartesian coordinate system to the cylindrical coordinate system.

$$\begin{bmatrix} S_{rr} & S_{r\vartheta} & S_{rz} \\ S_{\vartheta r} & S_{\vartheta\vartheta} & S_{\vartheta z} \\ S_{zr} & S_{z\vartheta} & S_{zz} \end{bmatrix} = \begin{bmatrix} \cos\vartheta & \sin\vartheta & 0 \\ -\sin\vartheta & \cos\vartheta & 0 \\ 0 & 0 & 1 \end{bmatrix} \begin{bmatrix} S_{xx} & S_{xy} & S_{xz} \\ S_{yx} & S_{yy} & S_{\vartheta z} \\ S_{zx} & S_{xy} & S_{zz} \end{bmatrix} \begin{bmatrix} \cos\vartheta & -\sin\vartheta & 0 \\ \sin\vartheta & \cos\vartheta & 0 \\ 0 & 0 & 1 \end{bmatrix} \quad (7.1)$$

in which (e_x, e_y, e_z) is the unit vector in the Cartesian coordinate system, and (e_r, e_ϑ, e_z) refers to the unit vector in the cylindrical coordinate system. S denotes the stress tensor, and ϑ is the direction of each particle located in the cylindrical coordinate system. The coordinates of a particle are calculated by the following equation for the cylindrical coordinate system

$$\begin{cases} r = \sqrt{x^2 + y^2} \\ \vartheta = \tan^{-1}\left(y/x\right) \\ z = z \end{cases} \quad (7.2)$$

where (x, y, z) are the coordinates of the particle in the Cartesian coordinate system. In the cylindrical coordinate system, the coordinates are denoted as (r, ϑ, z).

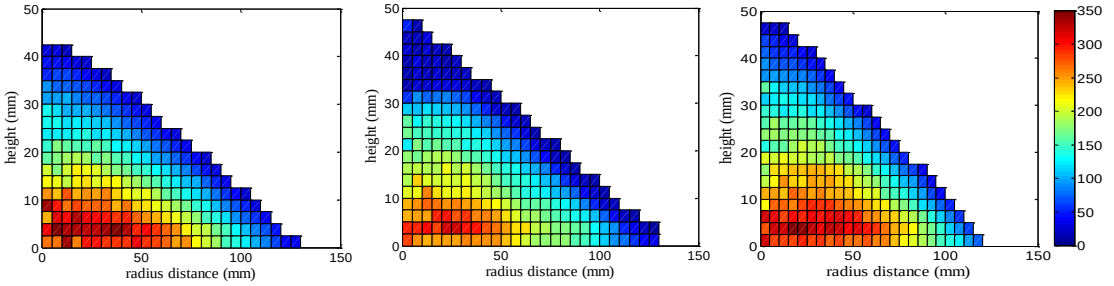
To obtain the spatial distribution, the stress tensor of each particle was first calculated in the cylindrical coordinate system. A hollow cylinder region is applied to obtain the spatial distribution of stress components. The region has a radius distance ranging from $R_{d(i-1)}$ to $R_{d(i)}$ and a height in the range of $\left[h_{d(i-1)}, h_{d(i)}\right]$, in which $R_{d(i)}$ and $h_{d(i)}$ refer to the i^{th} representative radius distances and heights respectively. The centre coordinates are used to determine the location of the particles. The initial and interval radius distances are set to $5mm$. For the height, the starting point and interval value are selected to be $2.5mm$.

The results of the stress components are presented in Figure 7.3 to Figure 7.6 for various preparation methods at the final stage. The base layer contains the largest stress with the

maximum value appearing in the z-axis component of the stress tensor. The core regions, within the radius distance of $30mm$ and height of $10mm$, are subjected to higher magnitudes of $\sigma_{rr}, \sigma_{\theta\theta}$ and σ_{zz} under rain deposition and boundary removal methods. With regards to the point deposition test, it produces larger values at a radius distance of around $40mm$. Reagrding the stress $\sigma_{rr}, \sigma_{\theta\theta}, \sigma_{zz}$ in the region near the free surface, the rain deposition test produces the smallest values compared with the boundary removal and point deposition tests.

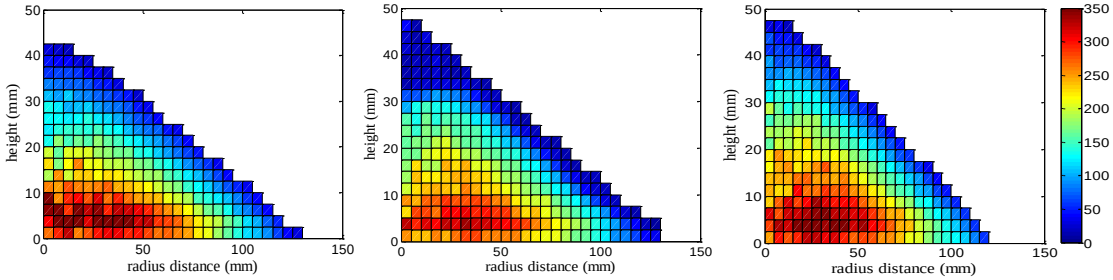
In the (r, z) space, within the radius distance of $10mm$, the point deposition test produces a larger magnitude of stress than the boundary removal and rain deposition tests. In addition, the point deposition test contains a higher percentage of the larger stress in this direction with the radius distance of $(35, 70)mm$ and height of $10mm$, in contrast with the boundary removal and rain deposition methods.

The results of stress field suggest that the rain deposition method decreases the stress (all three principal stresses) at the top surface than the boundary removal and point deposition methods. A more isotropic condition is observed for the boundary removal method when comparing the value of σ_{rz}. However, for the point deposition test, it contains a higher percentage of the rotated principal stresses indicated by the wide distribution of the larger value of σ_{rz}. In such a case, the point deposition test increases the anisotropic condition of the specimen.



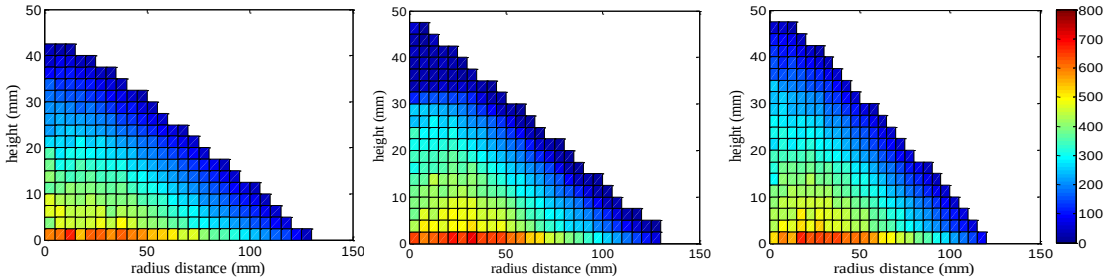
(a) boundary removal (b) rain deposition (c) point deposition

Figure 7.3 The behaviour of σ_{rr} at the final stage with various preparation methods



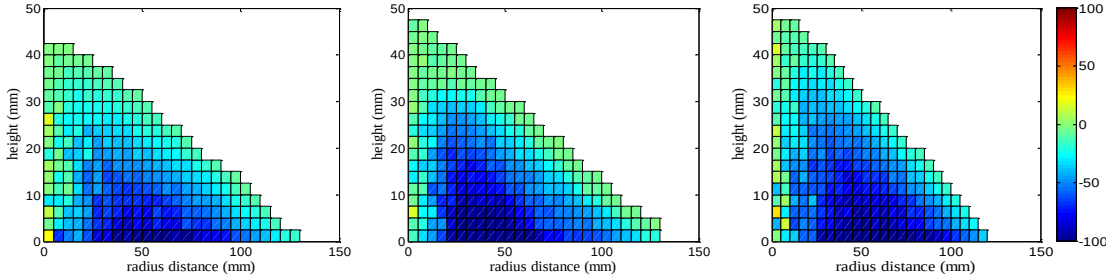
(a) boundary removal (b) rain deposition (c) point deposition

Figure 7.4 The behaviour of $\sigma_{\theta\theta}$ at the final stage with various preparation methods



(a) boundary removal (b) rain deposition (c) point deposition

Figure 7.5 The behaviour of σ_{zz} at the final stage with various preparation methods

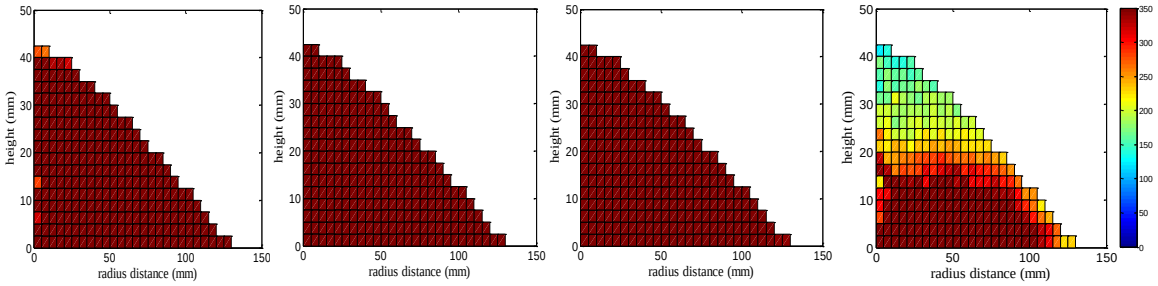


(a) boundary removal (b) rain deposition (c) point deposition

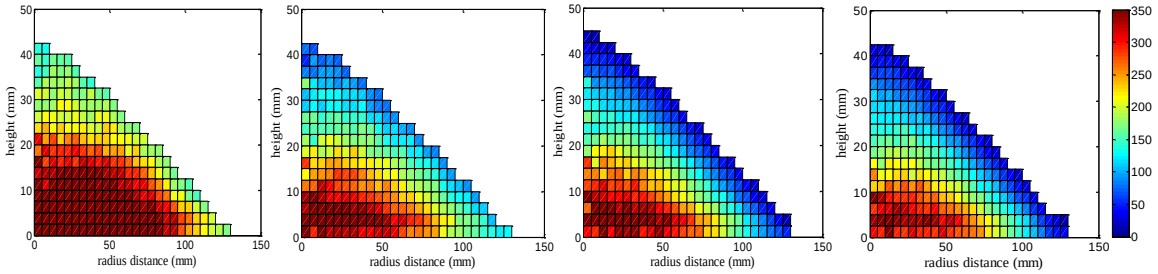
Figure 7.6 The behaviour of σ_{rz} at the final stage with various preparation methods

The counter-intuitive phenomenon is suggested relating to the dynamic formation process. Hence, the progressive spatial distribution of the stress components is observed in different preparation methods to further investigate the impact of loading paths on the stress field. Figure 7.7 to Figure 7.10 present the progressive spatial distribution of the stress components in the boundary removal test. To capture the loading effect on the formation of sand pile in the progressive stages, it observes the stress behaviour under the same region as the sand pile at the final stage. Thus, the region is not rectangular at the initial stage.

Owing to the higher height of the specimen, the magnitude of all the three principal stresses is much larger in the initial stages. The stresses of σ_{rr}, $\sigma_{\theta\theta}$ and σ_{zz} exhibit a similar behaviour during the formation process, with a decrease in the region near the top surface first after removing the boundary. Then, lower stresses develop to the free surface of the sand pile. Regarding σ_{rz}, in the intermediate stages, larger magnitude of stress appears near the edge of the boundary along with larger displacements of particles. After the specimen achieving the equilibrium condition, the magnitude of σ_{rz} reduces in this region.

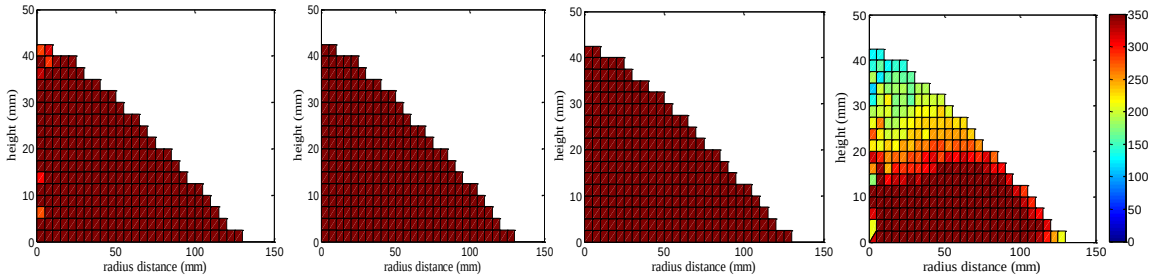


(1) 0s (2) 0.017s (3) 0.051s (4) 0.204s

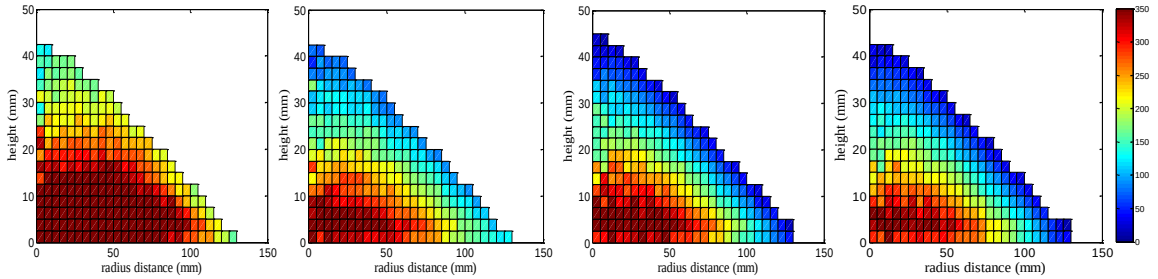


(5) 0.3403s (6) 0.6806s (7) 1.7015s (8) 2.7224s

Figure 7.7 The progressive behaviour of σ_{rr} for the boundary removal test

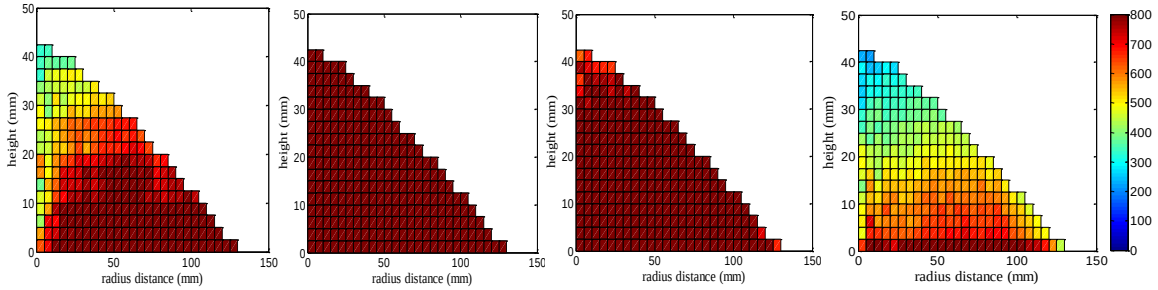


(1) 0s (2) 0.017s (3) 0.051s (4) 0.204s

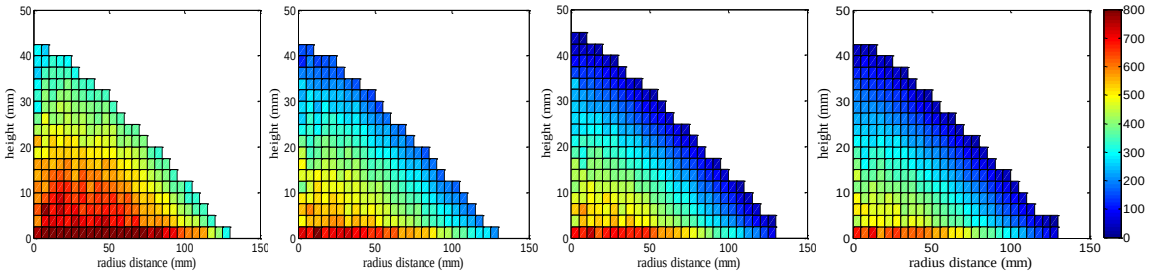


(5) 0.3403s (6) 0.6806s (7) 1.7015s (8) 2.7224s

Figure 7.8 The progressive behaviour of $\sigma_{\theta\theta}$ for the boundary removal test

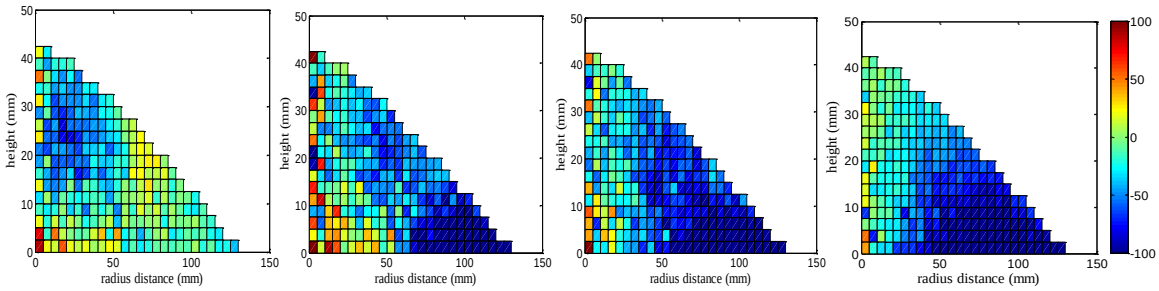


(1) 0s (2) 0.017s (3) 0.051s (4) 0.204s

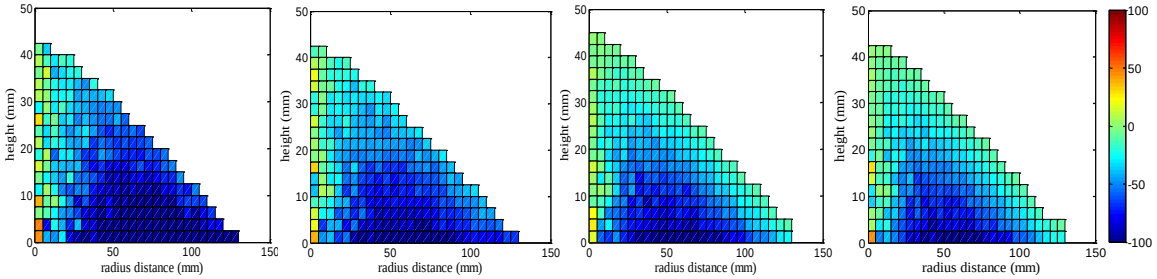


(5) 0.3403s (6) 0.6806s (7) 1.7015s (8) 2.7224s

Figure 7.9 The progressive behaviour of σ_{zz} for the boundary removal test



(1) 0s (2) 0.017s (3) 0.051s (4) 0.204s

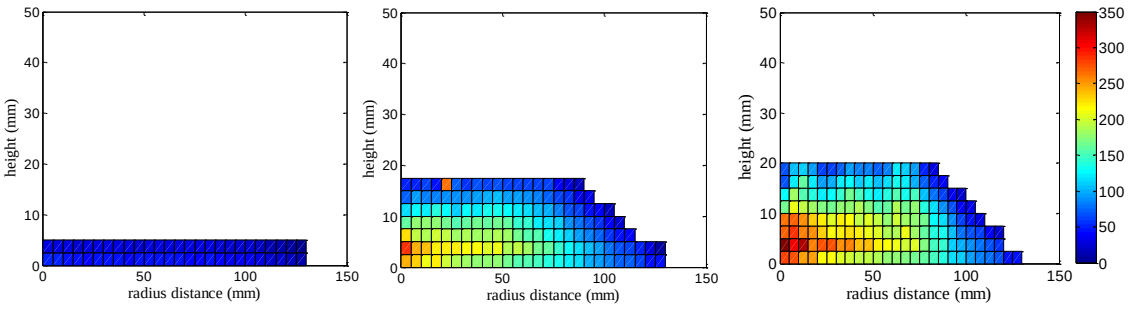


(5) 0.3403s (6) 0.6806s (7) 1.7015s (8) 2.7224s

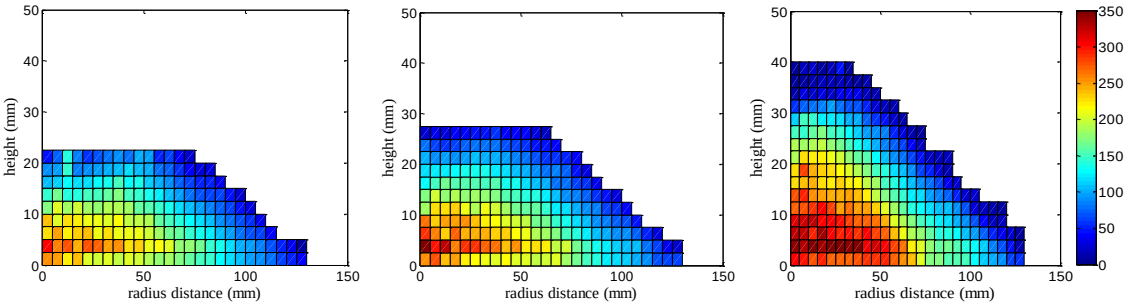
Figure 7.10 The progressive behaviour of σ_{rz} for the boundary removal test

Figure 7.11 to Figure 7.14 display the behaviour of stress components in the rain deposition test. In the progressive stages, higher stress magnitudes (of all the three principal stresses) were found in the core region than in other regions. The lowest magnitudes of σ_{rr}, $\sigma_{\theta\theta}$ and σ_{zz} appear near the free surface of the specimen at each stage. However, regarding σ_{rz}, the lowest value occurred within the core region at each stage. At the initial stages, the peak stress of σ_{rz} appears near the edge of the boundary. With the continuous deposition of

particles, the larger-magnitude stress transfers from the radius distance of 100*mm* to the radius distance of approximately 50*mm* inside the sand pile. It is suggested that the specimen is under a more isotropic condition in the core region.

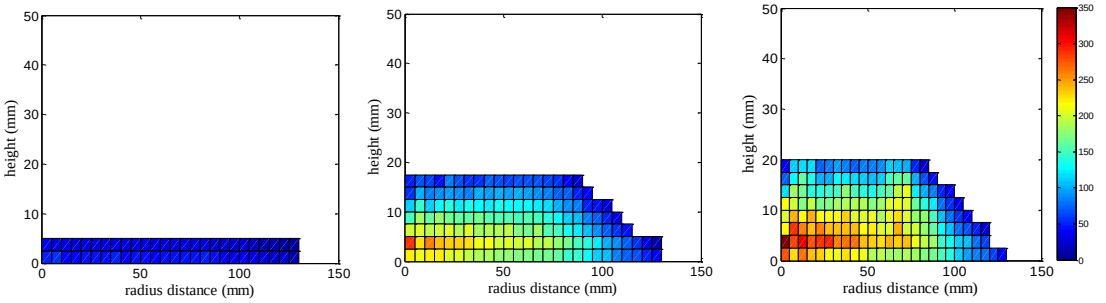


(1) 8.798s (2) 12.474s (3) 13.647s

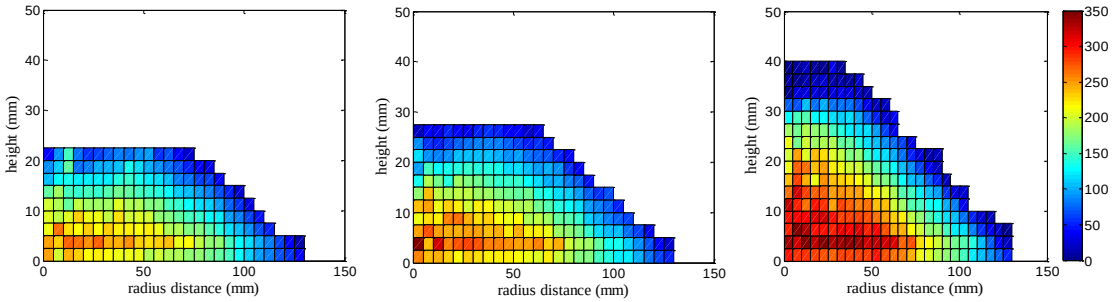


(4) 14.272s (5) 17.557s (6) 20.731s

Figure 7.11 The progressive behaviour of σ_{rr} for the rain deposition test

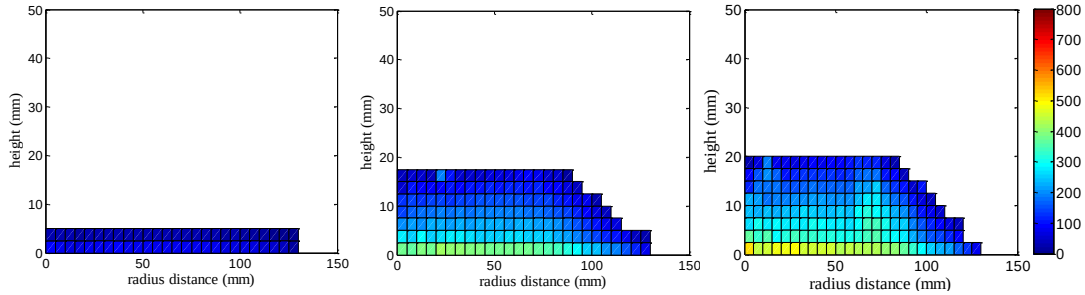


(1) 8.798s (2) 12.474s (3) 13.647s

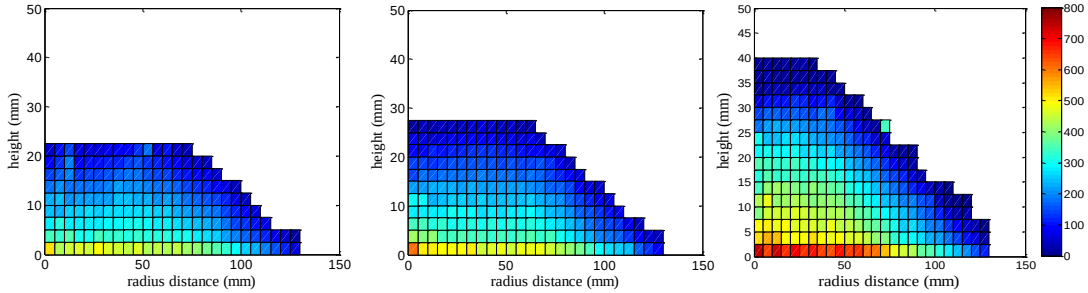


(4) 14.272s (5) 17.557s (6) 20.731s

Figure 7.12 The progressive behaviour of $\sigma_{\theta\theta}$ for the rain deposition test

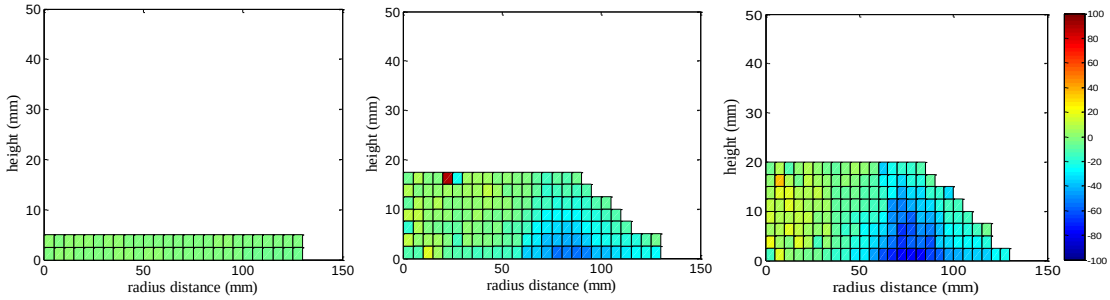


(1) 8.798s (2) 12.474s (3) 13.647s

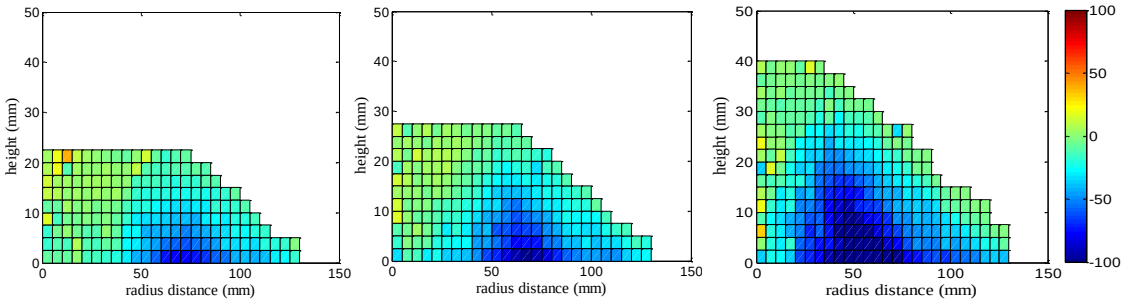


(4) 14.272s (5) 17.557s (6) 20.731s

Figure 7.13 The progressive behaviour of σ_{zz} for the rain deposition test



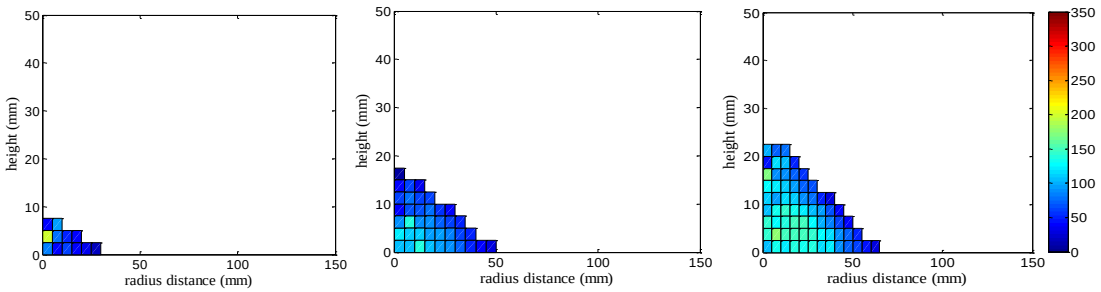
(1) 8.798s (2) 12.474s (3) 13.647s



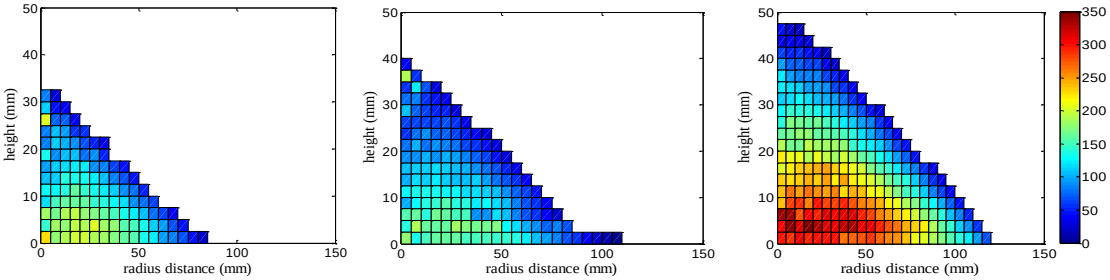
(4) 14.272s (5) 17.557s (6) 20.731s

Figure 7.14 The progressive behaviour of σ_{rz} for the rain deposition test

For the point deposition test, the behaviour of stress components is presented in Figure 7.15 to Figure 7.18. The peak stress (for all the three principal stresses) is shown to develop from the radius distance of $0mm$ to the radius distance of $35mm$ inside the sand pile. The stresses of σ_{rr}, $\sigma_{\theta\theta}$ and σ_{zz} are approximately zero at the free surface of the sand pile. With regards to σ_{rz}, the value is smaller at the initial stage. It also transfers from the radius distance of $5mm$ to the radius distance of approximately $50mm$ during the sand pile formation. The region within the radius distance of $15mm$ sees a larger magnitude of σ_{rz} than the boundary removal and rain deposition tests at each stage, which indicates that the concentrated loading of particles increases the anisotropic condition of the materials.

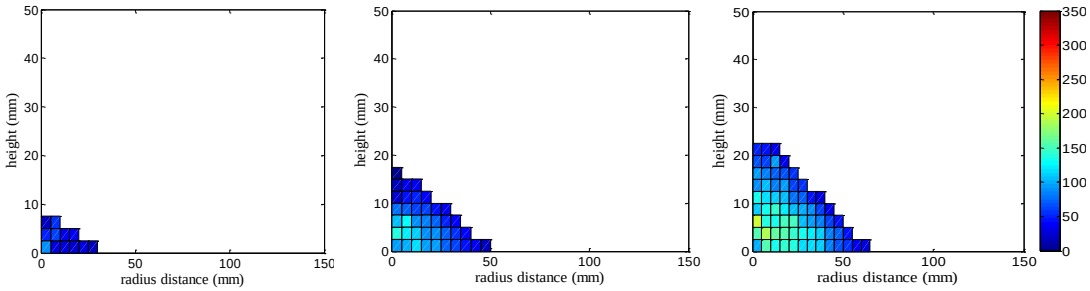


(1) 1.583s (2) 5.292s (3) 12.192s

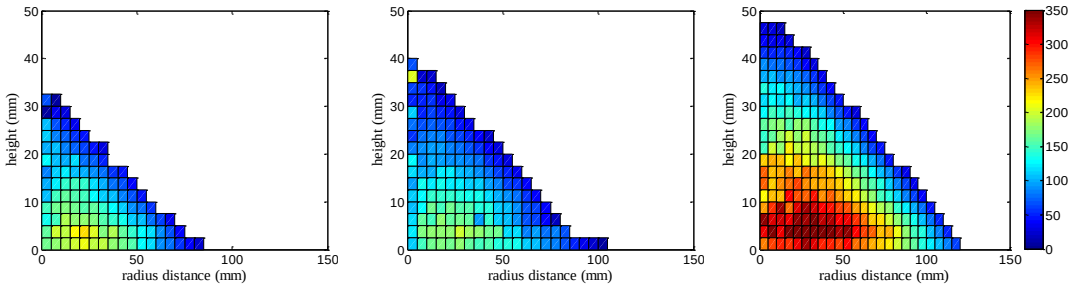


(4) 22.876s (5) 37.912s (6) 71.136s

Figure 7.15 The progressive behaviour of σ_{rr} for the point deposition test

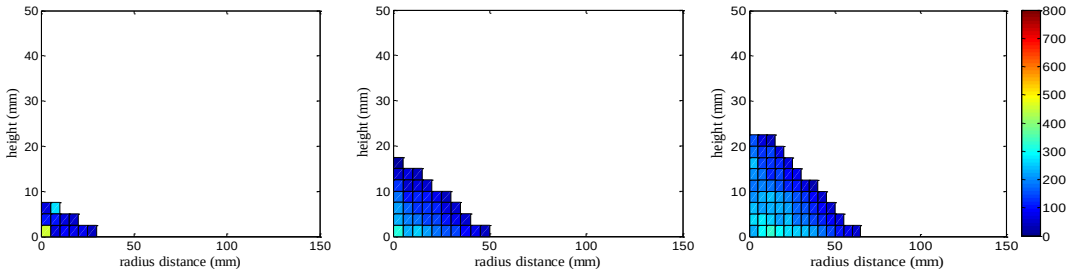


(1) 1.583s (2) 5.292s (3) 12.192s

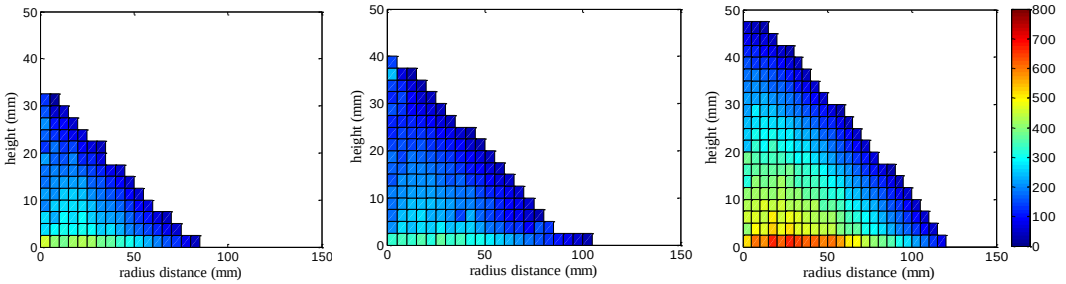


(4) 22.876s (5) 37.912s (6) 71.136s

Figure 7.16 The progressive behaviour of $\sigma_{\theta\theta}$ for the point deposition test

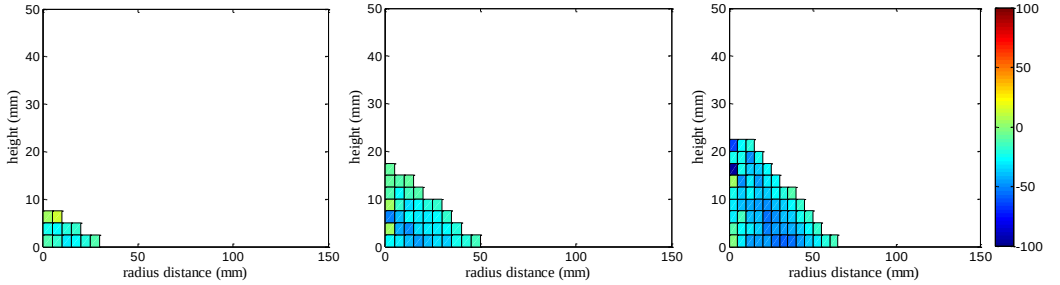


(1) 1.583s (2) 5.292s (3) 12.192s

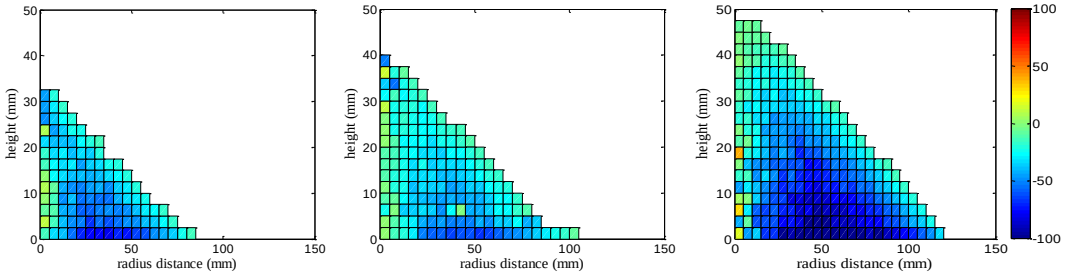


(4) 22.876s (5) 37.912s (6) 71.136s

Figure 7.17 The progressive behaviour of σ_{zz} for the point deposition test



(1) 1.583s (2) 5.292s (3) 12.192s

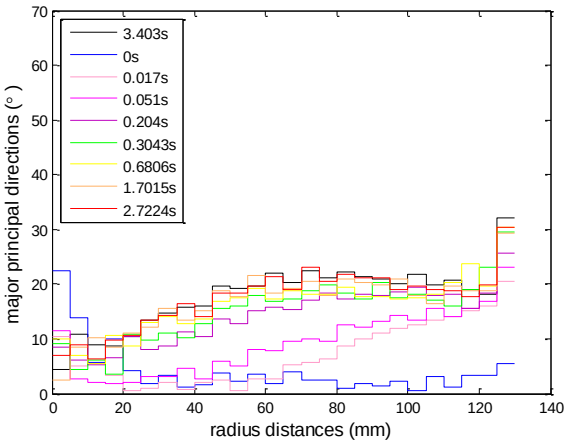


(4) 22.876s (5) 37.912s (6) 71.136s

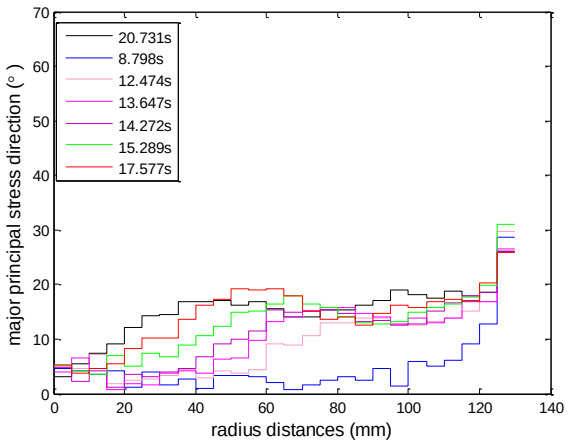
Figure 7.18 The progressive behaviour of σ_{rz} for the point deposition test

The corresponding evolution of major principal stress direction is further observed for the layer of $[0,2.5]mm$ under various preparation methods as presented in Figure 7.19. The direction in the graphs refers to the angle with the *z*-axis. The point deposition test produces a relatively larger direction of the major principal stress during deposition than the rain deposition method, in particular within the radius distances of $20mm$. The rain deposition test produces a similar principal direction within this region at different stages. In the

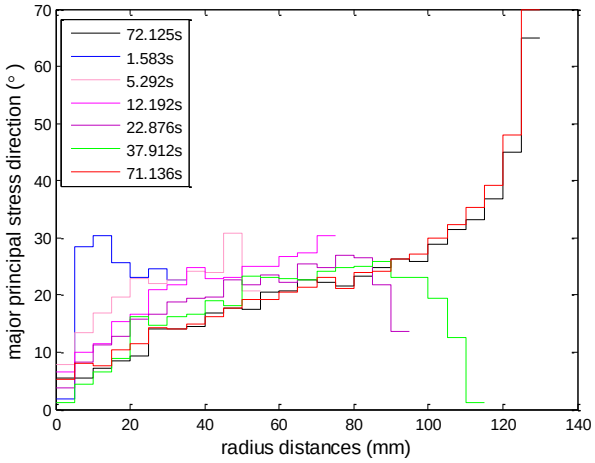
intermediate region, within the span of $[20,60]mm$, the boundary removal and rain deposition methods produce an increase of the principal stress direction during simulation. However, regarding the point deposition method, it is reduced for the sand pile formation.



(1) boundary removal test



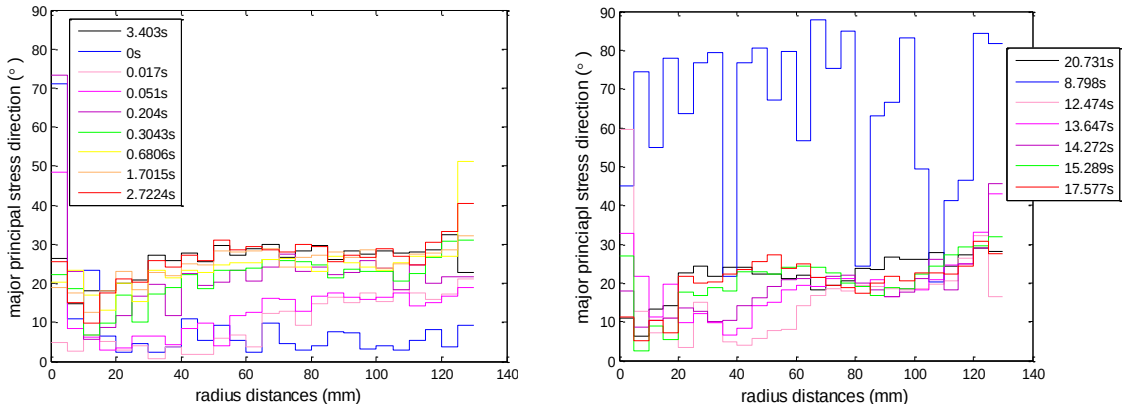
(2) rain deposition test



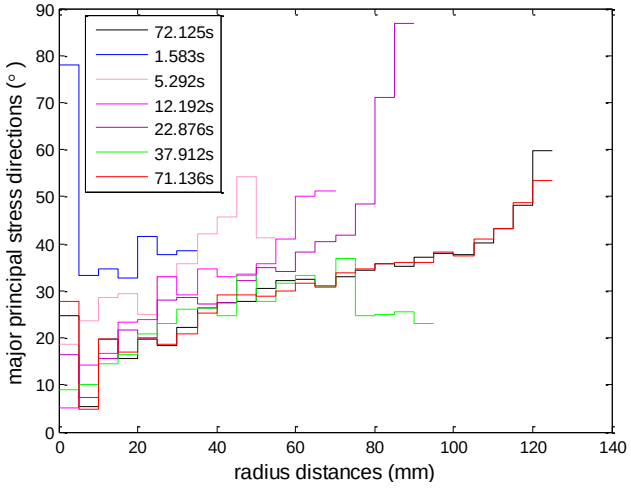
(3) point deposition test

Figure 7.19 The progressive direction of major principal stress for the layer of [0,2.5]*mm*

For the layer of $[2.5,5]mm$, the direction is larger than the layer of $[0,2.5]mm$ for all the three tests according to Figure 7.20. For the rain deposition test, at the initial stage, owing to the smaller number of particles and the impact of packing, it produces a higher angle for the major principal stress. Afterwards, it drops quickly with the deposition of particles. A larger angle of principal stress direction is observed underneath the apex for the point deposition method.



(1) boundary removal test (2) rain deposition test



(3) point deposition test

Figure 7.20 The directions of major principal stress direction for the layer of [2.5,5]mm

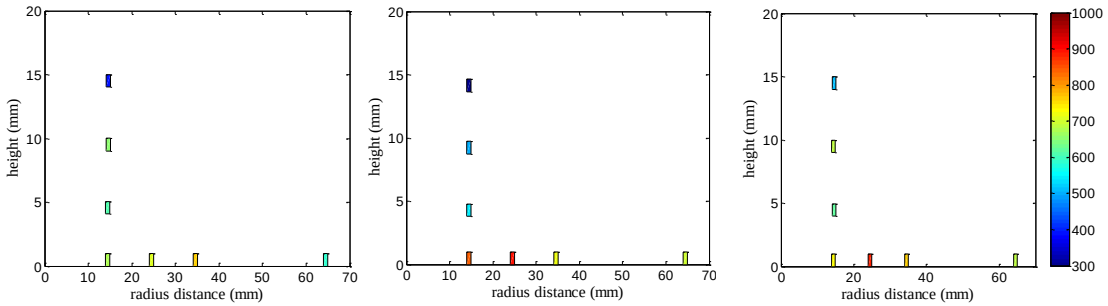
According to the results, underneath the apex, the mechanism of granular materials under the rain deposition test behaves as the loading path of triaxial compression owing to the similar major principal stress direction near zero in the progressive stages. However, for the point deposition test, particles encompass a rotational loading path with respect to the change of the principal stress direction during deposition underneath the apex. Furthermore, with the knowledge of the RVE material response in Chapter 6, it identifies that the granular materials contain a larger plastic deformation for the point deposition test.

7.2.4 The stress behaviour at representative element regions

In order to further identify the impact of loading path, the pressures of a number of particles are traced during the formation process. The particles in different regions (i.e. particles located at different radius distances and heights) are defined at the final stage. Consequently, the particles are traced back via the identified number and the radius during the sand pile formation.

Four different radius distance values of $15mm$, $25mm$, $35mm$ and $65mm$ are used to observe and trace the pressure distribution on the base plane. To reduce the fluctuation of the results, the pressures are averaged over the particles located inside the radius distance with a span of $1mm$ taken to be one average particle size. Three different heights of, $5mm$, $10mm$ and $15mm$, are selected within the radius distances in the range of $[14,15]mm$ to further trace the particles inside the sand pile. Approximately 800 particles are traced during the simulation. The centre coordinates are considered to determine the location of particles. For each hollow cylinder region, it is represented by the average value of the particles.

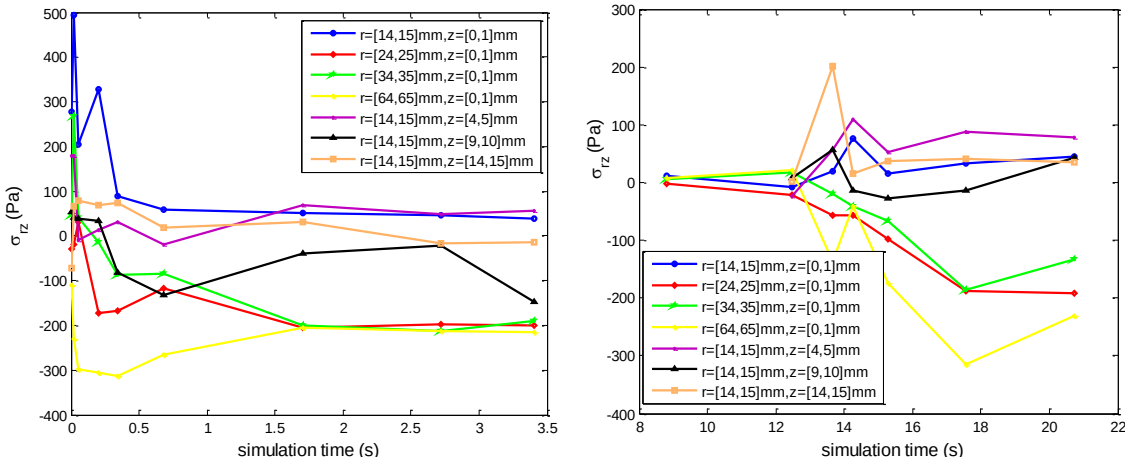
Figure 7.21 below shows the behaviour of the p value at the final stage and represents the locations of particles in the three preparation methods. Different stress behaviour is observed for the elements in the same region with various construction histories. The peak pressure appears in the core region at each stage for both the boundary removal and rain deposition tests. Regarding the point deposition test, the peak pressure occurs at the radius distance of approximately $25mm$.



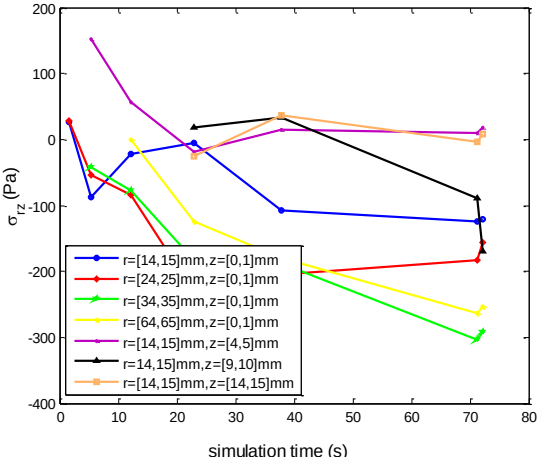
(1) boundary removal (2) rain deposition (3) point deposition

Figure 7.21 Trace of p value at the final stage for the three preparation methods

Section 7.2.3 shows that the significant difference appears for the stress σ_{rz} under various preparation method. To present the impact of construction history, results of the progressive behaviour of stress σ_{rz} are illustrated in Figure 7.20 at different regions. The behaviour of other stress components are presented in Appendix C.1. The point deposition test sees the largest value at each region among all three tests. The boundary removal test produces smaller stress in the (r,z) space. A smaller stress value is observed at the initial stages in the rain deposition test. In addition, within the radius distance of $15mm$, the stress is approximately zero after sample achieving the equilibrium condition.



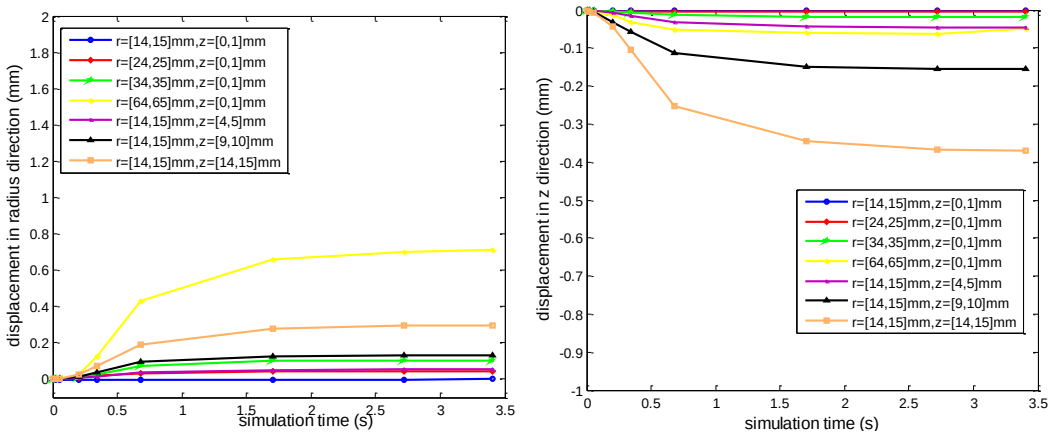
(a) boundary removal (b) rain deposition



(c) point deposition

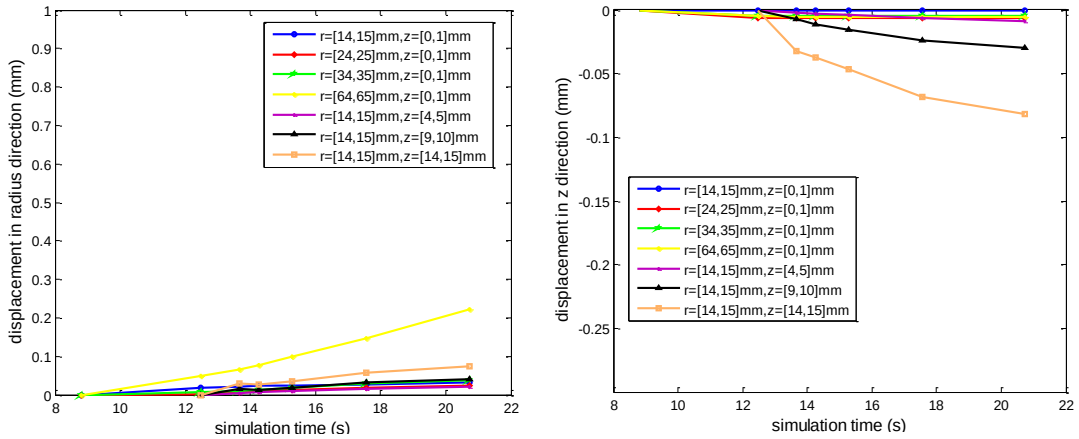
Figure 7.22 The progressive behaviour of traced stress component σ_{rz}

Furthermore, the displacement is also taken into account to observe the impact of construction history. For each region, the displacement is decomposed into components in the radius and z directions respectively. To calculate the displacement, the coordinates are first estimated in each region (treated as the average centre coordinates of particles located in the region) at each stage. Then, the progressive displacement is estimated with reference to displacements in the initial traced stage. According to the graphs, the rain deposition test produces smaller displacements, in particular for the particles interacted with the base plane. The point deposition test sees the largest displacements for all the regions.



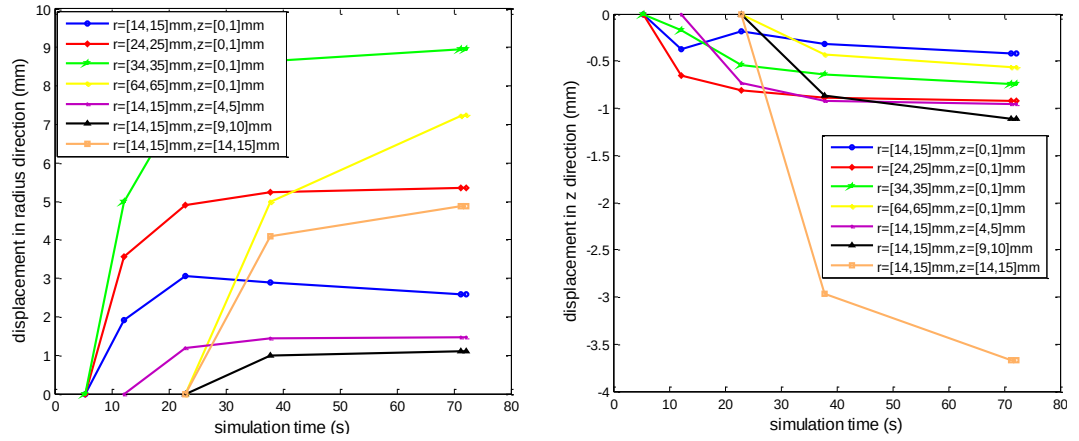
(1) radius direction (2) z direction

(a) boundary removal test



(1) radius direction (2) z direction

(b) rain deposition test



(1) radius direction (2) z direction

(c) point test

Figure 7.23 The displacement of traced region with different construction histories

7.3 Comparison with the continuum theory

As presented in Chapter 2, Wittmer et al. (1996) proposed a continuum theory based on the fixed principal stress directions to observe the pressure dip phenomenon on the base plane. They assumed that $\sigma_{rr} = \sigma_{\theta\theta}$ at all points. The normalised pressure (estimated as $p/(\rho g h)$, where p is the normal pressure, ρ and h refer to the density and height of sand piles respectively) in the point deposition test is compared with the solutions by Wittmer et al.

(1996) in Figure 7.24. The tendency of the simulation results is similar to the results from the continuum theory. For σ_{zz}, the results using continuum theory give a similar prediction, in particular with the normalised radius distance larger than 0.35. It is shown that the magnitude of σ_{rz} is larger compared with the results from the simulations. In general, the continuum theory yields similar but not identical results to the simulations without the consideration of the boundary properties and the principal stress directions distrbution.

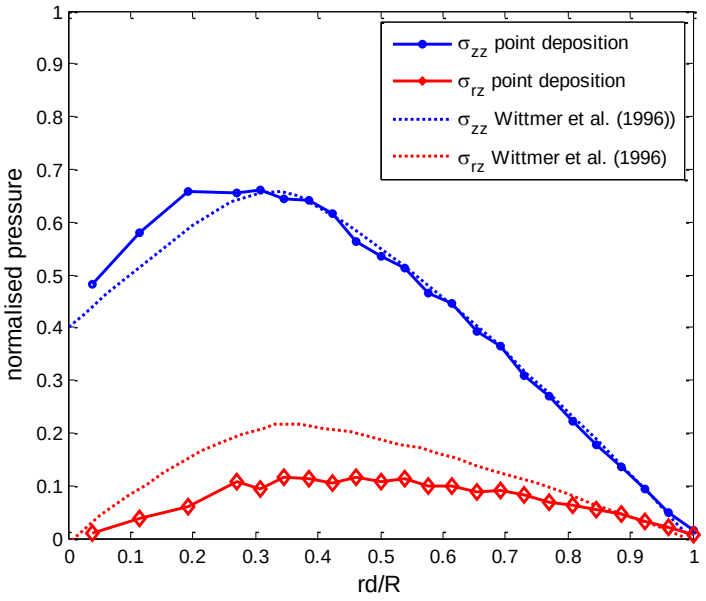


Figure 7.24 The normalised pressure distribution for the point deposition test

The continuum mechanical approach determined the stress distribution based on some closures with the relationship of the stress components as reviewed in Chapter 2. Employing the results of stress tensor, the relationship of the different closures can be validated from the results of σ_{rr} which shows that the relationship is more appropriate for the IFE model under the passive condition. For the FPA model, the tendency is similar to the simulation results. However, the value is much larger compared with the simulation results. It may be related to the negligence of the stress $\sigma_{\theta\theta}$ in the relationship.

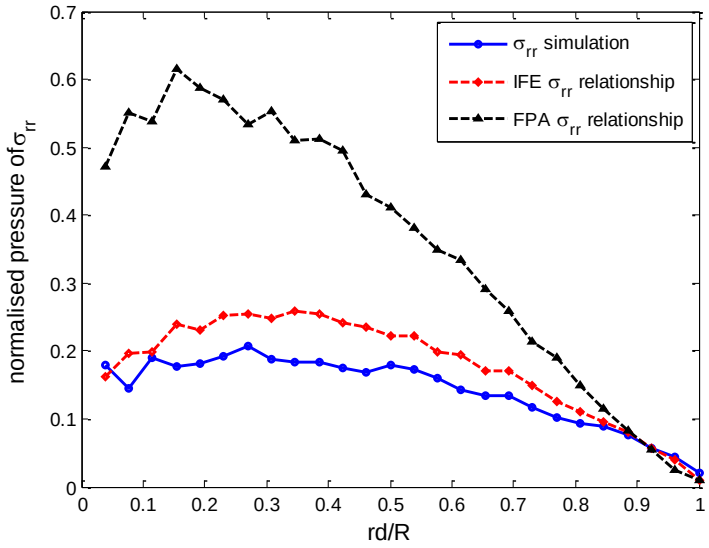


Figure 7.25 The validation of the closures for the determination of stress distribution

7.4 Observations of internal structure

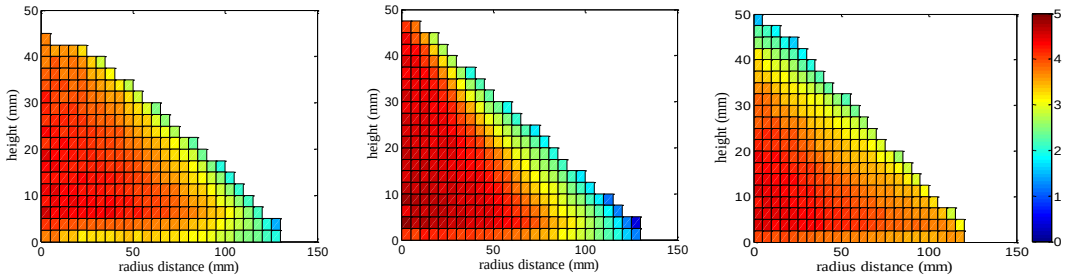
The structure of granular materials may lead to anisotropic behaviour under various loading conditions. Material anisotropy always has a significant impact on the structural stress-strain responses, according to extensive experimental studies. The feature of stress distribution suggests that different internal structure results from different construction histories. The fabric is quantified by the coordination number and orientation-related fabric tensor consisting of contact normal. It is employed to observe the progressive fabric anisotropy in order to provide an insight into the material behaviour.

7.4.1 Progressive distribution of average coordination number

The coordination number in the assemblies of granular materials relates to the mechanism of a random arrangement of constituent particles. In order to represent the shape of the sand pile, the average coordination number is measured inside the sand pile under the cylindrical coordinate system. The hollow cylinder region, with the radius distance ranging from $R_{d(i-1)}$

to $R_{d(i)}$ and the height in the range of $\left[h_{d(i-1)}, h_{d(i)}\right]$, is also applied to observe the spatial distribution of average coordination number. To obtain the results, firstly, the number of contacts for each particle is calculated. Then, the results are averaged with particles located in the hollow cylinder region. The starting point and interval radius distance are both selected as $5mm$, approximately the size of five average particles. For heights, the starting point and interval distance are set to $2.5mm$.

Figure 7.26 provides the distribution of average coordination number with various preparation methods. The coordination number is uniformly distributed inside the sand pile in the boundary removal test. A relatively smaller average coordination number appears nears the edge of the boundary. For the rain deposition test, it produces the largest average coordination number in the core region than the boundary removal and rain deposition tests, with the lowest value appears near the free surface of the sand pile. The point deposition test shows a smaller average coordination number near the top surface of the sand pile.

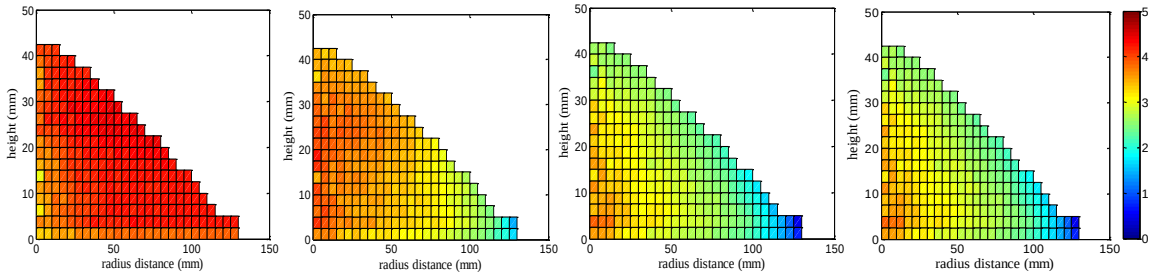


(1) boundary removal (2) rain deposition (3) point deposition

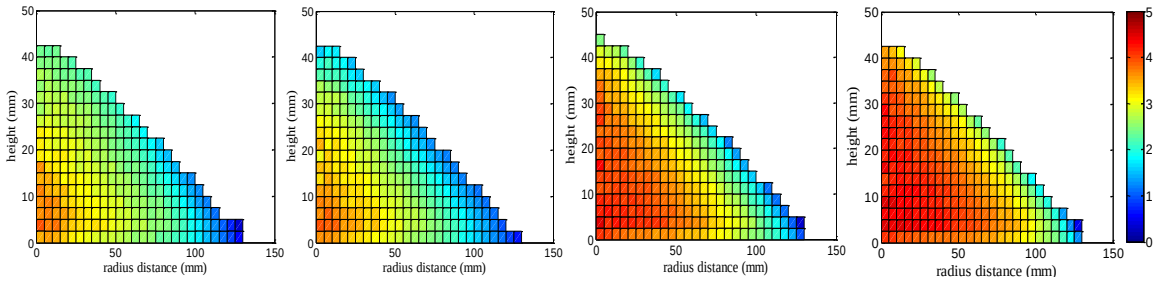
Figure 7.26 Average coordination number at the final stage with various preparation methods

To observe the impact of construction history, the progressive average coordination number is presented in Figure 7.27 to Figure 7.29. In the boundary removal test, the average coordination number is uniformly distributed on the plane at the initial stage. Underneath the central apex, it contains a larger average coordination number at each stage. After removing the boundary, a relatively smaller average coordination number appears near the

free surface of sand pile, as a result of larger displacements of particles. The average coordination number decreases first in the core region. Then, after achieving the equilibrium condition, it increases again in this region.



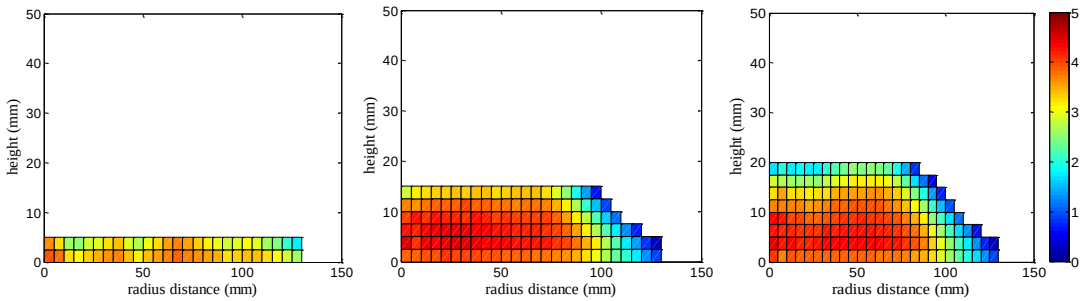
(1) 0s (2) 0.017s (3) 0.051s (4) 0.204s



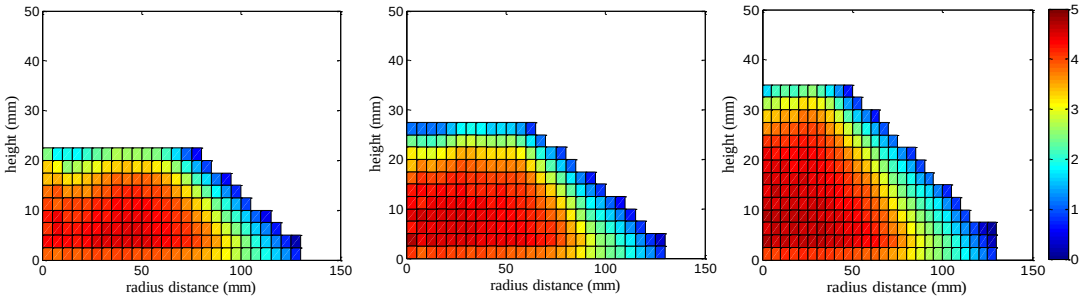
(5) 0.3403s (6) 0.6806s (7) 1.7015s (8) 2.7224s

Figure 7.27 Progressive average coordination number for the boundary removal method

In the rain deposition test, the region near the free surface of sand pile contains the lowest value of average coordination number, owing to the larger displacements of particles. The peak average coordination number also appears in the core region at each stage, which indicates that a lower number of voids exist in the core region.



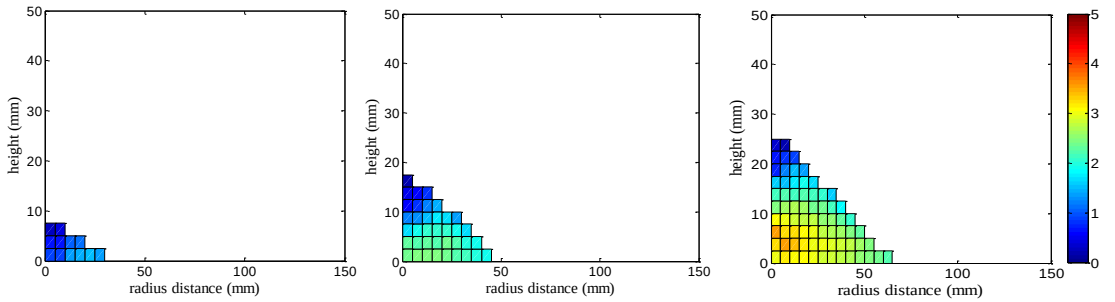
(1) 8.798s (2) 12.474s (3) 13.647s



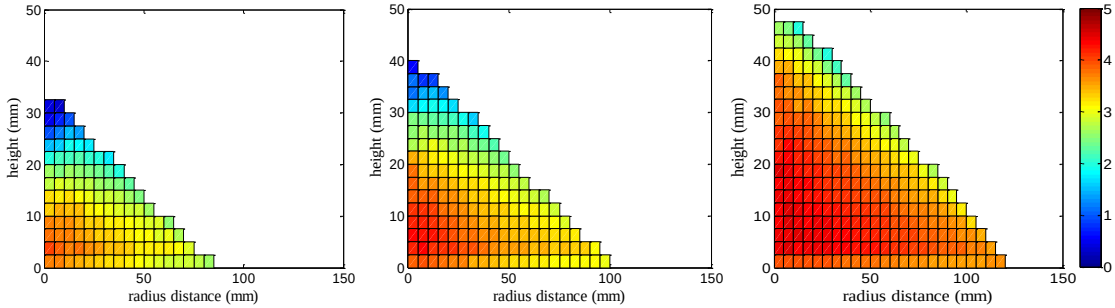
(4) 14.272s (5) 17.557s (6) 20.731s

Figure 7.28 Progressive average coordination number of rain deposition test

In the point deposition test, the specimen should be under a relatively loose condition near the top surface and result in a smaller average coordination number, depending on the loading of particles. Compared with the boundary removal and rain deposition tests, the point deposition test produces a smaller average coordination number in the core region with a larger value occurring near the edge of the boundary for each stage, which suggests that the specimen has a higher possibility of forming arches under the central apex.



(1) 1.583s (2) 5.292s (3) 12.192s



(4) 22.876s (5) 37.912s (6) 71.136s

Figure 7.29 Progressive average coordination number for point deposition test

7.4.2 Progressive spatial distribution of fabric anisotropy

Oda (1972) proposed that the anisotropy of granular materials is mainly due to the biased distribution of the contact normal. In this project, the fabric anisotropy is studied through the local scale and the spatial distribution during the formation of the sand pile.

7.4.2.1 Observation of local anisotropy ---- core region

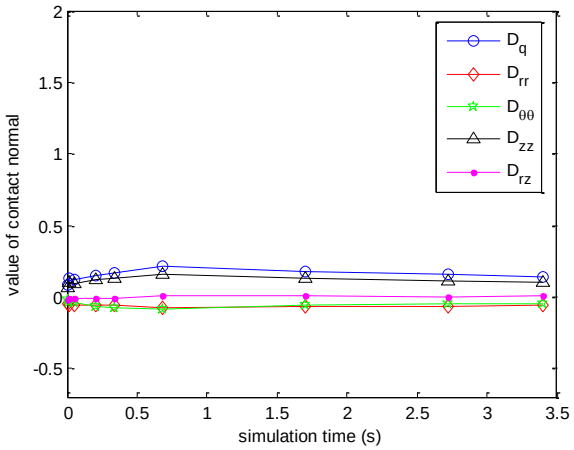
To further identify the impact of construction history, the characteristics of contact normal are studied on a cylindrical element, containing around 10,000 particles with a radius distance of $30mm$ and a height of $10mm$, located in the core region during the progressive stages. Particles are considered within the region as long as the central coordinates located inside. The fabric tensor is obtained first with the total value for each particle which is then averaged with the number of contacts. Eq.(7.3)–Eq.(7.4) gives the estimation of the contact normal tensor $\left(N_{ij}\right)$ and deviatoric contact normal tensor $\left(D_{ij}\right)$ for each particle.

$$N_{ij} = \frac{1}{\omega_p} \sum \boldsymbol{n}_i \boldsymbol{n}_j \tag{7.3}$$

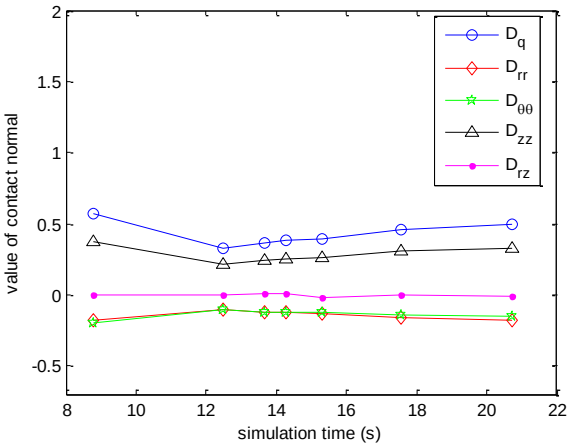
$$D_{ij} = 7.5\left(N_{ij} - \delta_{ij}\right) \tag{7.4}$$

where ω_p refers to the coordination number of each particle. The degree of fabric anisotropy is estimated as $\sqrt{3D_{ij}D_{ji}/2}$. The results are displayed in Figure 7.30 for the three preparation methods, involving the characteristics of the magnitude of fabric anisotropy and fabric components. The component located in the $\left(r,z\right)$ space is approximately zero in all the three methods. In addition, the largest value appears in the *z*-direction of the fabric tensor. The magnitude in boundary removal method is similar at different stages, compared with the other two methods. At the initial stage of the rain deposition method, due to the

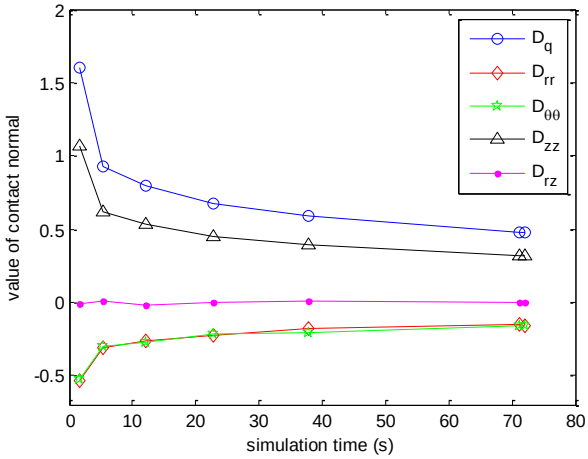
small number of deposited particles, the degree of fabric anisotropy is relatively larger. And then it decreases at the stage of 12.192s followed by a slight increase. Regarding the point deposition method, the largest magnitude of fabric anisotropy appears at the initial stage. Then, the degree continuously reduces and reaches a similar magnitude to the result of rain deposition test at the final stage.



(1) boundary removal



(2) rain deposition



(3) point deposition

Figure 7.30 The progressive contact normal behaviour within the region of r=30mm, z=10mm

7.4.2.2 Observation of fabric anisotropy ---- surface region

To further investigate the local fabric anisotropy, the element located in the surface region is studied under the impact of particles loading. The cylindrical coordinate system is

applied to define the surface region of the specimens in the (r,z) spaces, with the application of the average surface angle and the radius distance. R_d denotes the radius distance of each stage, and the region in the radius direction is defined as the range of $[R_d - 10, \mathrm{R}_d]mm$, approximately ten times the size of the average particle. Combined with the result of the average surface angle, the surface region can be determined. Figure 7.31 below gives an example of the surface region in the three preparation methods.

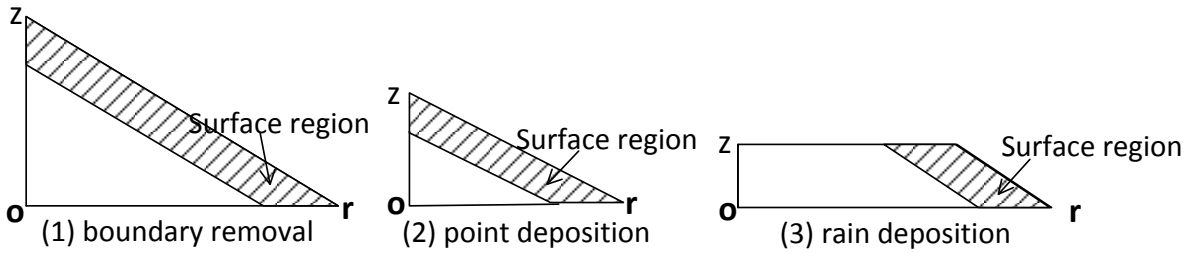
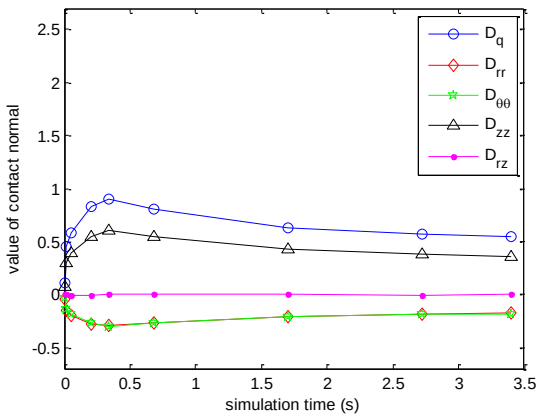
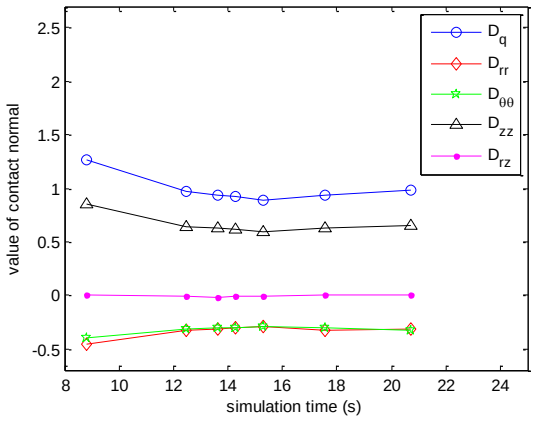


Figure 7.31 Surface region in the progressive stage with different methods

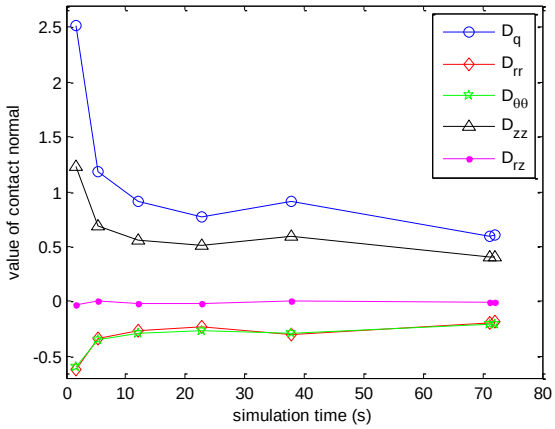
The central coordinate is also employed to determine the location of particles. According to Figure 7.32, a larger degree of fabric anisotropy is observed in the surface region than the results of the core region for all the three tests. After removing the boundary, owing to the larger displacement of particles, the degree of fabric anisotropy increases immediately. In the point deposition test, a higher degree of fabric anisotropy is observed at the initial stage and then reduces due to the loading of particles, with a smaller magnitude than the result of rain deposition test at the final stage.



(1) boundary removal



(2) rain deposition



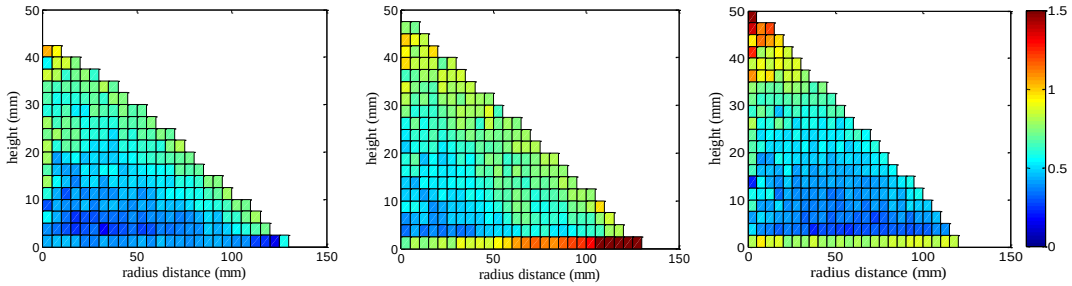
(3) point deposition

Figure 7.32 The anisotropy degree of the contact normal in the surface region

7.4.2.3 Spatial distribution of fabric anisotropy

To further present the internal structure, the spatial distribution of fabric tensor subjected to various construction histories is also studied. The hollow cylindrical region is defined the same as that applied for determining the spatial distribution of stress tensor in Section 7.3. Figure 7.33 displays the degree of fabric anisotropy at the final stage using various preparation methods. For the boundary removal test, compared with the other two methods, it produces the smallest degree of fabric anisotropy for the sand pile within the height of $20mm$.

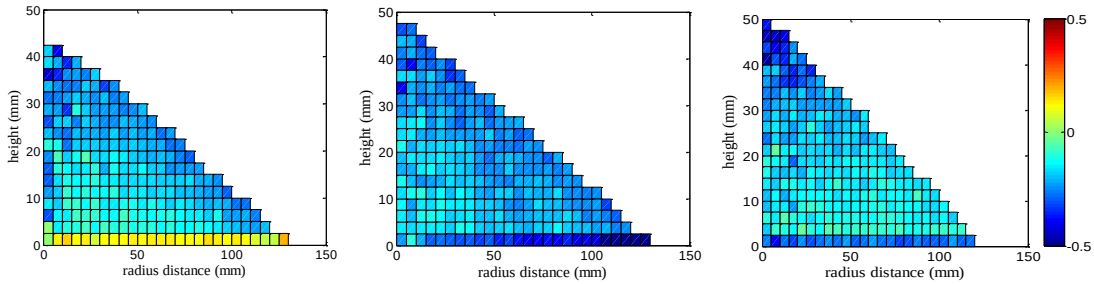
With regards to the rain deposition test, the lowest degree of fabric anisotropy appears within the radius distance of $20mm$. A larger degree of fabric anisotropy is observed from the radius distance of $50mm$ for the base layer. The point deposition test produces a higher magnitude of fabric anisotropy near the top surface of the sand pile, with a relatively larger degree in the core region than the other two construction histories.



(a) boundary removal (b) rain deposition (c) point deposition

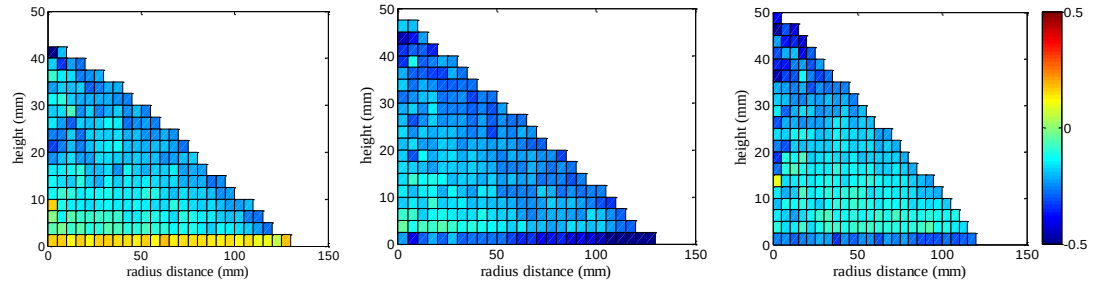
Figure 7.33 Anisotropy degree within sand pile at the final stage

The spatial distribution of fabric components at the final stage is studied in Figure 7.34 to Figure 7.35. For each method, the fabric component of D_{zz} has the largest value. D_{rz} is approximately zero inside the sand pile in all the three methods. The fabric components show a similar characteristic to the behaviour of the degree of fabric anisotropy. The boundary removal test exhibits lower values of fabric anisotropy $D_{rr}, D_{\theta\theta}, D_{zz}$ compared with the other two methods. The rain deposition test sees smaller values of $D_{rr}, D_{\theta\theta}, D_{zz}$ in the core region, with larger magnitudes near the free surface of the sand pile. However, for the point deposition test, a relatively larger values of $D_{rr}, D_{\theta\theta}, D_{zz}$ occurs near the top surface of the specimen.



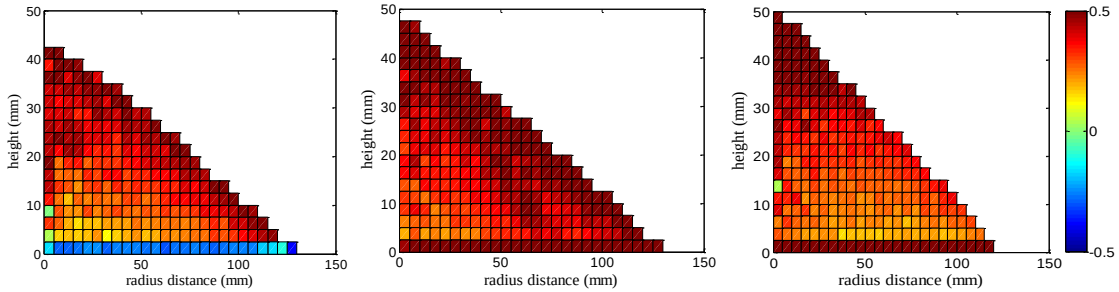
(a) boundary removal (b) rain deposition (c) point deposition

Figure 7.34 The behaviour of D_{rr} at the final stage with various preparation methods



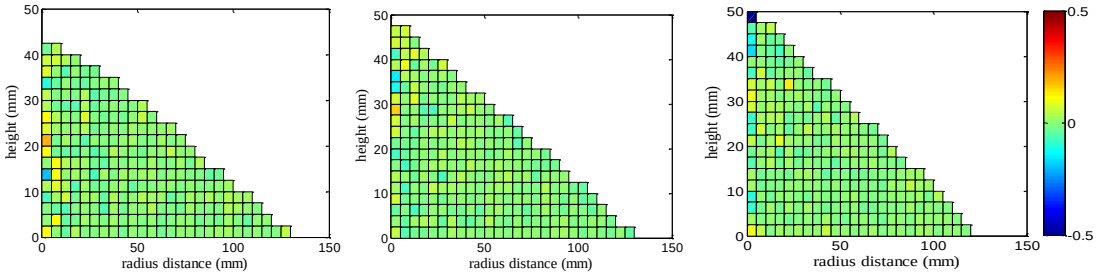
(a) boundary removal (b) rain deposition (c) point deposition

Figure 7.35 The behaviour of $D_{\theta\theta}$ at the final stage with various preparation methods



(a) boundary removal (b) rain deposition (c) point deposition

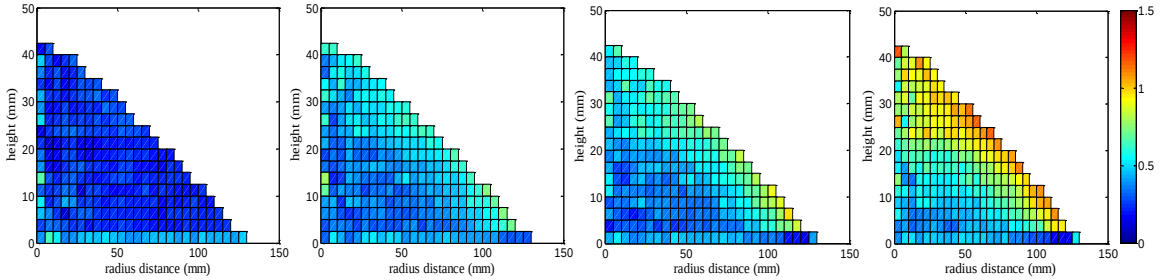
Figure 7.36 The behaviour of D_{zz} at the final stage with various preparation methods



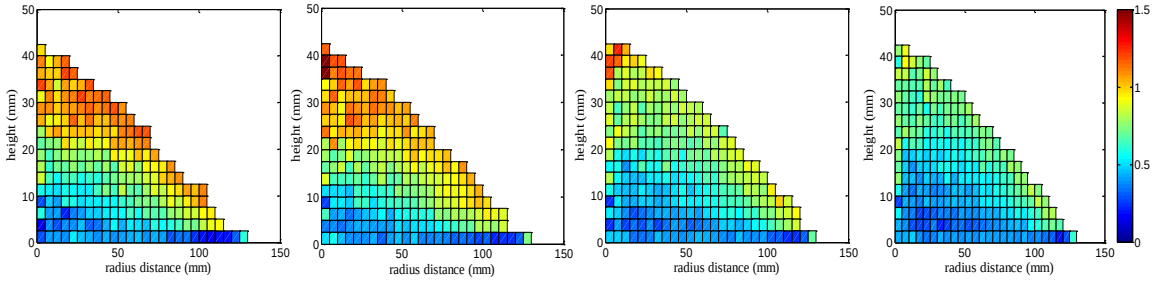
(a) boundary removal (b) rain deposition (c) point deposition

Figure 7.37 The behaviour of D_{rz} at the final stage with various preparation methods

To further observe the impact of construction history, the degree of fabric anisotropy is studied at the progressive stages. For the boundary removal test, a uniform distribution with the lowest degree of fabric anisotropy is observed at the initial stage. After removing the boundary, the core region shows a lower degree of fabric anisotropy at each stage. From 0.017s to 0.6806s, particles near the free surface of the specimen experience larger displacements, resulting in the higher magnitude of fabric anisotropy. Then, with the process to achieve the equilibrium condition, the fabric anisotropy reduces in this region.



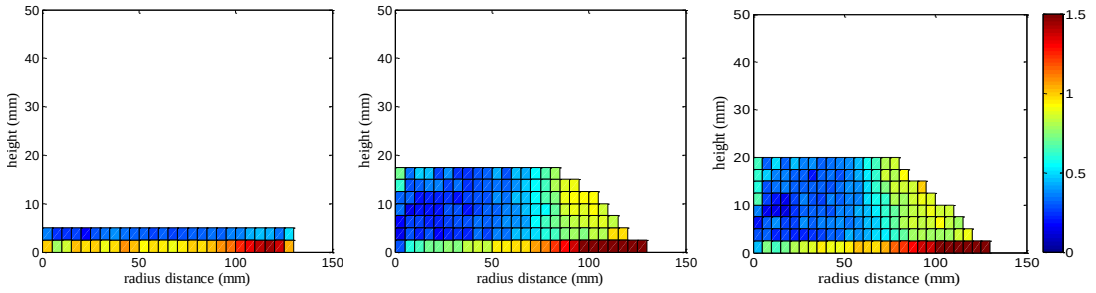
(1) 0s (2) 0.017s (3) 0.051s (4) 0.204s



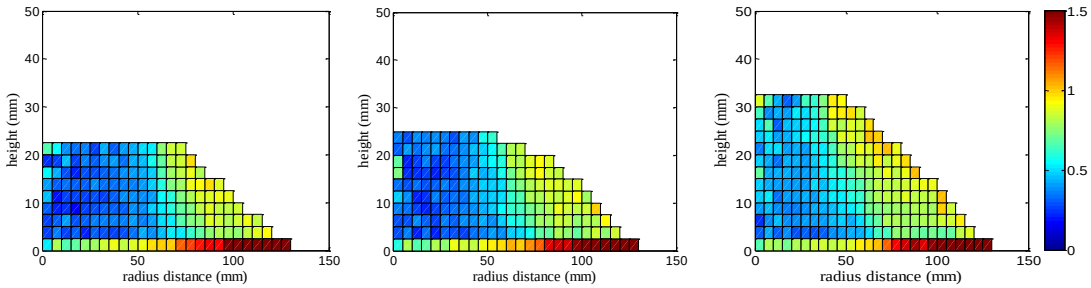
(5) 0.3403s (6) 0.6806s (7) 1.7015s (8) 2.7224s

Figure 7.38 The degree of fabric anisotropy at progressive stages for boundary removal test

Figure 7.39 presents the fabric anisotropy magnitude history in the rain deposition test. For each stage, the core region shows a lower value of fabric anisotropy, with a larger magnitude near the free surface of sand pile depending on the larger displacements of particles.



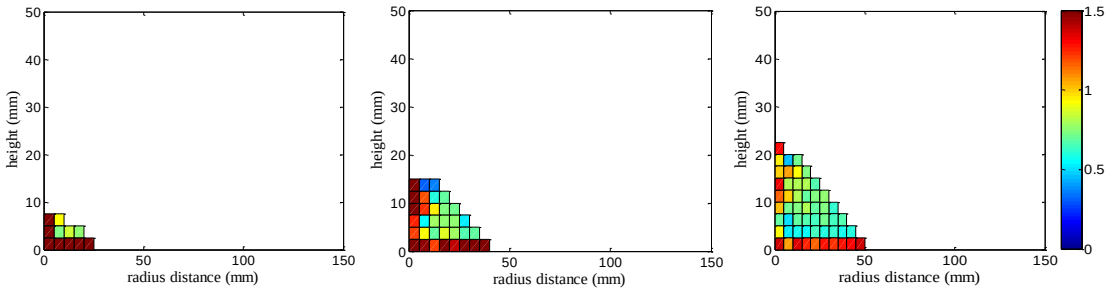
(1) 8.798s (2) 12.474s (3) 13.647s



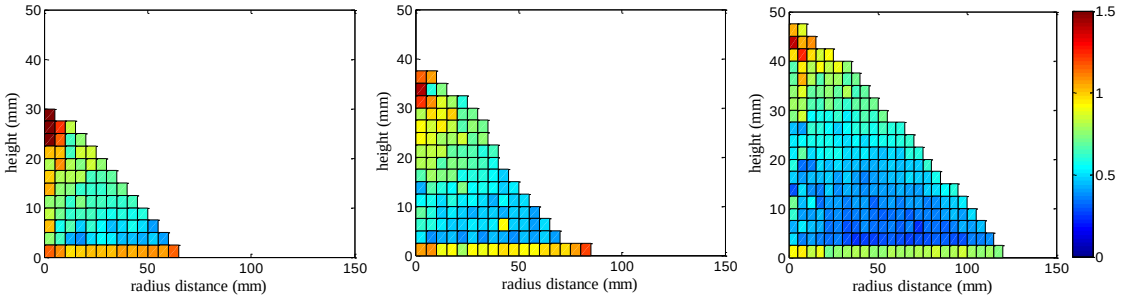
(4) 14.272s (5) 17.557s (6) 20.731s

Figure 7.39 The progressive degree of fabric anisotropy for the rain deposition test

The point deposition test sees a higher degree of fabric anisotropy in the region under the particles deposition. The largest value occurs at the initial stage owing to the small number of particles. Compared with the boundary removal and rain deposition tests, within the radius distance of 30*mm*, the point deposition test shows a larger degree of fabric anisotropy in the progressive stages.



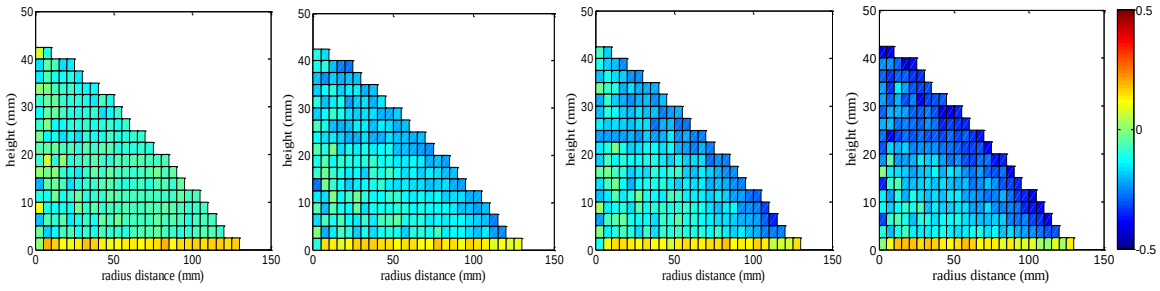
(1) 1.583s (2) 5.292s (3) 12.192s



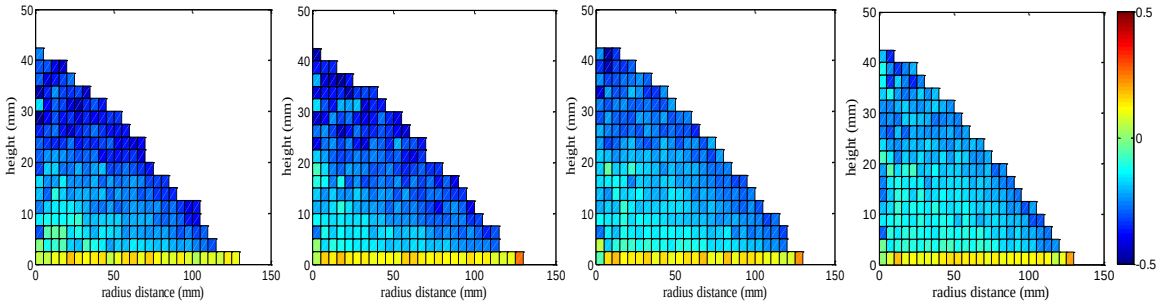
(4) 22.876s (5) 37.912s (6) 71.136s

Figure 7.40 The progressive degree of fabric anisotropy for the point deposition test

The behaviour of fabric components is also studied during the process of sand pile formation. Figure 7.41 to Figure 7.44 present the behaviour at the progressive stages inside the specimen for the boundary removal method. The boundary removal test shows the lowest degree of fabric anisotropy D_{rr}, $D_{\theta\theta}$ and D_{zz} at the initial stage. In the intermediate stages, from 0.204s to 1.7015s, the specimen exhibits largest magnitudes of fabric anisotropy, in particular in the region near the free surface of the specimen. The fabric anisotropy in the (r,z) space is near zero at each stage which means that the sample is under a more isotropic condition with this preparation method.

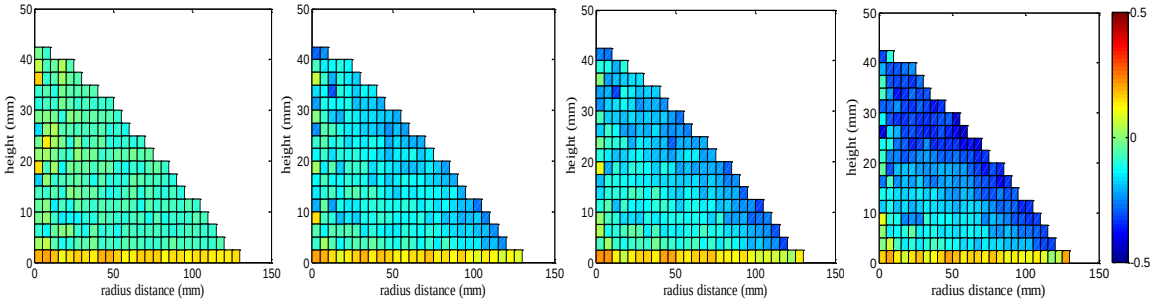


(1) 0s (2) 0.017s (3) 0.051s (4) 0.204s

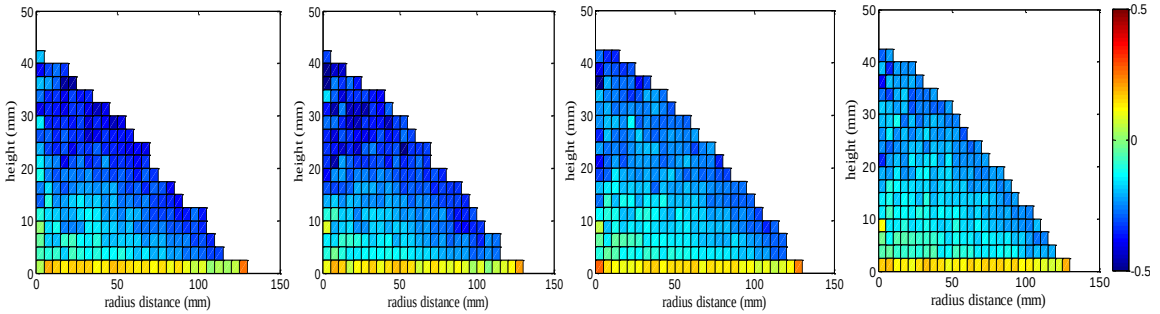


(5) 0.3403s (6) 0.6806s (7) 1.7015s (8) 2.7224s

Figure 7.41 The progressive behaviour of D_{rr} for the boundary removal test

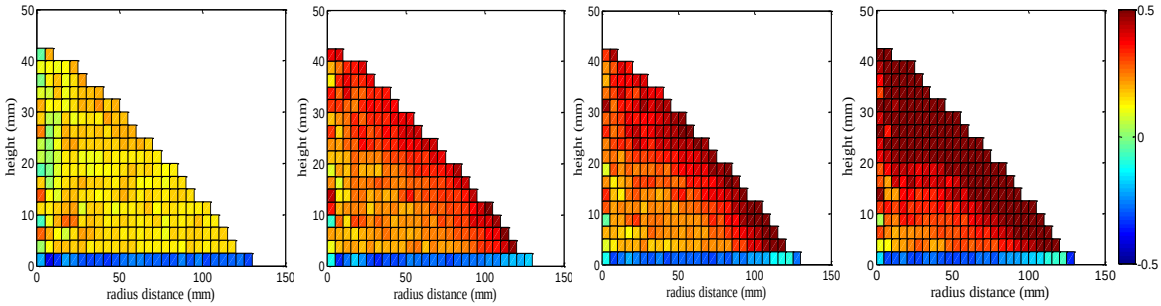


(1) 0s (2) 0.017s (3) 0.051s (4) 0.204s

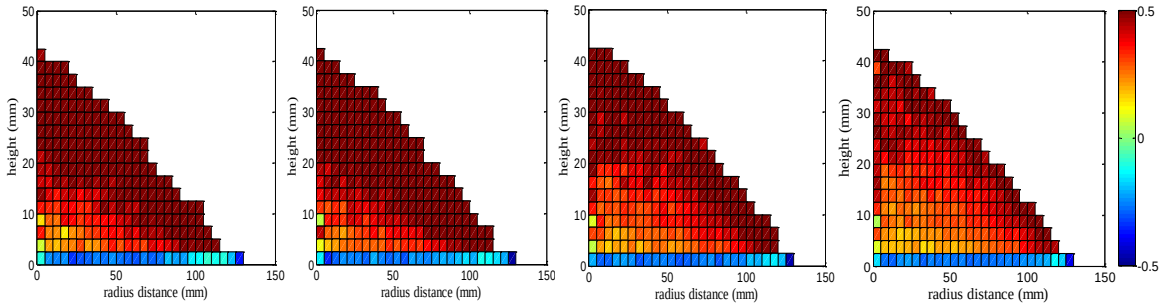


(5) 0.3403s (6) 0.6806s (7) 1.7015s (8) 2.7224s

Figure 7.42 The progressive behaviour of $D_{\theta\theta}$ for the boundary removal test

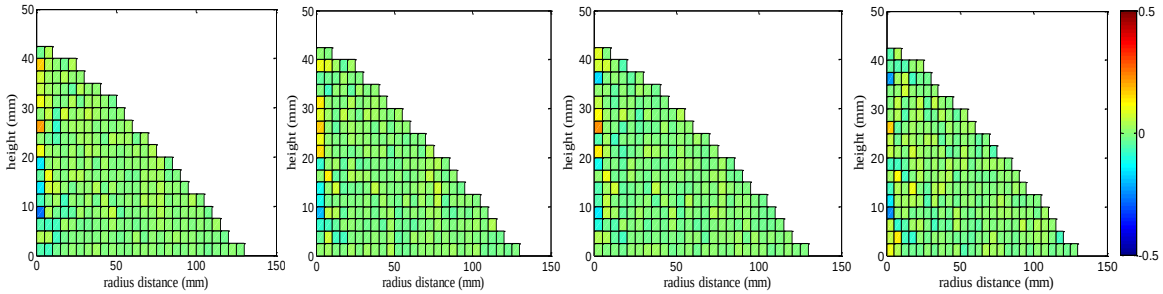


(1) 0s (2) 0.017s (3) 0.051s (4) 0.204s

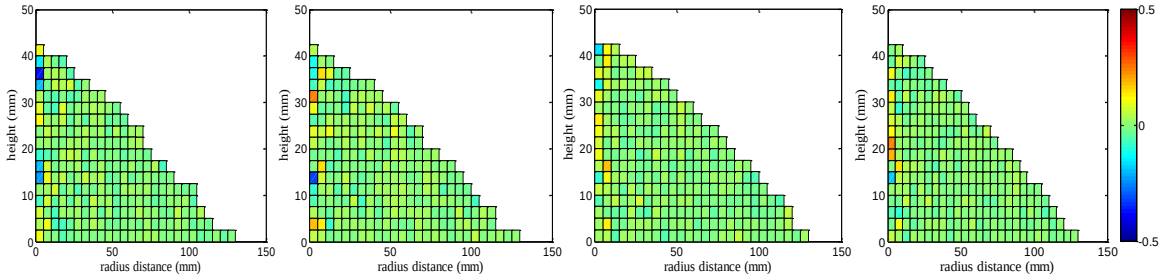


(5) 0.3403s (6) 0.6806s (7) 1.7015s (8) 2.7224s

Figure 7.43 The progressive behaviour of D_{zz} for the boundary removal test



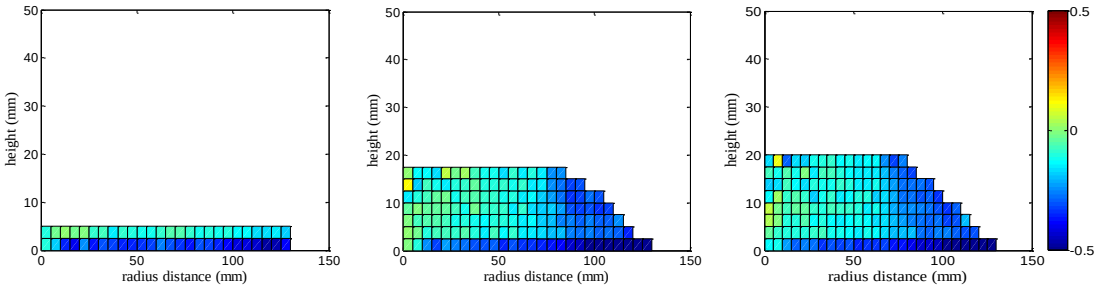
(1) 0s (2) 0.017s (3) 0.051s (4) 0.204s



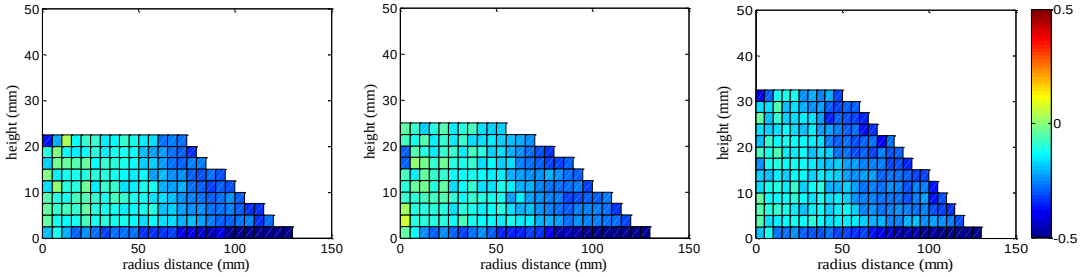
(5) 0.3403s (6) 0.6806s (7) 1.7015s (8) 2.7224s

Figure 7.44 The progressive behaviour of D_{rz} for the boundary removal test

For the rain deposition test, the fabric component in the (r,z) space is also around zero at each stage. The fabric component D_{zz} shows the largest value among all components of the fabric tensor at each stage. The characteristics of D_{rr}, $D_{\theta\theta}$ and D_{zz} are similar to the behaviour of the degree of fabric anisotropy, with a lower value of D_{rr}, $D_{\theta\theta}$ and D_{zz} observing in the core region and a larger magnitude appearing near the free surface of the specimen at each stage.

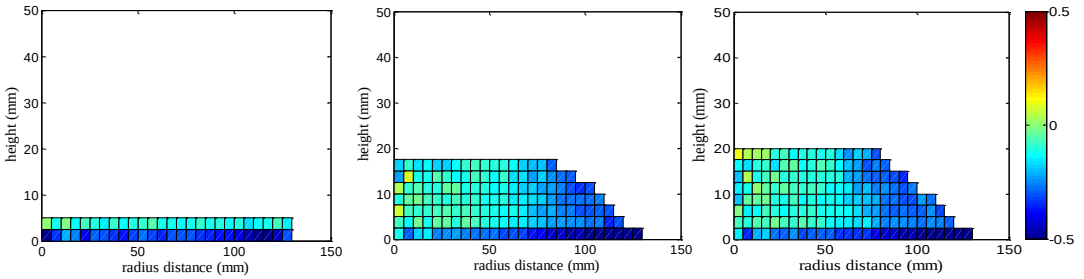


(1) 8.798s (2) 12.474s (3) 13.647s

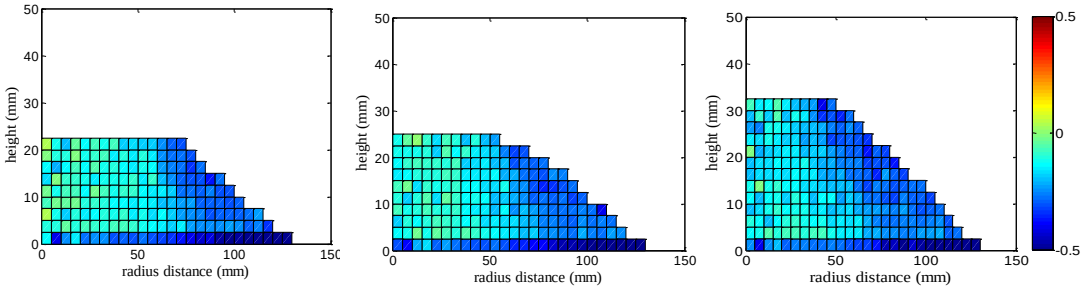


(4) 14.272s (5) 17.557s (6) 20.731s

Figure 7.45 The progressive behaviour of D_{rr} for the rain deposition test

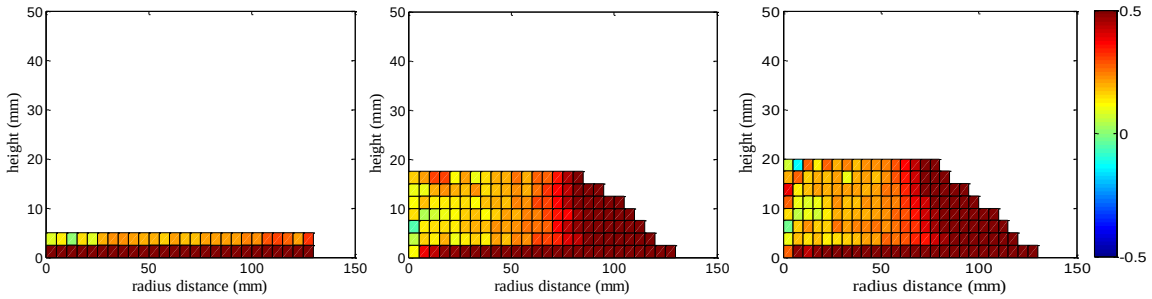


(1) 8.798s (2) 12.474s (3) 13.647s

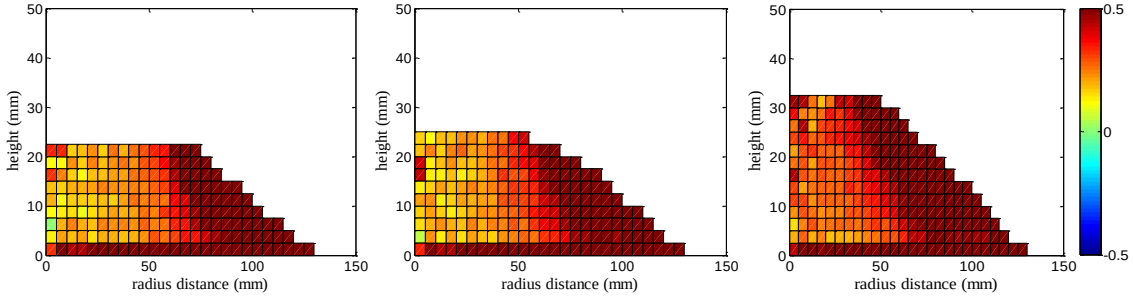


(4) 14.272s (5) 17.557s (6) 20.731s

Figure 7.46 The progressive behaviour of $D_{\theta\theta}$ for the boundary removal test

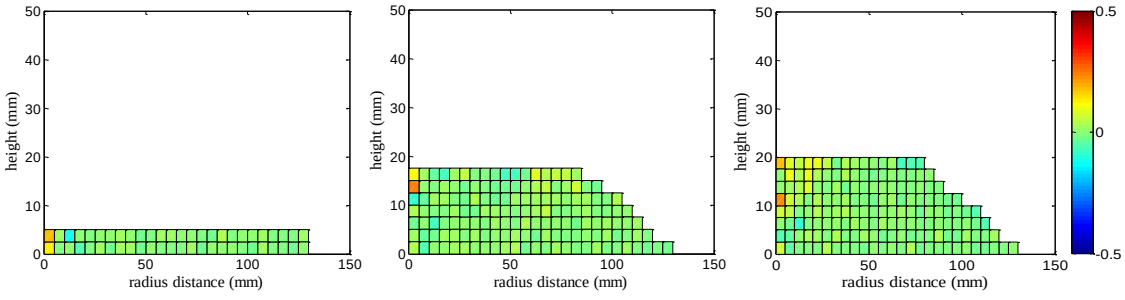


(1) 8.798s (2) 12.474s (3) 13.647s

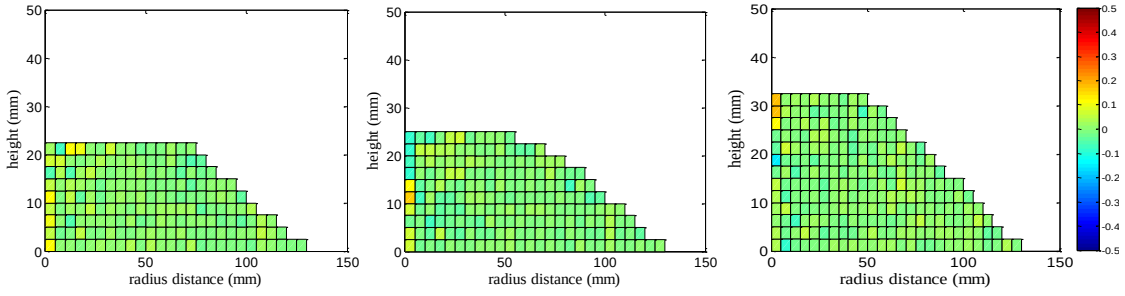


(4) 14.272s (5) 17.557s (6) 20.731s

Figure 7.47 The progressive behaviour of D_{zz} for the rain deposition test



(1) 8.798s (2) 12.474s (3) 13.647s

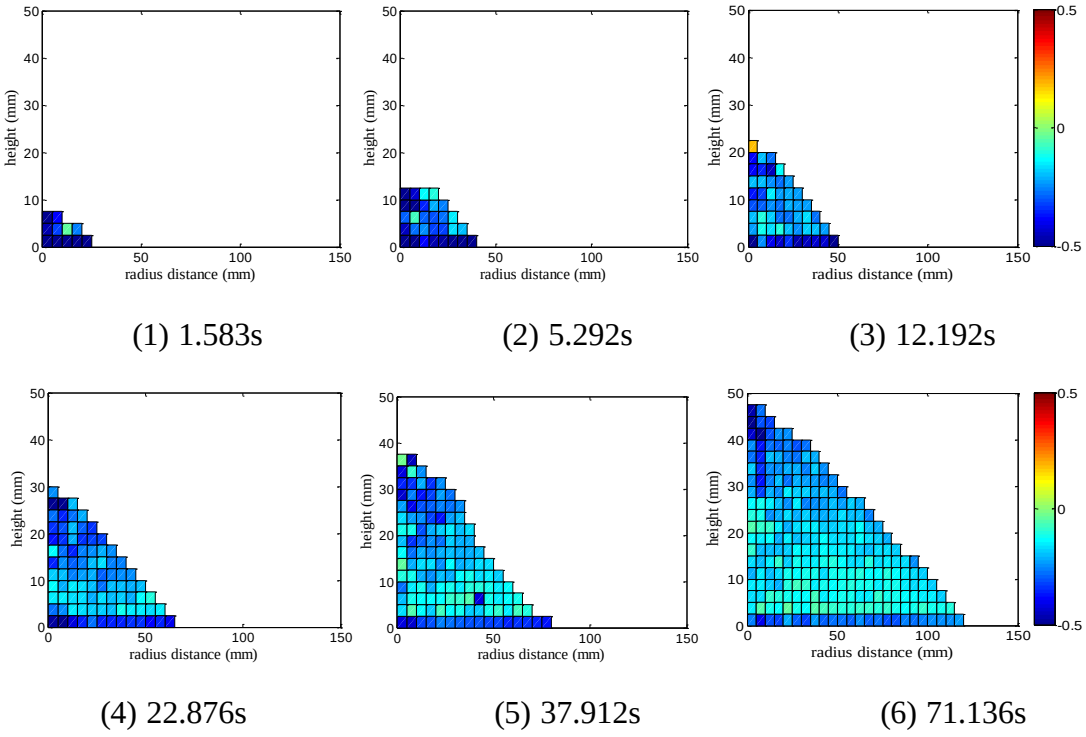


(4) 14.272s (5) 17.557s (6) 20.731s

Figure 7.48 The progressive behaviour of D_{rz} for the rain deposition test

The point deposition test shows the largest value of fabric anisotropy at the initial stage owing to the small number of particles. With the continuous deposition of particles, the

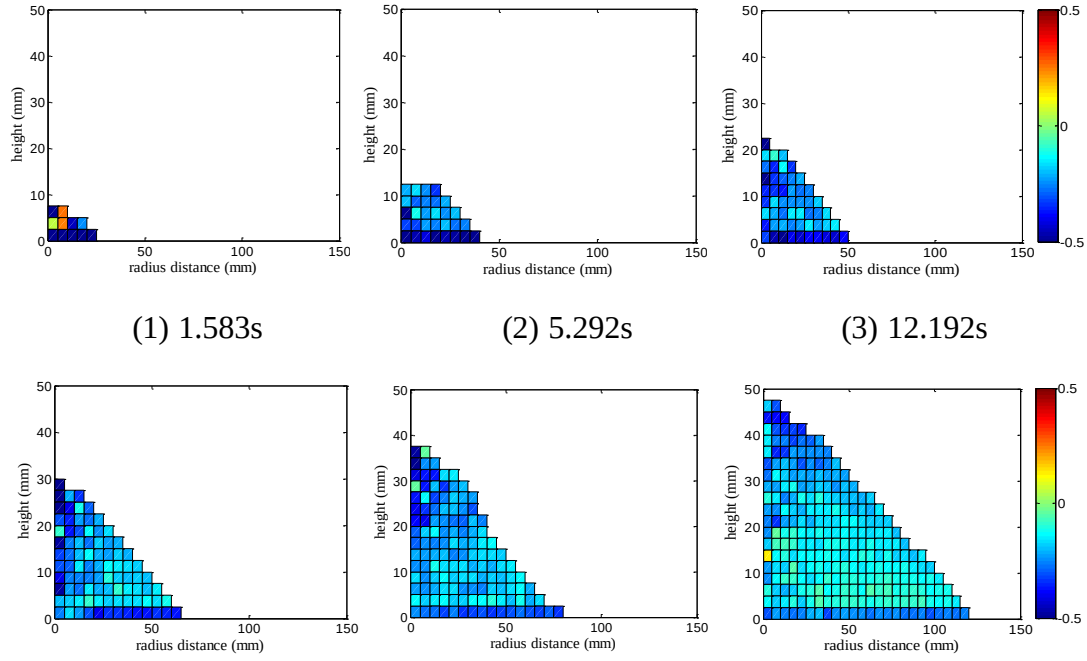
value of D_{rz} maintains around zero from 5.292s. In the progressive stages, D_{zz} is larger near the top surface due to the impact of particles loading.



(1) 1.583s (2) 5.292s (3) 12.192s

(4) 22.876s (5) 37.912s (6) 71.136s

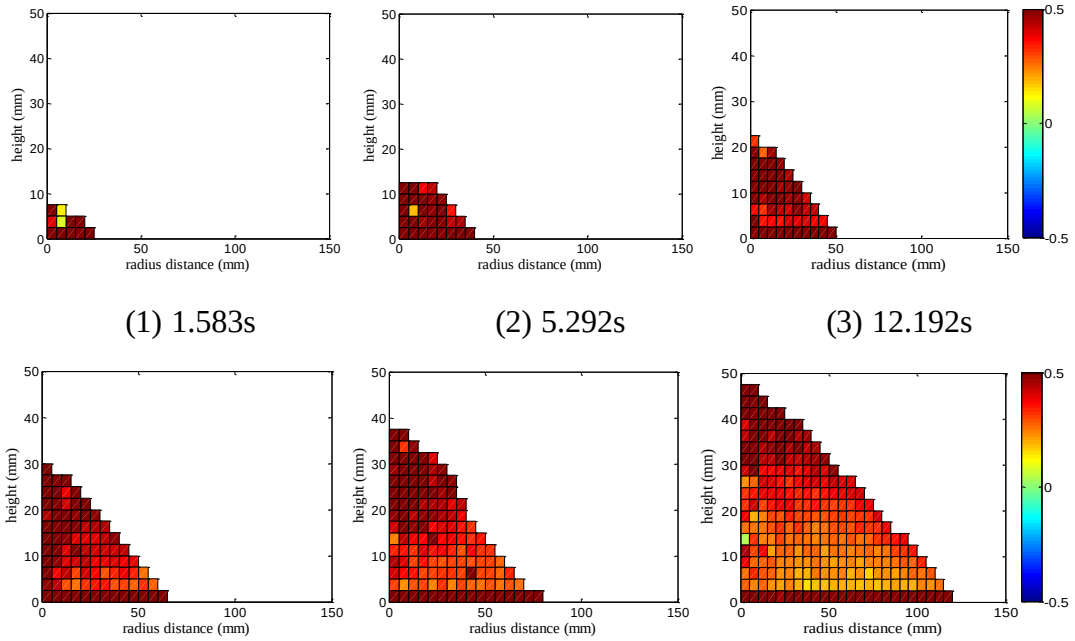
Figure 7.49 The progressive behaviour of D_{rr} for the point deposition test



(1) 1.583s (2) 5.292s (3) 12.192s

(4) 22.876s (5) 37.912s (6) 71.136s

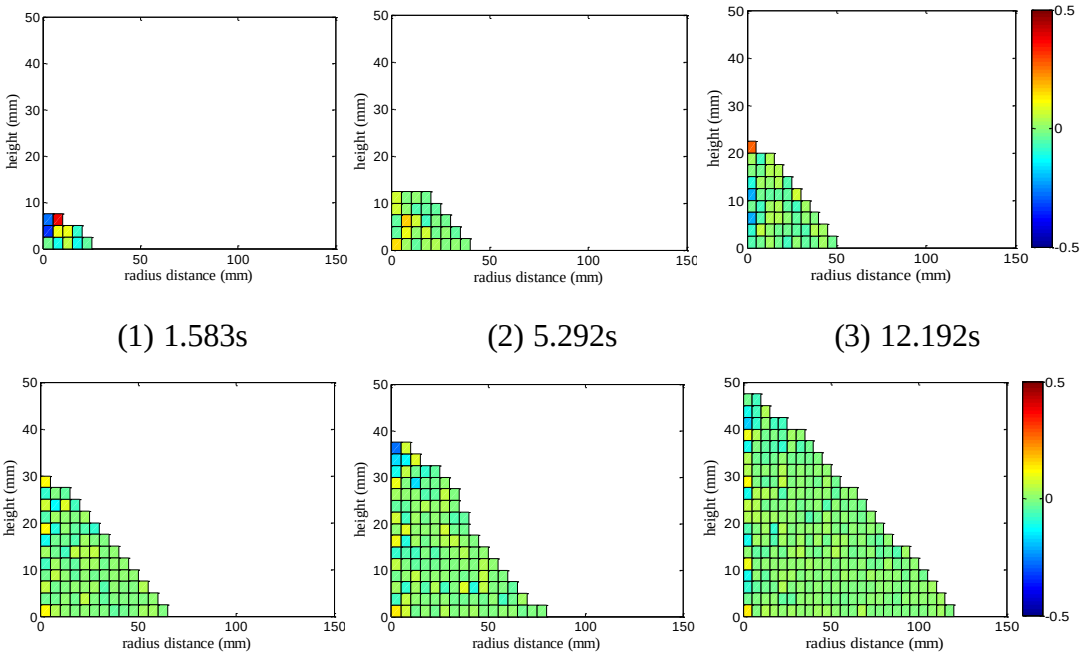
Figure 7.50 The progressive behaviour of $D_{\theta\theta}$ for the point deposition test



(1) 1.583s (2) 5.292s (3) 12.192s

(4) 22.876s (5) 37.912s (6) 71.136s

Figure 7.51 The progressive behaviour of D_{zz} for the point deposition test



(1) 1.583s (2) 5.292s (3) 12.192s

(4) 22.876s (5) 37.912s (6) 71.136s

Figure 7.52 The progressive behaviour of D_{rz} for the point deposition test

7.5 Observations of contact force behaviour

The behaviour of the contact force is also taken into account to further capture the material behaviour with the impact of construction history. Eq.(7.5) to Eq.(7.7) give the estimation of contact force tensor for each particle (averaged over the number of contacts).

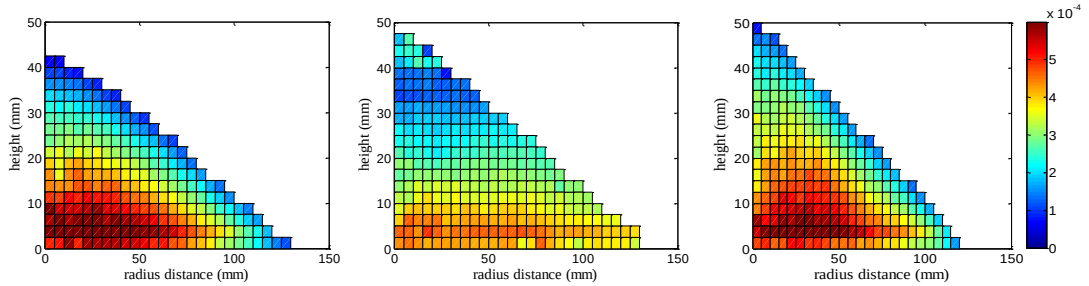
$$K_{ij} = \frac{1}{E_0}\frac{1}{\omega_p}\iint_{\Omega}\left\langle f_{cont}\right\rangle\Big|_{\boldsymbol{n}_i}\otimes\boldsymbol{n}_j d\Omega \tag{7.5}$$

$$f_0 = \frac{\iint_{\Omega} f_{cont_i}\boldsymbol{n}_i d\Omega}{E_0} = K_{ii} \tag{7.6}$$

$$G_{ij} = \frac{3K_{ij}}{K_{ii}} - \delta_{ij} \tag{7.7}$$

in which K_{ij} is the contact force tensor, G_{ij} is the deviatoric contact force tensor for each particle, and ω_p is the coordination number of each particle.

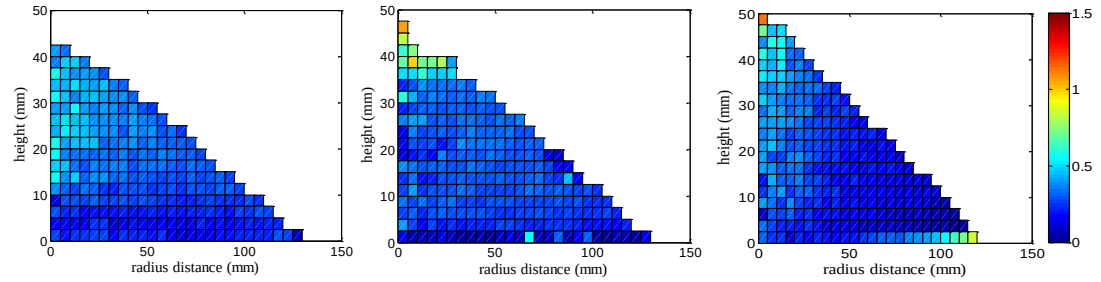
The characteristics of deviatoric contact force tensor are observed inside the sand pile with the spatial distribution in the $r-z$ space. The hollow cylinder region is applied to obtain the spatial distribution of deviatoric contact force tensor. The behaviour of the directional average contact force $\left(f_0\right)$ and the contact force anisotropy $\left(G_q\right)$ is observed in Figure 7.53 and Figure 7.54 respectively with various preparation methods. The boundary removal test sees a larger value of the average contact force in the core region. For the rain deposition test, the larger value of contact force appears uniformly on the base plane. The average contact force reduces when increasing the height. The point deposition test shows a higher percentage of larger average contact force at the radius distance of $40mm$, with the lowest value appearing near the free surface of the sand pile.



(1) boundary removal (2) rain deposition (3) point deposition

Figure 7.53 The characteristics of f_0 at the final stage

The samples show smaller degree of contact force anisotropy, compared with the degree of fabric anisotropy. In addition, the contact force anisotropy is almost uniformly distributed inside the core region for the three tests, with a larger magnitude appearing near the top surface of the sand pile.

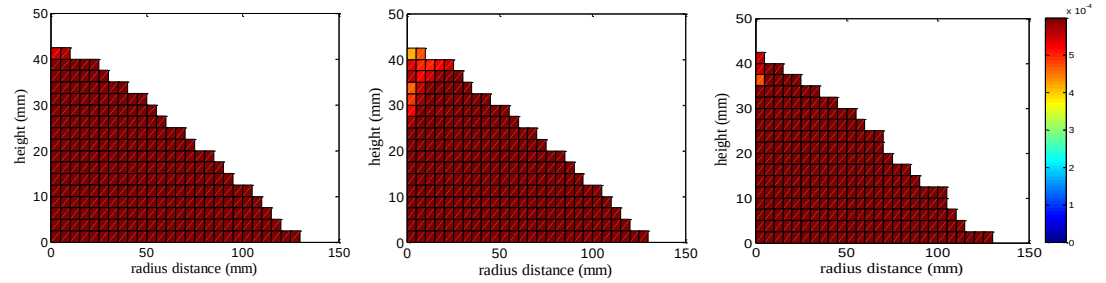


(1) boundary removal (2) rain deposition (3) point deposition

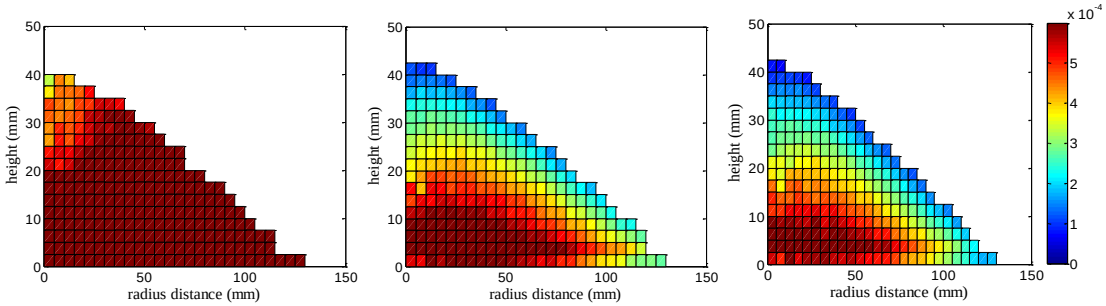
Figure 7.54 The characteristics of contact force anisotropy at the final stage

Figure 7.55 and Figure 7.56 present the progressive behaviour of contact force tensor for the boundary removal test. At the initial stages, due to the higher height of the specimen, it produces a much larger direction average contact force. After removing the boundary, the forces located in the top surface region decrease first and transfer to the centre of the specimen at the height of approximately $20mm$. Then, the weak average contact force develops to the free surface of the specimen. From 1.7015s, the core region sees larger

magnitudes of average contact force with smaller values observing near the free surface of the specimen.



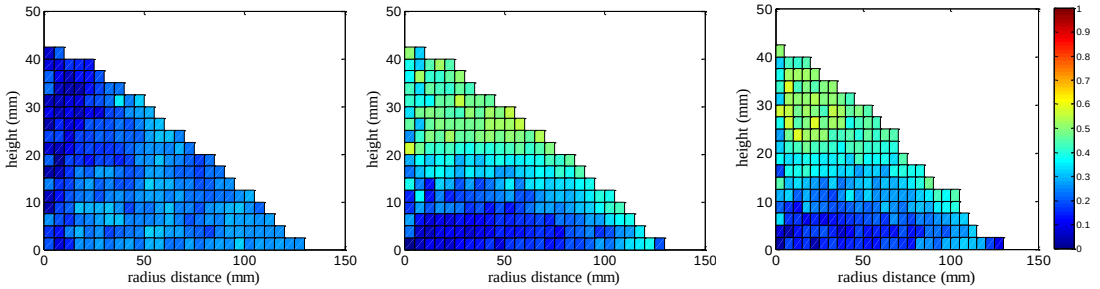
(1) 0s (2) 0.204s (3) 0.3403s



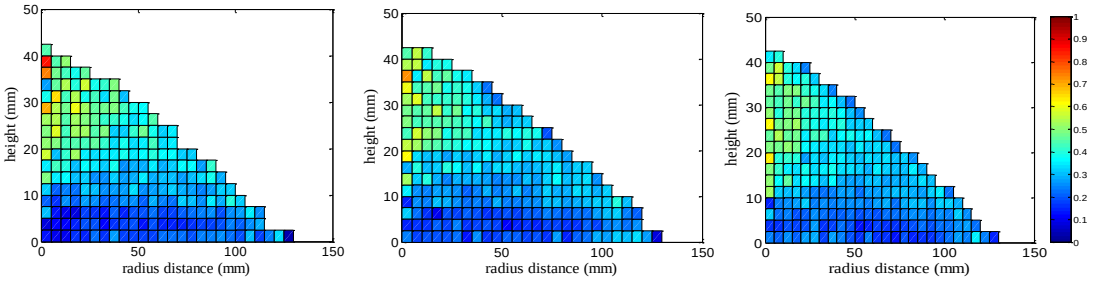
(4) 0.6806s (5) 1.7015s (6) 2.7224s

Figure 7.55 The progressive behaviour of average contact force for the boundary removal test

The degree of contact force anisotropy at different stages is similar. It is almost uniformly distributed at the base layer for each stage. A relatively larger magnitude of contact force anisotropy is observed near the top surface of the sand pile in the progressive stages.



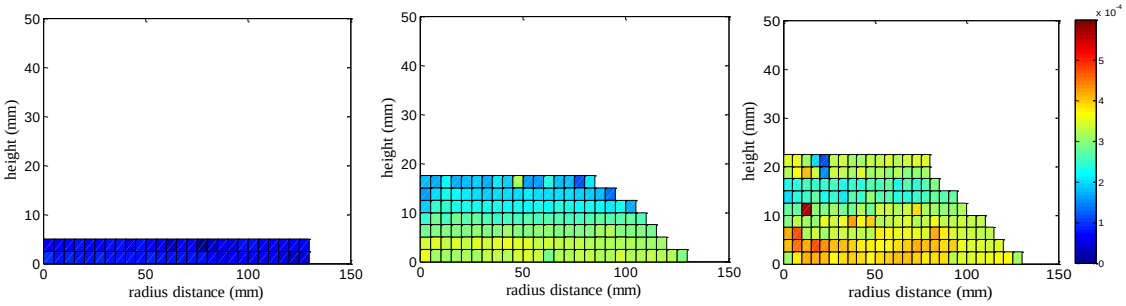
(1) 0s (2) 0.204s (3) 0.3403s



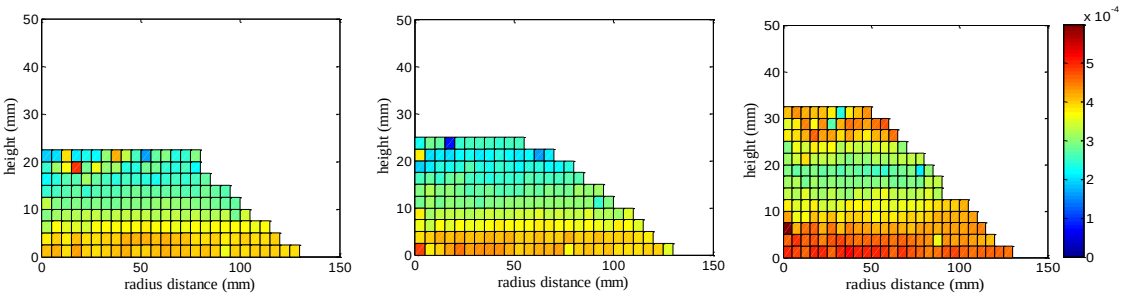
(4) 0.6806s (5) 1.7015s (6) 2.7224s

Figure 7.56 The progressive behaviour of contact force anisotropy for the boundary removal test

Figure 7.57 and Figure 7.58 present the progressive spatial distribution of average contact force and contact force anisotropy in the rain deposition test. The average contact force is increased layer by layer with this preparation method. The larger contact force is uniformly distributed in the base layer at each stage. With the development of sand pile, the peak value of average contact force is also increased. Regarding the contact force anisotropy, a larger magnitude is observed at the initial stage, owing to the small number of particles. The specimen also shows a lower degree of contact force anisotropy in comparison with the degree of fabric anisotropy. For the top surface, the magnitude is relatively larger due to the loading of particles.

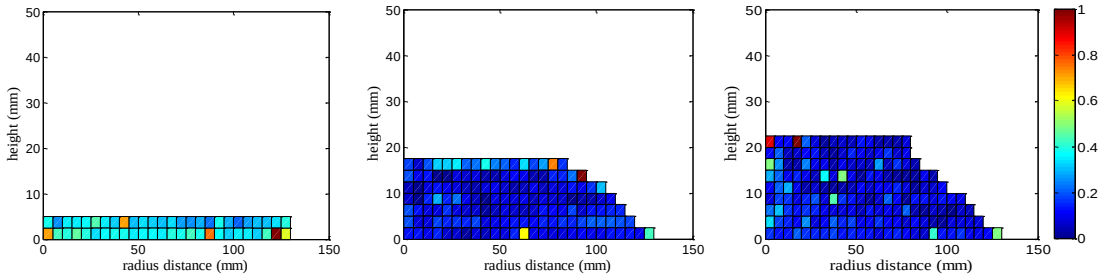


(1) 8.798s (2) 12.474s (3) 13.647s

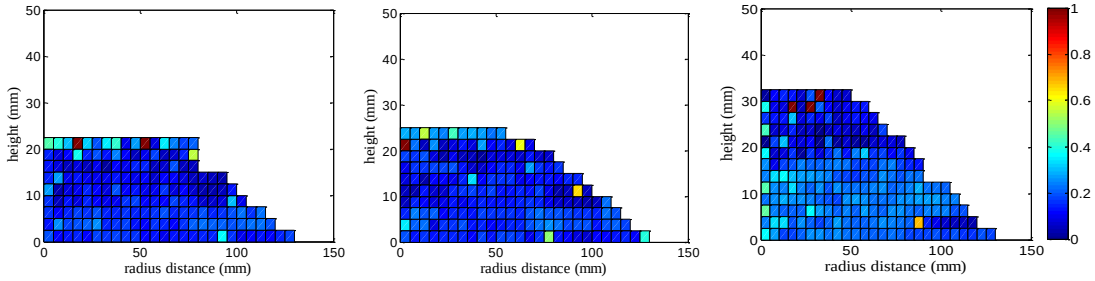


(4) 15.289s (5) 17.557s (6) 20.731s

Figure 7.57 The progressive behaviour of average contact force for the rain deposition test



(1) 8.798s (2) 12.474s (3) 13.647s



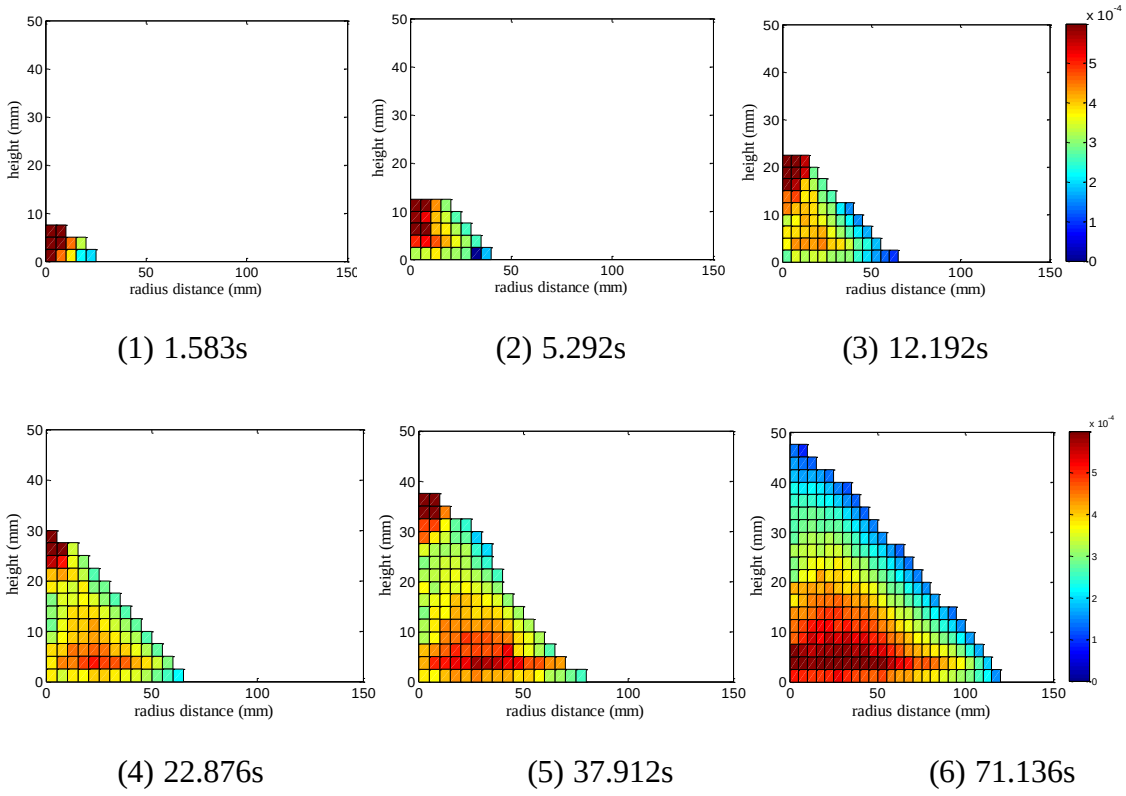
(4) 15.289s (5) 17.557s (6) 20.731s

Figure 7.58 The progressive behaviour of contact force anisotropy for the rain deposition test

The point deposition test sees a larger average contact force in the core region at the initial stage. Then, the radius distance within which the peak value occurs is increased with the development of sand pile. For each stage, the region under the loading of particles shows a relatively higher value of average contact force.

With regards to the characteristics of contact force anisotropy, at the initial stage, the value is larger due to the small number of particles. With the continuous generation of particles, the degree of contact force anisotropy is reduced inside the specimen. For the progressive

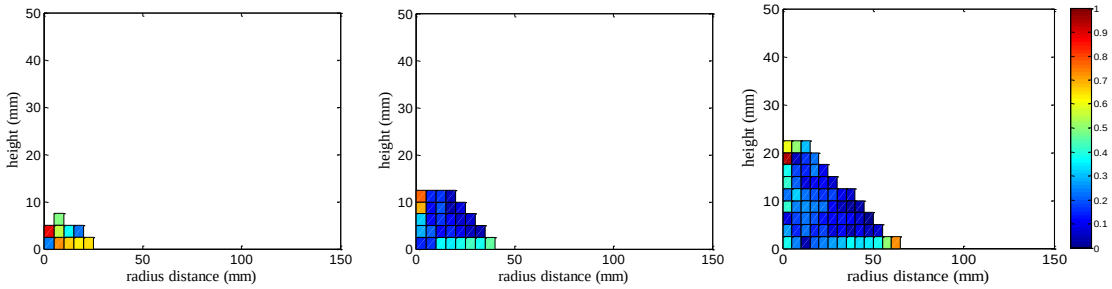
stages, this method produces a higher degree of contact force anisotropy near the top surface and the edge of the boundary, owing to the larger displacements and a smaller number of particles.



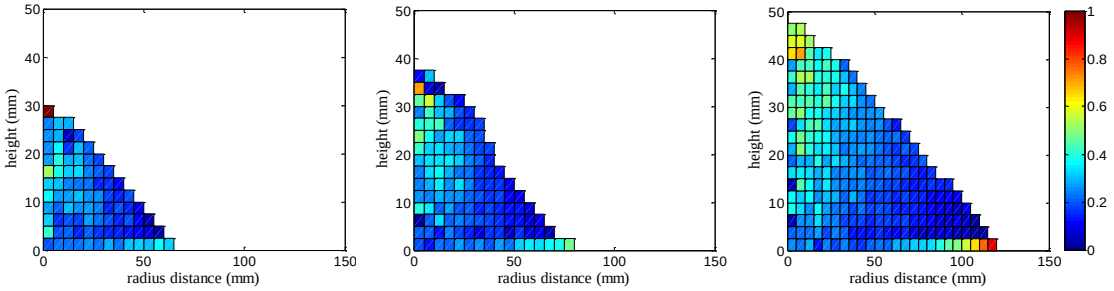
(1) 1.583s (2) 5.292s (3) 12.192s

(4) 22.876s (5) 37.912s (6) 71.136s

Figure 7.59 The progressive behaviour of average contact force for the point deposition test



(1) 1.583s (2) 5.292s (3) 12.192s



(4) 22.876s (5) 37.912s (6) 71.136s

Figure 7.60 The progressive behaviour of contact force anisotropy for the point deposition test

7.6 Summary

This chapter investigates the particle-scale mechanisms of material behaviour considering different construction histories. It aims to explain the pressure dip phenomenon in terms of the factors of stress, fabric and contact force. The characteristics of these factors are studied at different progressive stages and at the local-scale with the spatial distribution inside the sand pile.

The stress tensor is applied to estimate the stress behaviour of each particle inside the structure. It is demonstrated that the stress tensor could capture the stress field inside the sand pile, through the comparison with the pressure profile on the base plane using the Voronoi tessellation method. For the spatial distribution of stress in the principal stress directions, higher values appear in the core region for both the boundary removal and rain deposition tests. Significant difference observes for the stress history of σ_{rz} under various preparation methods. In the core region, the rain deposition test contains the smallest values compared with the other two tests. In addition, under the process of boundary removal and rain deposition methods, larger values transfer from the surface to the intermediate region of the specimen. However, for the point deposition test, the higher values develop from the core region to the intermediate region with the continuous deposition of particles.

In addition, the point deposition test produces a larger rotation of the principal stress direction than the rain deposition and boundary removal tests. It suggests that granular materials, underneath the central apex, are under a triaxial compression loading path and a rotational loading path for the rain deposition method and point deposition method respectively.

Different characteristics of displacement are observed via tracing the stress state of elements at different regions in various preparation methods. The largest displacement is observed with the point deposition test for each region, with the smallest displacement appearing under the rain deposition test.

The results are compared with the proposed continuum theory to explain the pressure dip phenomenon. It is shown that the continuum theory produces larger results than the simulation results. The closure relationship is also validated using the point deposition test. The results present that the FPA relationship produces a larger estimation of σ_{rr}, which indicating the consideration of stress $\sigma_{\theta\theta}$ and distribution of principal stress directions in the closure relationship.

An obvious difference is observed for the directional average contact force following different procedures. The boundary removal and rain deposition tests produce higher average contact force in the core region at each stage. However, for the point deposition test, a larger average contact force shows in the core region first and develops to the intermediate region with the continuous deposition of particles.

The material behaviour has a relationship with the characteristics of the particle arrangement and associated voids. The average coordination number and fabric tensor, in terms of the contact normal, are studied to explain this phenomenon. The point deposition

test shows that the core region has a relatively lower value of the average coordination number, in particular in the progressive stages. This increases the probability of the formation of arches which results in the pressure dip phenomenon. Furthermore, the boundary removal and rain deposition tests produce a larger degree of progressive fabric anisotropy near the free surface of the sand pile. However, the point deposition test produces a higher magnitude of fabric anisotropy in the central region at the progressive stages than the other two methods.

Based on the aforementioned characteristics of stress, contact force and fabric, the pressure dip phenomenon is suggested relating to the larger magnitude of σ_{rz} and the arches formation with respect to the smaller average coordination number and larger rotation of principal stress directions as well as higher potential plastic deformation. In addition, it also depends on the construction histories, e.g. a higher degree of fabric anisotropy and force anisotropy appears in the core region during the formation stage under point deposition.

Chapter 8 Conclusions and future work

This project investigates the pressure dip phenomenon of the sand pile with different construction histories. The main observations of the pressure dip phenomenon and material responses are summarised in the following.

8.1 Observations of sand piles

The characteristics of surface angles and void ratios are observed inside the sand pile at the final stage in Chapter 4. The three methods form the similar average void ratio, approximately 0.675, at the final stage. The point deposition test forms a relatively looser layer near the base plane, compared with the boundary removal and rain deposition test.

For the behaviour of surface angles, the point deposition test produces a larger angle for the layer near the top surface with a smaller value for the base layer in comparison with the other two tests. It agrees with the assumption proposed by Liffman et al. (1992), which suggests that this kind of shape containing a larger probability to produce the pressure dip phenomenon.

The boundary removal method and rain deposition method produce a peak pressure in the centre. A pressure dip phenomenon appears underneath the central apex for the point deposition test. The feature of stress is studied with the structure at the height of $5mm$, $10mm$, $15mm$ and $20mm$ respectively at the final stage. It shows the intermediate principal stress ratio is approximately 0.2 for the three tests. Similar behaviour is observed for the characteristics of p and q, with larger magnitudes observed for the boundary removal and rain deposition tests, in particular with the core region.

8.2 Three-dimensional developed numerical algorithm

A virtual experimental model is successfully developed into the open-sourced software LIGGGHTS for studying continuum material behaviour under the specified loading paths. Chapter 5 provides the details of the implementation of the numerical algorithm in LIGGGHTS. The typical simulation results of the drained true triaxial shear test and the drained rotation shear test have been presented and validated with the previous researchers. It demonstrates the developed numerical technique is a powerful tool to perform the typical loading paths of laboratory tests in the three-dimensional.

The uniformity of sample is studied in Chapter 5 to determine the size and shape of the polyhedral boundary to be used in Chapter 6 for observing the material behaviour. It shows the larger size of boundary would increase the uniformity of the specimen. In addition, a more uniform condition is observed with the boundary approaching a spherical shape under the stages of consolidation, triaxial shear and rotation shear respectively.

8.3 Constitutive material behaviour

Chapter 6 presents the study of material response with the effect of the void ratio, intermediate principal stress ratio, magnitudes and directions of the principal stress and the initial state respectively under the specified loading paths. Compared with the results in Chapter 5, the peak stress ratio and critical stress ratio are smaller with a wide PSD. The largest critical friction angle is observed at $b = 0.5$ with the value around $21°$, similar to the average repose angle $21.4°$ of the three sand pile tests.

A sample prepared with the deposited method is performed to study the impact of initial structure. The deposited sample is under a relatively looser condition than the sample

generated with the radius expansion method. In such a case, the stress ratio of the deposited sample increases gradually, with a lower value obtained at the critical stage than the radius expansion sample during shearing.

Compared with the triaxial shear tests, the rotation shear tests produce a larger deformation, in particular with a higher stress ratio. In addition, the deposited sample increases the diameter of strain trajectory larger with the increase of stress ratio, compared with the radius expansion prepared sample during rotation.

The SFF relationship is employed to explain the internal structure on the constitutive behaviour of granular materials. With a lower intermediate principal stress ratio value, it reduces the magnitude of fabric anisotropy and increases of the degree of contact force anisotropy. For the deposited sample, it contains larger values of average coordination number and directional average contact force, compared with the radius expansion prepared sample. However, with respect to the degree of fabric anisotropy and force anisotropy, the deposited sample contains a lower value at each shear strain. Regarding the SFF relationship, thus, the deposited sample produces a relative lower deviatoric stress during the shearing.

8.4 Interpretation the pressure dip phenomenon of sand pile

The progressive characteristics of stress, contact force and fabric are studied in Chapter 7 following different procedures to explain the pressure dip phenomenon. The results are observed with the spatial distribution inside the sand pile.

During the progressive stages, different behaviour of stress field is observed with various preparation methods. The boundary removal and rain deposition tests produce a larger stress σ_{rz} near the free surface of the specimens first and develops to the intermediate region during the formation process. However, for the point deposition test, a higher stress σ_{rz} appears in the core region at the initial stage and transfers to the intermediate region with the development of sand pile. It shows the point deposition method produces a larger shear stress in the (r,z) space at the progressive stages.

In addition, underneath the apex, the granular materials refer to under a triaxial compression loading path and a rotational loading path for the rain deposition test and point deposition test respectively depending on the behaviour of the major principal stress direction. This suggests that the point deposition test would result in a higher probability of arches formation and contains a larger plastic deformation.

A larger stress is observed employing the continuum theory, compared with the result of point deposition test. The closure relationship is also validated with the simulation results. The result of σ_{rr} is much larger from FPA model. Hence, it is suggested considering the boundary properties and the distributions of principal stress directions for the continuum theory.

With regards to the average coordination number, for the point deposition method, it indicates larger voids ratio contained in the core region, with a higher degree of fabric anisotropy observing at the progressive stages. It implies that the constitutive phenomenon has a relationship with the path of the construction history. From Chapter 6, it shows the uniform deposition method produces a less shear resistant and a higher plastic deformation than the isotropic sample prepared by the radius expansion method. Regarding the point

deposition test, owing to the larger fabric anisotropy, the specimen would contain a significant plastic deformation and a lower confining pressure in the deposited region than the boundary removal method.

Furthermore, significant differences are observed for the evolution of average contact force following various construction histories. For the boundary removal test, after removing the boundary, the weak contact force first appears near the top surface and develops to the free surface until achieving the equilibrium condition. With regards to the rain deposition test, the strong contact force appears in the base layer at the intialt stage and transfers to the intermediate region layer by layer. However, towards the point deposition test, it first observes the strong contact force in the core region and then develops to the intermediate region with the development of sand pile.

Based on the aforementioned, the pressure dip phenomenon suggests having a relationship with the memory effect of fabric anisotropy. The sample contains a higher probability for the arches formation under the point deposition test, with respect to the larger rotation of principal stress direction and less average coordination number in the core region. In addition, material responses obtained from RVE simulations indicate that particles may experience a higher plastic deformation under the point deposition. These aspects may result in the pressure dip phenomenon.

8.5 Recommendations for future work

Compared with the FEM and experimental methods, the DEM could directly obtain the particle-scale information. In addition, it simulates the granular materials with the smaller assumptions. However, it requires higher computation effort and could only mimic the limited dimension of a system than FEM. Due to the limitation of the previous version of

LIGGGHTS, it could only simulate the spherical particles in this project. This would have an impact to model the real properties of granular materials. Recently, the software is updated and released the version to simulate the non-spherical particles with the clumped function. With this shape, it could form the sand pile with a repose angle close to the experimental result and would have an increase of the degree of pressure dip. The characteristics of stress, force and fabric could be studied and compared with the results of spherical particles to further explain this counter-intuitive phenomenon. Thus, it is recommended to develop this technique with the non-spherical particles for future DEM study.

The point deposition test contains larger values for the degree of fabric anisotropy and the degree of contact force anisotropy, which indicates to the formation of pressure dip phenomenon. Depending on the elementary material behaviour, the larger magnitude of fabric anisotropy is suggested relating to more significant strain responses. To better understand this phenomenon, it suggests observing the local strain behaviour inside the sand pile. In addition, the results of stress distribution could improve the continuum theory for understanding the pressure dip phenomenon.

Furthermore, the impact of loading history could be observed via the observation of the material responses under the specified loading paths, with the initial structure extracting from the results of sand piles and imposing to the RVE elementary boundary. The results could also be compared with the constitutive modelling and improve constitutive theories of granular materials.

According to the results of Chapter 5 and Chapter 6, different stress-strain responses are observed with different particle size distribution. It is interesting to observe the characteristics of strength, fabric and failure surface of granular materials under different

particle size distribution. In addition, the impact of cohesion could be considered with the constitutive behaviour of granular materials and the formation of the pressure dip phenomenon.

Based on the DEM results, the parameters, such as the maximum principal stress directions, confining pressure and deviatoric stress, could be obtained from the particle-scale mechanisms analysis inside the sand pile. This information could be employed in FEM to observe the system behaviour and simulate the real-scale properties of granular materials.

Furthermore, the software could be coupled with the CFD method to mimic the granular-fluid system. The motion of the particles is resolved with the DEM, while the fluid flow is calculated with the CFD software. It could develop this virtual experimental technique to be coupled with the CFD method for obtaining the material behaviour with the impact of fluid flow, such as the unsaturated granular material, seepage and earth dams. It could further provide an insight of the infrastructural stability. With the multi-scale observations of granular materials, it could enrich the development of constitutive modelling of granular materials.

Appendix

A. Sand pile

A.1 Impact of friction coefficient

Eight different friction coefficients tests, 0.0, 0.1, 0.2, 0.3, 0.4, 0.6, 0.8 and 1.0, implemented in order to investigate the friction coefficient on the relation with the repose angle. Tests are performed with the boundary removal method. The properties of particles and boundary are the same as the full-scale simulation tests, except for the value of Young's modulus. The value of Young's modulus is reduced to 5MPa to save the computation effort. About 1,341,500 particles are generated with a volume fraction of 0.26 for all the tests except the test with $\mu = 1$. The volume fraction is 0.394 with about 2,030,000 particles for $\mu = 1$. Particles are inserted but do not overlap with each other. After particles deposited, the sand layer thickness is about 50mm. Table A.1 below gives the sand layer thickness and the average void ratio after deposition. The average void ratio decreases with the increase of friction coefficient and indicates that densest sample is formed with $\mu = 0$. Figure A.1 displays the relationship between μ and repose angle (θ).

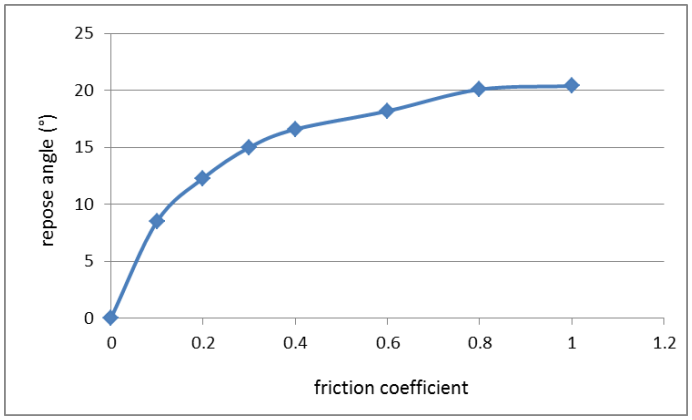


Figure. A.1 Repose angle on the relationship of friction coefficient

Table A.1 Sand pile with different friction coefficient

Friction coefficient	Particles number (generation)	Sand layer thickness (mm)	Average void ratio	Repose angle (°)
0.0	1,341,500	44.5	0.514	0
0.1	1,341,500	45.1	0.0507	8.5
0.2	1,341,500	47.9	0.477	12.3
0.3	1,341,500	48.4	0.472	15
0.4	1,341,500	49	0.467	16.6
0.6	1,341,500	49.5	0.462	18.2
0.8	1,341,500	50.5	0.453	20.1
1.0	2,030,000	70.1	0.0326	20.4

A.2 Preliminary tests of boundary removal method

A.2.1. Simulation scheme

The preliminary tests are performed first to design the numerical model. In order to reduce the simulation time, the sizes of particles are increased by 5 times as $[6 \pm 2] mm$. Other properties for the particles and boundary are the same as the full-scale simulation. The baffle is also generated at the beginning of the tests with the particle size of $4mm$ in radius. The procedures for the preliminary tests are the same as that for the full-scale simulation. It aims to estimate the calculation effort and finalise the full-scale simulation tests with the parameters of the sand pile height. In addition, it could also be compared with the full-scale simulation tests for the impact of the particle size. Owing to the small number of particles, it would be a good starting point for the microscopic data analyses.

Considering the boundary removal method, the sand pile is generated with the movement of particles to achieve the critical condition. The parameter for the deposit height is treated as a vital factor in the formation of the heap. It should be higher enough to form the heap at the final stage. However, with regard to the simulation time, the value could not be to larger, in particular with the full-scale simulation test. Hence, a series of tests are performed to choose the appropriate value of the deposit height. The initial height is also considered as $h_i = 75mm$ calculated with the repose angle of $30°$. Seven tests are performed with the heights of layer $\left(h'\right)$ assumed as $0.6h$, $0.9h$, $1.2h$, $1.5h$, $2.25h$, $3.0h$ and $6h$. The heights, defined as the region for particles inserting, are taken as five times corresponding to the height of each layer, as $150mm$, $225mm$, $300mm$, $375mm$, $562.5mm$, $750mm$ and $1500mm$ respectively. Owing to the spherical particles, the average repose angle is around $20.9°$ and the height of the sand pile is smaller than the assumed value. Hence, the initial height is re-set as $h_0 = 49.64mm$. The results of deposit layers are modified as $0.75h_0$, $1.1h_0$, $1.5h_0$, $1.8h_0$, $2.6h_0$, $3.5h_0$ and $6.9h_0$ for the data analysis below.

A.2.2. Observations of sand pile formation

Progressive procedures are also investigated and presented with the various deposit heights as Figure A.2. It only considers the behaviour of particles during the stage of sand pile formation. Figures are displayed with the velocity of each particle during the formation process. In order to present the behaviour inside the piles, a cross-section plane is employed in the centre of the heaps in the x-axis direction. Four stages are selected for each test to present the progressive behaviour. For each test, the initial stage $\left(t = 0\right)$ refers to the stage of the particles deposited and achieved the equilibrium condition. The final stage $\left(t = T\right)$

is the stage that particles formed the heap and reached the equilibrium condition again. Two intermediate stages are selected as $0.05T$ and $0.2T$ for each test. At each stage, according to the graphs, the velocity is smaller for particles that remained to generate the heap, in comparison with the particles appearing near the surface of the samples. For the pre-set height of $0.75h_0$, the value is not enough to form the conical shape as the Figure A.2(a)-(4). Considering tests of $1.1h_0$, $1.5h_0$ and $1.8h_0$, the heights of the conical heap are around $45mm$. While, for tests of $2.6h_0$, $3.5h_0$ and $6.9h_0$, the heights of the sand pile are around $48mm$, only increasing a bit as one average particle size.

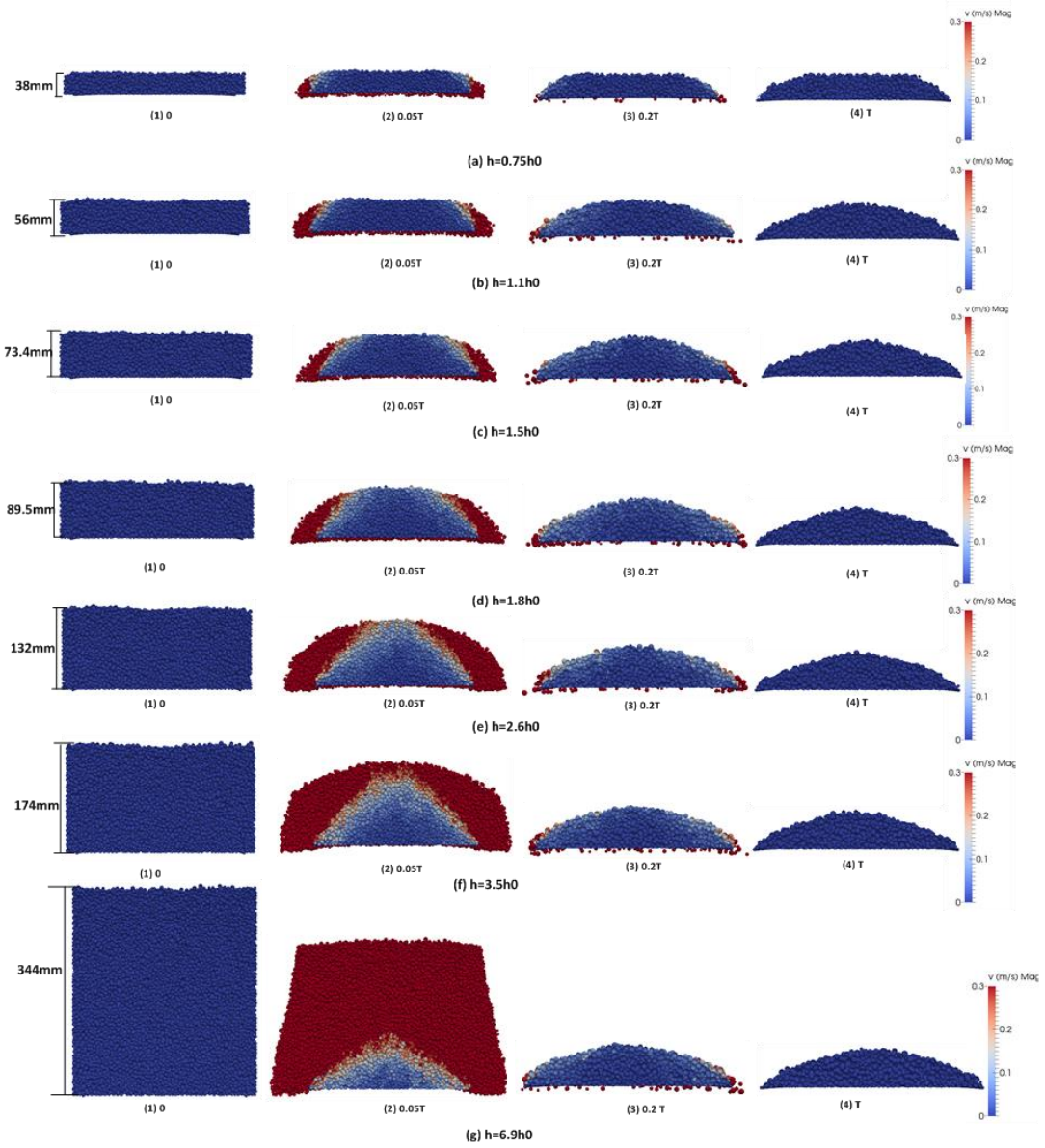


Figure A.2The progressive behaviour of the series of tests

A.2.3. Observations of the sand pile shape

Figure A.3 below gives the shape of the sand pile at the final stage of the tests. With respect to the lower height of $0.75h_0$, the sample has not formed the shape of the pile and does not take into account for the following data analysis. According to the figure, the shapes are similar except for the test with the deposit height of $1.1h_0$. It seems a larger plane occurring near the top surface for this test.

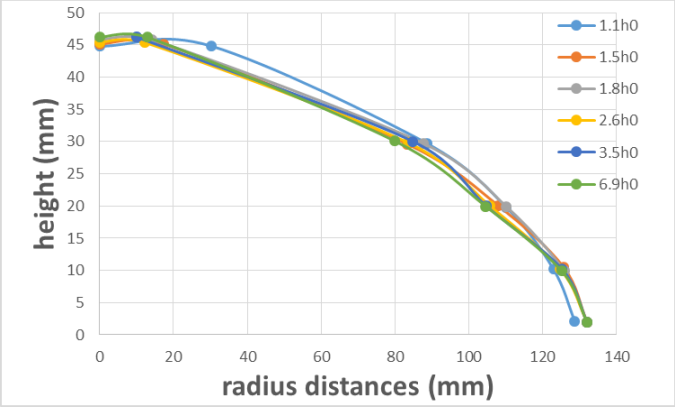


Figure A.3 The shape of sand piles for the tests

The following graphs present the characteristics of void ratio and surface angles at the final stage with different layers. Similar behaviour observes for the samples prepared with different deposit heights. It shows that the surface angle increases with the decrease of the layer height. The feature of the void ratio is also similar as the denser condition appearing in the middle layers in comparison with the layer near the base plane, without the consideration of the top layer. It may be related to the shape and a lower number of particles for this layer, which reducing the void ratio in this layer. The dimension of the base plane is around 22 times of an average particle. For the height, it is around 7 times of an average particle. In such a case, it has an impact of the surface with a flatter shape near the top of the piles.

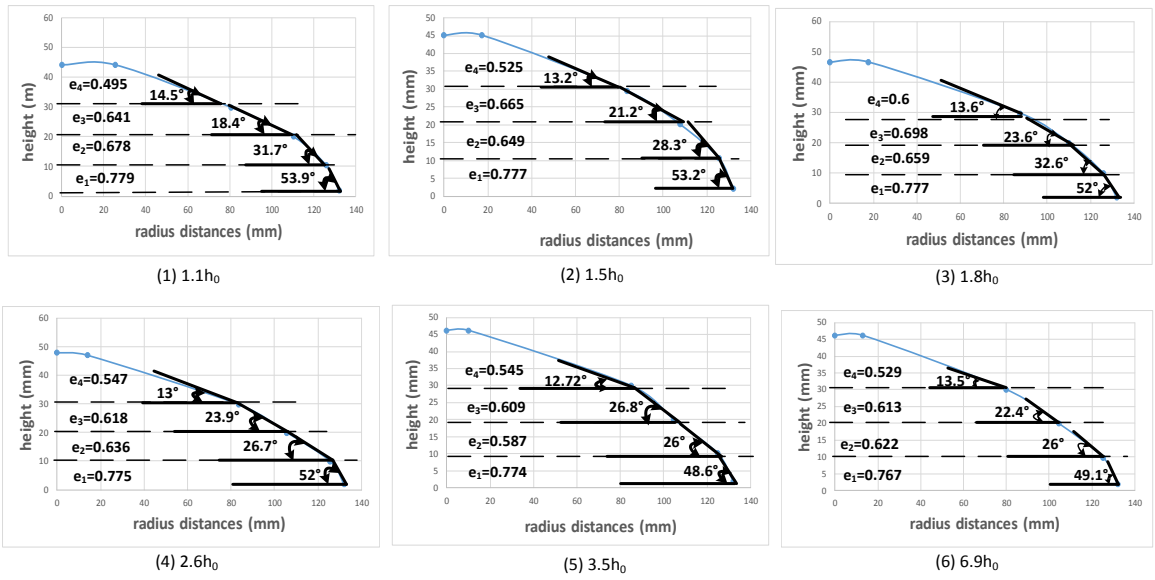


Figure A.4 The surface angle and void ratio of each layer for the tests

A.2.4. Stress distribution on the base plane

The following graph presents the pressure profile on the base plane with the test of $1.5h_0$ using the average scheme. For each region, it is estimated as the total contact force dividing the area of the region. A higher pressure is obtained at the initial region owing to the small area and lower number of particles.

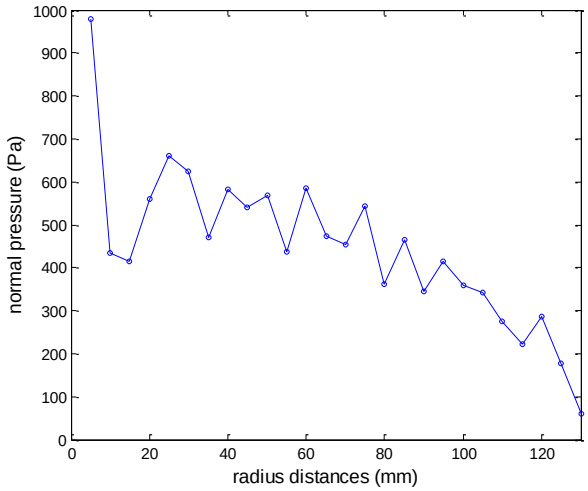
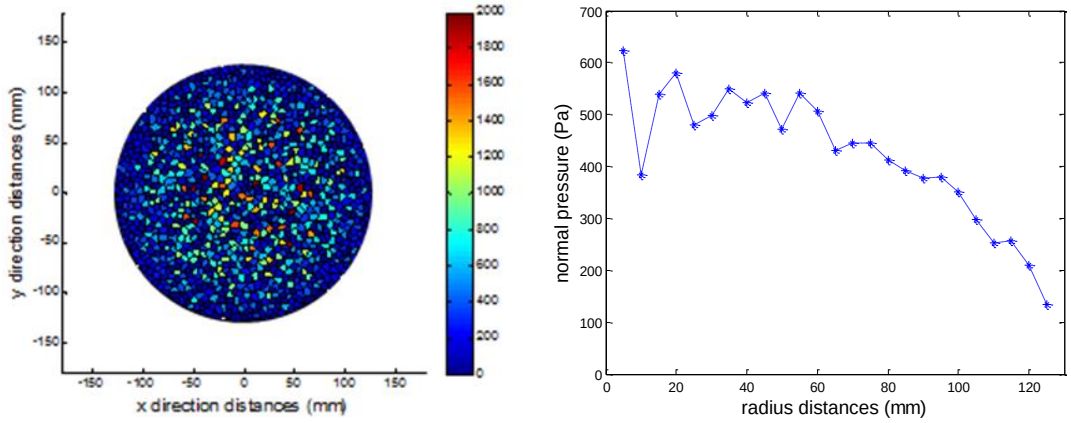


Figure A.5 The normal pressure distribution using average scheme

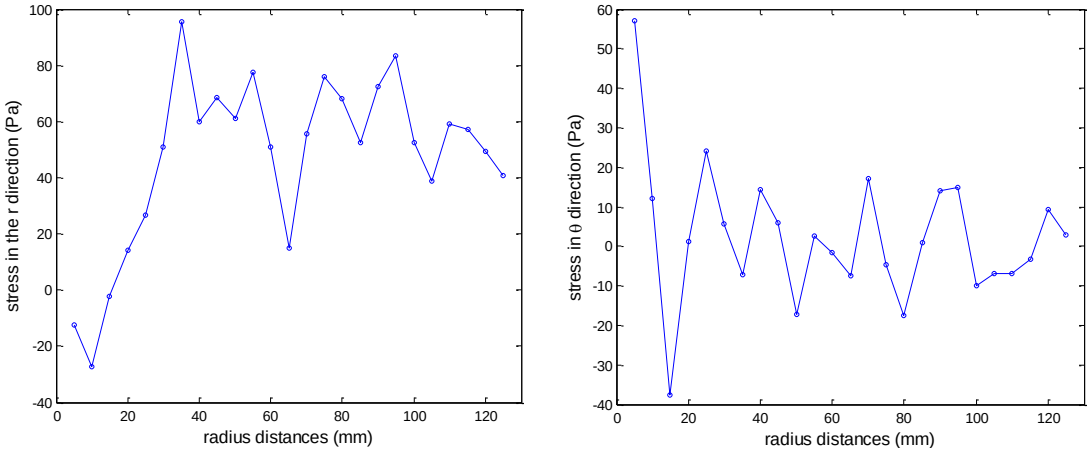
Taken the test of $1.5h_0$ as an example, it presents the pressure distribution on the base plane at the ultimate stage in the following graphs. Figure A.6(1) gives the information of each Voronoi cell with the colour bar representing the normal pressure on the base plane. It shows that the peak pressure appears under the central apex. The pressure profile is also plotted at the representative radius distances as Figure A.6(2). The starting and interval representative radius distances are all selected as $5mm$, around one average particle size. For each radius distance, as the red circles in Figure A.5 above, the average normal pressure refers to the sum of each normal pressure, whose cell lay on this radius distance, dividing the number of particles. The peak pressure is observed in the core region. Compared with Figure A.5, the trendy is similar for the two methods. Employing the average scheme, the results are a bit larger at each radius distance.



(a) voronoi tessellation (b) representative radii

Figure A.6 The evolution of normal pressure at the ultimate stage

Figure below presents the shear stress in the radial direction and hoop direction respectively. The results are more fluctuated owing to the small number of particles. For the shear stress in the radial direction, the peak stress appears in the radius of $35mm$. The shear stress is around zero for the hoop direction. Due to the small number of particles in the central, the shear stress in the radial direction and hoop direction are both not equalling to zero.



(1) radial direction (2) hoop direction

Figure A.7 The evolution of shear stress with the radius distances

Concerning the factor of deposit height, the behaviour of normal pressure is similar with different deposit heights. The major difference appears in the core region due to the small number of particles. For all the tests, the peak pressure emerges under the central apex of the sand piles.

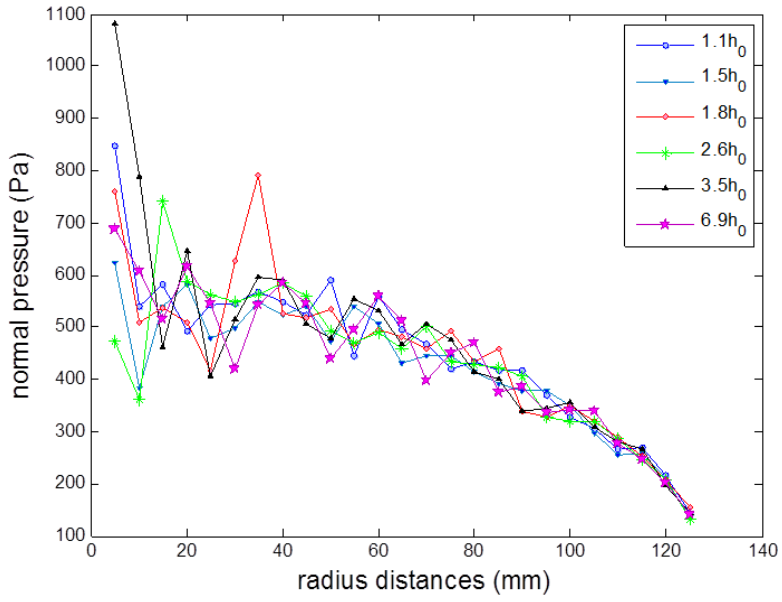
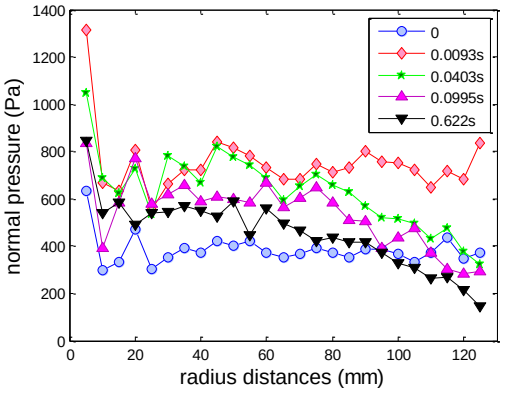


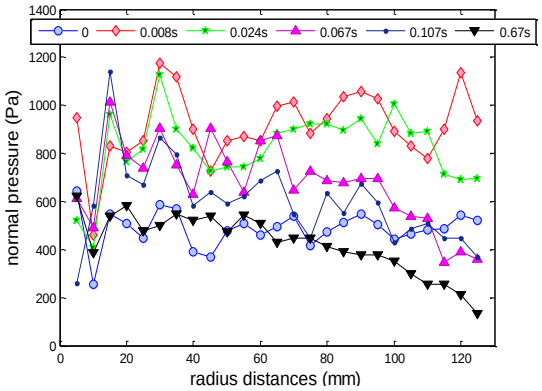
Figure A.8 The pressure distribution with different deposit heights

A.2.5. Observation of sand pile formation process

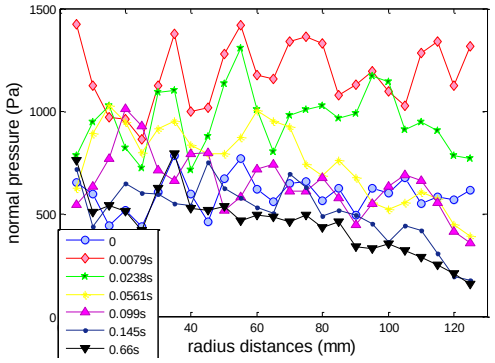
The factor of construction history refers to the other critical factor that resulting in the counter-intuitive phenomenon. A few temporal stages are considered with this preparation method to observe the progressive behaviour. The height of the sample is recorded to determine the critical progressive stages. Figure A.9 below displays the evolution of normal pressure on the base plane at different stages. For the tests, after removing the cylindrical boundary, the normal pressure on the base plane increases first. Then, the peak value of the normal pressure decreases during the formation of the sand pile. At each progressive stage, the peak pressure appears in the core region according to the graphs. Increasing the height of deposit layer, the pressure increases higher at the initial stage after removing the boundary.



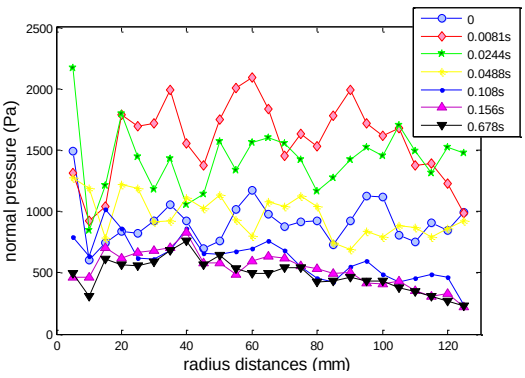
(a) $1.1h_0$



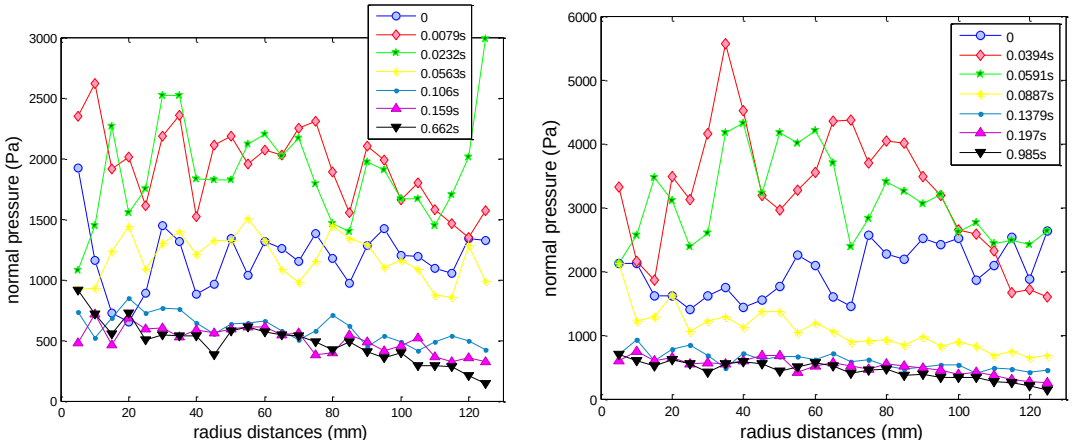
(b) $1.5h_0$



(c) $1.8h_0$



(d) $2.6h_0$



(e) $3.5h_0$ (f) $6.9h_0$

Figure A.9 The evolution of pressure distribution at different stages

The results show that the sand piles producing the similar shape of the sand pile and pressure distribution at the final stage with different heights of the deposit. According to the results, the behaviour is similar as long as the deposit height is larger than the height of the heap. For the full-scale simulation, concerning the computation effort, it is better to choose a lower deposit height of the sample. In order to guarantee enough number of particles inserted, the deposit height is selected as $1.5h_0$.

A.3 The impact of baffle

This part carries out the preliminary tests to study the influence of baffle on the behaviour of surface angle. Tests are performed with the boundary removal method under the Hertz contact model. Particles are uniformly distributed with the diameter in the span of $[1.2 \pm 0.4]mm$. To reduce the computation effort, the Young's modulus is decreased to 5MPa. The procedures are the same as the full-scale simulations. 2,030,000 number of particles, based on Section A.1, are generated for the preparation of samples. Two tests are carried out, one is with the baffle and the other one is without the baffle. Table A.2 below

presents the surface angles at different layers within the height of $40mm$. It shows the baffle has an influence of the surface angles. However, the effect is not that significant.

Table A.2 The results of surface angles inside sand pile

	With the baffle	**Without the baffle**
$[0,10]mm$	25.51°	23.87°
$[10,20]mm$	20.96°	21.95°
$[20,30]mm$	20.63°	21.45°
$[30,40]mm$	17.31°	19.57°

B. Developed technique for RVE material behaviour

B.1 Information of the algorithm in LIGGGHTS

The following flow chart presents the programme of boundary information in LIGGGHTS.

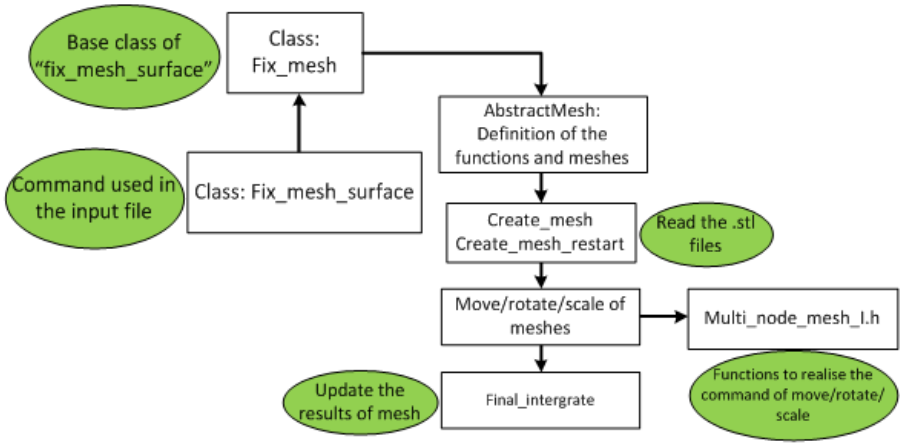


Figure B.1 The flow chart of the programme for the boundary information in LIGGGHTS

The following flow chart provides the programme for the estimation of contact forces and contact points in LIGGGHTS. It also includes the procedures for outputting the results with this software.

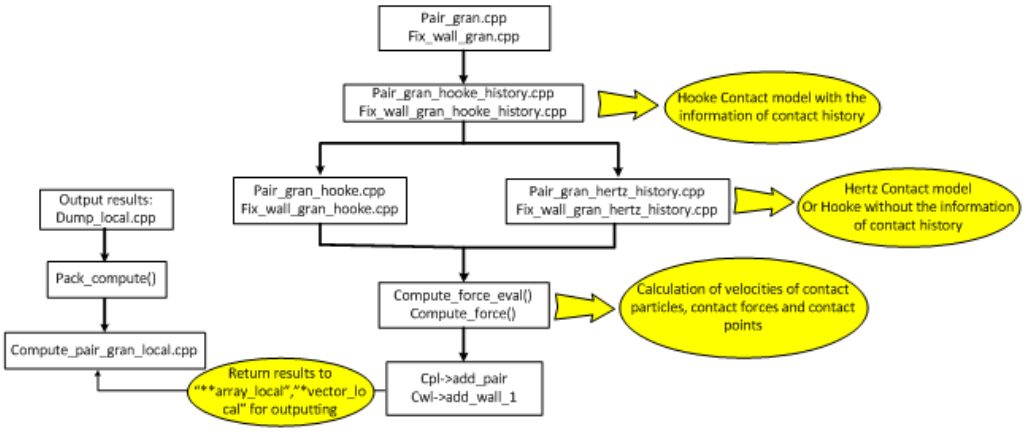
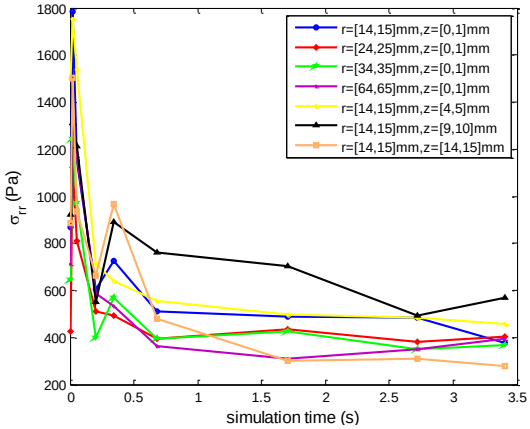


Figure B.2 The flow chart for the calculation of contact forces in LIGGGHTS

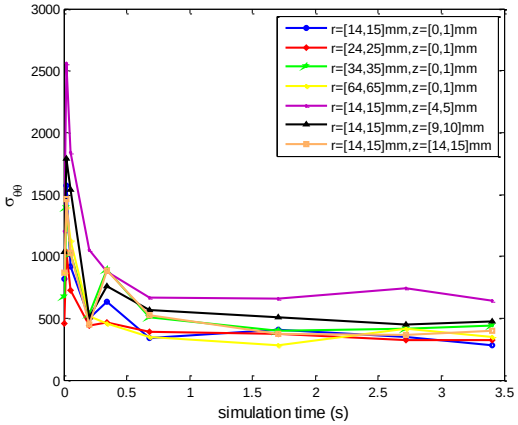
C. Particle-scale mechanisms of sand piles

C.1 The stress behaviour at different representative element regions

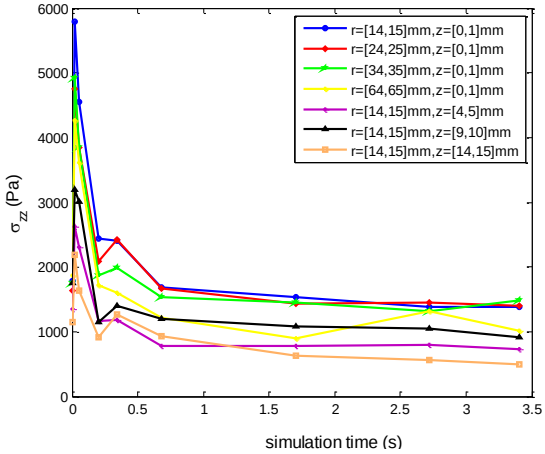
Figure C.1 to Figure C.3 present the progressive stress behaviour under various preparation methods respectively. The evolution of stress in the principal stress directions is similar in each test. In the boundary removal method, for each region, the pressure firstly increases after removing the boundary and then continuously reduces during the formation of the sand pile. However, for the rain and point deposition tests, the pressure increases continuously with the particle deposition during the development of the sand pile.



(a) σ_{rr}

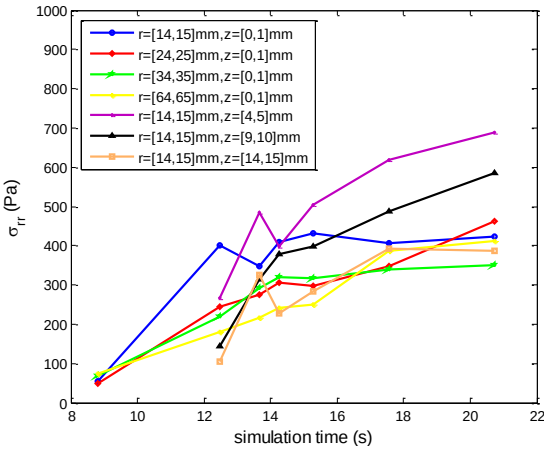


(b) $\sigma_{\theta\theta}$

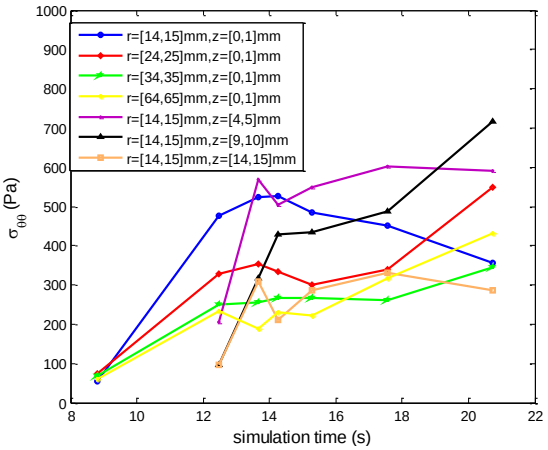


(c) σ_{zz}

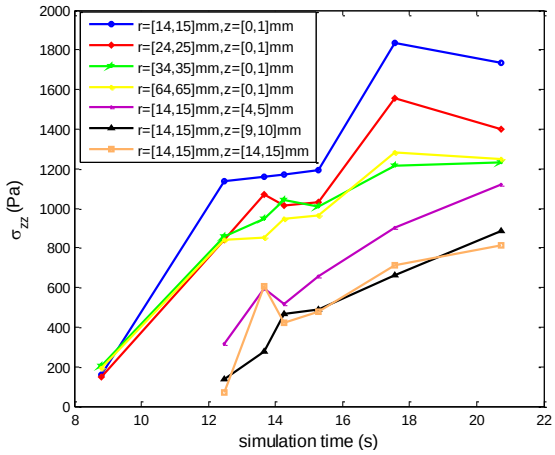
Figure C.1 The progressive behaviour of stress components for the boundary removal test



(a) σ_{rr}

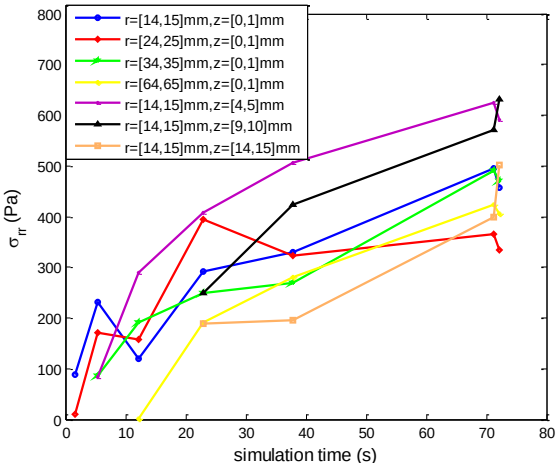


(b) $\sigma_{\theta\theta}$

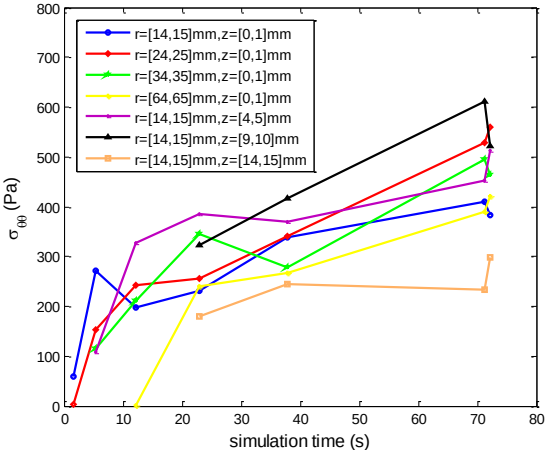


(c) σ_{zz}

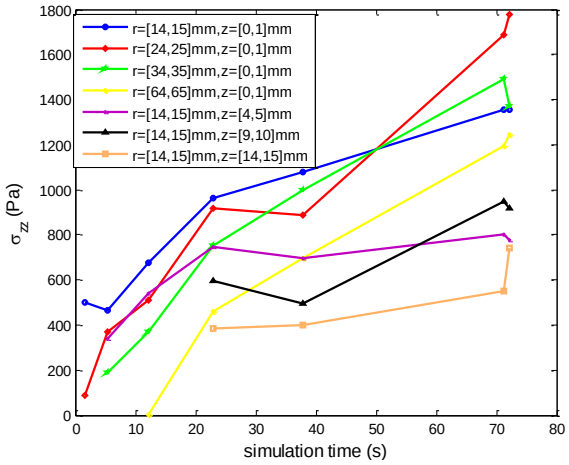
Figure C.2 The progressive behaviour of stress components for the rain deposition test



(a) σ_{rr}



(b) $\sigma_{\theta\theta}$



(c) σ_{zz}

Figure C.3 The progressive behaviour of stress components for the point deposition test

References

Ai, J. (2010). "Particle scale and bulk scale investigation of granular piles and silos." PHD thesis, The University of Edinburgh.

Ai, J., Chen, J. F., Rotter, J. M., & Ooi, J. Y. (2011). "Numerical and experimental studies of the base pressures beneath stockpiles." Granular Matter **13**: 133-141.

Ai, J., Ooi, J. Y., Chen, J., Rotter, J. M., & Zhong, Z (2013). "The role of depostion process on pressure dip formation underneath a granular pile." Mechanics of materials **66**: 160-171.

Al Hattamleh, O., Muhunthan, B., & Zbib, H. M. (2005b). "Stress distribution in granular heaps using multi-slip formulation." International Journal for Numerical and Analytical Methods in Geomechanics **29**(7): 713-727.

Alshibli, K. A., & Hasan, A. (2008). "Spatial variation of void ratio and shear band thickness in sand using X-ray computed tomography." Géotechnique **58**(4): 249-257.

Anand, L., & Gu, C. (2000). "Granular materials: constitutive equations and strain localization." Journal of the Mechanics and Physics of Solids **48**(8): 1701-1733.

Arthur, J. R. F., Chua, K. S., & Dunstan, T. (1977). "Induced anisotropy in a sand." Géotechnique **27**: 13-30.

Arthur, J. R. F., Chua, K. S., Dunstan, T., & Rodriguez, C. J. I. (1980). "Principal stress rotation: a missing parameter." J. Geotech. Eng., ASCE **106**: 419-433.

Bathurst, R. J., & Rothenburg, L. (1990). "Observations on stress-force-fabric relationships in idealized granular materials." Mechanics of Materials **9**: 65-80.

Belkhatir, M., Missoum, H., Arab, A., Della, N., & Schanz, T. (2011). "Undrained shear strength of sand-silt mixture: Effect of intergranular void ratio and other parameters." KSCE Journal of Civil Engineering **15**(8): 1335-1342.

Bolton, M. D. (1986). "The strength and dilatancy of sands." Géotechnique **36**: 65-78.

Bouchaud, J. P., Cates, M. E., & Claudin, P. (1995). "Stress distribution in granular media and nonlinear wave equation." J. Phys. I France **5**(6): 639-656.

Bouchaud, J. P., Cates, M. E., & Claudin,P. (1995). "Stress distribution in granular media and nonlinear wave equation." J. Phys. I France **5**: 639-656.

Brewer, R. (1964). "Fabric and mineral analysis of soils." John Wiley and Sons, Inc: 129-158.

Broms, B. B., & Casbarian, A. O. (1965). "Effects of rotation of the principal stress axes and of the intermediate principal stree on the shear strength." In Proceedings of the sixth International Conference on Soil Mechanics and Foundation Engineering, Montréal, Que., : 8-15.

Casagrande, A., & Carrillo, N. (1944). "Shear failure of anisotropic materials." Journal of the Boston Society of Civil Engineers **31**: 122-135.

Cates, M. E., Wittmer, J. P., & Claudin, P. (1998). "Development of stresses in cohensionless poured sand." Phil. Trans. R. Soc. Lond. A **356**: 2535-2561.

Cates, M. E., Wittmer, J. P., Bouchaud, J. P., & Claudin, P. (1999). "Jamming and static stress transmission in granular materials." American Institute of Physics **9**(3): 511-522.

Chang, C. S., ASCE, M., & Yin, Z. Y. (2010). "Micromechanical modelling for inherent anisotropy in granular materials." Journal of Engineering Mechanics **136**: 830-839.

Chang, C. S., Matsushima, T., & Lee, X. (2003). "Heterogeneous strain and bonded granular strucutre change in triaxial specimens studied by computed tomography." ASCE **129**(11): 1295-1307.

Cui, L., & O'Sullivan, C. (2006). "Exploring the macro- and micro-scale response of an idealised granular material in the direct shear apparatus." Géotechnique **56**(7): 455-468.

Cundall, P. A. (1988). "Formulation of a three-dimensional distinct element model—— Part I. A scheme to detect and represent contacts in a system composed of many polyhedral blocks." Int. J. Rock Mech. Min. Sci. & Geomech. Abstr. **25**(3): 107-116.

Cundall, P. A., & Strack, O. D. L. (1978). "BALL-A progam to model granular media using the distinct element method." Technical note.

Cundall, P. A., & Strack, O. D. L. (1979). "The distinct element method as a tool for research in granular media, Part II." Report to National Science Foundation concerning Grant ENG76-20771: Dept. of Civil and Minerval Engineering, University of Minnesota.

Cundall, P. A., & Strack, O. D. L. (1979). "A discrete numerical model for granular assemblies." Geotechnique **29**(1): 47-65.

Derakhshani, S. M., Schott, D. L., & Lodewijks, G. (2015). "Micro-macro properties of quartz sand: Experimental investigation and DEM simulation." Powder Technology **269**: 127-138.

Desrues, J., Chambon, R., Mokni, M., & Mazerolle, F. (1996). "Void ratio evolution inside shear bands in triaxial sand specimens studied by computer tomography." Géotechnique **46**(3): 529-546.

Doanh, T., Dubujet, Ph., & Protière, X. (2013). "On the undrained strain-induced anisotropy of loose sand." Acta Geotechnica **8**: 293-309.

Dou, X., Mao, Y. J., & Zhang, Y. W. (2014). "Effects of contact force model and size distribution on microsized granular packing." Journal of Manufacturing Science and Engineering **136**(2): 021003 (021001-021009).

Drescher, A., & De Josselin, D. J. (1972). "Photoelastic verification of a mechanical model for the flow of a granular material." J. Mech. Phys. Solids **20**: 337-351.

Edwards, S. F., & Oakeshott, R. B. S. (1989). "The transmission of stress in an aggregate." Physical D **38**: 88-92.

Fonseca, J., O'sullivan, C., Coop, M. R., & Lee, P. D. (2013). "Quantifying the evolution of soil fabric during shearing using scalar parameters." Géotechnique **63**: 818-829.

Geng, J. F., Longhi, E., Behringer, R .P., & Howell, D. W. (2001b). "Memory in two-dimensional heap experiments." Physical Review E **64**(6): 060301(060301)-060301(060304).

Gennaro, V. D., Canou, J., Dupla, J. C., & Benahmed, N. (2004). "Influence of loading path on the undrained behaviour of a medium loose sand." Can. Geotech. J. **41**: 166-180.

Goldsmith, W. (1960). "Impact: the theory and phsical behaviour of colliding solids." London: Edward Arnold.

Hertz, H. R. (1882). "Ueber die Beruehrung elastischer Koerper (On the contact between elastic bodies)." J. reine und angewandte Mathematik **92**: 156-171.

Hong, D. C. (1993). "Stress distribution of a hexagonally packed granular pile." Physical Review E **47**(1): 760-762.

Hosseininia, E. S. (2007). "Investigating the micromechanical evolutions within inherently anisotropic granular materials using discrete element method." Granular Matter **14**: 483-503.

Hu, M. Y., O'Sullivan, C., Jardine, R. R., & Jiang, M. J. (2010). "Stress-induced anisotropy in sand under cyclic loading." Granular Matter **12**(5): 469-476.

Hummel, F. H., & Finnan, E. J. (1920). "The distribution of pressure on surfaces supporting a mass of granular material." Proc. Instn. Civil Eng. **212**: 369-392.

Huntley, J. M. (1993). "Vacancy effects on the force distribution in a two-dimensional granular pile." Physical Review E **48**(5): 4099-4101.

Ishihara, K., & Li, S.-I., (1972). "Liquefaction of saturated sand in triaxial torsion shear test." Soils and Foundations **12**(2): 19-39.

Ishihara, K., & Towhata, I., (1983). "Sand response to cyclic rotation of principal stress directions as induced by wave loads." Soils and Foundations **23**(4): 11-26.

Janssen, H. A. (1895). "Versuche über getreidedruck in silozellen." Zeitschrift Verein Ingenieure **39**: 1045-1049.

Jardine, R. J., & Menkiti, C. O. (1999). "The undrained anisotropy of K_0 consolidated sediments." In: Geotechnical Engineering for Transportation Infrastructure. Balkema, Rotterdam: 1101-1108.

Johnson, K. L. (1985). "Contact mechanics." Cambrige University Press.

Jotaki, T., & Moriyama, R. (1979). "On the bottom pressure distribution of the bulk materials piled with the angle of repose." Journal of the society of Powder Technology Japan **16**(4): 184-191.

Kanatani, K.-I. (1984). "Distribution of directional data and fabric tensors." International Journal of Engineering Science **22**(2): 149-164.

Kloss, C., & Goniva, C. (2010). "LIGGGHTS-A new open source discrete element simulation software." Proceedings of the fifth international conference on discrete element methods, London, UK, 25-26 August, ISBN 978-0-9551179-8-5.

Klotz, C., Beutinger, P. H., & Vermeer, P. A. (2003). "Effects of inherent anisotropy and mode of sheearing on the behaviour of geomaterials." 16th Engineering Mechanics Conference, University of Washington, Seattle, USA.: 16-17-2003.

Konagai, K., Tamura, C., Rangelow, P., & Matsushima, T. (1992). "Laser-aided tomography: A tool for visulization of changes in fabric of granular assemblage." Struct. Eng./Earthquake Eng. **9**(30): 193-201.

Kruyt, N. P. (2012). "Micromechanical study of fabric evolution in quasi-static deformation of granular materials." Mechanics of Materials **44**: 120-129.

Kumruzzaman, M., & Yin, J. H. (2010). "Influence of principal stress direction on the stress-strain-strength behaviour of completely decomposed granite." Architecture and Civil Engineering, Facta Universitatis **8**: 79-97.

Kurkuri, M. D., Randall, C., & Losic, D. (2012). "New method of measuring the angle of repose of hard wheat grain." In Chemeca 2012: Quality of life through chemical engineering: 23-26 September 2012, Wellington, New Zealand. Barton, A.C.T.: Engineers Australia, 2012: 1814-1821.

Lade, P. V. D., J. M. (1973). "Cubical triaxial tests on cohesionless soil." Journal of Soil Mechanics and Foundations **99**: 793-812.

Lee, X., & Dass, W. C. (1993). "An experiment study of granular packing structure changes under loads." In C. Thornton, editor, Powders & Grains **93**: 17-22.

Li, E. L., & Bagster, D. F. (1990). "A new block model of heaps." Powder Technology **63**: 277-283.

Li, X., & Yu, H.-S. (2009). "Influence of loading direction on the behaviour of anisotropic granular materials." International Journal of Engineering Science **47**: 1284-1296.

Li, X., & Yu, H.-S. (2010). "Numerical investigation of granular material behaviour under rotational shear." Géotechnique **60**(5): 381-394.

Li, X., & Yu, H.-S. (2011). "Applicability of stressforcefabric relationship for non-proportional loading." Computers & Structures **89**(11-12): 1094-1102.

Li, X., & Yu, H.-S. (2013). "On the stress-force-fabric relationship for granular materials." International Journal of Solids and Structures **50**(9): 1285-1302.

Li, X., & Yu, H.-S. (2014). "Fabric, force and strength anisotropies in granular materials: a micromechanical insight." Acta Mechanica **225**(8): 2345-2362.

Li, X., Yang, D. S., & Yu, H.-S. (2016). "Macro deformation and micro structure of 3D granular assemblies subjected to rotation of principal stress axes." Granular Matter **18**(53).

Li, X., Yu, H.-S., & Li, X.-S. (2013). "A virtual experiment technique on the elementary behaviour of granular materials with DEM." International Journal for Numerical and Analytical Methods in Geomechanics **37**: 75-96.

Li, X. S., & Dafalias, Y. F. (2000). "Dilatancy for cohesionless soils." Géotechnique **50**: 449-460.

Li, X. S., & Dafalias, Y. F. (2012). "Anisotropic Critical State Theory: Role of Fabric." Journal of Engineering mechanics **138**: 263-275.

Li, Y., Xu, Y., & Thornton, C. (2005). "A comparison of discrete element simulations and experiments for 'sandpiles' composed of spherical particles." Powder Technology **160**(3): 219-228.

Liffman, K., Chan, D. Y. C., & Hughes, B. D. (1992). "Force distribution in a two dimensional sandpile." Powder Technology **72**: 255-267.

Liffman, K., Chan, D. Y. C., & Hughes, B. D. (1994). "On the stress depression under a sandpile." Powder Technology **78**: 263-271.

Liu, J. G., Sun, Q. C., & Jin, F. (2011). "The influence of flow rate on the decrease in pressure beneath a conical pile." Powder Technology **212**(1): 296-298.

Lizak, M. J., Conradi, M. K., & Fry, C. G. (1991). "NMR imaging of gas imbibed into porous ceramic." J. Magn. Reson **95**: 458-557.

Lumay, G., Boschini, F., Traina, K., Bontempi, S., Remy, J.-C., Cloots, R., & Vandewalle, N. (2012). "Measuring the flowing properties of powders and grains." Powder Technology **224**: 19-27.

Mindlin, R. D. (1949). "Compliance of elastic bodies in contact." Trans. ASME, Series E, Journal of Applied Mechanics **16**: 259-268.

Miura, K., Miura, S., & Toki, S. (1986). "Deformation behaviour of anisotropic dense sand under principal stress axes rotation." Soils and Foundations **26**(1): 36-52.

Mulilis, P. J., Seed, H. B., Chan, C., Mitchell, J. K., & Arulanandan, K. (1977). "Effect of sample preparation on sand liquefaction." Journal of the Geotechnical Engineering Division **103**(2): 91-109.

Nakashima, H., Shioji, Y., Kobayashi, T., Aoki, S., Shimizu, H., & Miyasaka, J. (2011). "Determining the angle of repose of sand under low-gravity conditions using discrete element method." Journal of Terramechanics **48**(1): 17-26.

Nakata, Y., Hyodo, M., Murata, H., & Yasufuku, N. (1998). "Flow deformation of sands subjected to principal stress rotation." Soils and Foundations **38**: 115-128.

Naughton, P. J., & O'Kelly, B. C. (2004). "The induced anisotropy of Leighton Buzzard sand." Proceedings Advances in Geotechnical Engineering: The Skempton Conference, London, 29th-31st March, 2004 **1**: 556-567.

O'Sullivan, C., & Bray, J. D. (2004). "Selecting a suitable time step for discrete simulations that use the central difference time intergration scheme." Engin. Comput. **21**: 278-303.

O'Sullivan, C., & Cui L. (2009). "Fabric evolution in granular materials subjected to drained, strain controlled cyclic loading." 6th International Conference on the Micromechanics of Granular Media, Publisher: AMER INST PHYSICS: 285-+, ISSN:0094-0243X.

Ochiai, H., & Lade, P.V. (1983). "Three-dimensional behaviour of sand with anisotropic fabric." Journal of Geotechnical Engineering **109**: 1313-1328.

Oda, M. (1972a). "Initial fabrics and their relations to mechanical properties of granular material." Soils and Foundations **12**: 17-36.

Oda, M. (1978). "Co-ordination number and its relation to shear strength of granular materals." Soils and Foundations **17**(2): 29-42.

Oda, M., & Iwashita, K. (1999). "Introduction to mechanincs of granular materials." A.A.Balkema, Rotterdam.

Oda, M., & Nakayama, H. (1989). "Yield function for soil with anisotropic fabric." Journal of Engineering Mechanics **115**(1): 89-104.

Oda, M., Nemat-Nasser, S., & Konishi, J. (1985). "Stress-induced anisotropy in granular masses." Soils and Foundations **25**(3): 85-97.

Oda, M., Takemura, T., & Takashi, M. (2004). "Microstructure in shear band observed by microfocus X-ray computed tomography." Géotechnique **54**(8): 539-542.

Ooi, J. Y., Ai, J., Zhong, Z., Chen, J. F., & Rotter, J. M. (2008). "Progressive pressure measurements beneath a granular pile with and without base deflection." Structures and granular solids: from scientific principles to engineering applications, London **CRC Press**: 87-92.

Ouadfel, H., & Rothenburg, L. (2001). "'Stress-force-fabric' relationship for assemblies of ellipsoids." Mechanics of Materials **33**(4): 201-221.

Papadimitriou, A. G., Dafalias, Y. F., & Yoshimine, M. (2005). "Plasticity modeling of the effect of sample preparation method on sand response." Soils and Foundations **45**(2): 109-123.

Parry, R. H. G. (1954). "Measurement of pressure distribution across the base of triangular section granular masses." MEng. thesis, Unoversity of Melbourne.

Parteli, E. J. R. (2013). "Using LIGGGHTS for performing DEM simulations of particles of complex shapes with the multisphere method." In: DEM6-6th International Conference on Discrete Element Method: 217-222.

Peacock, W. H., & Seed, H. B. (1968). "Sand liquefaction under cyclic loading simple shear conditions." In: Proceeding of ASCE **SM3**: 689-707.

Renzo, D. A., & Maio, Di F. P. (2004). "Comparison of contact-force models for the simulations of collisions in DEM-based granular flow codes." Chemical Engineering Science **59**: 525-541.

Rothenburg, L., & Bathurst, R. J. (1989). "Analytical study of induced anisotropy in idealizedd granular materials." Géotechnique **39**(4): 601.

Rothenburg, L., & Bathurst, R. J. (1993). "Influence of particle eccentricity on micromrchanical behavior of granular materials." Mechanics of Materials **16**(1-2): 141-152.

Rowe, P. W. (1962). "The stress-dilatancy relation for static equilibrium of an assembly of particles in contact " Proc., Royal Soc.: 500-527.

Savage, S. B. (1997). "Problems in the statics and dynamics of granular materials." Powders and Grains **97**: 185-194.

Savage, S. B. (1998). " Modeling and granular material boundary value problems." Physics of Dry Granular Media: 25-96.

Schellart, W. P. (2000). "Cohesion and friction coefficients of dry granular materials." Geological society of australia abstracts **59**: 441-441.

Schellart, W. P. (2000). "Shear test results for cohesion and friction coefficients for different graular materials: scaling implications for their usage in analogue modelling." Tectonophysics **324**: 1-16.

Sitharam, T. G., Dinesh, S. V., & Shimizu, N. (2002). "Micromechanical modelling of monotonic drained and undrained shear behaviour of granular media using three-dimensional DEM." International Journal for Numerical and Analytical Methods in Geomechanics **26**(12): 1167-1189.

Smid, J., & Novosad, J. (1981). "Pressure distribution under heaped bulk solids." Proceedings of 1981 Powtech. Conf., Ind. Chem. Eng. Symp. **63**: D3/V/1-D3/V/12.

Sutherland, H. B., & Mesdary, M. S. (1969). "The influence of the intermediate principal stress on the strength of sand." In Proceedings of the seventh international conference on soil mechanics and foundation engineering, Mexico city: 391-399.

Tanimoto, K., Nakamura, J., & Fudo, R. (1981). "Application of acoustic emission in in-situ test." Proc., 10th Int. Conf. on Soil Mechanics and Foundation Engineering, Stockholm, June 15-19, International Society of Soil Mechanics and Foundation Engineering **2**: 573-576.

Thornton, C. (2000). "Numerical simulation of deviatoric shear deformation of granular media." Géotechnique **50**: 43-53.

Thornton, C., & Zhang, L. (2010). "On the evolution of stress and microstructure during general 3D deviatoric straining of granular media." Géotechnique **60**(5): 333-341.

Tong, Z. X., Zhang, J.-M., Yu, Y. L., & Zhang, G. (2010). "Drained deformation behaviour of anisotropic sands during cyclic rotation of stress principal axes." Journal of Geotechanical and Geoenvironmental Engineering, ASCE **136**(11): 1509-1518.

Trollope, D. H. (1956). "The stability of wedges of granular material." PhD thesis, University of Melbourne.

Trollope, D. H. (1957). "The systematic arching theory applied to the stability analysis of embankments." Proc. 4th Intn, Conf. Soil Mech. and Found. Engnr, London: 382-388.

Trollope, D. H., & Burman, B. C. (1980). "Physical and numerical experiments with granular wedges." Geotechnique **30**(2): 137-157.

Tsuji, Y., Tanaka, T., & Ishida, T. (1992). "Lagrangian numerical simulation of plug flow of cohesionless particles in a horizontal pipe." Powder Technology **71**: 239-250.

Vaid, Y. P., Aivathayalan, S., & Stedman, D. (1999). "Influence of specimen-reconstituing method on the undrained response of sand." Geotechnical Testing Journal, GTJODJ **22**(3): 187-195.

Vaid, Y. P., Sayao, A., Hou, E. H., & Negussey, D. (1990). "Generalized stress path dependent soil behaviour with a new hollow cylinder torsional apparatus." Canadian Geotechnical Journal **27**: 601-616.

Vanel, L., Howell, D., Clark, D., Behringer, R. P., & Clement, E. (1999). "Memories in sand: Experimental tests of construction history on stress distributions under sandpiles." Physical Review E **60**(5): 5040-5043.

Vu-Quoc, L., & Zhang, X. (1999). "An elastoplastic contact force-displacement model in the normal direction: displacement-driven version." Proc. R. Soc. Lond. A **455**: 4013-4044.

Walton, O. R. (1993). "Numerical simulation of inelastic, frictional particle-particle interactions." In: Roco MC, editor. Particulate Two-Phase Flow, Stoneham, MA: Butterworth-Heinemann: 844-911 [chapter 825].

Wang, J. P., Li , X., & Yu, H.-S. (2015). "Amicromechanical interpretation of the capilliary effect of unsaturated granular material in a pendular state." 14th International Conference of International Association for Computer Methods and Recent Advances in Geomechanics, IACMAG 2014: Kyoto; Japan: 1563-1568.

Wang, L. B., Frost, J. D., & Lai, J. S. (2004). "Three-dimensional digital representation of granular material micorstructure from X-ray tomography imaging." J. Comput. Civ. Eng. **18**(1): 28-35.

Widulinski, L., Kozicki, J., & Tejchman, J. (2009). "Numerical simulations of Triaxial test with sand using DEM." Archives of Hydro-Engineering and Environmental Mechanics **56**(3-4): 149-171.

Wittmer, J. P., Claudin, P., Cates, M. E., & Bouchaud, J. P. (1996). "An explanation for the central stress minimum in sand piles." Nature **382**(25): 336-338.

Wood, D. M. (1991). "Soil behaviour and critical state soil mechanics." Cambrige University Press.

Yang, D. S. (2014). "Microscopic study of granular material behaviours under general stress paths." PhD thesis, University of Nottingham.

Yang, D. S., Li, X., & Yu, H.-S. (2015). "Fabric evolution of 3D granular materials in rotational shear." Geomechanics from Micro to Macro - Proceedings of the TC105 ISSMGE International Symposium on Geomechanics from Micro to Macro, IS-Cambridge 2014 **1**: 85-90.

Yang, L. T. (2013). "Experimental study of soil anisotropy using hollow cylinder testing." PhD thesis, The University of Nottingham.

Yang, Z. X., & Li, X. (2007). "Undrained anisotropy and rotational shear in granular soil." Géotechnique **57**: 371-384.

Yang, Z. X., Li, X. S., & Yang, J. (2007). "Undrained anisotropy and rotational shear in granular soil." Géotechnique **57**(4): 371-384.

Yimsri, S., & Soga, K. (2011). "Effects of soil fabric on behaviours of granular soils: Microscopic modeling." Computers and Geotechnics **38**: 861-874.

Yoshimine, M., & Koike, R. (2005). "Liquefaction of clean sand with stratified structure due to segregation of particle size." Soils and Foundations **45**(4): 89-98.

Yoshimine, M., Ishihara, K., & Vargas, W. (1998). "Effects of principal stress direction and intermediate principal stress on undrained shear behaviour of sand." Soils and Foundations **38**(3): 179-188.

Yu, H.-S., Yang, L. T., Li, X., & Wanatowski, D. (2015). "Experimental investigation on the deformation characteristics of granular materials under drained rotational shear." Geomechanics and Geoengineering: An International Journal.

Zhang, D., & Whiten, W. J. (1996). "The calculation of contact forces between particles using spring and damping models." Powder Technology **88**(1): 59-64.

Zhao, J. D., & Tong, S. (2013). "Coupled CFD-DEM simulation of fluid-particle interaction in geomechanics." Powder Technology **239**: 248-258.

Zheng, Q. J., & Yu, A. B. (2014). "Why have continuum theroies previously failed to describe sandpile formation?" Physical Review Letters **113**: 068001(068001)-068001(068005).

Zhou, C., & Ooi, J. (2009). "Numerical investigation of progressive development of granular pile with spherical and non-spherical particles." Mechanics of materials **41**(6): 707-714.

Zhou, Y. C., Wright, B. D., Yang, R. Y., Xu, B. H., & Yu, A. B. (1999). "Rolling friction in the dynamic simulation of sandpile formation." Physica A **269**: 536-553.

Zhou, Y. C., Xu, B. H., Yu, A. B., & Zulli, P. (2002). "An experiment and numerical study of the angle repose of coarse spheres." Powder Technology **125**(1): 45-54.

Zhou, Y. C., Xu, B. H., Zhou, R. P., Yu, A. B., & Zulli, P. (2003). "Stress distribution in a sandpile formed on a deflected base." Advanced Powder Technology **14**: 401-410.

Zhou, Z. Y., Zou, R. P., Pinson, D., & Yu, A. B. (2014). "Angle of repose and stress distribution of sandpiles formed with ellipsoidal particles." Granular Matter **16**: 695-709.

Zhu, H. N., Mehrabadi, M. M., & Massoudi, M. (2006). "Three-dimensional constitutive relations for granular materials based on the dilatant double shearing mechanism and the concept of fabric." International Journal of Plasticity **22**(5): 826-857.

Zhu, H. P., Zhou, Z. Y., Yang, R. Y., & Yu, A. B. (2007). "Discrete particle simulation of particulate systems: Theoretical developments." Chemical Engineering Science **62**: 3378-3396.

Zhu, J. Y., Liang, Y. Y., & Zhou, Y. H. (2013). "The effect of the particle aspect ratio on the pressure at the bottom of sandpiles." Powder Technology **234**: 37-45.

Zuriguel, I., & Mullin, T. (2008). "The role of particle shape on the stress distribution in a sandpile." Proceedings of the Royal Society A: Mathematical, Physical and Engineering Sciences **464**(2089): 99-116.

Zuriguel, I., Mullin, T., & Rotter, J. M. (2007). "Effect of particle shape on the stress dip under a sandpile." Physical Review Letters **98**(2): 028001(028001)-028001(028004).